

THE UNIVERSITY OF CHICAGO

SEARCHING FOR DFSZ AXINOS AT THE ATLAS EXPERIMENT, AND DEVELOPING  
NOVEL MACHINE LEARNING METHODS FOR HIGH-ENERGY PHYSICS

A DISSERTATION SUBMITTED TO  
THE FACULTY OF THE DIVISION OF THE PHYSICAL SCIENCES  
IN CANDIDACY FOR THE DEGREE OF  
DOCTOR OF PHILOSOPHY  
DEPARTMENT OF PHYSICS

BY  
JAN TUZLIĆ OFFERMANN

CHICAGO, ILLINOIS  
DECEMBER 2024

Copyright © 2024 by Jan Tuzlić Offermann  
All Rights Reserved

# CONTENTS

LIST OF FIGURES . . . . .	vii
LIST OF TABLES . . . . .	xvi
ACKNOWLEDGMENTS . . . . .	xxi
1 INTRODUCTION . . . . .	1
1.1 A road-map for this thesis: where to find things . . . . .	2
1.2 How to read this thesis: some notes on structure . . . . .	3
2 THE STANDARD MODEL OF PARTICLE PHYSICS, AND SUPERSYMMETRY . . . . .	5
2.1 The Standard Model . . . . .	5
2.1.1 Properties of the Standard Model . . . . .	6
2.1.2 Particles of the Standard Model . . . . .	13
2.2 Issues with the Standard Model . . . . .	25
2.2.1 Dark Matter . . . . .	26
2.2.2 The hierarchy problem . . . . .	26
2.3 Supersymmetry . . . . .	27
2.3.1 The Minimal Supersymmetric Standard Model . . . . .	28
3 AXION AND AXINO PHYSICS . . . . .	31
3.1 Peccei-Quinn theory, and the QCD axion . . . . .	31
3.1.1 CP symmetry and violation . . . . .	31
3.1.2 Peccei-Quinn theory . . . . .	34
3.2 Axinos, and their Phenomenology at Collider Experiments . . . . .	36
4 THE ATLAS EXPERIMENT . . . . .	41
4.1 The Large Hadron Collider (LHC) . . . . .	41
4.1.1 The LHC experiments . . . . .	43
4.1.2 Producing the LHC proton beam . . . . .	44
4.1.3 Proton beam structure . . . . .	44
4.1.4 Colliding beams: Luminosity and Pileup . . . . .	46
4.2 The ATLAS Experiment . . . . .	51
4.2.1 A Foreword: Some Collider Terminology and Concepts . . . . .	52
4.2.2 The ATLAS Inner Detector . . . . .	60
4.2.3 The ATLAS Magnet System . . . . .	65
4.2.4 The ATLAS Calorimeters . . . . .	68
4.2.5 The ATLAS Muon Spectrometer . . . . .	72
4.2.6 The ATLAS Triggering System . . . . .	80
4.2.7 Phase-I Upgrade . . . . .	83
4.2.8 Phase-II Upgrade . . . . .	84

5	SEARCHING FOR DISPLACED VERTICES AND MISSING TRANSVERSE ENERGY AT THE ATLAS EXPERIMENT . . . . .	99
5.1	Introduction . . . . .	99
5.1.1	What is an analysis? . . . . .	100
5.1.2	Searching for long-lived particles: Some general comments . . . . .	100
5.2	Signal Models . . . . .	101
5.2.1	Gluino $R$ -hadrons . . . . .	102
5.2.2	Wino-Bino co-annihilation . . . . .	103
5.2.3	Higgs Portal . . . . .	105
5.2.4	Axinos . . . . .	106
5.3	Event Reconstruction . . . . .	108
5.3.1	Inner Detector Reconstruction . . . . .	109
5.3.2	High-Level Object Reconstruction . . . . .	114
5.4	Event Selection, Region Definitions and Expected Yields . . . . .	122
5.4.1	Defining event regions, and blinding . . . . .	122
5.4.2	Common signal region definitions: the MTR . . . . .	124
5.4.3	1 VSI DV Analysis Channel . . . . .	130
5.4.4	1 FV Analysis Channel . . . . .	137
5.4.5	2 FV Analysis Channel . . . . .	145
5.4.6	Expected Signal Yields . . . . .	147
5.5	Background Estimation . . . . .	153
5.5.1	Inclusive Background Estimate: 1 DV Analysis Channels . . . . .	156
5.5.2	Combined Background Estimate for the 1 VSI DV Analysis Channel . . . . .	160
5.5.3	Inclusive Background Estimate: 2 FV Analysis Channel . . . . .	171
5.5.4	Summary of Background Estimates . . . . .	175
5.6	Uncertainties . . . . .	175
5.6.1	Background Estimate Uncertainties . . . . .	176
5.6.2	Summary of Background Uncertainties . . . . .	180
5.6.3	Signal Yield Uncertainties . . . . .	181
5.7	Results: Yields and Setting Limits . . . . .	191
5.7.1	Event Yields . . . . .	191
5.7.2	Setting Limits: Constraining Our Signal Models . . . . .	195
5.7.3	Final Remarks . . . . .	207
6	LORENTZ-EQUIVARIANT MACHINE LEARNING . . . . .	208
6.1	Computer vision: A motivational story . . . . .	208
6.2	Equivariant Neural Networks, and PELICAN . . . . .	211
6.2.1	Equivariant Network Architectures . . . . .	211
6.2.2	PELICAN . . . . .	212
6.3	Identifying hadronic top quark decays with PELICAN . . . . .	215
6.3.1	Measuring momenta in top quark decays . . . . .	216
6.4	Conclusions, and further directions . . . . .	222
7	CONCLUSION . . . . .	227

APPENDICES . . . . .	228
APPENDIX A DISPLACED VERTICES AND MISSING TRANSVERSE ENERGY SEARCH AT THE ATLAS EXPERIMENT: OVERFLOW . . . . .	228
A.1 Tracking in ATLAS: A brief review . . . . .	228
A.2 Overlap Removal . . . . .	231
A.3 Tracking and Secondary Vertexing Efficiency . . . . .	232
A.4 Missing transverse energy triggers . . . . .	233
A.5 Comparison of MTR and PTR Kinematics . . . . .	237
A.6 Track Jets . . . . .	237
A.7 The SuperLooseBadLLP Jet Cleaning Working Point . . . . .	240
A.8 Dead TileCal Modules . . . . .	241
A.9 VSI Track Hit Pattern Check . . . . .	242
A.10 Material Map Veto . . . . .	242
A.11 Axino Signal Sensitivity . . . . .	245
A.12 Inclusive Background Estimate: Extended EDP . . . . .	245
A.13 Inclusive Background Estimate: The Hybrid Method . . . . .	248
A.14 Hadronic Interactions Background Estimate Validation . . . . .	249
A.15 Accidental Crossing Background Estimate Details . . . . .	251
A.15.1 Producing Mass Templates . . . . .	251
A.15.2 Estimating Accidental Crossing Rate . . . . .	254
A.16 Tracking Systematic uncertainty Estimate Details . . . . .	255
A.17 Asymptotic Likelihood Test Statistic . . . . .	257
APPENDIX B SPECIAL RELATIVITY AND THE LORENTZ GROUP . . . . .	260
B.1 Metrics and Minkowski Space . . . . .	260
B.2 Lorentz Transformations . . . . .	262
B.3 Invariance, Covariance, and Equivariance . . . . .	265
APPENDIX C THE HIGGS BOSON HIERARCHY PROBLEM . . . . .	267
APPENDIX D THE NEUTRON ELECTRIC DIPOLE MOMENT . . . . .	270
D.1 Charge, parity and time reversal transformations . . . . .	270
D.2 Connecting the neutron electric dipole moment to CP violation . . . . .	271
D.3 Measuring the nEDM . . . . .	272
APPENDIX E HADRONIC JETS . . . . .	274
E.1 Color confinement: Why are jets necessary? . . . . .	274
E.2 Reconstructing jets: Inputs and Algorithms . . . . .	276
E.2.1 The anti- $k_t$ algorithm . . . . .	277
E.2.2 Infrared and Colinearity Safety . . . . .	279
E.2.3 Inputs to clustering: Identifying showers and displacement . . . . .	280
E.2.4 Jet energy scale calibrations . . . . .	280

APPENDIX F	PARTICLE DETECTORS . . . . .	283
F.1	Sampling Calorimeters . . . . .	283
F.2	Electromagnetic and Hadronic Calorimeters . . . . .	284
F.3	Gaseous Detectors: Proportional Counters and Geiger-Müller Tubes . . . . .	285
F.4	Photomultiplier Tubes . . . . .	286
APPENDIX G	MEASURING PHOTOMULTIPLIER TUBE DARK CURRENTS FOR THE MILLIQAN EXPERIMENT . . . . .	289
G.1	The milliQan experiment . . . . .	289
G.2	Characterizing PMT dark current . . . . .	289
REFERENCES	. . . . .	294

## LIST OF FIGURES

2.1	The particle content of the Standard Model, indicating the mass, electric charge and spin of each particle, as well as left- and right-handed hypercharge and weak isospin charges. Modified from Ref. [8], with the particle masses taken from Ref. [9]. The top quark mass shown here is the result from direct measurements at the LHC (currently in tension with indirect measurements from electroweak precision data, via cross-section measurements, at the level of $\sim 1.7\sigma$ [9]). The neutrino mass limits from Ref. [9] correspond with limits on $m_{\nu x}^{2(\text{eff})} \equiv \sum_i  U_{xi} ^2 m_{\nu i}^2$ where $U$ is the PMNS matrix and $x \in \{e, \mu, \tau\}$ (see Section 2.1.2.1). For the electron neutrino $\nu_e$ , mass measurements corresponding to antineutrino $\bar{\nu}_e$ are used. . . . .	7
2.2	An example Feynman diagram, including a loop. Particles only present in intermediate states can be off-shell. Here, explicit particle labels have been omitted for clarity. . . . .	15
2.3	An example Feynman diagram of muon decay. . . . .	17
2.4	Lifetimes and masses of the Standard Model. Some particles are excluded, such as quarks other than the top quark (which hadronize before decay, as discussed in Appendix E.1), or hadrons where multiple (excited) states have very similar masses and lifetimes. Modified from Ref. [26], with masses taken from Ref. [9]. . . . .	19
3.1	An overview of current limits on axions, in terms of axion mass and axion-photon coupling. Note that as shown in (b), under the assumption of SUSY, the DFSZ axion line shifts. Taken from Ref. [82], with (b) modified to show the SUSY DFSZ line. . . . .	37
3.2	The $\tilde{\chi}_1^0$ mean lifetime $c\tau$ as a function of its mass, as approximated by Equation 3.9. Taken from Ref. [84]. . . . .	39
4.1	A schematic of the accelerators used to produce the proton beam used by the LHC [86], together with the various experiments that utilize these accelerators – note that the four main experiments are stationed along the LHC ring, while others are connected to the smaller accelerators that feed into the LHC. The relevant sequence for the LHC is LINAC4 $\rightarrow$ BOOSTER $\rightarrow$ PS $\rightarrow$ SPS $\rightarrow$ LHC. . . . .	42
4.2	A schematic of the charge-exchange injection performed during the injection of $H^-$ ions from Linac4 into the PSB. Modified from Ref. [90]. . . . .	45
4.3	An outline of the original proposed LHC bunch structure. Note that the current bunch structure is different than that shown here, but the general principles are unchanged: the inter-bunch spacings are set by the PS $\rightarrow$ SPS $\rightarrow$ LHC injection scheme. Modified from Ref. [94]. . . . .	47
4.4	A schematic showing the crossing of two proton beams – or rather bunches of protons – at some crossing angle $\phi$ . For the high-luminosity (HL) LHC upgrade, the proton bunches will be rotated via RF pulses from <i>crab cavities</i> prior to collision, so that the two bunches will maximally overlap at the collision point [97]. . . . .	49

4.5	Various Standard Model cross-sections as measured by the ATLAS experiment, indicated by the (parton-level) final state produced. “Jets” refers to the collimated streams of hadrons produced by quark and gluon emission, discussed in Section 4.2.1.5 and Appendix E. The proton-proton cross-section is also included in the left-most bin. From Ref. [98]. . . . .	50
4.6	The integrated luminosity of $pp$ collisions delivered to the ATLAS experiment. Note the increase in the maximum slope of the curves after 2012, corresponding with an increase in the maximum instantaneous luminosity. Taken from Ref. [99].	51
4.7	The $B^0$ -meson lifetime in the lab reference frame, as a function of its speed $\beta$ (as a fraction of the speed of light in vacuum). . . . .	58
4.8	A highlight of the components of the ATLAS Inner Detector. Taken from Ref. [104].	61
4.9	An overview of the ATLAS Inner Detector design, highlighting the barrel and end-cap components of each detector system. Taken from Ref. [105]. . . . .	62
4.10	Renderings of the Pixel detector, showing (a) an exploded side view of the barrel and end-cap sections, and (b) a frontal view of the barrel section. Produced using the VP1 software package [108]. . . . .	63
4.11	A cross-sectional diagram of the Pixel and SCT detectors. Produced using the VP1 software package [108]. . . . .	65
4.12	A highlight of the components of the ATLAS magnet system. Taken from Ref. [104].	67
4.13	A highlight of the components of the ATLAS calorimeters. Taken from Ref. [104].	69
4.14	Diagrams showing the basic layout of the (a) barrel and (b) end-cap sections of the ATLAS liquid argon calorimeter. Taken from Ref [118]. . . . .	70
4.15	A schematic showing the structure of the ATLAS liquid argon calorimeter in the central barrel section. Note that the calorimeter consists of three concentric cylindrical structures with differing $\eta$ granularity. Taken from Ref. [118]. . . . .	71
4.16	A schematic of a single TileCal module. Taken from Ref. [120]. . . . .	73
4.17	A rendering of the TileCal structure. Taken from Ref. [120]. . . . .	73
4.18	A schematic showing the division of TileCal into different towers. Taken from Ref. [121]. . . . .	74
4.19	A highlight of the components of the ATLAS muon spectrometer. Taken from Ref. [104]. . . . .	74
4.20	A schematic of the muon spectrometer layout. Taken from Ref. [122]. . . . .	75
4.21	A cross-section of a Monitored Drift Tube in the ATLAS muon spectrometer. Note the curved drift path produced by the muon, which is a consequence of the MDT being located within the detector’s magnetic field. Taken from Ref. [122].	77
4.22	A schematic of a Resistive Plate Chamber in the ATLAS muon spectrometer, showing multiple units encased in the insulating “sandwich structure”. Taken from Ref. [122]. . . . .	78
4.23	A schematic of Thin Gap Chambers in the ATLAS muon spectrometer, showing both “triplet” and “doublet” configurations with the TGCs spaced apart by paper honeycomb structures. Note that the gap sizes shown have been enlarged for detail. Taken from Ref. [122]. . . . .	79

4.24	A schematic of a Cathode Strip Chamber in the ATLAS muon spectrometer. Taken from Ref. [122]. . . . .	79
4.25	An overview of the ATLAS TDAQ system for Run 2. Note that this system has since been significantly updated for Run 3. Also note that the Fast Tracker (FTK) was not deployed – it was used only for testing purposes, and the project has since been deprecated. Taken from Ref. [124]. . . . .	82
4.26	A schematic of the MicroMegas detectors. Taken from Ref. [126]. . . . .	84
4.27	An overview of the ATLAS TDAQ system for Run 3. Taken from Ref. [130]. . . . .	85
4.28	An overview of the ITk and HGTD layout. Taken from Ref. [134]. . . . .	86
4.29	An overview of the ATLAS TDAQ system for the Phase-II upgrade. Taken from Ref. [136]. . . . .	87
4.30	An overview of the Global Event Processor design. Taken from Ref. [135]. . . . .	88
4.31	The (a) uncalibrated and (b) calibrated trigger jet mean $E_T$ response, as a function of jet $\eta$ (and binned in jet $E_T$ ). The calibration is evaluated in MC simulation with respect to EM-scale Particle Flow jets (which are first calibrated with respect to truth-level jets). . . . .	90
4.32	A CNN topo-cluster classifier network architecture, corresponding with “CNN (separated EMB1 layer)” in Figures 4.36 and 4.36. The “EMB” and “Tile” images correspond with samplings of the electromagnetic barrel and Tile calorimeters. Taken from Ref. [141]. . . . .	91
4.33	Topo-cluster kinematics for the MC simulation used to train and test the topo-cluster classifiers, showing the (a) number of cells per cluster, (b) uncalibrated cluster energy, (c) cluster $\eta$ , and (d) truth cluster energies. . . . .	92
4.34	Topo-cluster images produced by a charged pion and a neutral pion in (a) the 3 EMB calorimeter samplings, and (b) the 3 TileCal samplings. Each pion has an energy of approximately 115 GeV, and $\eta = 0.6$ . . . . .	94
4.35	Topo-cluster images produced by a charged pion and a neutral pion in (a) the 3 EMB calorimeter samplings, and (b) the 3 TileCal samplings. Each pion has an energy of approximately 13 GeV, and $\eta = -0.7$ . . . . .	95
4.36	A set of ROC curves for various neural network methods developed for $\pi^\pm/\pi^0$ classification in the ATLAS calorimeters. The existing LCW method is also shown for comparison. . . . .	96
4.37	The false positive rate – the rate at which the classifier incorrectly identifies $\pi^0$ topo-clusters as $\pi^\pm$ topo-clusters – at a set of different fixed true positive rates, for the classifiers shown in Figure 4.36. . . . .	97
5.1	The “gluino $R$ -hadron” process. Note that the hadronization of the gluino is not explicitly shown in the Feynman diagram, but is implied: the gluino decay vertices are displaced. Taken from Ref. [143]. . . . .	103
5.2	The “Wino-Bino co-annihilation ” process. Taken from Ref. [143]. . . . .	104
5.3	An example Higgs Portal process, where the Higgs boson is produced by gluon-gluon fusion. This analysis targets this Higgs production mechanism – production with an associated vector boson ( $VH$ ) – as well as production with associated top quarks ( $ttH$ ) and production via gluon-gluon fusion. . . . .	105

5.4	An example Feynman diagram of the axino process. The $Z^*$ is very off-shell, and its decay products effectively invisible to the detector. Taken from Ref. [143].	107
5.5	An overview of the parameter grid used to scan the axino model. Here, $m_{n1}$ refers to the $\tilde{\chi}_1^0$ mass, and $m_{\text{axino}}$ to the $\tilde{\chi}_5^0$ mass (which is the same as the pure axino mass).	107
5.6	BDT scores for the 3 BDTs used by the fuzzy vertexing algorithm. Adapted from Ref. [143].	116
5.7	An overview of the production of seed collections and final vertex merging, in the fuzzy vertexing algorithm. Taken from Ref. [143].	116
5.8	The distribution of the azimuthal direction of $\vec{\cancel{E}}_T$ in the MTR, with and without a standard jet cleaning selection applied. The peaks correspond with NCB from beam halo effects, and the standard jet cleaning has practically no effect on the distribution – necessitating construction of a dedicated NCB veto. Taken from Ref. [143].	128
5.9	The distribution of the azimuthal direction of $\vec{\cancel{E}}_T$ in the MTR, with and without the NCB veto applied. The veto significantly reduces the magnitude of the peaks in the distribution, bringing it closer to the expected flat shape <sup>[1]</sup> . Taken from Ref. [143].	129
5.10	The distribution of the azimuthal direction of $\vec{\cancel{E}}_T$ , in the MTR, with and without the dead tile module veto applied. For reference, the distribution with and without the NCB veto is also shown, as in Figure 5.9. On top of the NCB veto, the dead tile module further reduces the peaks (although less significantly). Taken from Ref. [143].	130
5.11	The track cleaning efficiency for a range of gluino $R$ -hadron signal models, in the 1 VSI DV analysis channel. Studies of the effect of selections and cleanings on MC simulations of signal processes, like this one, are a crucial tool in designing an analysis. Taken from Ref. [143].	133
5.12	The signal, validation and control regions for the 1 VSI DV analysis channel, depicted in the $(m_{\text{DV}}, N_{\text{tracks}}^{\text{DV}})$ plane, with (a,b) fine and (c,d) merged binning. The track cleanings and baseline DV-level selections (Tables 5.4.3.1 and 5.4.3.2) are implicit. Taken from Ref. [143].	136
5.13	A test of the FV track cleaning efficiency for a set of Wino-Bino co-annihilation MC samples, as well as a background $Z \rightarrow \nu\bar{\nu} + \text{jets}$ sample for reference. The track cleanings remove relatively few FVs from the signal samples, at least when compared with the significant elimination of background FVs – significantly improving the signal-to-background ratio. Taken from Ref. [143].	141
5.14	Track $p_T$ distributions for a range of signal processes (“WB” = Wino-Bino co-annihilation, “HP” = Higgs Portal), as well as MC simulation background (“BKG” = $Z \rightarrow \nu\bar{\nu} + \text{jets}$ ). For each signal model, the legend indicates the particle masses ( $(m_{\tilde{\chi}_2^0}, m_{\tilde{\chi}_1^0})$ for Wino-Bino co-annihilation, $m_S$ for Higgs Portal), and the LLP mean lifetime/displacement. Taken from Ref. [143].	142

5.15	Expected signal yields for the gluino $R$ -hadron signal model, for (a) fixed $m(\tilde{\chi}_1^0) = 100$ GeV and (b) fixed $\delta m(\tilde{g}, \tilde{\chi}_1^0) = 100$ GeV. Taken from Ref. [143]. . . . .	150
5.16	Expected signal yields for the Wino-Bino co-annihilation model, for (a,b) $\Delta m(\tilde{\chi}_2^0, \tilde{\chi}_1^0) = 20$ GeV and (c,d) $\Delta m(\tilde{\chi}_2^0, \tilde{\chi}_1^0) = 30$ GeV. Taken from Ref. [143]. . . . .	151
5.17	Expected signal yields for the Wino-Bino co-annihilation model, for (a,b) $\Delta m(\tilde{\chi}_2^0, \tilde{\chi}_1^0) = 40$ GeV and (c,d) $\Delta m(\tilde{\chi}_2^0, \tilde{\chi}_1^0) = 50$ GeV. Taken from Ref. [143]. . . . .	152
5.18	Expected event yields for the Higgs Portal signal model, in the (a) 1 and (b) 2 FV SRs. Taken from Ref. [143]. . . . .	154
5.19	Expected signal yields for the axino signal model, for the (a) $h \rightarrow b\bar{b}$ and (b) $Z \rightarrow q\bar{q}$ channels. Note that these both correspond with $m_a = 1138$ $\mu$ eV, which in turn corresponds with $f_a = 5 \times 10^9$ GeV. None of the channels are appreciably sensitive to the other tested value of $f_a = 5 \times 10^{10}$ GeV. Taken from Ref. [143]. . . . .	155
5.20	The track density estimation method, performed in the PTR with $N_{\text{tracks}}^{\text{DV}} \geq 4$ , $m_{\text{DV}} > 5$ GeV, outside detector material, for the 1 VSI DV analysis channel. The histograms correspond with (a) the number of DVs, (b) the number of events, and (c) the resulting EDP. The non-integer counts are a consequence of pileup re-weighting, whereby PTR events are re-weighted so that the event pileup distribution matches that of the MTR. Taken from Ref. [143]. . . . .	158
5.21	Fits performed to estimate the HI contribution to the background. Note that fits are performed in both the inside and outside material regions. For the latter, the SR is blinded. Modified from Ref. [143]. . . . .	163
5.22	A schematic of measuring the distance in $S$ between (a) same-event and (b) different-event DV pairs, for estimating the merging rate for the MV estimate method. Taken from Ref. [143]. . . . .	167
5.23	Example distributions of $S^2$ for DVs within the same event, and within mixed events. The (a) full distributions show good agreement in the $S > 10$ region (after application of the scale factor), while (b) the $S < 10$ region shows a deficit in DV pairs in the same-event distribution, which is used to compute the $S^2$ -dependent merging rate via the ratio between the two distributions: the merging rate is the difference of this ratio from unity. Taken from Ref. [143]. . . . .	168
5.24	A schematic of the AX background estimate process, whereby we use $K_S^0$ candidates identified in data to estimate and parameterize an AX'ing rate, and collect kinematics of likely AX'ing tracks. We use this information to model the AX background by attaching the AX'ing tracks to real DVs outside the SR. Taken from Ref. [143]. . . . .	170
5.25	An example mass template produced as part of the AX background estimate, showing the integration of the different regions to produce estimated numbers of background events. Taken from Ref. [143]. . . . .	170
5.26	The combined background estimate, for the SR, as well as the fine-binned VRs. Taken from Ref. [143]. . . . .	172

5.27	The mean and standard deviation for the background estimate for the 1 VSI DV analysis channel, computed using the pseudo-experiment method to simulate the effects of Poisson statistics, in the merged VR bins. VR1, which nominally has $1228 \pm 203$ estimated background events, is excluded for better color scaling of the plot. Taken from Ref. [143]. . . . .	177
5.28	A comparison of the number of pileup vertices in the MTR and PTR. The lack of a bump in the 50-60 region of the PTR distribution is due to the enforced orthogonality of the MTR and PTR selections. Taken from Ref. [143]. . . . .	179
5.29	Various measurements of the strong coupling at the $Z$ -boson mass scale. The Particle Data Group 2023 world average is $\alpha_s(m_Z^2) = 0.1180 \pm 0.0009$ . Taken from Ref. [9]. . . . .	184
5.30	An example $\cancel{E}_T$ trigger <i>turn-on</i> curve, showing the $\cancel{E}_T$ trigger efficiency (with respect to a muon trigger) as a function of $\cancel{E}_T^{\mu}$ . As the $\cancel{E}_T^{\mu}$ increases, the trigger efficiency gradually reaches its plateau near 100% efficiency. The ratio of data versus MC simulation efficiency curves is used to determine the scale factor to apply to the MC simulation, and its uncertainty. Taken from Ref. [143]. . . . .	187
5.31	A comparison of data and MC simulation $K_S^0$ yields, as a function of $R_{xy}$ . Taken from Ref. [143]. . . . .	189
5.32	The estimated tracking inefficiency, as a function of $R_{xy}$ . Taken from Ref. [143].	189
5.33	Tracking systematic uncertainties for the gluino $R$ -hadron model, in the 1 VSI DV analysis channel, for fixed (a) $m_{\tilde{\chi}_1^0} = 100$ GeV and (b) $\Delta m(\tilde{\chi}_1^0, \tilde{g}) = 100$ GeV, corresponding with the signal yield shown in Figure 5.15. . . . .	190
5.34	Tracking systematic uncertainties for the Wino-Bino co-annihilation model, in the 1 FV analysis channel. Taken from Ref. [143]. . . . .	191
5.35	Two different visualizations of the single event in the 1 VSI DV SR. Primary vertices are shown in blue, with secondary $b$ -tagging vertices in yellow and VSI vertices in red. Note that the actual tracks are not visualized. The two views show (a) a zoomed-in view of the beampipe, featuring EMTopo jets (yellow cones), and (b) a zoomed-out view, showing the cutaways of the Pixel, SCT and TRT sections of the inner detector, surrounding the beampipe. The signal-like DV is one of the two inside the beampipe, near the origin of the EMTopo jets. . . . .	193
5.36	Preliminary limits on the gluino $R$ -hadron model, in terms of (a-c) $\tilde{g}$ mass and ( $R$ -hadron) lifetime, and (d) $\tilde{g}$ and $\tilde{\chi}_1^0$ mass. Taken from Ref. [143]. . . . .	201
5.37	Preliminary limits on the gluino $R$ -hadron model cross-section, as a function of $\tilde{g}$ mass with (a) fixed $\tilde{g}$ - $\tilde{\chi}_1^0$ mass splitting and (b) fixed $\tilde{\chi}_1^0$ mass, and as a function of (c) $\tilde{\chi}_1^0$ mass with fixed $\tilde{g}$ mass. Uncertainty bands are set not using the asymptotic assumption described in Appendix A.17, but rather by modeling the test statistic probability distribution function via the Monte Carlo method with $10^4$ pseudo-experiments. Taken from Ref. [143]. . . . .	202
5.38	Preliminary limits on the Wino-Bino co-annihilation model, in terms of $\tilde{\chi}_2^0$ mass and lifetime. Taken from Ref. [143]. . . . .	203
5.39	Preliminary limits on the Wino-Bino co-annihilation model, in terms of $\Delta m(\tilde{\chi}_2^0, \tilde{\chi}_1^0)$ and $\tilde{\chi}_2^0$ lifetime. Taken from Ref. [143]. . . . .	203

5.40	Preliminary limits on the Wino-Bino co-annihilation process cross-section. Taken from Ref. [143]. . . . .	204
5.41	Preliminary limits on the Higgs Portal branching ratio, as a function of the scalar $S$ lifetime. We suppress the observed limit uncertainties for improved legibility. Taken from Ref. [143]. . . . .	205
5.42	Preliminary limits on the axino model cross-section, in terms of (a) $\tilde{\chi}_1^0$ mass, (b) $\tilde{\chi}_2^0$ (axino) mass, (c) $\tilde{\chi}_1^0$ lifetime, and (d) axion mass. Taken from Ref. [143]. . .	206
6.1	An schematic of a 2D convolution performed in a CNN. Taken from Ref. [216].	209
6.2	A schematic of a typical CNN architecture. Taken from Ref. [216]. . . . .	209
6.3	A schematic of “unfurling” a particle calorimeter to produce jet images in the $(\eta, \phi)$ plane. These can be fed into a CNN to perform jet flavor tagging. Taken from Ref. [220]. . . . .	210
6.4	A schematic of the basic PELICAN architecture layout. Taken from Ref. [222].	213
6.5	The 15 binary arrays of rank 4 that represent the basis elements of the permutation equivariant aggregators of PELICAN. Each $2 \times 2$ square contains a smaller $2 \times 2$ square in each position. The larger square represents the output tensor, with each smaller square representing the input tensor and the dots indicating which elements are aggregated from the input tensor and placed in this location of the output tensor. The first row consists of aggregators that are “rank-0” in terms of tensor dimension $N$ , such as the identity mapping and trace. The second consists of “rank-1” aggregators that aggregate over rows, columns or the diagonal. The third consists of “rank-2” aggregators that aggregate over both rows and columns. Taken from Ref. [222]. . . . .	215
6.6	Jet kinematic distributions from the top-tagging benchmark dataset in Ref. [237].	217
6.7	Receiver operating characteristic (ROC) curves for a set of top-tagging neural networks, evaluated on the top-tagging benchmark. These networks are also summarized in Table 6.1. . . . .	219
6.8	Jet kinematic distributions from the $W$ -boson regression dataset [246]. . . . .	221
6.9	$W$ -boson mass as predicted by PELICAN, targeting the (left) true and (right) contained $W$ -boson 4-momentum. The distribution is separated into FC and non-FC jets, depicted with proportional bin heights – for each bin, the ratio of FC and non-FC jets is depicted by the (linear) ratio of the bins, with the combined distribution drawn on a logarithmic scale. Taken from Ref. [222]. . . . .	223
6.10	Top quark tagging background rejection (at 30% signal efficiency) as a function of number of network parameters, for neural networks evaluated on the dataset in Ref. [237]. Here, nPELICAN and nPELICAN <sub><math>N</math></sub> are low-parameter modifications of PELICAN which may be amenable to use in TDAQ systems – and PELICAN <sub>IRC</sub> is an infrared and colinearity-safe modification of the original network (Appendix E.2.2), discussed in Ref. [222]. In addition to the networks shown in Table 6.1, this plot also includes points corresponding with the Boost Invariant Polynomials [253] and DisCo-FFS [254]. Taken from Ref. [250]. . . .	226

A.1	An overview of track construction in the ATLAS inner detector, showing the construction of track seeds, candidates and final tracks. Taken from Ref. [260].	230
A.2	An example of how tracks reconstructed in the ATLAS inner detector are parameterized in terms of angles ( $\theta$ , $\phi$ ), impact parameters ( $d_0$ , $z_0$ ) and $ \vec{p} /m$ . Taken from Ref. [261].	231
A.3	LLP tracking efficiency with and without LRT tracking for (a) $R$ -hadron sample and (b) a Wino-Bino sample, as a function of the DV radial position $R_{xy}$ . The acceptance is defined as the ratio of number of true LLP decays for which two true reconstructed charged particles are reconstructed, and the number of true LLP decays within the fiducial volume with two charged particles with $p_T > 1$ GeV and $ \eta  < 5$ . Taken from Ref [143].	233
A.4	The number of tracks reconstructed per LLP for (a) $R$ -hadron sample and (b) a Wino-Bino sample. The $R$ -hadron sample has, on average, more tracks reconstructed per track, and thus is expected to have a higher estimated tracking efficiency than the Wino-Bino sample, as shown in Figure A.3. Taken from Ref [143].	234
A.5	A comparison of MTR and PTR, in terms of (a) number of EMTopo jets, (b) number of track jets, (c) number of PV-associated tracks, (d) scalar sum of $p_T^2$ of all PV-associated tracks, and (e) number of pileup vertices. Taken from Ref. [143].	238
A.6	An illustration of the <code>Classical</code> hit pattern check algorithm for the VSI secondary vertexing algorithm, for two DVs. Note that in the example on the right, the DV is located within the B-layer, and the required and forbidden hits are both located outside of this layer. Taken from Ref. [170].	243
A.7	The (a) <code>GEANT4</code> -based and (b) data-based material maps. The material map veto effectively removes DVs found to be inside the detector material. Taken from Ref. [143].	244
A.8	Expected signal yields for the axino signal model with the $h \rightarrow b\bar{b}$ decay channel, in the various SRs. Taken from Ref. [143].	246
A.9	Expected signal yields for the axino signal model with the $Z \rightarrow q\bar{q}$ decay channel, in the various SRs. Taken from Ref. [143].	247
A.10	Expected signal yields for the axino signal model with the $h \rightarrow b\bar{b}$ decay channel, with $f_a = 5 \times 10^{10}$ GeV, in the 2 FV SR. Taken from Ref. [143].	247
A.11	Fits performed to estimate the HI contribution to the background, both the inside and outside material regions, on a $Z \rightarrow \nu\bar{\nu} + \text{jets}$ MC simulation sample. Modified from Ref. [143].	250
A.12	Mass template used for the AX background estimate, showing the regions integrated for the different VRs. The integration for the SR covers the $> 10$ GeV region for the (4 + 1), (5 + 1) and (6 + 1) templates.	253
A.13	DV mass distributions, for 2- and 3-track DVs, for three different radial regions. For the 3-track DVs, we reconstruct 2-track masses for each choice of 2-tracks, which produces a combinatorial background. We fit all of these peaks to extract the number of $K_S^0$ candidates, which we use for the AX'ing rate estimation. Taken from Ref [143].	256

A.14	The (a,c,e) comparison of $K_S^0$ candidate yields in MC simulation and data, and (b,d,f) the resulting estimated tracking uncertainties for VSI DVs, separated by year. Taken from Ref [143]. . . . .	258
A.15	The (a) comparison of $K_S^0$ candidate yields in MC simulation and data, and (b) the resulting estimated tracking uncertainties for FVs. Taken from Ref [143]. . . . .	259
C.1	Diagrams contributing to the correction to the Higgs self-energy. . . . .	268
D.1	A schematic of the spin chamber used to measure the nEDM via Larmor precession. Taken from Ref. [58]. . . . .	273
E.1	Two examples of QCD processes that we may observe in proton-proton collisions. The left diagram corresponds to scattering of gluons to quarks (an $s$ -channel process), and the right with the scattering of quarks to quarks (a $t$ -channel process). . . . .	275
E.2	Clustering of the same set of pseudojets (energy deposits) by the (a) anti- $k_t$ , (b) Cambridge-Aachen, and (c) $k_t$ algorithms. Modified from Ref. [180]. . . . .	278
E.3	An overview of the different stages of the jet energy scale calibration method in ATLAS. Taken from Ref. [211]. . . . .	282
F.1	The different supply voltage regions in which proportional and Geiger-Müller counters operate. The latter operates in a voltage regime where all pulses, independent of incoming particle energy, are of the same magnitude. Taken from Ref. [315]. . . . .	287
F.2	A diagram of a photomultiplier tube coupled with a scintillator. Taken from Ref. [326]. . . . .	287
G.1	A rendering of the milliQan (a) demonstrator, (b) bar, and (c) slab detectors. Taken from Ref. [115, 330]. . . . .	290
G.2	The search sensitivity of the miliQan demonstrator, in terms of the charge and mass of the target milli-charged particles. Taken from Ref. [330]. . . . .	290
G.3	A diagram of the experimental setup used to measure PMT dark current, as well as perform linearity measurements. For dark current measurements, the LED pulser was turned off. . . . .	292
G.4	The dark count rate for the R878 PMT, as measured using the setup in Figure G.3, with a falling $-10$ mV trigger used to count negative voltage pulses produced by the PMT. Note that while the measured quantity shows clear dependence on the supply voltage – a good sign that this measurement was not distorted or bottle-necked by a potential low sampling rate of the data acquisition system – it is not consistent with the final, in-situ dark rate measurement described in Ref. [115]. . . . .	293

## LIST OF TABLES

4.1	An overview of the layers of the barrel section of the Pixel Detector, including the Insertable B-Layer. For the radial position, the average for the sensitive components of the layer is provided. Taken from Ref. [103, 106]. . . . .	62
4.2	Overview of the (a) barrel and (b) end-cap layers of the SCT. For the barrel layers, each has a half-length of 746.7 mm and a pitch of 80 $\mu\text{m}$ . For the end-cap layers, strip pitches range from 54.53 $\mu\text{m}$ to 90.34 $\mu\text{m}$ , and each layer has a maximum radius of 560 mm. Taken from Ref. [103]. . . . .	64
4.3	An overview of the design parameters of the Transition Radiation Tracker. Taken from Ref. [109]. . . . .	66
4.4	An overview of the central solenoid design parameters. Taken from Ref. [117]. . . . .	67
4.5	An overview of the design parameters of the (a) barrel and (b) end-cap toroid magnets Taken from Ref. [116]. . . . .	68
4.6	An overview of the different sections of the LAr calorimeter. This includes both the electromagnetic calorimeter (EMB + EMEC), and parts of the hadronic calorimeter (HEC + FCAL). . . . .	70
4.7	An overview of the different samplings of the ATLAS liquid argon calorimeter EMB and EMEC. Granularity is reported as $(\Delta\eta, \Delta\phi)$ . Reproduced from Ref. [118]. . . . .	71
5.1	An overview of the gluino $R$ -hadron signal model parameters, over which we scan. For the gluino-neutralino mass difference, only two values are used (as shown). . . . .	102
5.2	An overview of the Wino-Bino co-annihilation signal model parameters, over which we scan. . . . .	104
5.3	An overview of the Higgs Portal signal model parameters, over which we scan. . . . .	106
5.4	An overview of the axino signal model parameters, over which we scan. The range in $\tilde{\chi}_1^0$ lifetime $\tau$ given here is derived using Eq. 3.9. . . . .	107
5.5	A comparison of standard and large radius tracking parameters. Note in particular the much looser maximum $d_0$ and $z_0$ cuts among the “forward tracking” cuts. Taken from Ref. [143]. . . . .	110
5.6	Criteria for defining selected tracks for the VSI secondary vertexing algorithm. Taken from Ref. [143]. . . . .	112
5.7	Criteria for defining associated tracks for the VSI secondary vertexing algorithm. Here, $\text{sig}(x) = x/\sigma_x$ is a measure of the significance of a quantity $x$ with respect to its resolution $\sigma_x$ . . . . .	112
5.8	Criteria for defining selected tracks for the fuzzy secondary vertexing algorithm. Here, $N_{\text{Si}}$ refers to the number of silicon hits – which includes the Pixel and SCT detectors. Taken from Ref. [143]. . . . .	114
5.9	An overview of the samples used to train the 3 BDTs used in the fuzzy vertexing algorithm. Each BDT is trained with one of the three signal processes, targeting different lifetimes. Taken from Ref. [143]. . . . .	115

5.10	An overview of the input variables for the BDTs used in the fuzzy vertexing algorithm. Here, $\text{sig}(x) = x/\sigma_x$ is a measure of the significance of a quantity $x$ with respect to its resolution $\sigma_x$ . One may notice a certain level of redundancy in the input variables – namely the use of $\Delta\eta$ and the difference in innermost hit category, which will correlate with the individual $\eta$ and hit category inputs. In practice, including these additional variables allows constructing a decision tree with additional granularity with respect to these properties, within a single “cycle” of the full list of input variables. Taken from Ref. [143]. . . . .	115
5.11	Criteria for merging 2-track seeds into primary seeds in the fuzzy vertexing algorithm. Criterion $A$ is applied separately to the $x$ -, $y$ - and $z$ -components of the 2-track seeds. In criterion $B$ , $\sum p_T^{\text{sub}}$ refers to the sum of the $p_T$ of the two tracks associated with the seed being merged, and $\phi_{\text{max}}$ is the maximum azimuthal angle between the tracks in the primary seed, and the tracks in the substitute seed. The last criteria is found to prevent the merging of large numbers of background seeds, particularly inside the beam-pipe region. Taken from Ref. [143]. . . . .	117
5.12	An overview of electron candidate requirements. Note that this excludes any veto on the $ \eta  \in [1.37, 1.52]$ “crack region”, a section of the calorimeter with 5-10 $X_0$ (radiation lengths) of material before the first calorimeter layer [175] which is thus often vetoed in electron identification. Taken from Ref. [143]. . . . .	118
5.13	An overview of muon candidate requirements. Note that there is no track-to-vertex association requirement. Taken from Ref. [143]. . . . .	118
5.14	An overview of photon candidate requirements. Taken from Ref. [143]. . . . .	119
5.15	An overview of anti- $k_t$ , $R = 0.4$ EMTopo jet candidate requirements. For the (f)JVT working point definitions, see Ref. [184]. Taken from Ref. [143]. . . . .	120
5.16	An overview of the event-level selections that define our event cleaning. Taken from Ref. [143]. . . . .	125
5.17	An overview of the event-level selections that define the MTR. This is common to all SRs. Taken from Ref. [143]. . . . .	125
5.18	Selections that define the photon-triggered region (PTR). HLT refers to the High-Level Trigger (Section 4.2.6.2). Taken from Ref. [143]. . . . .	126
5.19	An overview of the selections that define the NCB veto. Taken from Ref. [143].	128
5.20	The dead tile module veto is defined as an event containing an EMTopo jet that matches all criteria. Taken from Ref. [143]. . . . .	129
5.21	An overview of the 1 VSI DV track cleanings. Taken from Ref. [143]. . . . .	132
5.22	An overview of the baseline VSI DV-level selections, which require an event to have at least 1 DV that passes all these selections. This is common to the 1 VSI DV VRs and SR, the latter having additional selections. Taken from Ref. [143].	134
5.23	An overview of the signal VSI DV-level selections, which require an event to have at least 1 DV that passes all these selections, in addition to the selections in Table 5.22. Here, “selected track” refers to DV tracks passing the VSI selection criteria in Table 5.6. Taken from Ref. [143]. . . . .	135

5.24	An overview of the region definitions for the 1 VSI DV analysis channel. Note that the DVs used in the DV-level selections always have track cleanings applied, as outlined in Table 5.4.3.1. Taken from Ref. [143]. . . . .	137
5.25	An overview of the binning of the VRs and CRs for the 1 VSI DV analysis channel, indicating both region binning systems. Taken from Ref. [143]. . . . .	138
5.26	An overview of the event-level selections for the 1 and 2 FV SRs. Taken from Ref. [143]. . . . .	138
5.27	An overview of the selections that define the strict NCB veto. Note that this is similar to the standard NCB veto (Table 5.19), except that it has an extra condition and requires all its conditions to be met for an event to pass. Taken from Ref. [143]. . . . .	139
5.28	An overview of the FV track cleanings. In the selections above, $\{\alpha(\text{track}, \overline{V-DV})\}$ is computed $\forall V \in [PV, \{PU\}]$ , where $\{PU\}$ refers to the set of pileup vertices in the event. Taken from Ref. [143]. . . . .	140
5.29	An overview of the baseline FV-level selections, for the 1 FV analysis channel. Note that the $N_{\text{seeds}}^{\text{DV}}$ and material veto conditions are lifted for some of our VR definitions, as will be discussed in Section 5.4.4.5. Taken from Ref. [143]. . . .	143
5.30	An overview of FV-level SR selections, for the 1 FV SR. Taken from Ref. [143].	144
5.31	An overview of the VR definitions used for the 1- and 2-FV analysis channels. Event-level selections are applied, as well as baseline FV selections (except as noted otherwise). The $VR9_{\text{inside}}$ and $VR9_{N_{\text{seeds}}}$ regions are similar to the SR, except for different material map and $N_{\text{seeds}}^{\text{DV}}$ conditions. Taken from Ref. [143].	146
5.32	An overview of the baseline FV-level selections, for the 2 FV analysis channel. Taken from Ref. [143]. . . . .	147
5.33	An overview of FV-level SR selections, for the 2 FV SR. Note that the lower bound on the FV mass is much lower than in the 1 FV SR. Taken from Ref. [143].	148
5.34	An overview of the VR and SR definitions for the 2 FV analysis channel. Note that for VR8, the loose material veto is used as opposed to the standard strict one (Appendix A.10), and the $m_{\text{DV}}$ condition is changed to $m_{\text{DV}} > 0$ due to signal contamination. Taken from Ref. [143]. . . . .	149
5.35	An overview of the 1 VSI DV background estimate results, as well as the observed number of events in the VRs. VR8 is omitted as it was ultimately not used during validation of this method. The hybrid method corresponds to an additional validation method described in Appendix A.13. Uncertainties are a combination of statistical uncertainties, as well as non-linearity and pileup systematic uncertainties (Section 5.6.1); the systematic uncertainties can be asymmetric but – with little loss in precision – we report symmetrized errors here for simplicity. Taken from Ref. [143]. . . . .	159
5.36	An overview of the 1 FV background estimate results, as well as the observed number of events in the VRs. Uncertainties are treated as in Table 5.35, and are omitted from the hybrid method validation for simplicity. For the various VR definitions, see Table 5.31. Taken from Ref. [143]. . . . .	161

5.37	The HI background estimate results. Note that the expected numbers of events cover many orders of magnitude, depending on the region. Taken from Ref. [143].	164
5.38	The MV background estimate results. Taken from Ref. [143].	166
5.39	The AX background estimate results. Taken from Ref. [143].	171
5.40	A comparison of the background estimates for the 1 VSI DV analysis channel. Taken from Ref. [143].	172
5.41	An overview of the background estimate results for the 2 FV analysis channel, for the VRs and SR. Uncertainties on the background estimates reported here are given as a combination of statistical, pileup and non-linearity uncertainties, treated as independent of one another. Taken from Ref. [143].	174
5.42	A summary of the background estimates for the SRs of all analysis channels. Uncertainties are symmetrized for simplified reporting – the asymmetries are very small, as the uncertainty is dominated by the (symmetric) statistical component. Taken from Ref [143].	175
5.43	An overview of background estimate uncertainties for the three analysis channels. Note that the reported uncertainties for each analysis channel are not necessarily the same. Due to how the systematic uncertainties are modeled, only the uncertainty for the 1 VSI DV channel is reported as asymmetric, with the asymmetry being very small. Taken from Ref. [143].	180
5.44	A summary of the background estimates and observed event yields in all the SRs. Taken from Ref. [143].	192
5.45	An overview of event-level observables for the single event in the 1 VSI DV SR. The run and event numbers are unique indices used to identify this event in ATLAS data. Taken from Ref. [143].	193
5.46	An overview of properties of the signal-like DV in the 1 VSI DV SR. A track selection status of 1 corresponds with a selected track, and 0 with an associated track. Taken from Ref. [143].	194
6.1	An overview of a number of top-tagger metrics on the top-tagging benchmark: network accuracy (fraction of correctly classified results, using a score threshold of 50%), area under the ROC curve, background rejection (the inverse of background efficiency) at a fixed 30% signal efficiency, and the number of learnable parameters. The three different instances of PELICAN correspond with different configurations in terms of Reproduced from Ref. [222].	218
6.2	$W$ -boson 4-momentum regression results. Here, “PELICAN JH” refers to PELICAN applied only to JH-tagged jets, and similarly “PELICAN FC” refers to PELICAN applied only to FC jets. Here we report PELICAN results for models trained to reconstruct the truth-level $W$ -boson 4-momentum. Taken from Ref. [222].	223

6.3	$W$ -boson 4-momentum regression results. Here, “PELICAN JH” refers to PELICAN applied only to JH-tagged jets, and similarly “PELICAN FC” refers to PELICAN applied only to FC jets. Here we report PELICAN results for models trained to reconstruct the contained $W$ -boson 4-momentum. Note that the resolutions are still computed with respect to the truth $W$ -boson 4-momentum, and that the results for JH are repeated from Table 6.2 (as that method is independent of the PELICAN regression target). Taken from Ref. [222]. . . . .	224
A.1	An overview of the $\cancel{E}_T$ triggers. The $\cancel{E}_T^{\text{HLT}}$ and $\cancel{E}_T^{\text{L1}}$ refer to $\cancel{E}_T$ as computed by the High-Level Trigger and Level-1 Trigger systems, respectively. The algorithm choice refers to the $\cancel{E}_T^{\text{HLT}}$ computation. . . . .	237
A.2	Selection requirements for (a) track jet’s constituent tracks, and (b) track jets clustered from these tracks. Taken from Ref. [143]. . . . .	239
A.3	An overview of the “Loose” track criteria. $N_{\text{Si}}$ refers to silicon hits (Pixel and SCT detectors), $N_{\text{shared}}^{\text{modules}}$ to the number of modules shared with other tracks (1 module corresponds with 1 Pixel hit or 2 SCT hits). $N_{\text{holes}}$ refer to <i>holes</i> , which are non-existing but expected measurement points for a given track, excluding disabled modules. Taken from Ref. [265]. . . . .	239
A.4	An overview of the selections that define the SuperLooseBadLLP jet cleaning working point. Note that a jet that meets any of the criteria fails the jet cleaning. Taken from Ref. [143]. . . . .	241
A.5	Location of the dead TileCal modules. Taken from Ref. [268]. . . . .	241
A.6	An overview of the extended regions used for the track density background estimate method, for the 1 VSI DV analysis channel. Note that these region definitions partly coincide with the merged bins in Table 5.25, and that these bins are not entirely independent of one another. Taken from Ref. [143]. . . . .	248
A.7	Results from the MC closure tests for inside and outside material. DV counts from the material map fit are compared to the truth level selections. . . . .	251

## ACKNOWLEDGMENTS

We start with perhaps the most difficult task described in this document, because there are so many people for me to thank – and in ways to which I probably cannot do justice in words. I will try nonetheless, and I apologize for any omissions (which there certainly are).

I would like to start by thanking my thesis advisor, David W. Miller, for the amazing guidance and mentorship he has provided me over the past six years. Thank you for encouraging my curiosity, and for teaching me how to be a more thorough researcher.

I would also like to thank Benjamin Rosser – both for his help as one of the contacts for our ATLAS analysis team, and his guidance as a mentor.

I also want to thank the other members of my ATLAS analysis team, with special thanks to Evan Michael Carlson and Risa Ushioda for their help – and my phenomenologist colleagues Gabe Hoshino and Keisuke Harigaya at UChicago, for their help in developing the axino physics interpretation of our analysis.

I also thank the graduate students, past and present, in the Miller lab and the UChicago ATLAS group – with special thanks to Emily Smith, Timothy Hoffman, Kristin Dona and Teresa Du. I have met some incredible people during my time here, and I am very grateful for the advice, support – and friendship – that I found in this group. On a similar note, I would like to thank Alex Bogatskiy and Umang Mehta for their invaluable help as colleagues and friends.

I would also like to give special thanks to Henry Frisch, for spurring my interest in particle detector technologies, and for allowing me to organize lunch talks for the high-energy physics group at the EFI.

Lastly, I would like to thank my parents, Maja and Eddy, for their love and the incredible amount of support they have given me in pursuing my interests and dreams.

# CHAPTER 1

## INTRODUCTION

Physics is the process of discovering and studying the laws of nature; of understanding the cosmos and how it functions. It is also, at its core, a process of model-building: as physicists, we build models that attempt to explain how the universe functions. We test these models through the process of the scientific method, resulting in predictive tools that allow us to explain, at some level, what the universe is made of and the mechanisms by which natural phenomena occur. Over the course of this enterprise, physicists have studied processes that span an enormous breadth of scales in terms of size, from the motions of planetary bodies and galaxies to the interactions of subatomic particles – and through thoughtful modeling and careful experimentation, have produced theories that can successfully predict and describe phenomena across this broad range. Here, we will turn our attention to the study of the shortest length-scales yet probed, where we try to understand the fundamental building blocks of the universe and their interactions.

It is in this realm – what we refer to as *high-energy physics* – where we currently seek to address some of the deepest mysteries in physics and the shortcomings of our current knowledge. What is the particle nature of the dark matter that seems to constitute a majority of the universe? How is our current model of high-energy physics, for all its successes, incompatible with our similarly successful model of gravitation? And why does our model seem to need extremely precise tuning of its parameters, lest it return predictions entirely inconsistent with reality? Addressing these questions requires not only the ability to modify the Standard Model, our current best description of high-energy physics, to address these shortcomings, but also the ability to *verify* aspects of any new model via experimentation.

Experimental high-energy physicists approach this problem by measuring the interactions of subatomic particles at – as the name of the field may imply – extremely high energies, whereby they can study the particles' fundamental interactions. This can be done using

high-energy particles that the universe provides us – cosmic rays produced from energetic sources such as supernovae and quasars – or by producing them in particle accelerators, where they can then be collided inside detectors that measure the energy and momenta of the outgoing products of particle interactions induced by the collisions. As of writing this thesis, the highest-energy particle accelerator in the world is the Large Hadron Collider [1] (LHC), located on the French-Swiss border near Geneva, Switzerland. Stationed along the collider are multiple detectors, such as the ATLAS [2] and CMS [3] experiments, that measure the high-energy collision of proton beams. This allows for performing precision measurements of the Standard Model, as well as searching for evidence of new physics – whether indirectly through tensions between experimental observations and Standard Model predictions, or directly through the discovery of new fundamental particles or interactions.

In this thesis, we will focus on a search for new physics targeting candidate models for explaining dark matter, as well as resolving a multiple examples of model fine-tuning that make the Standard Model seem awkwardly fit to our observations of nature. We will also turn our attention to some of the computational tools and methods we use when analyzing our measurements of high-energy particle interactions, and how directly incorporating well-established elements of our fundamental theories of nature into these tools can improve their performance and extend their usefulness. Along the way, we will review the Standard Model of physics, the new models we seek to investigate, and the ATLAS experiment. In each case, we ask a simple question with a complex answer: What is it made out of, and how does it behave?

## **1.1 A road-map for this thesis: where to find things**

We have quite a number of topics to cover in order to contextualize the search for new physics described in Chapter 5 – and while we will only delve so deeply into each, this will still amount to a sizeable review. We will start with a review the Standard Model of

particle physics in Chapter 2, together with a common (hypothetical) extension known as *supersymmetry* – wherein we will touch upon some fundamental topics in quantum field theory, the general theoretical framework of which the Standard Model is a particular example. We will follow this with a discussion of *axion physics* in Chapter 3, another popular theory of Beyond-Standard Model physics – which we will couple with supersymmetry to yield *axino physics*. In Chapter 4 we will review the design and functioning of the ATLAS experiment, and also how the LHC delivers proton beams to it. After our in-depth review of the new physics search in Chapter 5, targeting supersymmetric models (including one with axinos), we will briefly but importantly touch upon developments in the field of equivariant machine learning in Chapter 6 and its applications to high-energy physics.

## 1.2 How to read this thesis: some notes on structure

Throughout this thesis, there will be plentiful footnotes. These bring up topics or asides that may be of help in understanding the various concepts that are introduced – or simply details that I think are interesting but which may distract from the main points. Some will also explicitly reference external sources, that are not directly referenced in the body text. Some of these are review papers, which provide general overviews of particular topics – and in some cases, pedagogical explanations and derivations of results. Others are historical papers, which are often treated as “common knowledge” and thus rarely cited. While there is a certain amount of subjectivity or arbitrariness to how I cite these papers – for example, almost any topic referenced from a common quantum field theory textbook is likely available in some older original source – I think it is important to occasionally emphasize that even aspects of the field that researchers take for granted were at some point noteworthy discoveries, and their discoverers deserving of acknowledgement. These historical sources may also be genuinely interesting to the reader, as they are largely available online and provide a window into how the field operated in the past.

You may also notice that most mathematical expressions in this thesis are followed by boxes, that contain a brief explanation of the various terms that appear in them. At the risk of being verbose, I will employ these unless all the terms have previously appeared in another expression in the same (sub)section<sup>[1]</sup>, so that these expressions can be referenced more easily without needing to find all the definitions within the prose that surrounds them.

---

1. While this notation may not be strictly conventional, I adopt it as an extension of the small-font typography used in Ref. [4], a well-known (if every so slightly dated) quantum field theory textbook.

# CHAPTER 2

## THE STANDARD MODEL OF PARTICLE PHYSICS, AND SUPERSYMMETRY

In this chapter we will outline the basics of the Standard Model (SM) of particle physics, our most complete description of the known fundamental particles that comprise matter, and three of the four fundamental forces that govern their interactions. Specifically, we will review the model’s particle content, as well as a couple key mechanisms relevant to further discussions. We will also review some of the existing issues and limitations of the SM and see how *supersymmetry*, a popular extension of the SM, seeks to address these.

### 2.1 The Standard Model

The Standard Model (SM) of particle physics is a quantum field theory that describes the fundamental building blocks of Nature, at the shortest length scales<sup>[1]</sup> that we are able to probe. It describes all the known *elementary particles* that constitute our Universe, and three of the four fundamental forces that describe their interactions – the electromagnetic, weak<sup>[2]</sup> and strong forces<sup>[3]</sup>.

One difficulty in succinctly describing the SM is that of finding a good place to start. As it is a quantum field theory, we may try to write down the Lagrangian of the entire theory from which its dynamics may be derived via the Euler-Lagrange equations. However given

---

1. High-energy physicists will interchangeably talk about “length scales” and “energy scales”, one being the inverse of the other: Short length scales correspond with high energy scales. This is in reference to the quantum mechanical concept of the *de Broglie* wavelength, the energy-dependent wavelength at which a particle can be described as a wave – which is a consequence of so-called “particle-wave duality” [5].

2. As we will discuss further on, the weak and electromagnetic forces can be described as a unified *electroweak* force. That we observe it as two separate forces is then a consequence of the mechanism of *spontaneous symmetry-breaking*.

3. The SM does not contain a description of gravity, which is instead modeled by the theory of general relativity. These two theories have so far not been unified – the first of (numerous) issues we will see that motivate extending the SM.

the complexity of the model, this is cumbersome and not particularly instructive<sup>[4]</sup>. A more natural starting point may be the set of fundamental particles it describes, which we can then organize into different *sectors* that correspond with the different fundamental forces and the corresponding *symmetry groups*.

The particle content of the SM is outlined in Figure 2.1, which also highlights some of the particles’ intrinsic quantities. Let us briefly review what these quantities mean and how they fit into the theory, before returning explicitly to the particle content.

### 2.1.1 Properties of the Standard Model

The particle content of the SM is outlined in Figure 2.1, which also highlights some of the particles’ intrinsic quantities. We will review these quantities below.

#### 2.1.1.1 Mass

We sometimes refer to the mass as *invariant mass*, which is a reference to the fact that it is invariant under transformations by the *Lorentz group*, the group of all transformations in the Minkowski spacetime that describes physics under the theory of special relativity [10]<sup>[5]</sup>. In fact, the mass of a particle can be defined as the Minkowski norm of its energy-momentum vector (or *4-momentum*), which is the length of the vector in Minkowski spacetime:

$$m = \sqrt{E^2 - |\vec{p}|^2}, \tag{2.1}$$

- |  |
|--|
| <ul style="list-style-type: none"> <li>• <math>m</math> is the particle mass,</li> <li>• <math>E</math> is the particle energy,</li> <li>• <math>\vec{p}</math> is the particle momentum.</li> </ul> |
|--|

---

4. For examples of how one might approach the SM via the Lagrangian picture, see Refs. [6, 7]. The latter in particular focuses on “constructing” the Lagrangian piece-by-piece.

5. For a brief review of special relativity and the Lorentz group, see Appendix B.

# Standard Model of Elementary Particles

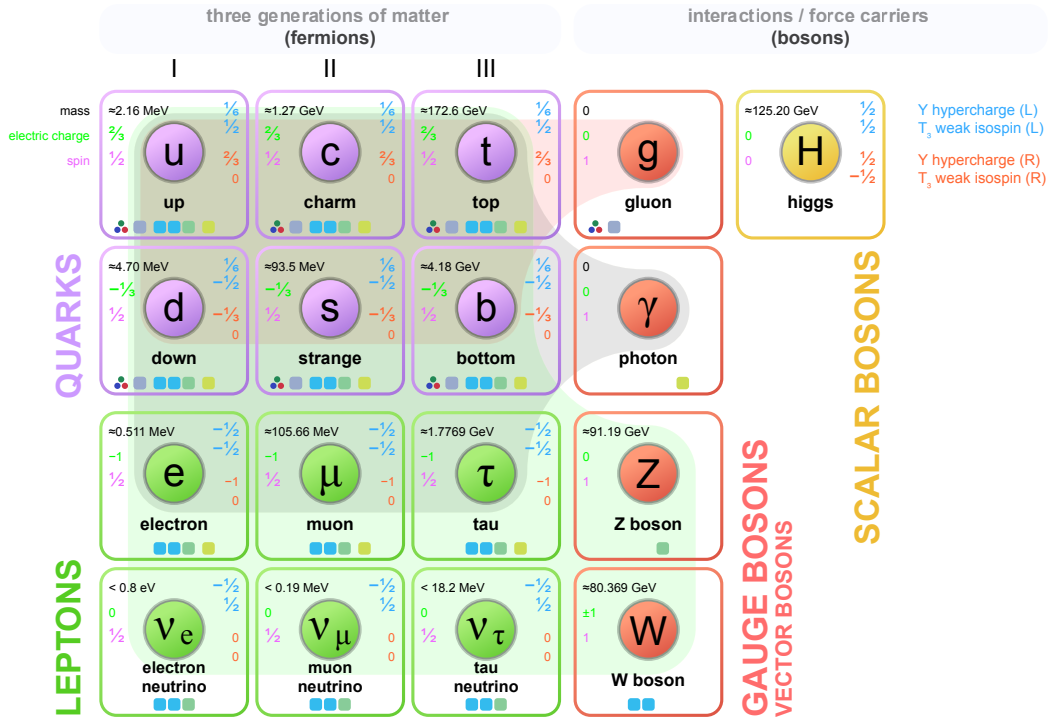


Figure 2.1: The particle content of the Standard Model, indicating the mass, electric charge and spin of each particle, as well as left- and right-handed hypercharge and weak isospin charges. Modified from Ref. [8], with the particle masses taken from Ref. [9]. The top quark mass shown here is the result from direct measurements at the LHC (currently in tension with indirect measurements from electroweak precision data, via cross-section measurements, at the level of  $\sim 1.7\sigma$  [9]). The neutrino mass limits from Ref. [9] correspond with limits on  $m_{\nu x}^{2(\text{eff})} \equiv \sum_i |U_{xi}|^2 m_{\nu i}^2$ , where  $U$  is the PMNS matrix and  $x \in \{e, \mu, \tau\}$  (see Section 2.1.2.1). For the electron neutrino  $\nu_e$ , mass measurements corresponding to antineutrino  $\bar{\nu}_e$  are used.

where we are using the  $c = 1, \hbar = 1$  convention<sup>[6]</sup>. This expression is sometimes referred to as the *mass-energy equivalence formula*.

Each particle has an associated mass  $m_0$ , that all *real* particles of that species will share. In quantum field theories there are also *virtual* particles – intermediate states that participate in particle interactions, but which are not a part of the final products of these interactions. These virtual particles can be *off-shell*, so that their mass differs from  $m_0$ <sup>[7]</sup>, however the amplitude of an interaction will decrease the more any involved virtual particle’s mass differs from  $m_0$ . Thus if we try to measure the mass of some particle  $X$  through a decay like  $X \rightarrow YY$ , where we reconstruct the mass of the sum of the stable  $Y$  particles, we do not find a delta function-like mass distribution, but instead a (relativistic) *Breit-Wigner distribution* [11] <sup>[8]</sup> centered on  $m_0$ .

### 2.1.1.2 Spin

A particle has a *spin angular momentum* (or simply *spin*<sup>[9]</sup>)  $S$ , given by

$$S = \sqrt{s(s+1)}, \tag{2.2}$$

- $s = n/2$  is the spin quantum number,
- $n \in \mathbb{Z}$  is an integer.

---

6. We shall use this convention throughout this thesis, except in places where explicitly using the speed of light – for example, when discussing particle displacements as in Section 4.2.1.4, where we explicitly want the particle displacement in length units. This convention, known as “natural” or Planck units, is convenient as it removes the need for lots of factors of  $c$  and  $\hbar$ , and owing to the units of these quantities there is always only one unambiguous way to use them to convert to “real” units.

7. Another common way of phrasing this phenomenon is that virtual particles may violate the mass-energy equivalence formula.

8. In actual experiment where our particle detector has limited energy and angular resolutions, this distribution is further convolved, typically with some Gaussian distribution.

9. While historically thought of as actual angular momentum – corresponding to a spinning, massive body – this interpretation has been dropped in favor of a more abstract approach as particles are treated as point-like (and thus a concept of them spinning is not well-defined). Whatever the interpretation, the effects of spin are very real as demonstrated in the Stern-Gerlach experiment [12] (although the experiment’s demonstration of particles’ intrinsic spin was not understood at first [13]).

where  $s$  is referred to as the *spin quantum number* and is either a half-integer or integer.

Particles with half-integer spins are known as *fermions*, and those with integer spins as *bosons*, and these two different types of particles obey different statistics: Two fermions cannot occupy the same space and have the same quantum numbers, a phenomenon known as the *Pauli exclusion principle*. By contrast, two or more bosons can occupy the same state. These two very different behaviours can be understood within the framework of quantum field theory as a consequence of whether or not particle creation operators acting on a state commute or anti-commute<sup>[10]</sup>.

In the language of quantum field theory, we often refer to bosons as *scalars* and fermions as *spinors*, owing to how these objects are represented owing to their spins.

In the SM, the fermions are specifically modeled<sup>[11]</sup> as *Dirac* fermions. These are given by the solution  $\psi$  to the Dirac equation,

$$(i\cancel{D} - m) \psi = 0 , \tag{2.3}$$

- $\cancel{D} = \partial_\mu + ieA_\mu$  is the gauge-covariant derivative,
- $A_\mu$  is the gauge field,
- $m$  is the particle mass,
- $\psi$  is the Dirac fermion wave-function.

which describes the dynamics of a free (uncoupled) Dirac fermion.

---

10. For details see Ref. [14], where it is explained in Chapters 2 and 3 how Klein-Gordon (scalar) fields obey bosonic *Bose-Einstein statistics*, whereas Dirac fields obey fermionic *Fermi-Dirac statistics*.

11. The possible exception to this statement are the neutrinos of the SM. Whether they are Dirac fermions or Majorana fermions – meaning that they are their own antiparticles – is an open question [15].

### 2.1.1.3 Charge

Perhaps the most familiar kind of charge is the electric charge. It appears in the expression for the Coulomb force that exists between two point-like electric charges,

$$||\vec{F}_{\text{Coulomb}}|| \propto \frac{|q_1 q_2|}{r^2} . \quad (2.4)$$

- $q_i$  is the magnitude of the  $i$ 'th electric charge,
- $r$  is the distance between the charges.

However, the SM contains other types of charges, such as the *color charge* carried by the quarks and gluon. We can define charge a little more formally in the context of the SM, with some help from group and representation theory<sup>[12]</sup>. This requires introducing the notion of *gauge transformations*, which are transformations performed by operating on the Lagrangian of a theory by an element of a Lie group<sup>[13]</sup>.

The SM has multiple gauge symmetry groups, associated with different sectors of the theory: the fields of the SM can perhaps be best described as abstract objects with different representations under these groups, and thus they interact differently with them. The combined gauge symmetries of the SM are given by

$$\text{SU}(3)_C \times \text{SU}(2)_L \times U(1)_Y , \quad (2.5)$$

- $\text{SU}(3)_C$  is the  $3 \times 3$  *special unitary* group – the Lie group consisting of all  $3 \times 3$  matrices with a determinant of 1 – corresponding with color charge,
- $\text{SU}(2)_L$  is the  $2 \times 2$  special unitary group, which only involves left-handed fermions,
- $U(1)_Y$  is the group of all complex numbers with an absolute value of 1.

where the subscripts indicate details of these gauge symmetries:

---

12. For a very brief review of group theory, see Ref. [6], Section 10.1.1.

13. A lot more can be said about symmetries in general, and gauge symmetries in particular. As shown by Noether's theorem [16], symmetries of the action of a theory are fundamentally important in describing that theory, as they indicate the presence of a conserved quantity. For a review of gauge symmetries, see Ref. [17].

- $SU(3)_C$  corresponds with *color charge*, which has three components (red, green and blue).
- $SU(2)_L$  is the *weak isospin group*. The subscript indicates that only *left-handed* fermions interact via charged weak currents<sup>[14]</sup>.
- $U(1)_Y$  corresponds with (weak) hypercharge<sup>[15]</sup>.

In the language of representation theory, charges we allude to above can be defined as the generators of the gauge symmetry groups of the SM, so that a given particle’s charge indicates how it transforms under actions by elements of the corresponding gauge symmetry groups.

While gauge groups corresponding with color charge, weak isospin and hypercharge appeared in the above description, one corresponding with electromagnetism did not. This is not an error of omission, but rather a consequence of the fact that the electric charge is a linear combination of weak isospin and hypercharge given by

$$Q = T_3 + \frac{1}{2}Y . \tag{2.6}$$

- $T_3$  is the 3<sup>rd</sup> component of weak isospin,
- $Y$  is hypercharge.

It is the charge associated with the  $U(1)_{EM}$  gauge symmetry, which the SM acquires after electroweak symmetry-breaking of  $SU(2)_L \times U(1)_Y \rightarrow U(1)_{EM}$  as we shall discuss later.

In quantum field theory, we are sometimes interested in whether a particular theory exhibits *charge conjugation symmetry*; that is, whether or not the theory is invariant under

---

14. A particle’s handedness or *chirality* voerns how it transforms under parity transformations (Appendix D.1). We will discuss this a little bit in Section 2.1.1.4.

15. The terms “hypercharge” and “weak hypercharge” are typically used as synonyms, but historically had different meanings.

the transformation that takes particles to antiparticles. For Dirac fermions, this acts as [6]

$$C : \psi \rightarrow -i\gamma_2\psi^* . \quad (2.7)$$

- $\psi$  is a Dirac fermion,
- $\gamma_2 \equiv i\sigma_2 \otimes \sigma_2$  is a Dirac gamma matrix,
- $\sigma_2$  is the Pauli matrix  $((0, -i), (i, 0))$  .

#### 2.1.1.4 Chirality

The listings of hypercharge and weak isospin quantum numbers in Figure 2.1 show two values per fermion, which correspond with so-called left- and right-handed fermions. A fermion's handedness, or *chirality*, refers to which irreducible representation of the Lorentz group under which it transforms [6]. As noted in Section 2.1.1.2, we model the fermions of the SM as Dirac fermions. These can be represented as doublets of *Weyl* fermions<sup>[16]</sup> – also known as *Weyl spinors* – of which there are left- and right-handed varieties:

$$\psi = \begin{bmatrix} \psi_L \\ \psi_R \end{bmatrix} , \quad (2.8)$$

where the two Weyl spinors are different irreducible representations of the Poincaré group. In quantum field theory, we say that a theory is a chiral theory if it is not symmetric under chiral transformation ( $L \leftrightarrow R$ ). We can also say that such theories are not invariant under *parity transformations* of the form

$$P : (t, \vec{x}) \rightarrow (t, -\vec{x}) , \quad (2.9)$$

---

16. At this point, we have (however briefly) mentioned Dirac, Weyl and Majorana fermions. For a review of these different types, see Ref. [18].

which (together with time reversal transformations) are part of the full Lorentz group<sup>[17]</sup>. One example of a chiral theory is that of weak interactions, as demonstrated by the Wu experiment [19] in the asymmetry in the distribution of electrons produced by the weak decay of a polarized  $^{60}\text{Co}$  atoms.

A related but somewhat less abstract concept is that of *helicity*, which is the projection of a particle's spin onto its direction of motion. Chirality and helicity are equivalent for massless particles<sup>[18]</sup>.

## 2.1.2 *Particles of the Standard Model*

Having briefly outline some of the intrinsic properties of the SM particles, let us now explicitly list the particles.

### 2.1.2.1 Fermions

There are twelve fermions, a subset of which comprise all the stable massive matter in the SM. Six of these fermions are the *leptons*, associated purely with the electroweak sector. There are 3 flavors of (electromagnetically-)charged leptons – electron, muon, tau – each with an associated neutrally-charged neutrino. Of the charged leptons, only the electron is stable. All three neutrinos are stable, but they exhibit the special behaviour of oscillating between flavor states as they interact with matter, as has been observed in numerous experiments [20–23]. This is a consequence of the flavor eigenstates being different than the mass eigenstates, with the mixing between the two described by the Pontecorvo-Maki-Nakagawa-Sakata (PMNS)

---

17. See Appendix B regarding the Lorentz group.

18. Note that while chirality is a Lorentz-invariant quantity, helicity is not: for a massive particle, its momentum is a frame-dependent quantity. For further discussion of chirality, helicity and spin, see Section 11.1 of Ref. [6].

matrix [24]  $U$  as

$$\begin{bmatrix} \nu_e \\ \nu_\mu \\ \nu_\tau \end{bmatrix} = U \begin{bmatrix} \nu_1 \\ \nu_2 \\ \nu_3 \end{bmatrix}. \quad (2.10)$$

- $\nu_a, a \in \{e, \mu, \tau\}$  are neutrino flavor eigenstates,
- $U$  is the  $3 \times 3$  PMNS matrix,
- $\nu_i, i \in \{1, 2, 3\}$  are neutrino mass eigenstates.

The other six fermions are *quarks*, associated with the strong sector and carrying the associated *color* charge. The quarks also carry electromagnetic charge.

1. We do not observe bare quarks as a consequence of the phenomenon of *color confinement*, which relates to the properties of the strong force by which the quarks interact with one another<sup>[19]</sup>.
2. By contrast, we do observe bound states consisting of combinations of (anti)quarks, known as *hadrons*. Those with two quarks are known as *mesons*, and those with three quarks as *baryons*. There are no stable mesons, and one stable baryon – the proton<sup>[20]</sup>.

### 2.1.2.2 Bosons

There are five bosons in the SM. This includes 4 gauge bosons associated with the strong and electroweak forces, as well as the Higgs boson.

The gauge bosons are often referred to as *force carriers*, as they mediate interactions in their associated sectors: the gluon for the strong force, the photon for the electromagnetic force, and the  $W$  and  $Z$  bosons for the weak force. Of these gauge bosons, only the photon and gluon are stable – but they are also massless.

---

19. See Appendix E.1

20. To be clear, we do commonly observe other baryons in stable matter, namely neutrons. However, neutrons are not stable in isolation.

The Higgs boson is a scalar boson – specifically an example of a *Nambu-Goldstone* boson associated with the eponymous Higgs potential. It arises due to the spontaneous symmetry-breaking of the Higgs potential, specifically a mechanism known as *electroweak symmetry breaking*, which breaks the  $SU(2)_L \times U(1)_Y$  gauge symmetry to  $U(1)_{EM}$ , and gives the SM particles their masses.

### 2.1.2.3 Particle decays

To describe particle decays – and in fact all high-energy particle interactions – we typically use *Feynman diagrams*, such as the example diagram in Figure 2.2. Read left-to-right, it shows the interaction of two fermions to produce a gauge boson, which decays to scalar and gauge bosons: these then decay to fermions, with the scalar boson propagator including a *loop*<sup>[21]</sup>. Feynman diagrams are not only useful pictorial representations of processes, but also serve as computational tools: interpreted using *Feynman rules*, they can be translated into computations that can be used to compute the transition probabilities, or *matrix elements*, between the quantum states corresponding with the initial and final particles in the diagram.

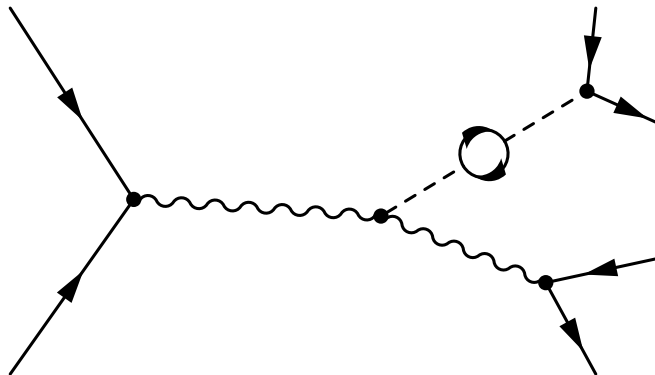


Figure 2.2: An example Feynman diagram, including a loop. Particles only present in intermediate states can be off-shell. Here, explicit particle labels have been omitted for clarity.

Thus the question of what decays are possible can be rephrased as one of how many

---

21. We will discuss these a little more in Section 2.1.2.6.

Feynman diagrams one can create, with one particle in the initial state and multiple particles in the final state<sup>[22]</sup>. The types of connections (or *vertices*) allowed between the particles (or *propagators*) in the diagram corresponds with what couplings – direct interactions between particles – are available in the quantum field theory. The shading in Figure 2.1 indicates the allowed couplings in the SM. Furthermore, the theory imposes some conservation laws that constrain possible processes. Due to energy conservation, a particle’s decay products must have equal or lower mass<sup>[23]</sup>. Decays must also obey certain constraints on preserved quantum numbers: charge must be conserved, as well as quantities such as lepton and baryon numbers (the number of leptons minus anti-leptons, and the number of quarks minus anti-quarks, respectively). Even with these constraints, we are left with an infinite number of diagrams we can draw, particularly due to the phenomenon of loops – we can always attach more and more loops to a given diagrams’ propagators<sup>[24]</sup>. Here we will only cover the basic decays that will help guide our discussions in Chapters 5 and 6, focusing on those corresponding with *tree-level* diagrams – those without loops.

Among the charged leptons, muons may decay to a combination of electrons, neutrinos and photons (within the above-mentioned constraints), such as<sup>[25]</sup>

$$\begin{aligned}
 \mu^- &\rightarrow e^- \nu_e \nu_\mu, & (2.11) \\
 \mu^- &\rightarrow e^- \nu_e \nu_\mu \gamma, \\
 \mu^- &\rightarrow e^- \nu_e \nu_\mu e^+ e^-.
 \end{aligned}$$

---

22. We typically exclude from this definition the processes where the same particle appears in the initial and final states, such as *bremstrahlung* (or “braking radiation”) processes like  $e^- \rightarrow \gamma e^-$ .

23. Although this in principle limits what kinds of decays are possible, keep in mind the discussion of off-shell particles in Section 2.1.1.1. Thus, what might be thought of as “forbidden” decays are possible processes, as long as they are only intermediate steps in some larger process (as the off-shell particles cannot be stable final states).

24. This may sound worrisome from the computational side of the theory, as one can generate an infinite number of diagrams describing the transition between two given quantum states. We will touch upon this in Section 2.1.2.6.

25. Note that this is not a complete list, but just some representative decays.

where the decays are mediated by (virtual) gauge bosons, as shown in the Feynman diagram in Figure 2.3.

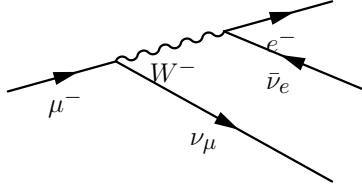


Figure 2.3: An example Feynman diagram of muon decay.

Tau neutrinos have similar leptonic decays,

$$\tau^- \rightarrow e^- \nu_e \nu_\tau, \quad (2.12)$$

$$\tau^- \rightarrow \mu^- \nu_\mu \nu_\tau,$$

but are sufficiently massive that they can also decay hadronically,

$$\tau^- \rightarrow \pi^- \pi^0 \nu_\tau, \quad (2.13)$$

$$\tau^- \rightarrow \pi^- \nu_\tau.$$

The  $W^-$ ,  $Z^-$  and Higgs bosons exhibit both leptonic and hadronic decay channels. The  $W^-$  and  $Z^-$  bosons can decay as

$$W \rightarrow q_i \bar{q}_j, \quad (2.14)$$

$$W \rightarrow l \nu,$$

$$Z \rightarrow q_i \bar{q}_i,$$

$$Z \rightarrow \bar{l} l,$$

- $q_i$  is a quark,
- $l$  is a charged lepton,
- $\nu$  is a neutrino.

where the available decays are constrained by the bosons electric charge (if any). For the hadronic decay channels, the branching ratios of the different  $W$ -boson decays are given by the Cabbibo-Kobayashi-Maskawa (CKM) matrix that describes the mixing between the weak interaction and mass eigenstates of the down-type quarks,

$$\begin{bmatrix} d' \\ s' \\ b' \end{bmatrix} = V \begin{bmatrix} d \\ s \\ b \end{bmatrix}. \quad (2.15)$$

- $\{d', s', b'\}$  are the weak interaction doublet partners of the down-type quarks,
- $V$  is the  $3 \times 3$  CKM matrix,
- $\{d, s, b\}$  are the down-type quark mass eigenstates.

The Higgs boson has perhaps the richest set of decay channels, as it can decay into a pair of fermions (a fermion and anti-fermion) or into a pair of gauge bosons. With these decay products themselves featuring a range of available decays (namely the  $t$ ,  $W$  and  $Z$ ), the set of potential final states is vast.

#### 2.1.2.4 Particle lifetimes

One striking property of the SM is how few stable particles there are, both in terms of fundamental particles and the (composite) hadrons. By “stable”, we mean that the particle does not undergo decay – at least on any observable timescale<sup>[26]</sup>.

Figure 2.4 provides an overview of particle lifetimes. Many of the particles – including the relatively massive Higgs,  $W$ - and  $Z$ -bosons – are sufficiently unstable to be “detector-prompt”, by which we mean that in all collider experiments to date, their decays are fast enough to effectively be instantaneous. As will be discussed in Section 4.2.1.4 and Chapter 5, particles

---

<sup>26</sup>. For example, the proton is a stable particle in the SM. Nonetheless there is ongoing effort to observe proton decay, as certain beyond-SM theories allow for proton decay processes. Measuring or bounding the decay rate thus bounds (or provides evidence for) such theories. At the present time, the proton mean lifetime bound is given by  $> 9.6 \times 10^{29}$  yr [25].

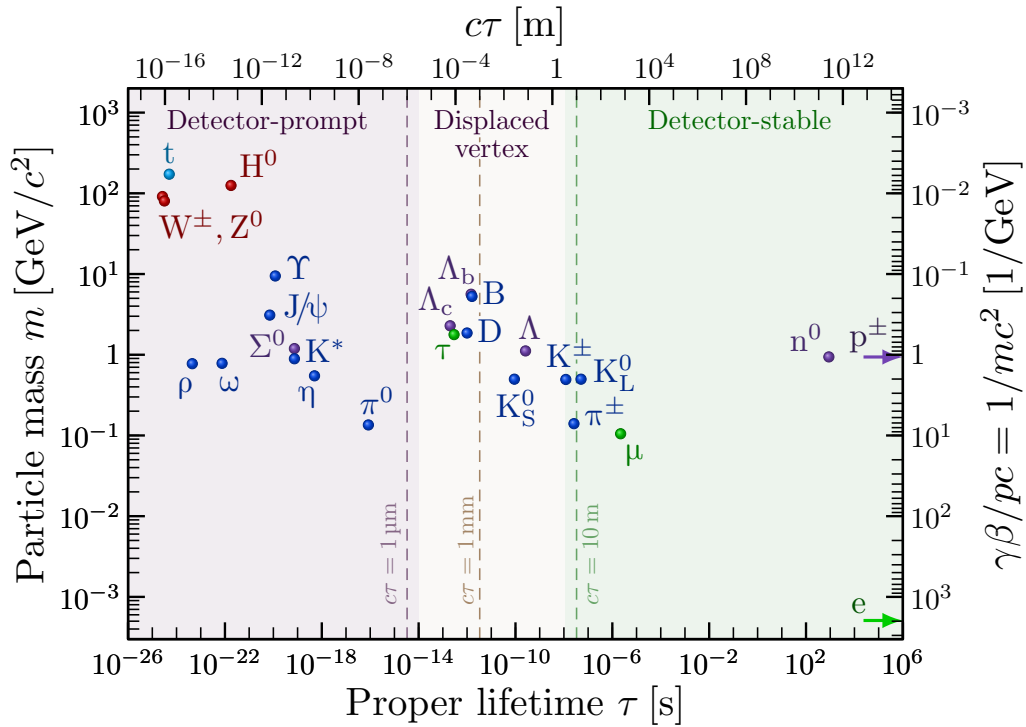


Figure 2.4: Lifetimes and masses of the Standard Model. Some particles are excluded, such as quarks other than the top quark (which hadronize before decay, as discussed in Appendix E.1), or hadrons where multiple (excited) states have very similar masses and lifetimes. Modified from Ref. [26], with masses taken from Ref. [9].

produced in collider experiments that have intermediate lifetimes (labeled as “Displaced vertex” in Fig. 2.4) may travel a measurable distance into the detector before subsequent decay. If the paths of their decay products can be traced, the decay vertex may be identified – which can be a useful search strategy for beyond-SM theories that include high-mass, long-lived particles.

### 2.1.2.5 Electroweak symmetry breaking

As noted in Section 2.1.2.2, the Higgs boson gives mass to the gauge bosons through the process of electroweak symmetry breaking – which is also the process whereby the electroweak gauge symmetry is broken, yielding the familiar electromagnetic sector. This is an example of a more general mechanism in quantum field theory known as *spontaneous symmetry breaking*. Sometimes analogized with a see-saw, the basic concept is that the Lagrangian of a quantum field theory may be constructed such that to minimize its potential, a field must take on a non-zero *vacuum expectation value* (VEV). Consider, for example, a simple Lagrangian of a scalar field given by [27]

$$\mathcal{L} = \frac{1}{2} (\partial_\mu \phi^*) (\partial^\mu \phi) + \frac{1}{2} m^2 |\phi|^2 - \frac{\lambda}{4} |\phi|^4, \quad (2.16)$$

- $\phi$  is a complex scalar field,
- $\partial_\mu$  is the 4-derivative,
- $\{m, \lambda\}$  are coefficients.

The  $m^2 |\phi|^2$  term looks like a “standard” mass term under the transformation  $m^2 \rightarrow -m^2$ . Note that this Lagrangian has a global  $U(1)$  symmetry, as it is invariant under the transformation  $\phi(x) \rightarrow \exp(i\theta)\phi(x)$  for any choice of  $\theta$ . However a consequence of this Lagrangian’s

---

27. See Chapter 29 of Ref. [6] for a fuller treatment of this phenomenon.

particular formulation is that it is minimized not at  $\phi = 0$ , but rather for

$$\phi = \sqrt{\frac{2m^2}{\lambda}} \exp(i\theta) . \quad (2.17)$$

where  $\theta$  can take on any value – the potential term is independent of it. We may want to rewrite the Lagrangian so that we expand this field around this minimum, which corresponds with its VEV. To do this, we will choose to set it as  $\theta = 0$  for simplicity, so that the VEV is real. Now, we can parameterize  $\phi(x)$  in terms of radial and axial modes, as

$$\phi(x) = \left( \sqrt{\frac{2m^2}{\lambda}} + \frac{1}{\sqrt{2}}\sigma(x) \right) \exp(i\pi(x)/F_\pi) , \quad (2.18)$$

- $\sigma(x)$  is the radial mode,
- $\pi(x)$  is the axial mode,
- $F_\pi$  is some real number (that we are free to choose).

so that we can now rewrite our Lagrangian in terms of the radial  $\sigma(x)$  and axial  $\pi(x)$  as

$$\begin{aligned} \mathcal{L} = & \frac{1}{2} (\partial_\mu \sigma)^2 + \left( \sqrt{\frac{2m^2}{\lambda}} + \frac{1}{\sqrt{2}}\sigma(x) \right)^2 \frac{1}{F_\pi^2} (\partial_\mu \pi)^2 \\ & - \left( -\frac{m^4}{\lambda} + m^2\sigma^2 + \frac{1}{2}\sqrt{\lambda}m\sigma^3 + \frac{1}{16}\lambda\sigma^4 \right) . \end{aligned} \quad (2.19)$$

Choosing  $F_\pi = 2m/\sqrt{\lambda}$  gives us a familiar, canonically-normalized kinetic term for  $\pi$ , which (as we can see from the potential terms) is massless while  $\sigma$  is not. This formulation of the Lagrangian is useful because, again, we are expanding it around the minimum (vacuum) of  $\phi$ . However, there were an infinite number of vacua from which we could choose from, corresponding with different values of  $\theta$ , and any choice would have been equally valid. Furthermore, it looks like our  $U(1)$  symmetry has vanished, because the Lagrangian is not invariant under transformations  $\sigma \rightarrow \exp(i\theta)$  or  $\phi \rightarrow \exp(i\theta)$ . The symmetry is not gone, but it has been hidden away: our theory is still symmetric under such transformations applied

to the original  $\phi(x)$ . The vacuum – whichever one we have chosen to expand the field about – has “broken” our symmetry. This is the phenomenon of spontaneous symmetry-breaking – of which electroweak symmetry breaking is an example. Before moving on to that specific case, it is worth noting that the massless field  $\pi(x)$  in our example is not some quirk of this particular model. Rather, any model that exhibits spontaneous breaking of a global symmetry will have a massless field, known as a Nambu-Goldstone boson [27, 28].

Turning our discussion from toy models back to the SM, the process of electroweak symmetry breaking is a particular example of this same phenomenon, where the Higgs field plays the role of  $\phi$  in our model<sup>[28]</sup>. We have a somewhat more complicated Lagrangian, given by

$$\mathcal{L} = -\frac{1}{4} (W_{\mu\nu}^a)^2 - \frac{1}{4} B_{\mu\nu}^2 + (D_\mu H)^\dagger (D_\mu H) + m^2 H^\dagger H - \lambda (H^\dagger H)^2, \quad (2.20)$$

- $W_{\mu\nu}^a$  are the SU(2) gauge boson field strengths,
- $B_{\mu\nu} = \partial_\mu B_\nu - \partial_\nu B_\mu$ , where  $B_\mu$  is the hypercharge gauge boson,
- $H$  is the Higgs multiplet, which is a complex doublet,
- $D_\mu(\dots) = \partial_\mu(\dots) - \frac{1}{2}igW_\mu^a\sigma^a(\dots) - \frac{1}{2}ig'B_\mu(\dots)$  is the gauge-covariant derivative,
- $\{g, g'\}$  are SU(2) and  $U(1)$  group coupling constants,
- $\sigma^i$  are the Pauli matrices,
- $\{m, \lambda\}$  are coefficients.

The gauge bosons correspond with the  $SU(2)_L$  and  $U(1)_Y$  gauge groups discussed in Section 2.1.1.3. Like in Equation 2.16, this Lagrangian has a potential that is minimized for a non-zero VEV for  $H$ . Without loss of generality, we can choose this so that we may rewrite  $H$  as

$$H = \exp\left(i\frac{\sqrt{\lambda}\pi^a\sigma^a}{m}\right) \left[ \begin{array}{c} 0 \\ \frac{1}{\sqrt{2}}\left(\frac{m}{\sqrt{\lambda}} + h\right) \end{array} \right]. \quad (2.21)$$

---

28. As with our toy example, a fuller treatment of this process can be found in Chapter 29 of Ref. [6]. In particular, we will avoid writing out the entire Lagrangian after diagonalization of masses, since the final expression is quite cumbersome (although useful for reading off Feynman rules).

We can eliminate the  $\pi^a(x)$  via a gauge transformation corresponding with the original Lagrangian's gauge symmetry – so we are free to do this to simplify things without actually modifying the theory itself<sup>[29]</sup>. Rewriting the Lagrangian using this expression for  $H$ , we find the mass terms come out as

$$\mathcal{L}_{\text{mass}} = \frac{g^2 m^2}{8\lambda} \left( \left( W_\mu^{(1)} \right)^2 + \left( W_\mu^{(2)} \right)^2 + \left( \frac{g'}{g} B_\mu - W_\mu^{(3)} \right)^2 \right). \quad (2.22)$$

This expression is not *diagonalized*, as we have some mixing between the  $B_\mu$  and  $W_\mu^{(3)}$  due to the last term. To diagonalize it, we choose the following basis, from which we identify the  $W$ - and  $Z$ -bosons of the Standard Model, as well as the electromagnetic field  $A_\mu$ :

$$W_\mu^\pm = \frac{1}{\sqrt{2}} \left( W_\mu^{(1)} \mp i W_\mu^{(2)} \right), \quad (2.23)$$

$$Z_\mu^0 = \frac{1}{\sqrt{g^2 + (g')^2}} \left( g W_\mu^{(3)} - g' B_\mu \right),$$

$$A_\mu = \frac{1}{\sqrt{g^2 + (g')^2}} \left( g' W_\mu^{(3)} + g B_\mu \right). \quad (2.24)$$

We find the electromagnetic field to be massless (as expected), while the  $W$ - and  $Z$ -boson masses are given by

$$m_W = \frac{1}{2} g \frac{m}{\sqrt{\lambda}}, \quad (2.25)$$

$$m_Z = m_W / \cos \theta_W,$$

where we have introduced the weak mixing angle  $\tan(\theta_W) = g'/g$  by convention.

---

29. In fact, the story is a little more complicated. Here we are following the naïve description of the so-called Higgs mechanism, as is done in textbooks such as Ref. [6]. However, the Higgs VEV is gauge-dependent and more generally, gauge symmetries cannot be spontaneously broken [29]. Nonetheless, this approach yields the correct results as a consequence of this particular theory's construction, and the Higgs mechanism can be reformulated in an entirely gauge-invariant manner [30]. For a pedagogical review of this phenomenon – including aspects well beyond the scope of our discussion of theory – see Ref. [31].

Returning to our Lagrangian, by focusing on the terms involving our field  $h(x)$  – which unlike the  $\pi^a(x)$ , is not eliminated by our choice of gauge – we find that it has mass

$$m_h = \sqrt{2}m . \tag{2.26}$$

From experimental measurements, we find these masses to be [9]

$$m_W = 80.3692 \pm 0.0133 \text{ GeV} ,$$

$$m_Z = 91.1880 \pm 0.0020 \text{ GeV} ,$$

$$m_h = 125.20 \pm 0.11 \text{ GeV} .$$

While this may seem all fine and well, the Higgs boson mass is suspiciously low given the contributions that this mass should receive from its many couplings. This is a sign that there might possibly be something missing from our model, and as we will discuss in Section 2.3, serves as motivation for a wide swathe of current searches for new physics.

### 2.1.2.6 Renormalization

Before moving on from our review of the SM, let us briefly touch upon the concept of *renormalization*, which is crucial to quantum field theory<sup>[30]</sup>. To understand this, we should first consider what exactly it is that we do in quantum field theory. At its core, the theory describes transitions between quantum states – as we depict in Feynman diagrams of high-energy particle processes. As noted earlier, these diagrams are tools that we can use to compute the probability of transitions between these quantum states, from which we can compute process *cross-sections*, or likelihoods, and decay rates. The presence of loops in Feynman diagrams can lead to divergences when computing process amplitudes, as their

---

<sup>30</sup>. A lot more can be said on this topic, and entire books have been written on the subject. For reference, see (for example) Part 3 of Ref. [6].

inclusion allows for producing an infinite number of diagrams describing processes between some given initial and final states. We can regulate these divergences in the theory by introducing *counterterms* into calculations, which add infinite contributions to intermediate steps in computations [6] in order to eliminate (or *regulate*) divergences. Importantly, any final results in computations should be independent of these counterterms. There are multiple techniques by which one can perform this regularization, such as introducing an energy cutoff scale, or (a little more abstractly) performing computations in a lower-dimensional space [32]. In the case of introducing an energy cutoff scale, this process can be interpreted as making a statement about the characteristic energy (or length) scale up to which the theory is valid.

## 2.2 Issues with the Standard Model

The Standard Model (SM) is a very successful theory, describing much of particle physics phenomenology and experimental results to an incredible degree of precision. However, it leaves open some important questions. There are phenomena that the SM does not describe, and the model is in need of significant *fine-tuning* in order to be consistent with experimental observations<sup>[31]</sup>. These shortcomings suggest that the SM is not a complete model, and motivates the search for beyond-Standard Model (BSM) physics<sup>[32]</sup>. Perhaps two of the most striking issues<sup>[33]</sup> with the SM are its inability to explain dark matter, and the fine-tuning necessary for the Higgs boson mass to match experimental findings.

---

31. We will discuss the concept of fine-tuning further below.

32. Here, we are focusing on extensions of the SM, which accounts for a significant portion of past and present theoretical physics research. There have been limited efforts – whether serious or simply exercises in model-building – to replace the SM, as in Ref. [33]. However, such models are well beyond the scope of this thesis.

33. It is important to note that these are not the only issues or open questions related to the SM. For example, absent from our discussion is the question of neutrino masses: where do they come from? The SM does not provide a mechanism, as the Yukawa coupling between the Higgs and fermions requires both left- and right-handed varieties of these particles, but right-handed neutrinos have not been observed (and are absent from the model). Multiple experiments have observed that neutrinos oscillate in flavor when passing through matter [20–23], which implies that they are massive, and that the mass eigenstates are different than the flavor eigenstates (Section 2.1.2.1).

### 2.2.1 Dark Matter

Astronomical observations of galaxy rotation curves [34] – the measurement of the speeds at which different parts of galaxies rotate – together with measurements of the cosmic microwave background [35–37], suggest the presence of so-called *dark matter* [38, 39], which is weakly-interacting and thus not directly observable<sup>[34]</sup>. In fact, the evidence suggests that dark matter accounts for the *majority* of matter in the universe. This dark matter may consist of one or many species of particles not currently described by the SM, but which may (weakly) couple to SM particles. Thus we may be able to directly detect their presence in the universe, or produce and detect them in particle colliders. Alternatively, we may indirectly measure their existence through how they may modify the parameters and dynamics of the known SM particles – the details of which may heavily depend on the dark matter model.

### 2.2.2 The hierarchy problem

In the SM, the Higgs boson mass receives contributions from all the particles to which it couples. This requires a high level of fine-tuning of model parameters, so that divergences in contributions from higher-order corrections cancel out across 30 orders of magnitude (see Appendix C) to make the SM consistent with observations. While such fine-tuning is possible, it may seem “unnatural” as succinctly described by physicist Gerardus t’Hooft:

The concept of causality requires that macroscopic phenomena follow from microscopic equations... One may either consider these microscopic properties to have been chosen at random by Nature, or attempt to deduce these from even more fundamental equations at still smaller length and time scales. In either case, it is unlikely that the microscopic equations contain various free parameters that are

---

34. There are, perhaps unsurprisingly, alternative theories that attempt to account for the astronomical observations without introducing new particles, such as *modified Newtonian dynamics* (MOND). However, these theories have largely fallen out of fashion, as current observations strongly favor dark matter [40].

carefully adjusted by Nature to give cancelling effects such that the macroscopic systems have some special properties [41].

Thus one can take the necessity of fine-tuning the SM as strong motivation (if not exactly hard evidence) of new physics. Specifically, this motivates extensions of the SM that would introduce some mechanism(s) to *dynamically* resolve the fine-tuning problem, and result in a theory where the phenomenology is no longer extremely sensitive to the exact values of certain model parameters.

## 2.3 Supersymmetry

From the last section, we are evidently in need of an extension of the SM that provides for new species of particles to serve as dark matter, and that resolves the fine-tuning problem of the Higgs boson mass. SUSY potentially fulfills both of these requirements<sup>[35]</sup>. The basic premise is that it introduces a new global symmetry, the eponymous *supersymmetry*, that relates the SM particles to a new set of particles that serve as their *super-partners*: Each SM boson has a super-partner fermion, and each SM fermion a super-partner boson, the super-partners having the same quantum numbers other than spin. The super-partner particles, or *sparticles*<sup>[36]</sup>, are joined together with their SM counterparts into *supermultiplets*, irreducible representations of the supersymmetry algebra in which the full theory is written [42]<sup>[37]</sup>. This global symmetry is broken at some high energy scale, so that the particles and sparticles have different masses.

That SUSY provides a possible explanation for dark matter may seem almost obvious on the surface level; it provides for new particles beyond those in the SM and one or many of these

---

35. While I will provide a high-level overview of SUSY, focusing on details necessary for motivating the phenomenological and experimental work described later on, a fuller review can be found in Ref. [42].

36. When discussing SUSY particles, it is conventional to name them by prepending an “s” onto fermions’ super-partners, or adding the suffix “-ino” onto bosons’. For example, “quark”  $\rightarrow$  “squark”, or “W-boson”  $\rightarrow$  “Wino”.

37. For some more (historical) context, see Ref. [43, 44] for a discussion of supermultiplets in the context of supersymmetric gauge theories – such as that we will discuss in Section 2.3.1.

may comprise the dark matter in the universe. It is also not the only BSM theory to fulfill this requirement. For example, the hypothetical *axion* of Peccei-Quinn theory [45] (discussed in Section 3.1) serves a dark matter candidate independent of SUSY. Other possibilities include the introduction of “sterile” right-handed neutrinos [46, 47], or “little Higgs” models [48, 49] – where the Higgs boson is a pseudo-Nambu-Goldstone boson of some new broken symmetry, and new particles are introduced to handle the Higgs boson couplings as well as the Higgs mass divergences.

The way in which SUSY resolves the hierarchy problem is a little more subtle: Bosonic and fermionic loop diagrams provide opposite-sign contributions when computing the Higgs boson mass. Due to how SUSY is constructed – specifically the relationship between SM particles and their super-partners – the parts of these diagrams divergent in the cutoff scale will cancel as shown in Appendix C.

There are different ways of extending the SM via SUSY. In the following section, we will review one particular way of doing this, called the “Minimal Supersymmetric Standard Model”, which will also feature in our discussion of axino physics in Section 3.2 and the ATLAS BSM search in Chapter 5.

### 2.3.1 *The Minimal Supersymmetric Standard Model*

The Minimal Supersymmetric Standard Model (MSSM) is the simplest way of extending the SM with SUSY, and is constructed on a relatively simple set of assumptions [50]:

- The MSSM is based on the same gauge symmetry as the SM, as in Eq. 2.5.
- Each SM fermion has a spin-0 super-partner. There are *two* chiral Higgsino superfields (up- and down-types) with scalar components given by

$$H_d = \begin{bmatrix} H_d^0 \\ H_d^- \end{bmatrix} \quad H_u = \begin{bmatrix} H_u^0 \\ H_u^+ \end{bmatrix}, \quad (2.27)$$

so that there are four scalar Higgsinos in total<sup>[38]</sup>.

- We assume the discrete, multiplicative symmetry of  $R$ -parity, where the operator  $R$  is given by

$$R = (-1)^{2s+3B+L} . \quad (2.28)$$

- $s$  is the spin quantum number (Section 2.1.1.2),
- $B$  is the baryon quantum number.
- $L$  is the lepton quantum number.

SM particles have quantum number  $R = +1$ , and SUSY particles have  $R = -1$ . The implications of this symmetry are significant: SUSY particles are produced in pairs and decay to odd numbers of SUSY particles, and the lightest SUSY particle (LSP) is stable. This last feature is particularly relevant to the dark matter, which might consist of stable LSPs.

- The theory exhibits *soft SUSY breaking*. In general, we want to construct a SUSY model whereby SUSY is a symmetry of the Lagrangian that is spontaneously broken at low energies, similar to electroweak symmetry breaking. In the effective Lagrangian – which describes the model below the SUSY breaking scale – we allow for the introduction of soft breaking terms, which are those with a positive mass dimension. This avoids introducing quadratic divergences in the quantum corrections to scalar particles' masses [52], which would otherwise introduce a serious issue in the model's basic structure.

Under these assumptions, we are free to construct a model with a very large number of parameters. Fortunately, we can apply a wide variety of phenomenological constraints – from past collider experiments as well as cosmological arguments and astrophysical observations –

---

38. The reason for having multiple Higgsinos is to resolve a *chiral anomaly*, as only supermultiplets of the same handedness can have Yukawa couplings to one another – so two supermultiplets are needed to have couplings to left- and right-handed fermions [51] – two charged, and two neutral components.

to constrain the parameter space [50]<sup>[39]</sup>.

Of particular consequence to experimental searches, we typically do not assume that the flavor eigenstates of the scalar and gauge boson superpartners are the same as their mass eigenstates, but rather that they mix, with the mixing given by

$$\begin{bmatrix} \tilde{\chi}_1^0 \\ \tilde{\chi}_2^0 \\ \tilde{\chi}_3^0 \\ \tilde{\chi}_4^0 \end{bmatrix} = N_{ij} \begin{bmatrix} \tilde{B} \\ \tilde{W} \\ \tilde{H}_d^0 \\ \tilde{H}_u^0 \end{bmatrix}, \quad (2.29)$$

- $\tilde{\chi}_i^0$  is the  $i$ 'th lightest neutralino,
- $N$  is a unitary  $4 \times 4$  matrix,
- $\{\tilde{B}, \tilde{W}\}$  are the Bino and neutral Wino,
- $\{H_u^0, H_d^0\}$  are the up- and down-type Higgsinos.

where the matrix  $N$  converts between the two bases. This can be thought of as analogous to neutrinos and the PMNS matrix in Section 2.1.2.1. <sup>[40]</sup>

---

39. In the existing literature, this is sometimes referred to as the *phenomenological MSSM* (pMSSM).

40. One practical consequence of the difference between mass and flavor eigenstates here is the use of nomenclature: high-energy physicists may use either basis depending on the context, and sometimes the flavor eigenstates are used colloquially to refer to the mass eigenstates in models where neutralinos are assumed to be mostly composed of only a subset of flavors, such as a neutralino composed only of up- and down-type Higgsinos.

## CHAPTER 3

### AXION AND AXINO PHYSICS

So far we have seen an overview of the Standard Model (SM) of particle physics, as well as supersymmetry (SUSY), an extension of the model that addresses some of the shortcomings of the SM – namely its lack of a description of dark matter, and the apparent fine-tuning of the Higgs boson mass.

In this section, I will describe the theoretical motivations for *Peccei-Quinn* (PQ) theory, another extension of the SM that addresses yet another fine-tuning problem in the SM, one related to observed violations of combined charge conjugation and parity symmetries. This theory yields a new scalar particle called the *axion*, and when combined with SUSY, a sparticle called the *axino*. I will describe the phenomenological consequences of the axino for collider-based particle physics experiments – which (partly) motivates the ATLAS analysis described later on in this thesis.

### 3.1 Peccei-Quinn theory, and the QCD axion

As we saw in the previous section, extending the SM via SUSY is partly motivated by the Higgs boson mass and the associated hierarchy problem, an example of a fine-tuning that can be resolved by introducing an extension of the original theory (resulting in some new particles). Another example of a fine-tuning problem in the SM is the so-called *strong CP problem*.

#### *3.1.1 CP symmetry and violation*

Charge conjugation parity (*CP*) symmetry, refers to whether or not a particular term in the Lagrangian is symmetric with respect to simultaneous charge conjugation and parity transformations, as discussed in Sections 2.1.1.3 and 2.1.1.4, respectively.

To see where the issue of  $CP$  violation arises, let us consider the portion of the SM that describes the interactions of quarks and gluons. The theory of these particles and their dynamics is called quantum chromodynamics (QCD), referring to the color charge that these particles carry. QCD is an example of a non-Abelian gauge theory, also known as a *Yang-Mills theory*. Its symmetry group is  $SU(3)$ , with the name “chromodynamics” alluding to the *color charge* the quarks carry under this group.

The Yang-Mills Lagrangian<sup>[1]</sup> can be written as [6, 53]

$$\begin{aligned} \mathcal{L}_{\text{QCD}} = & -\frac{1}{4}G_{\mu\nu}^a G^{\mu\nu a} - \frac{\theta g^2}{32\pi^2}G_{\mu\nu}^a G_{\alpha\beta}^a \epsilon^{\mu\nu\alpha\beta} \\ & + \psi_i^\dagger (i\gamma^\mu (D_\mu)_{ij} - m\delta_{ij}) \psi_j . \end{aligned} \quad (3.1)$$

- $G_{\mu\nu} = \partial_\mu A_\nu^a - \partial_\nu A_\mu^a + gf^{abc}A_\mu^b A_\nu^c$  is the field-strength tensor,
- $A_\mu$  is the gauge field,
- $g$  is a coupling constant,
- $f^{abc}$  are the structure constants of the gauge group generators' Lie algebra,
- $\psi_i$  is the fermion field,
- $(D_\mu)_{ij} = \partial_\mu \delta_{ij} - ig(T_a)_{ij}A_\mu^a$  is the gauge-covariant derivative,
- $T^a$  are the generators of the Lie algebra.

The second, so-called *theta term*, which is dependent on parameter  $\theta$ , is  $CP$ -odd. The phenomenon that this term is present in the Lagrangian is commonly referred to as *strong CP violation*. Its presence can be understood as a consequence of an *anomalous* global chiral symmetry: an anomalous symmetry is one present in the classical Lagrangian but not its quantum counterpart, as the classical action is invariant but the path integral measure changes [6]. In the case of QCD, this is a symmetry which transforms the fermions as

$$\psi \rightarrow \exp(i\gamma_5\theta)\psi , \quad (3.2)$$

---

1. Keep in mind that there are multiple conventions for how exactly the terms in the Lagrangian are defined – which has consequences for the various factors that appear. Such details are not particularly relevant to our current discussion, but are worth keeping in mind when consulting sources.

- $\gamma_5$  is a Dirac gamma matrix,
- $\theta$  is a parameter of the transformation.

which changes the fermion path integral measure as

$$\int \mathcal{D}\bar{\psi}\mathcal{D}\psi \rightarrow \int \mathcal{D}\bar{\psi}\mathcal{D}\psi \exp\left(i\theta \int \frac{g^2}{32\pi^2} G_{\mu\nu}^a G_{\alpha\beta}^a \epsilon^{\mu\nu\alpha\beta}\right), \quad (3.3)$$

thus yielding the theta term in Eq. 3.1<sup>[2]</sup>. In fact, one can perform chiral rotations of the quarks to transform  $\theta$  as

$$\theta \rightarrow \bar{\theta} \equiv \theta - \arg \det (Y_d Y_u) \quad (3.4)$$

- $\arg(\dots)$  is the argument function (of complex analysis),
- $\det(\dots)$  is the determinant,
- $\{Y_d, Y_u\}$  are Yukawa matrices.

where the Yukawa matrices  $\{Y_d, Y_u\}$  parameterize the quark-Higgs Yukawa couplings. However,  $\theta$  itself depends on the chiral rotation, and the upshot is that the term  $\bar{\theta} = \theta - \arg \det (Y_d Y_u)$  is invariant under these rotations.<sup>[3]</sup> In other words, we find that the theta term (now generalized with the replacement  $\theta \rightarrow \bar{\theta}$ ) is basis-invariant, and thus physically meaningful.

One observable consequence of  $\bar{\theta} \neq 0$  would be a proportional neutron electric dipole moment<sup>[4]</sup>  $d_n$ . However, the best current measurement of  $d_n$ , determined by studying the Larmor precession of ultra-cold neutrons in co-linear electric and magnetic fields, is  $d_n = (0.0 \pm 1.1_{\text{stat}} \pm 0.2_{\text{sys}}) \times 10^{-26} \text{e}\cdot\text{cm}$  [58]. In other words, we appear to live in a world with  $\bar{\theta} \approx 0$ , which requires a fine-tuning of the SM akin to the hierarchy problem (Appendix C). Alternatively, there may be some yet-undiscovered mechanism that dynamically eliminates

---

2. For a review of this phenomenon, see Ref. [54]. This QCD anomaly is an example of an Adler-Bell-Jackiw anomaly [55, 56], which occurs in quantum field theories with chiral fermions.

3. For a pedagogical review of this phenomenon, see Ref. [57].

4. See Appendix D.

the strong  $CP$  violation. The apparent need for such a mechanism – to avoid fine-tuning – is what we refer to as the strong  $CP$  problem.

### 3.1.2 Peccei-Quinn theory

One resolution to the strong  $CP$  problem is that of Peccei-Quinn (PQ) theory [45]. The theory introduces the PQ symmetry – a global, chiral anomalous  $U(1)_{\text{PQ}}$  symmetry .

The spontaneous breaking of the  $U(1)_{\text{PQ}}$  symmetry<sup>[5]</sup> yields a pseudo-Nambu-Goldstone boson, the *axion* [59, 60]. The inclusion of the axion yields an additional term in the Lagrangian [61],

$$\mathcal{L}_{\text{PQ}}^{\text{potential}} = \xi \frac{a}{f_a} \frac{g^2}{32\pi^2} G_{\mu\nu}^a G_{\alpha\beta}^a \epsilon^{\mu\nu\alpha\beta} . \quad (3.5)$$

- $\xi$  is the anomaly coefficient,
- $a$  is the axion field,
- $f_a$  is the axion decay parameter.

Combined with the QCD anomaly term, the new effective vacuum angle is  $\bar{\theta} + \xi\langle a\rangle/f_a$ , and the effective potential is then minimized for

$$\langle a \rangle = -\frac{f_a \bar{\theta}}{\xi} . \quad (3.6)$$

Thus the inclusion of this new scalar dynamically eliminates the strong  $CP$ -violation, and without the need for fine-tuning as this mechanism is not sensitive to the precise value of  $f_a$ .

Fortunately, PQ theory is testable: we can search for the axion. A potential dark matter

---

5. This is analogous to the electroweak symmetry-breaking discussed in Section 2.1.2.5.

candidate<sup>[6]</sup>, it has a mass given by [63–65]

$$m_a \sim 6\mu\text{eV} \frac{10^{12}\text{GeV}}{(f_a/N_{DW})}, \quad (3.7)$$

and it couples to photons with a coupling strength given by [63, 66–69]

$$g_{a\gamma\gamma} = \frac{\alpha}{2\pi} \frac{N_{DW}}{f_a} \left( \frac{E}{N} - \frac{2}{3} \frac{4+z}{1+z} \right) \quad (3.8)$$

- $\alpha$  is the fine structure constant,
- $N_{DW}$  is the domain wall number,
- $f_a$  is the axion decay parameter,
- $E$  is the electromagnetic anomaly of the axion axial current,
- $N$  is the color anomaly of the axion axial current,
- $z = m_u/m_d = 0.462 \pm 0.020$  is the ratio of up- and down-type quark masses [9].

Owing to the axion-photon coupling, one can search for axion production in the presence of a (strong) magnetic field as is done in direct-detection experiments<sup>[7]</sup> As noted as early as 1978 [59, 60], there was already strong evidence from particle physics experiments that the axion, at least as described in this early model, does not exist. As is often the case in physics, this was not a complete showstopper for axion phenomenology: further developments of and modifications to the PQ theory framework produced so-called “invisible axion” models. Featuring feebly-interacting axions, these models retain the PQ mechanism but are not as readily ruled out by cosmological arguments and astrophysical measurements. The two notable invisible axion models are the KSVZ [74, 75] and DFSZ [76, 77] models.

The KSVZ model introduces a Higgs singlet, and a fourth generation of quarks which carry PQ charge. By contrast, in the DFSZ model<sup>[8]</sup> – which will be our focus – the PQ charge

---

6. For a recent review of axion cosmology – how axions may explain dark matter, as well as cosmological bounds on different axion models – see Ref. [62].

7. For a (non-exhaustive) set of such experiments, see Ref. [70–73].

8. For a review of DFSZ axion models, see Ref. [78–80]. In addition, Ref. [81] provides a review of both KSVZ and DFSZ models, in addition to alternatives.

is carried by right-handed fermions (both quarks and leptons), as well as in an expanded Higgs sector containing two Higgs doublets and one complex scalar singlet.

### 3.2 Axinos, and their Phenomenology at Collider Experiments

While the implications of PQ theory are critically important for QCD, a part of the SM directly probed at collider experiments like ATLAS, the prospects for collider-based direct axion searches are quite dim. As shown in Figure 3.1, past and current collider experiments cannot compete with astrophysical observation and dedicated, axion direct-search experiments [82] in terms of probing increasingly small axion masses and axion-photon couplings. In fact, these experiments are generally sensitive to *axion-like particles*, which are scalar particles similar to axions but that do not necessarily obey the mass-decay parameter constraint of Eq. 3.7 – these also do not resolve the strong  $CP$  problem, and thus are arguably of less interest than the  $QCD$  axion (shown in yellow in Figure 3.1), but are nonetheless perfectly valid targets for BSM searches.

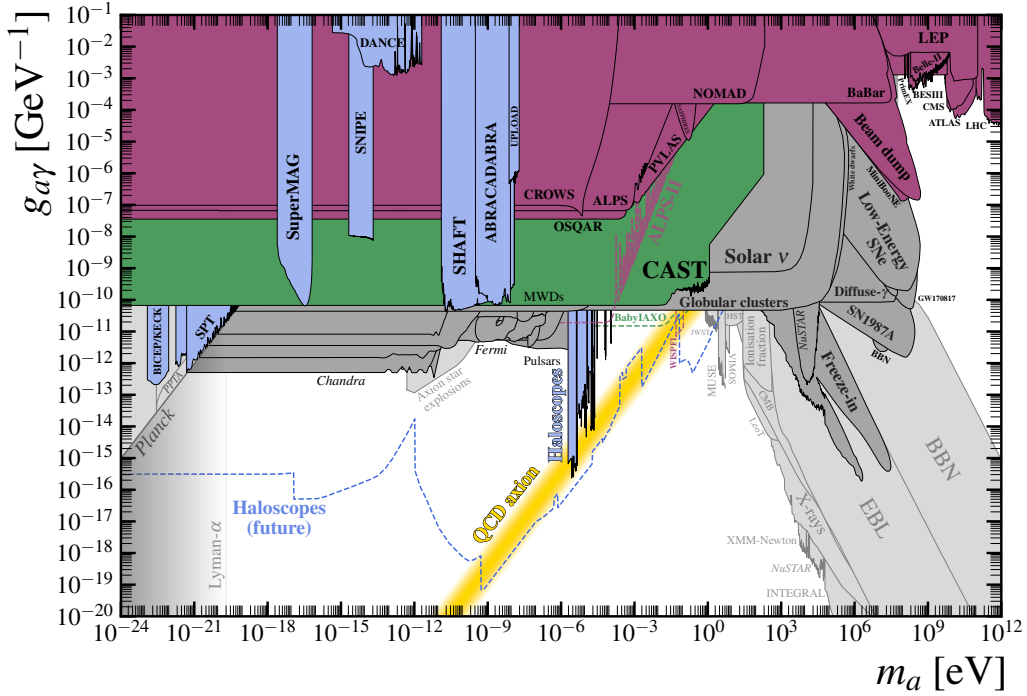
The story is a little different under the assumption of SUSY. Combining the MSSM with PQ theory, we may use a collider experiment in a search for the *axino*  $\tilde{a}$ , the fermionic superpartner of the axion<sup>[9]</sup>.

In particular we shall focus on a DFSZ axino model – which as a combination of PQ and MSSM theories, we shall refer to as the  $PQMSSM$  model. In this model, the axino couples to the Higgs and  $Z$ -bosons, as well as the Higgsinos<sup>[10]</sup>. Under the assumption that the axino to be the LSP, we may look for  $\tilde{H} \rightarrow \tilde{a} + h/Z$  decays. In fact, the axino may mix with the

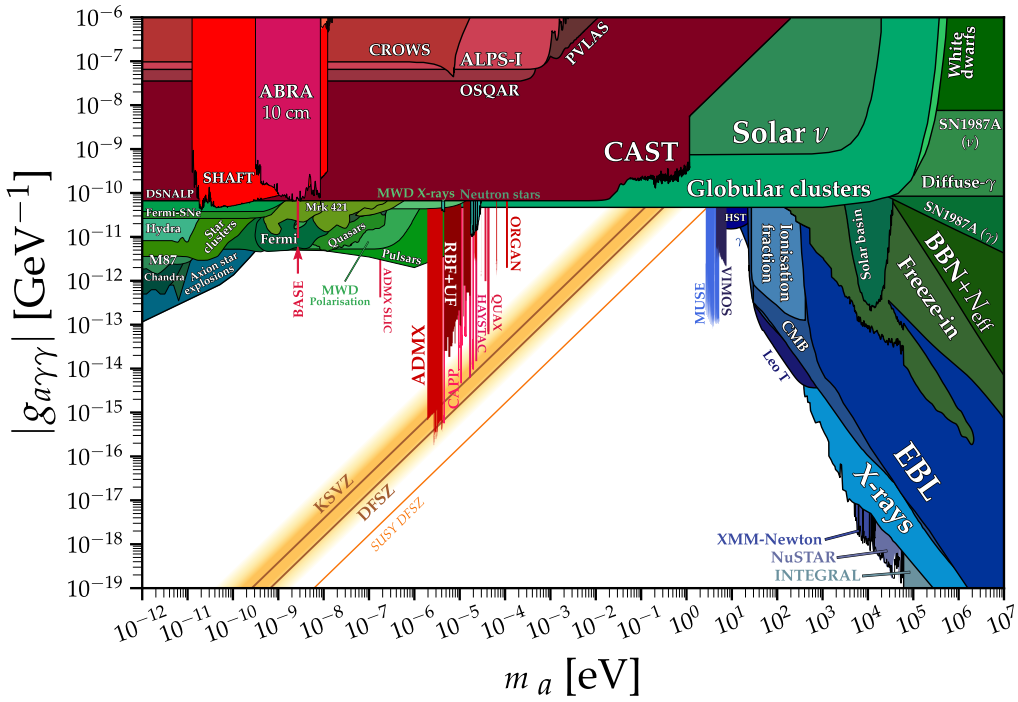
---

9. A lot of the following discussion is based on ongoing work on an axino phenomenology study, for which a paper is currently being written under the working title “Bridging the divide: axion and axino phenomenology at colliders and direct-detection experiments”. The authors are Gabe Hoshino, Kristin Dona, Keisuke Harigaya, David W. Miller, Bianca Pol, Benjamin Rosser, Cecilia Tosciri and myself.

10. While a little beyond the scope of our discussion, it is interesting to note that in PQMSSM, the PQ symmetry actually plays a role in generating the Higgsino mass. The Higgsino mass term in the MSSM must be taken to be around the electroweak scale – which seems reminiscent of the very fine-tuning that motivates SUSY in the first place. However, in PQMSSM this term is dynamically generated via the spontaneous breaking of the PQ symmetry [83].



(a)



(b)

Figure 3.1: An overview of current limits on axions, in terms of axion mass and axion-photon coupling. Note that as shown in (b), under the assumption of SUSY, the DFSZ axion line shifts. Taken from Ref. [82], with (b) modified to show the SUSY DFSZ line.

MSSM neutralinos, leading to a fifth neutralino  $\tilde{\chi}_5^0$ . We will assume the heaviest neutralinos  $\tilde{\chi}_3^0$  and  $\tilde{\chi}_4^0$  to be Wino- and Bino-like<sup>[11]</sup>, with the lighter  $\tilde{\chi}_1^0$  and  $\tilde{\chi}_2^0$  to be composed of up- and down-type Higgsinos. Then to describe the axino-neutralino mixing, we will introduce a fifth neutralino state  $\tilde{\chi}_5^0$ , which is almost purely axino with perturbative Higgsino coupling<sup>[12]</sup>. Computing lowest-order corrections to the MSSM neutralino mixing matrix in this theory, we find that the axino-Higgsino couplings are suppressed by a factor of  $1/f_a$ . This results in a suppressed rate of  $\tilde{H} \rightarrow \tilde{a}h/Z$  decay – or in terms of mass eigenstates,  $\tilde{\chi}_1^0 \rightarrow \tilde{\chi}_5^0 h/Z$  decay. This means that the  $\tilde{\chi}_1^0$  is long-lived, and we can approximate its lifetime as [84]

$$c\tau_{\tilde{\chi}_1^0} \approx 9 \text{ mm} \left( \frac{f_a}{1 \times 10^{10} \text{ GeV}} \right)^2 \left( \frac{1 \text{ TeV}}{m_{\tilde{\chi}_1^0}} \right)^3. \quad (3.9)$$

Thus for a particular PQ domain wall number  $N_{DW}$ , we can relate the  $\tilde{\chi}_1^0$  lifetime to the axion mass (Equation 3.7). As shown in Figure 3.2, using  $N_{DW} = 1$  we find that for  $\tilde{\chi}_1^0$  masses of  $\mathcal{O}(100 \text{ GeV}) - \mathcal{O}(1 \text{ TeV})$ , axion masses of  $\mathcal{O}(\mu\text{eV}) - \mathcal{O}(\text{meV})$  correspond with  $\tilde{\chi}_1^0$  displacements up to hundreds of millimeters. As shown in Figure 2.1.2.4, this corresponds with the “displaced vertex” range – where these particles are sufficiently long-lived that they will travel an appreciable distance into the detector before decay, but not so far that they are effectively detector-stable. As we will see in Section 4.2.2, these displacements in fact correspond with decays within the ATLAS charged particle tracking detector. This detector measures tracks produced by charged particles with very fine position resolution, and thus may be able to detect the presence of a long-lived  $\tilde{\chi}_1^0$  decay: the neutrally-charged  $\tilde{\chi}_1^0$  travels into the tracker unseen, but then decays with some of its decay products being charged (e.g.

---

11. By “Bino-like”, we refer to a neutralino that is mostly composed of a Bino. This corresponds with  $N_{11}^2 > \max\{N_{12}^2, N_{13}^2, N_{14}^2\}$  in Eq. 2.29. This is one of many assumptions we are making here – the essence of a lot of phenomenology is that we make a series of assumptions as to focus on particular subsets of physics models, and how we may go about searching for them.

12. We are breaking the convention of ordering the neutralino indices by mass, but this is perhaps preferable to shifting around all the indices and comparing this model to more “garden-variety” MSSM theories.

$h(b\bar{b})$  or  $Z(q\bar{q})$ ). This results in multiple charged particle tracks appearing from the point where the  $\tilde{\chi}_1^0$  decayed, which the tracker may thus identify as a displaced decay vertex<sup>[13]</sup>. From Figure 2.1.2.4, we see that there are no SM particles that yield displaced vertices with masses above approximately 1 GeV. While some of the  $\tilde{\chi}_1^0$  energy would be carried off by the (potentially massive)  $\tilde{a}$ , for a wide range of  $\tilde{\chi}_1^0$  and  $\tilde{a}$  masses we may expect enough left for producing a Higgs or  $Z$ -boson that, even off-shell, will yield a displaced vertex easily distinguishable from long-lived SM particles like lambda baryons, B-mesons, or kaons<sup>[14]</sup>.

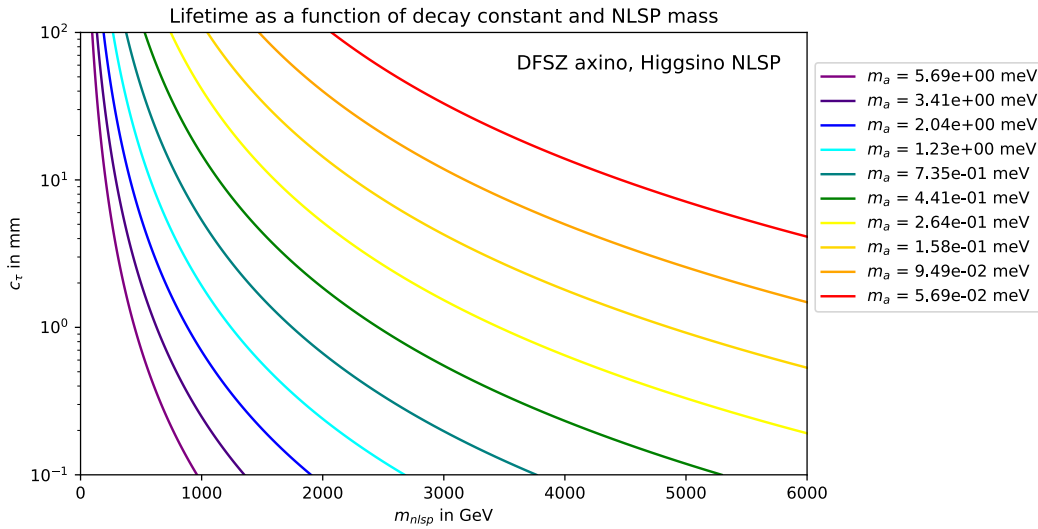


Figure 3.2: The  $\tilde{\chi}_1^0$  mean lifetime  $c\tau$  as a function of its mass, as approximated by Equation 3.9. Taken from Ref. [84].

We need not only speculate on how an experiment such as ATLAS might search for DFSZ axinos. As described in Chapter 5, we can actually perform a careful analysis of data collected by the experiment to search for evidence of this process, as well as a number of other BSM theories that similarly yield long-lived particles. Before delving into this analysis, however,

13. We will discuss this phenomenon a little more in the context of the ATLAS experiment in Section 4.2.1.4.

14. To be clear, a large section of the  $c\tau$  range covered in Figure 3.2 is also well beyond any of the meta-stable SM particle lifetimes, so we may have some sensitivity even if the  $\tilde{a}$  mass were to be more similar to these. However, we must keep in mind that even simply under the SM, there may be more sources of displaced vertices than meta-stable particles produced at the collider interaction point. We will discuss these backgrounds in detail in Chapter 5.

we will review how the ATLAS experiment functions. How does it receive the proton beams whose collisions it observes? What information does it capture from these collisions, and how? As we will see, the ATLAS detector is a complex machine that leverages a multitude of technologies developed over decades of radiation measurement, and that – together with its partner experiments at the Large Hadron Collider – provides an incredible laboratory for investigating the nature of high-energy particle physics.

# CHAPTER 4

## THE ATLAS EXPERIMENT

In this chapter, we will review the technical details of the ATLAS detector and its operation. ATLAS is perhaps best described as a “suite of detectors”, and we will focus on the different components – the charged particle tracker, the calorimeters, the muon spectrometer and the data acquisition system – with particular emphasis on some of the technologies and methods that are most relevant to the analysis that will be discussed in Chapter 5.

Before describing the detector, however, there is the matter of how it receives the proton beams whose collisions it observes. As a CERN accelerator physicist once commented to me, “high-energy physicists seldom think about where the beam comes from, and accelerator physicists seldom think about where it goes”. Thus we will first take a brief (but important) look at the Large Hadron Collider (LHC), the particle accelerator along which ATLAS is stationed, and how it operates. Without the LHC, the ATLAS experiment would not have any physics events to observe. Understanding the structure of the LHC proton beam, even at a very basic level, will help inform some details of how detectors like ATLAS are designed and operated, in regards to both data acquisition and the reconstruction of particles (and more generally “physics objects”) from this data.

### 4.1 The Large Hadron Collider (LHC)

The LHC [1, 85] is a circular particle accelerator and collider located near Geneva, Switzerland, at the European Center for Nuclear Research (CERN). It consists of a circular tube, approximately 27km in diameter and 80m underground. The inside of the tube, or *beam-pipe*, is a vacuum in which two beams of protons circulate in opposite directions. The beams are guided, focused and accelerated to high energies by means of radio-frequency (RF) cavities and superconducting magnets, and collided at four different *interaction points* along the ring,

each housing one of the four main LHC experiments. Figure 4.1 shows an outline of the LHC and the associated beam injection systems, together with the detectors stationed along the accelerator.

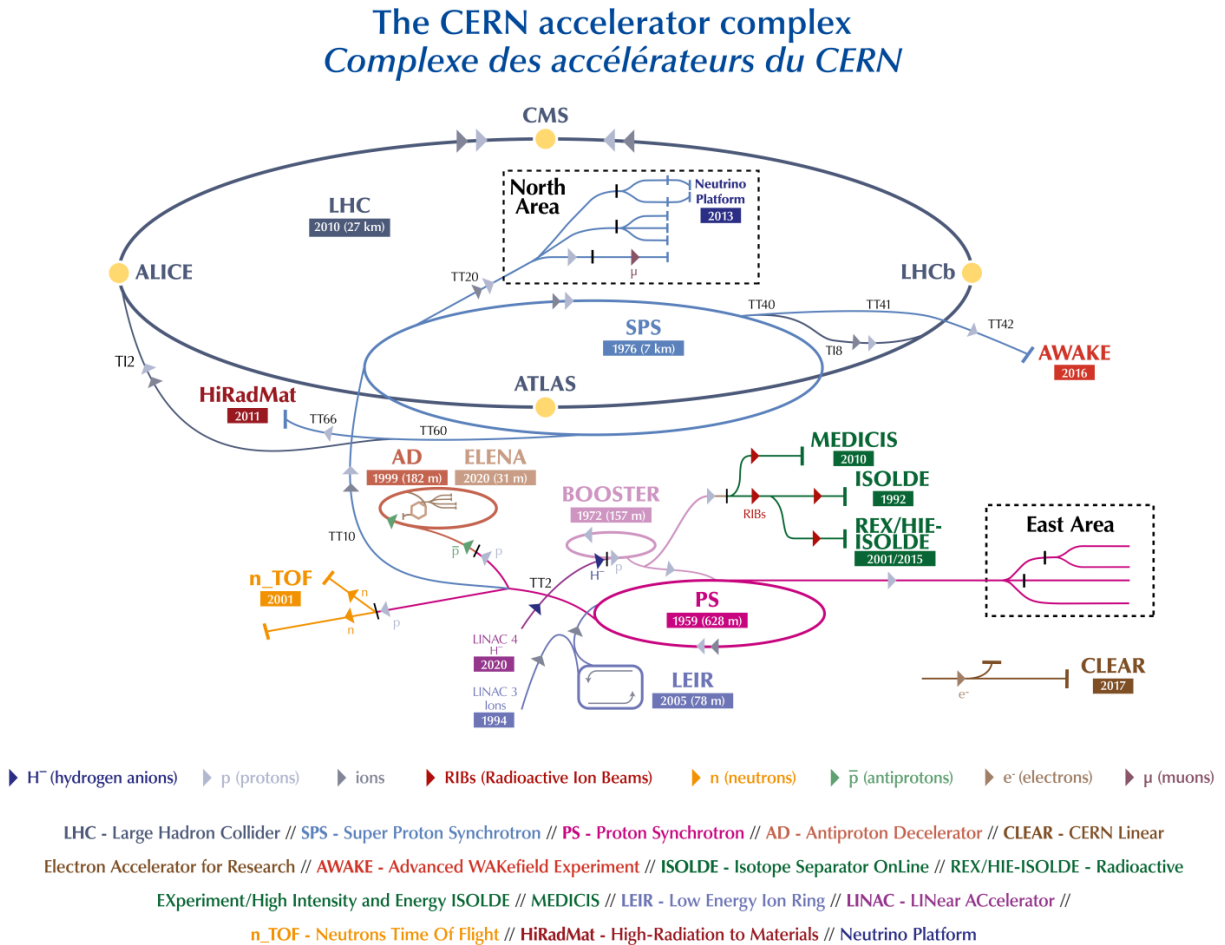


Figure 4.1: A schematic of the accelerators used to produce the proton beam used by the LHC [86], together with the various experiments that utilize these accelerators – note that the four main experiments are stationed along the LHC ring, while others are connected to the smaller accelerators that feed into the LHC. The relevant sequence for the LHC is LINAC4 → BOOSTER → PS → SPS → LHC.

### 4.1.1 The LHC experiments

The four main experiments associated with the LHC are ATLAS, CMS (Compact Muon Solenoid), LHCb (Large Hadron Collider beauty experiment) and ALICE (A Large Ion Collider Experiment)<sup>[1]</sup>.

ATLAS and CMS are both general-purpose detectors for studying proton-proton collisions, each consisting of a suite of sub-detectors – charged particle trackers, electromagnetic and hadronic calorimeters, and muon spectrometers – that collectively reconstruct the kinematics of particles produced in the collisions. These two detectors serve similar functions, probing similar physics, but they are not redundant (at least in the colloquial sense): the detectors differ in design, each having its advantages in measurement sensitivity, and they serve as cross-checks of each others’ results as they independently perform similar Standard Model measurements and searches for new physics. By contrast, the other two main experiments have more specialized functions:

- **LHCb**: Unlike the other detectors’ symmetric designs, LHCb has a “forward configuration” designed for measuring particles produced at a narrow angle with respect to the accelerator beam axis. It is optimized for reconstructing bottom quarks in the forward region, as a way of probing matter-antimatter asymmetry.
- **ALICE**: ALICE is designed primarily for studying *heavy ion* ( $\text{Pb}^+$ ) collisions<sup>[2]</sup>. These are produced by using an ion beam from Linac3 [87] in lieu of protons, as shown in Figure 4.1. This is particularly useful for studies of quantum chromodynamics (QCD), the interaction of quarks and gluons, through measuring the dynamics of quark-gluon plasma produced by colliding heavy nuclei.

---

1. One might notice that ATLAS is the only experiment whose name is not an abbreviation. It was historically an acronym for “**A** **T**oroidal **L**HC **A**pparatus”, but this has since been officially deprecated.

2. Note that while ATLAS and CMS are not dedicated to heavy ion collisions, they do also study these processes – and in fact, produce significant research output in this field.

### 4.1.2 Producing the LHC proton beam

Prior to 2020, the proton beams in the LHC were produced from hydrogen gas: Hydrogen molecules were ionized to yield hydrogen ions  $H^+$ , which are single protons. These were then accelerated by an “Alvarez-type” linear accelerator [88] (or *linac*), consisting of a series of radio-frequency (RF) cavities, and injected into the Proton Synchrotron booster (PSB) at 50 MeV. This first stage in beam production has been modified since the introduction of Linac4 [89]. Unlike its predecessor, this linac uses *negative* hydrogen ions ( $H^-$ ) consisting of one proton and two electrons. These ions are produced in a multi-step process [90], whereby  $H^+$  ions are made by introducing hydrogen gas into an ion source, and then back-scatter on a cathode, producing  $H^-$  ions [91–93]. These ions are then accelerated to 45 keV, at which point they enter the linac and are accelerated to 160 MeV before injection into the PSB<sup>[3]</sup>. Upon PSB injection, electrons are stripped from the  $H^-$  by means of interaction with a carbon stripping foil, to yield protons. It is in this injection process where the advantage of using  $H^-$  ions becomes apparent: The proton beam circulating in the PSB and the incoming  $H^-$  beam from Linac4, owing to their opposite charges, will converge when passed through a focusing magnet. This allows for easily merging the beams before the stripping foil. Figure 4.2 provides a schematic of this *charge-exchange injection* scheme.

### 4.1.3 Proton beam structure

Absent from the above description, the actual structure of the proton beams is crucial to understanding how collisions are performed, and what the resulting data look like. The word “beam” might imply a continuous stream of protons, but the LHC beams are anything

---

3. While the details of the Linac4 acceleration sequence are beyond the scope of this thesis, it is worth noting that this early stage in beam production is particularly complex, as it involves accelerating particles from being essentially at rest, to relativistic speeds – whereas the synchrotrons and the LHC only have to deal with beam particles in the relativistic regime. The acceleration performed by Linac4 thus involves a number of different accelerator technologies, as detailed in Ref. [89], and which I had chance to see during a visit to the Linac4 surface facility.

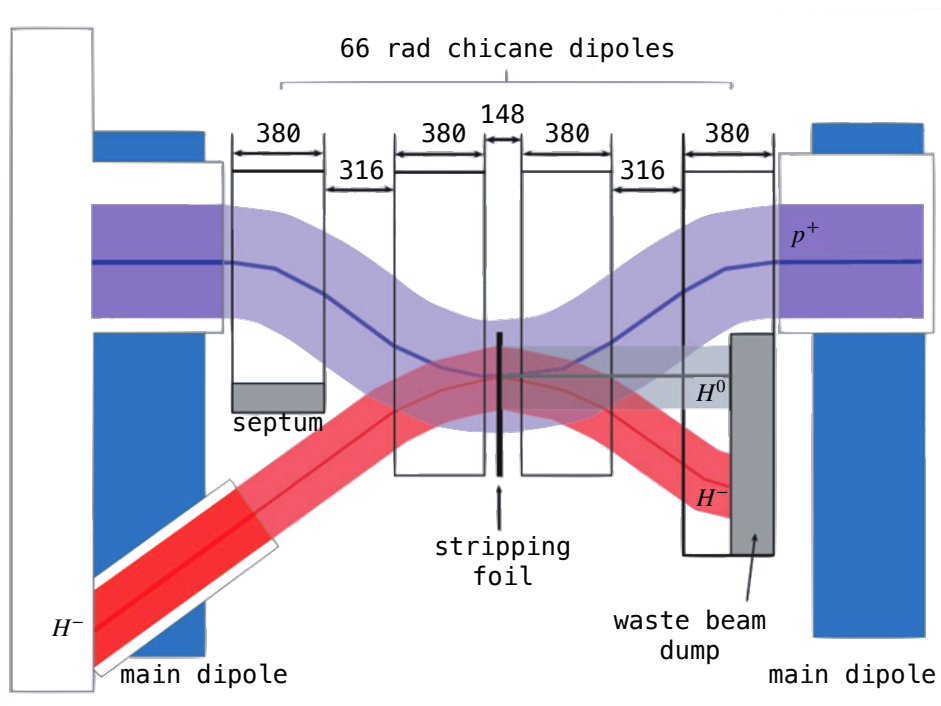


Figure 4.2: A schematic of the charge-exchange injection performed during the injection of  $H^-$  ions from Linac4 into the PSB. Modified from Ref. [90].

but an uninterrupted flow of single particles. On the contrary, they consist of *bunches* of  $\mathcal{O}(10^{11})$  protons, spaced out along the circular path they travel. Bunches are spaced 25 ns apart, with additional spacing between sets of bunches. Figure 4.3 shows this structure as proposed in the original LHC design. It is partly a consequence of how the beam is produced, but also driven by practical considerations, as the spacing between bunches sets the time window in which the detectors like ATLAS must operate: at the interaction point in ATLAS where the beams collide there is a *bunch crossing* every 25 ns, corresponding with a bunch crossing rate of 40 MHz, wherein  $pp$  collisions take place. Within that time-frame, the detector’s subsystems must detect the full collision, and the triggering and data acquisition must determine whether or not to record it <sup>[4]</sup>. That the beam consists of bunches (versus single protons) is also a practical consideration, as it increases the probability of a  $pp$  collision in each bunch crossing. In fact, we typically have multiple collisions per bunch crossing, as we will discuss in the following section.

#### 4.1.4 Colliding beams: Luminosity and Pileup

So far, we have established that the LHC proton beams consist of bunches of protons, with a bunch collision rate of 40 MHz. We can quantify the actual  $pp$  rate by understanding how these bunches interact. We typically model each proton bunch as a 3-dimensional Gaussian packet, and the two cross at some angle (as the beams are not exactly head-on at the collision point) [95] as shown in Figure 4.4. Then we can characterize the rate of collisions by computing the collision *luminosity* as

$$\mathcal{L} = \frac{N_1 N_2 f N_b}{4\pi\sigma_x\sigma_y} \left( \sqrt{1 + \left( \frac{\sigma_z \phi}{\sigma_x 2} \right)^2} \right)^{-1} \quad (4.1)$$

---

4. We will discuss this further in Section 4.2.6. The 40 MHz bunch collision rate has significant consequences for the ATLAS data acquisition scheme, as it requires using detector sub-systems with fast response, as well as specialized circuits and hardware that can process these signals with extremely low latency.

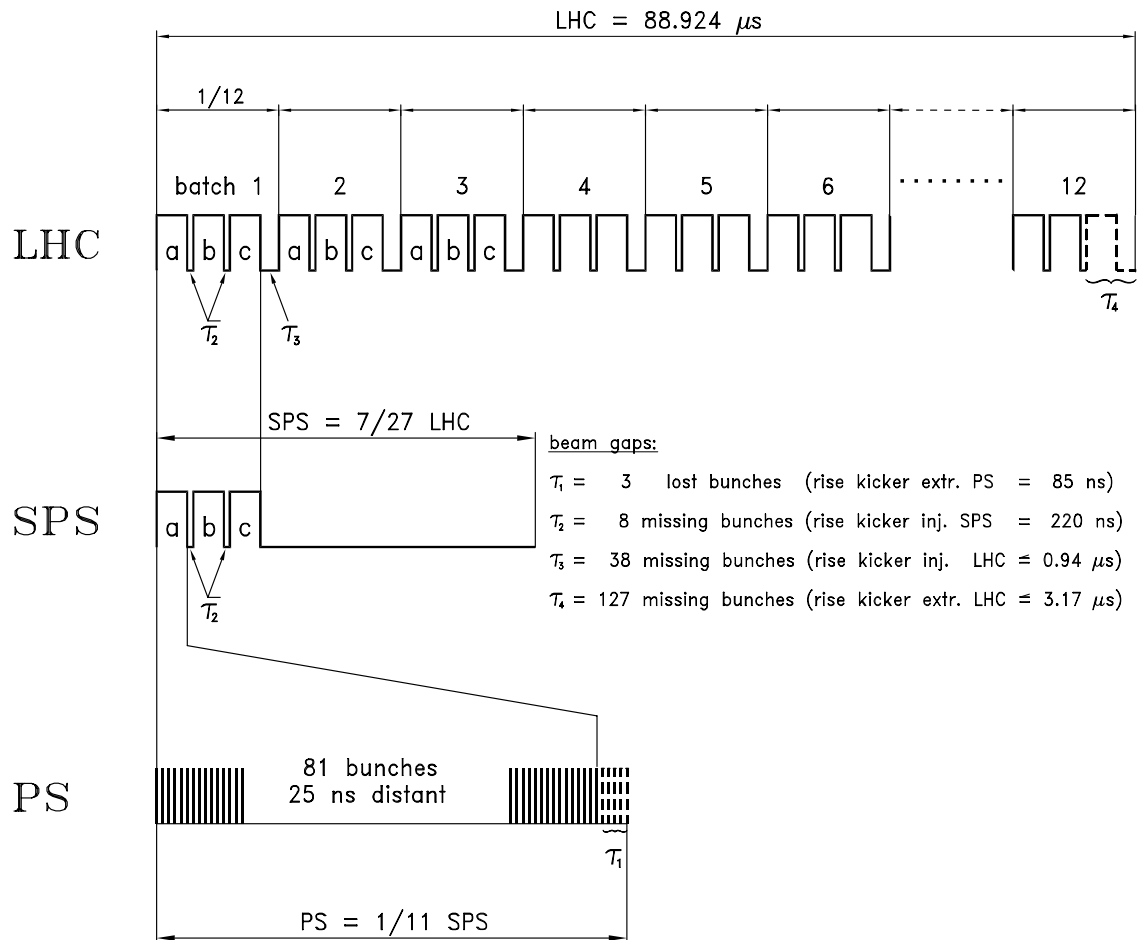


Figure 4.3: An outline of the original proposed LHC bunch structure. Note that the current bunch structure is different than that shown here, but the general principles are unchanged: the inter-bunch spacings are set by the PS  $\rightarrow$  SPS  $\rightarrow$  LHC injection scheme. Modified from Ref. [94].

- $N_i$  is the intensity of bunch  $i$ ,
- $f$  is the revolution frequency,
- $N_b$  is the number of bunches in the beam,
- $\sigma_i$  is the Gaussian width of the bunch along axis  $i$ ,
- $\phi$  is the crossing angle of the bunches.

where we assume that the crossing angle  $\phi$  is small. From Eq. 4.1, we can see that the units of luminosity are inverse area-time ( $\text{m}^{-2} \text{s}^{-1}$ ). As it turns out, the luminosity is also related to the *cross-section*  $\sigma$ , a measure of the probability of a particle collision, and can be written as

$$\mathcal{L} = \frac{1}{\sigma} \frac{dN}{dt} . \quad (4.2)$$

- $\sigma$  is the total cross-section,
- $N$  is the number of events (collisions),
- $t$  is time.

Cross-section is in units of area (commonly measured expressed in a unit known as the “barn”<sup>[5]</sup>), as it represents the area transverse to two particle’s relative motion, that they must enter in order to interact<sup>[6]</sup>. Thus, luminosity quantifies the rate at which collisions are produced, scaled by the cross-section. This quantity is particularly convenient because it can be used to determine the rate at which some particular process  $a$  happens, which would be given by

$$\frac{dN_a}{dt} = \mathcal{L} \cdot \sigma_a . \quad (4.3)$$

- $\mathcal{L}$  is the luminosity,
- $\sigma_a$  is the cross-section for process  $a$ .

Here, it is important to understand the difference between process-specific cross-sections – a

---

5. The name of this unit is in fact an allusion to agricultural barns, and was created by M. G. Holloway and C. P. Baker during the Manhattan Project [96].

6. In classical mechanics, this would depend on the size of the two finite-volume “particles”. As we are dealing with point-like particles, this is instead influenced not explicitly by their size, but by the forces by which they can interact.

measure of the likelihood of a particular process happening – versus the total cross-section for  $pp$  collisions, which just tells us the likelihood for *something* to happen (in other words, a sum over all possible processes). Figure 4.5 shows the various Standard Model cross-sections for the ATLAS experiment.

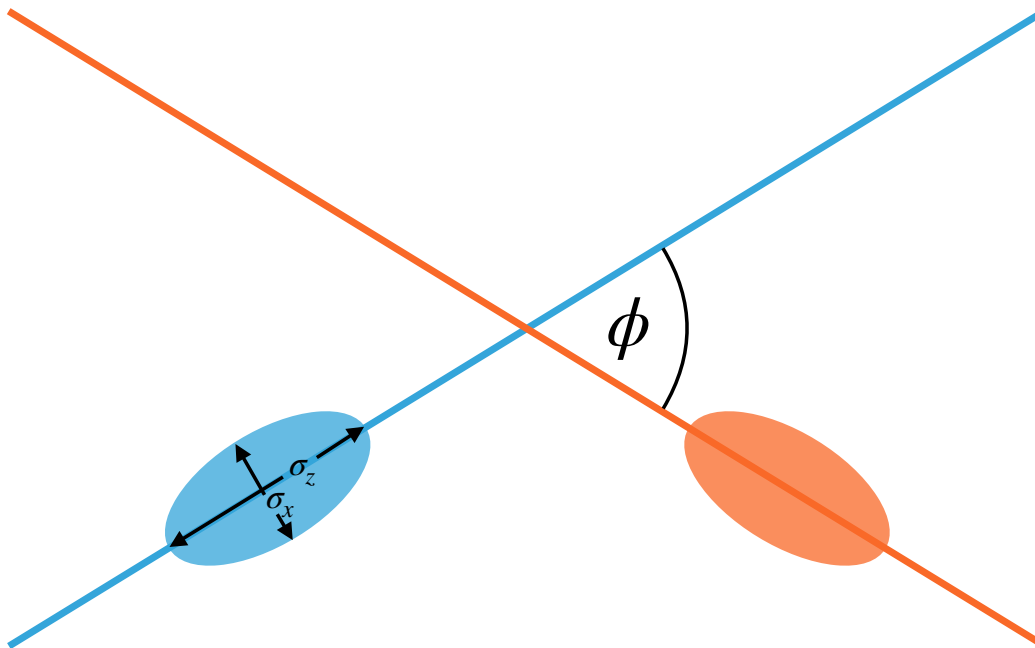


Figure 4.4: A schematic showing the crossing of two proton beams – or rather bunches of protons – at some crossing angle  $\phi$ . For the high-luminosity (HL) LHC upgrade, the proton bunches will be rotated via RF pulses from *crab cavities* prior to collision, so that the two bunches will maximally overlap at the collision point [97].

One can also integrate the luminosity over time, as a means of quantifying the amount of data collected. This is how collider experiments like ATLAS typically report collected data – and by multiplying the integrated luminosity by a particular process cross-section, we can compute the number of events of that process we expect to have produced. Figure 4.6 shows the integrated luminosity of  $pp$  collisions delivered to the ATLAS experiment, as a function of time.

# Standard Model Production Cross Section Measurements

Status: June 2024

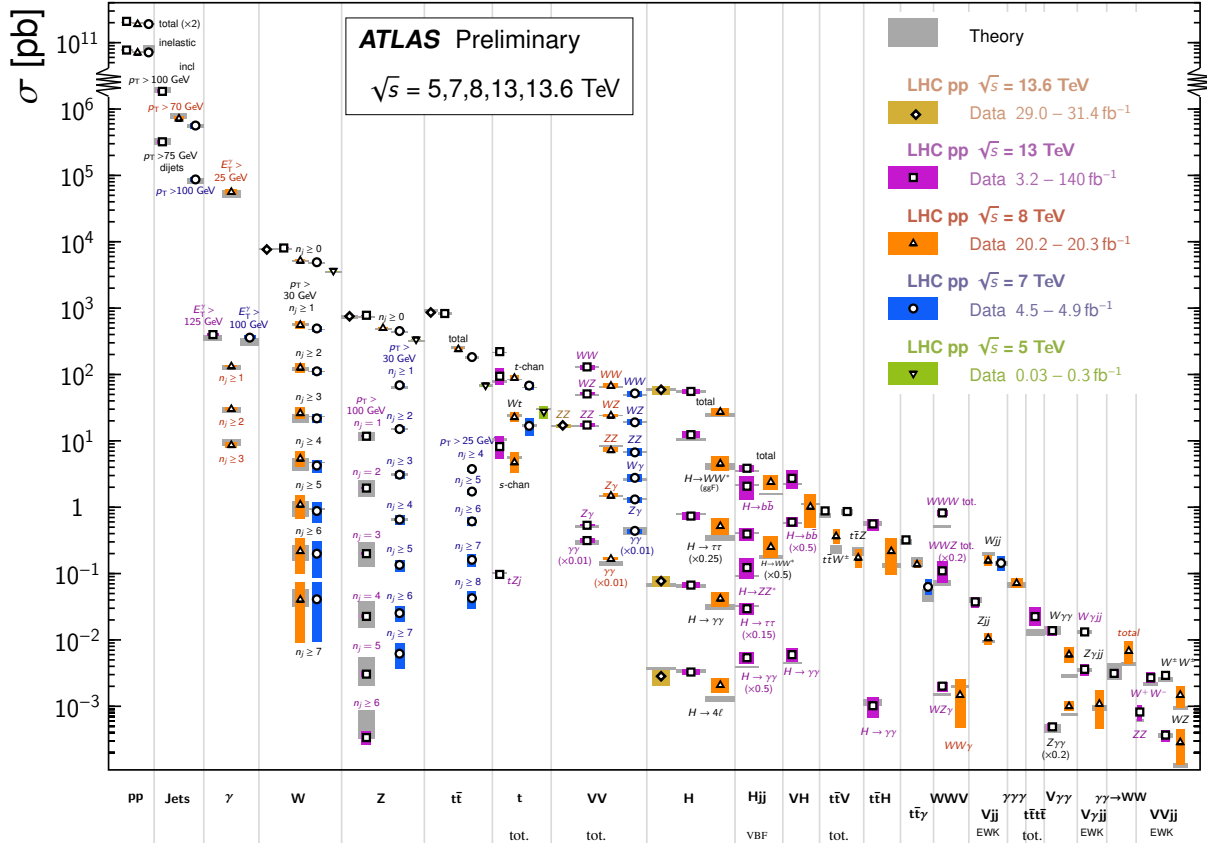


Figure 4.5: Various Standard Model cross-sections as measured by the ATLAS experiment, indicated by the (parton-level) final state produced. “Jets” refers to the collimated streams of hadrons produced by quark and gluon emission, discussed in Section 4.2.1.5 and Appendix E. The proton-proton cross-section is also included in the left-most bin. From Ref. [98].

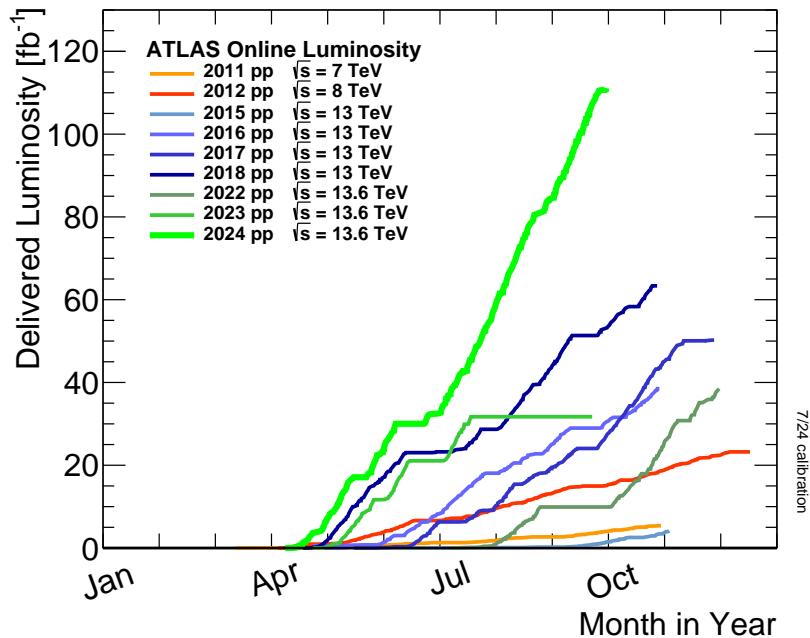


Figure 4.6: The integrated luminosity of  $pp$  collisions delivered to the ATLAS experiment. Note the increase in the maximum slope of the curves after 2012, corresponding with an increase in the maximum instantaneous luminosity. Taken from Ref. [99].

## 4.2 The ATLAS Experiment

In the following section, we will review the various sub-detectors that comprise the ATLAS experiment, as well as the triggering and data acquisition system interlinked with these sub-detectors that determines which events to save. As the ATLAS experiment undergoes a series of phased upgrades – one already performed, and another underway – we will review the “basic” detector structure and then the upgrades, with an emphasis on the “Phase 2” upgrade for the high-luminosity LHC (HL-LHC) era. This will be particularly instructive for highlighting some of my work regarding calibration of the ATLAS calorimeters for HL-LHC, and for contextualizing the later chapter on a new physics search at ATLAS in which I participated.

It is also instructive to review some basics about how particle detector technologies function: What are trackers and calorimeters? How do we actually measure particle momenta? Some

necessary context will be given when describing each detector system, but a more in-depth discussion of these fundamentals is reserved for Appendix F, for easy access and to avoid cluttering up the discussion of details specific to the ATLAS detector itself.

### 4.2.1 A Foreword: Some Collider Terminology and Concepts

Before reviewing the ATLAS detector, let us review some basic terminology that will help with describing its design and operation. Collider physics is no stranger to complex terminology and jargon, and the ATLAS experiment is no exception. To hopefully limit confusion, we will explicitly review a couple key terms that will be used throughout, and general concepts that inform both detector design and how we study the measurements that they perform.

#### 4.2.1.1 Coordinate Systems

When describing the geometry of the ATLAS detector and the particle collisions it measures, we conventionally define a Cartesian coordinate system where the  $z$ -axis coincides with the beam axis – that along which both beams enter ATLAS and collide. We then define the  $x$ - and  $y$ - axes so that the  $y+$  direction is vertically upwards. We often refer to the  $xy$ -plane as the *transverse plane*, as it is transverse with respect to the beam axis. Vectors in this plane are referred to as *transverse* vectors, such as the transverse momentum  $p_T$ .

The ATLAS detector has a cylindrical layout with respect to the  $z$ -axis, so we typically use a cylindrical coordinate system rather than the Cartesian one. The detector’s cylindrical geometry of the detector is no accident, and its choice is a consequence of the *symmetries* inherent to the proton-proton ( $pp$ ) collisions: there is no “preferred” direction in the transverse plane for particles produced in collisions<sup>[7]</sup> and thus it often makes more sense to describe

---

7. The only sort of “bias” in azimuthal direction comes from the gravitational field, but gravity is far weaker than the strong and electroweak forces that dominate particle interactions and is thus entirely negligible for our purposes.

particle positions and momenta in terms of their transverse (radial) components<sup>[8]</sup>, a polar angle  $\theta$  with respect to the  $z$ -axis, and an azimuthal angle  $\phi$ . Based on the preceding arguments we expect particles produced in  $pp$  collisions to be evenly distributed in  $\phi$  across events<sup>[9]</sup>. In other words, the system we are observing ( $pp$  collisions) is *cylindrically*-symmetric.

Note that our system is explicitly not *spherically*-symmetric, owing to the presence of the beam-line that defines the  $z$ -axis.

#### 4.2.1.2 Rapidity, Pseudo-rapidity and Angular Distances

There is one more quirk to how we typically discuss coordinates in the detector, which is that instead of using the polar angle  $\theta$ , we instead use a quantity called *pseudo-rapidity*. Firstly, we define the rapidity of a particle as<sup>[10]</sup>

$$y = \frac{1}{2} \ln \frac{E + p_z}{E - p_z} . \quad (4.4)$$

- $E$  is the particle's energy,
- $p_z$  is the  $z$ -component of the particle's momentum.

The rapidity is a meaningful quantity in the context of special relativity: it defines the Lorentz boost along  $\hat{z}$  necessary to move from the lab frame, to a frame where the particle's momentum is entirely perpendicular to the beam axis<sup>[11]</sup>. However this is not a purely *spatial*

---

8. Another reason why we typically discuss quantities like transverse momentum is that we know that by conservation of momentum, the transverse momenta of all the outgoing particles should balance out since the beam protons have no transverse momentum – as discussed in Section 4.2.1.6. By contrast, we do not know the total  $z$ -momentum of the system, as the proton's constituent quarks (which interact) carry unknown fractions of the total proton momentum; this is a phenomenon modeled by *parton distribution functions*. For a related review, see Ref. [100].

9. Whether or not this translates to *measuring* distributions of particles in  $\phi$  that are uniform is another matter – issues with detector component calibrations, malfunction, or misalignment may prevent this.

10. The usage of the symbol  $y$  for rapidity is perhaps inconvenient, given that this is *also* conventionally used for one of the Cartesian axes. However as we generally do not use Cartesian coordinates, there is typically little ambiguity in usage.

11. To be precise, it is the boost necessary to move to a frame where the particle's momentum along  $\hat{z}$  is zero: For a particle with  $\vec{p} \parallel \hat{z}$ , it is impossible to boost along  $\hat{z}$  such that  $\vec{p} \not\parallel \hat{z}$  *except* for boosting such that

quantity, as depends on a particle's energy  $E$ . In other words, we cannot deduce a particle's rapidity solely from its 3-momentum  $\vec{p}$ , as it will also receive a contribution from the particle's mass  $m$ . Thus while we can associate a rapidity with any 4-momentum  $p^\mu$ , we cannot use the rapidity as a component of our spatial coordinate system.

In a similar spirit, we can define a quantity which we will call *pseudo-rapidity*, that is spatial in nature. The pseudo-rapidity  $\eta$  is defined as

$$\begin{aligned} \eta &= \operatorname{arctanh} \left( \frac{p_z}{|\vec{p}|} \right) \\ &\equiv -\ln \left( \tan \left( \frac{\theta}{2} \right) \right) , \end{aligned} \tag{4.5}$$

The rapidity and pseudo-rapidity are related quantities: they are exactly equivalent for a massless 4-momentum, and as the rapidity can be expressed in terms of pseudo-rapidity as

$$y = \eta - \frac{1}{2} \tanh \eta \left( \frac{m}{p_T} \right)^2 + \mathcal{O} \left( \left( \frac{m}{p_T} \right)^4 \right) , \tag{4.6}$$

where  $p_T$  is the transverse component of the momentum, the two quantities are very similar when  $p_T \gg m$ .

As  $\eta$  is purely spatially defined, we can use it in lieu of  $\theta$  when describing positions in the detector. With this ingredient, we now have the coordinate system most commonly used in collider physics: radial position  $r$ , pseudo-rapidity  $\eta$  and azimuthal angle  $\phi$ .

Besides describing the positions of particles and orientations of their momenta in the collider, it is also useful to establish conventions for describing the distances between these objects, in both position- and momentum-space. In particular, we often describe distances

---

$|\vec{p}| = 0$ . Note that such a boost only exists for a massive particle, a massless particle (such as a photon) with  $\vec{p} \parallel \hat{z}$  has infinite rapidity.

between momenta in terms of angular distance  $\Delta R$ , which is given by

$$\Delta R = \sqrt{(\Delta y)^2 + (\Delta\phi)^2}. \quad (4.7)$$

- $\Delta y$  is the difference in rapidity,
- $\Delta\phi$  is the difference in azimuthal angle.

This is the Cartesian distance between two 4-momenta in the  $y - \phi$  plane. Following from our above discussion of pseudo-rapidity, it is convenient to substitute  $\eta$  for  $y$  to yield

$$\Delta R \approx \sqrt{(\Delta\eta)^2 + (\Delta\phi)^2} \quad (4.8)$$

in order to have a purely geometric definition.

### 4.2.1.3 Collider events and pileup

In collider experiments like ATLAS, we often speak about physics *events*. An event is the collision of two protons, and all the things that happen as a direct consequence: The production of some particle(s) via interaction between these protons' quarks, any subsequent particle decays, and propagation of the resulting (meta)-stable particles through the detector. At least, this describes an “idealized” event in a hadron collider like the LHC. As described in Section 4.1.3, the proton beams consist of bunches of protons, spaced 25 ns apart, and each bunch crossing results in multiple collisions. There are two consequences of this beam structure that complicate the picture of an event described above:

- Multiple protons collide in each bunch crossing. Thus each event actually corresponds to multiple, (nearly) simultaneous  $pp$  collisions.
- We measure an event via its interaction with our detector. The signals produced take a finite time to propagate: for example, the electrons we detect from the ionization of some material take some non-zero time to actually propagate from the point of

ionization to the electronic readout. This is sometimes slow enough that information from one event becomes mixed with that from a subsequent event.

These phenomena are collectively known as *pileup*, as they quite literally result in information from different *pp* collisions “piling up”. One can mitigate the latter effect, known as “out-of-time” pileup, by designing a detector with good timing resolution: the better one can precisely measure the time at which a particle passed through a particular detector component, the easier it can be associated with one bunch crossing or another. The former effect, known as “in-time” pileup, can be partly addressed through *primary vertexing*, the process of identifying a primary *hard-scatter interaction*, and the position where its corresponding collision took place.

#### 4.2.1.4 Primary and secondary vertexing

We are typically only interested in one *pp* collision per bunch crossing in our detector. The vast majority of collisions produce gluon or light quark-initiated hadronic showers, many of them at relatively low energies compared to the center-of-mass collision energy of  $\sqrt{s} = 13$  TeV. These are not interesting processes<sup>[12]</sup> for most Standard Model measurements and new physics searches, and can be thought of as some kind of background: We are most often interested in the most energetic collision in each bunch crossing, which may yield a similar interaction at higher energy or something rarer still, whether it be the production of heavy quarks, vector or Higgs bosons, or something else (such as new physics!).

When we reconstruct an event – combining information on charged particle trajectories from the tracker, and energy depositions from the calorimeters and muon spectrometer<sup>[13]</sup> to reconstruct particles – we can trace these reconstructed particles back to the positions of the

---

12. To further qualify this statement, these processes are typically considered uninteresting precisely because of their abundance. We are typically interested in the rarer interactions, of which we have produced (and measured) fewer.

13. We’ll discuss the systems specific to ATLAS further below in this section. For more basic details on the different types of particle detectors, see Appendix F.

$pp$  collisions from which they originated. We call these points in space and time *vertices*, and more specifically *primary vertices* (to distinguish them from the *secondary vertices* we shall discuss further below).

In order to identify the vertex corresponding with the  $pp$  interaction we wish to study in a given event, we identify the *hard-scatter vertex* as that with the highest  $\sum_i (p_{T,i}^2)$ , where the sum is taken over all reconstructed particles we associate with this vertex<sup>[14]</sup>. All the other primary vertices are then referred to as *pileup vertices*, the source of our in-time pileup. We may be able to identify the products of in-time pileup in our event reconstruction by tracing them back to these production vertices; however *pileup removal* is typically a more complex, multi-step process built in to our reconstruction algorithms that uses additional information to determine whether or not a given particle track or energy deposit is pileup-related.

As discussed in Section 2.1.2.4, many of the particles in the Standard Model (both fundamental and composite) are unstable, and decay on very short timescales: we may detect their presence in an event via the kinematics of their decay products, but their decays can be considered effectively instantaneous for most intents and purposes. We typically refer to these decays as *prompt*. By contrast, some particles have sufficiently long lifetimes that, when produced in a  $pp$  collision (or subsequent prompt decays), they will typically propagate a measurable distance before decay. We often refer to these particles as meta-stable or *long-lived*.

We can identify long-lived particles produced in an event by looking for *secondary* or *displaced vertices*, as we may trace their decay products to a vertex spatially separated from the hard-scatter vertex. The mean distance by which the particle’s decay vertex is displaced

---

14. It is important to note that while this is the most common definition – we are typically interested in the highest-energy collision – it is a choice nonetheless. We have multiple options for the algorithm used to identify the primary vertex, and although our choices may be well-motivated by the physics processes we study, they are by definition somewhat arbitrary. The sum of squares of transverse momenta is not the most elegant quantity, being the scalar sum of components of vectors that are almost never parallel, but it is a good metric for quantifying how energetic a particular  $pp$  interaction is.

from its production vertex is given by

$$\langle d \rangle = \beta \gamma c \tau, \quad (4.9)$$

- $c$  is the speed of light in vacuum,
- $\beta \equiv v/c$  is the particle's velocity as a fraction of  $c$ ,
- $\gamma = (1 - \beta^2)^{-1/2}$  is the Lorentz boost factor,
- $\tau$  is the particle's mean lifetime.

which depends on both its mean<sup>[15]</sup> lifetime  $\tau$  and speed  $\beta$  and may be used to identify the particle species. For example, the  $B$ -mesons have mean lifetimes of  $\mathcal{O}(10^{-3}\text{ns})$ , and thus may travel a few millimeters before decay if moving near the speed of light, as shown in Figure 4.7.

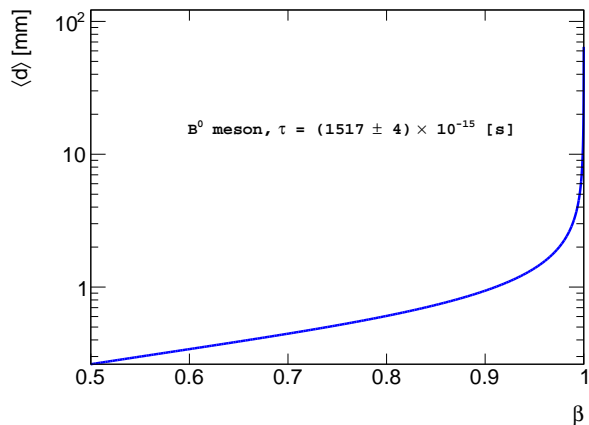


Figure 4.7: The  $B^0$ -meson lifetime in the lab reference frame, as a function of its speed  $\beta$  (as a fraction of the speed of light in vacuum).

#### 4.2.1.5 Jets: the manifestation of quarks and gluons

Perhaps one of the most important concepts in hadronic physics – the study of the strong sector – is that of a *jet*. These are at the most basic level<sup>[16]</sup>, collections of reconstructed

15. As a reminder, we discuss *mean* lifetimes as particle decay is a random Poisson process.

16. For a fuller review, see Appendix E.

particles, “objects” that we make in order to identify and reconstruct the showering and hadronization of gluons and quarks. As discussed in Section 2.1, we do not see “naked” quarks or gluons as a consequence of QCD color confinement. Instead, the emission of quarks or gluons in a  $pp$  collision results in the production of a collimated stream of hadrons<sup>[17]</sup> through the process of showering and subsequent hadronization. The resulting hadrons are detected via electromagnetic interactions with the detector’s charged particle tracker (if charged), and the deposition of their energy in the detector’s electromagnetic and hadronic calorimeters. Thus instead of directly measuring the 4-momentum of a quark or gluon ejected from a collision, we instead observe a spray of particles emanating outwards roughly in a cone.

Summing these particles’ 4-momenta will give the 4-momentum of the quark or gluon that initiated the shower, so if we wish to reconstruct the quark or gluon then our task is to identify the presence of such a cluster of particles in our detector’s reconstruction of the event, and correctly identify which reconstructed particles belong to this cluster. This task is complicated by a number of factors, including that there are typically many such clusters simultaneously present in an event, as a consequence of pileup. To identify these clusters, we construct *jets* from our reconstructed particles’ momenta. The details of this process, known as *jet clustering*, are described in Appendix E. For the present discussion, it suffices to say that we attempt to identify hadrons among our reconstructed particles, and cluster those that are close to one another in  $\Delta R$ .

---

17. Predominantly pions  $\pi^\pm$  and  $\pi^0$  (mesons composed of up- and down-type quarks) and kaons  $K^\pm$ ,  $K_L^0$  and  $K_S^0$  (mesons composed of an up- or down-type quark together with a strange quark).

### 4.2.1.6 Missing Transverse Energy

As the colliding beams have no momentum in the transverse direction<sup>[18]</sup>, we expect there to be no net transverse momentum in an event. However, we may not be able to directly measure all the particle momenta in an event. Specifically, neutrinos are effectively invisible to the ATLAS detector as they do not interact via electromagnetic or strong forces, and thus may carry off momentum and cause an imbalance in the net transverse momentum of the event<sup>[19]</sup>. We refer to this imbalance as *missing transverse energy*<sup>[20]</sup>, often denoted as  $\cancel{E}_T$ ,  $E_T^{\text{miss}}$  or “MET”. There are typically multiple ways to define this quantity, depending on what information is used from the ATLAS calorimeters and muon spectrometer, and how this information is used to reconstruct signals – for example, what jet clustering algorithm is employed.

### 4.2.2 The ATLAS Inner Detector

The ATLAS Inner Detector serves the purpose of reconstructing the tracks of charged particles, which is used (in conjunction with the other detector components) to identify electron, muon and photon<sup>[21]</sup> candidates, as well as for identification of displaced particle decays – which produce *displaced vertices* if their decay products are charged and produce tracks. Owing to its role, the Inner Detector is often referred to as the *tracker*. The portion of the detector nearest to the beam pipe in which the proton beams circulate and collide, it consists of a set of silicon tracking detectors – the Pixel and semiconductor tracking (SCT) systems – as

---

18. To be precise, the beams collide with a half-crossing angle of approximately  $160\ \mu\text{rad}$  [101, 102], resulting in some net transverse momentum for the  $pp$  collision system – however, this is so small as to be entirely negligible. Similarly, one can neglect any effects from small transverse momenta of the protons’ constituent partons.

19. The same holds true for certain beyond-Standard Model particles, such as those studied in Chapter 5.2.

20. This is arguably a bit of a misnomer, as we are really discussing momentum and not energy.

21. Combining the Inner Detector with other systems, photons can be identified precisely because they *do not* produce tracks. They may otherwise look similar (to the detector) as electrons, as they produce electromagnetic showers in the calorimeters described in Section 4.2.4 (and as discussed in Appendix F.2).

well as a transition radiation tracker (TRT) [103]. As will be discussed below, these detector systems use silicon pixels and strips, as well as “straw tube” technologies, to record particle hits from which tracks can be fitted. Unlike the calorimeter and muon spectrometer systems discussed in Section 4.2.4 and 4.2.5, the tracker is not meant to stop particles but rather interact with them minimally: the goal is to record particle trajectories but not appreciably alter their energies before they are measured by the other systems.

Figure 4.8 highlights the position of the ATLAS Inner Detector, and Figure 4.9 provides an overview of the Inner Detector design.

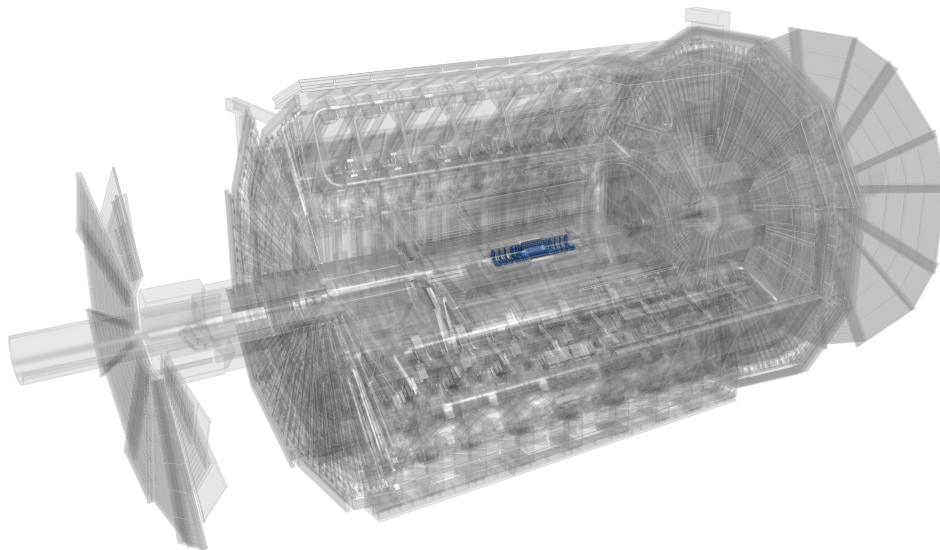


Figure 4.8: A highlight of the components of the ATLAS Inner Detector. Taken from Ref. [104].

#### 4.2.2.1 Pixel Detector

The (silicon) Pixel Detector consists of barrel and end-cap sections, and covers a region of  $|\eta| < 2.5$ . The barrel consists of 4 concentric layers of silicon  $pn$  junctions, segmented as pixels, to detect the passage of charged particles via ionization – these layers include 3 from the original detector design, as well as an additional “Insertable B-Layer” (IBL) that was later added so as to improve the identification of bottom quark-initiated jets via identification

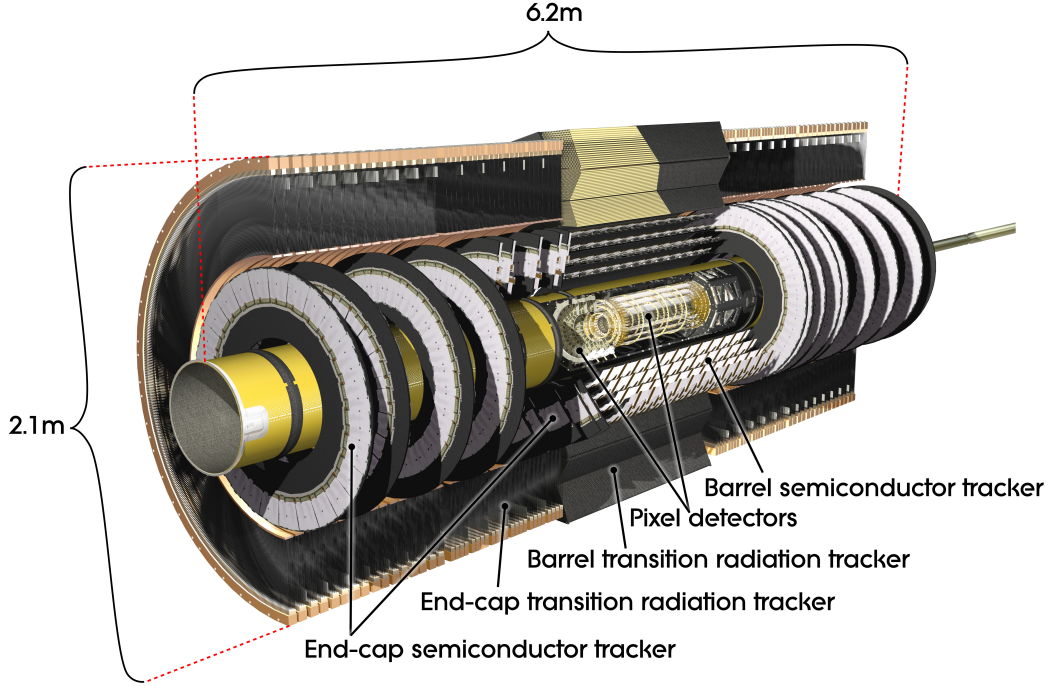


Figure 4.9: An overview of the ATLAS Inner Detector design, highlighting the barrel and end-cap components of each detector system. Taken from Ref. [105].

of displaced  $B$ -meson decays [106]. Each layer consists of an array of modules, each module containing 47232 pixels of pitch ( $400\ \mu\text{m} \times 50\ \mu\text{m}$ ) or ( $582.5\ \mu\text{m} \times 30\ \mu\text{m}$ ) in  $(z, \phi)$ , depending on the position [107]<sup>[22]</sup>. Table 4.1 provides an overview of the Pixel Detector barrel section.

Layer	$\langle R \rangle$ [mm]	Active half-length [mm]	Number of pixels ( $\times 10^6$ )
Insertable B-Layer (IBL)	33.25	330.15	6.02
B-Layer (BL)	50.5	385	13.2
Layer 1 (L1)	88.5	385	22.8
Layer 2 (L2)	122.5	385	31.2

Table 4.1: An overview of the layers of the barrel section of the Pixel Detector, including the Insertable B-Layer. For the radial position, the average for the sensitive components of the layer is provided. Taken from Ref. [103, 106].

22. The dimensions for the IBL are slightly different. Its pixels have pitch ( $250\ \mu\text{m} \times 50\ \mu\text{m}$ ) [106].

22. In fact, even in the absence of any NCB, the distribution is not entirely flat but exhibits a very gentle sinusoidal shape, with a small excess in the  $-\phi$  region and deficit in the  $+\phi$  region. This is due to the very

The end-cap sections consist of silicon pixels arranged in concentric rings to form disks. The silicon components consist of  $150\ \mu\text{m}$ -thick trapezoid plates,  $5.3\ \text{cm}$  in height and with inner and outer edges of  $1.249\ \text{cm}$  and  $1.491\ \text{cm}$ , respectively. These are divided into  $300\ \mu\text{m} \times 50\ \mu\text{m}$  pixels, as in the barrel section. Figure 4.10 provides a rendering of the barrel and end-cap sections.

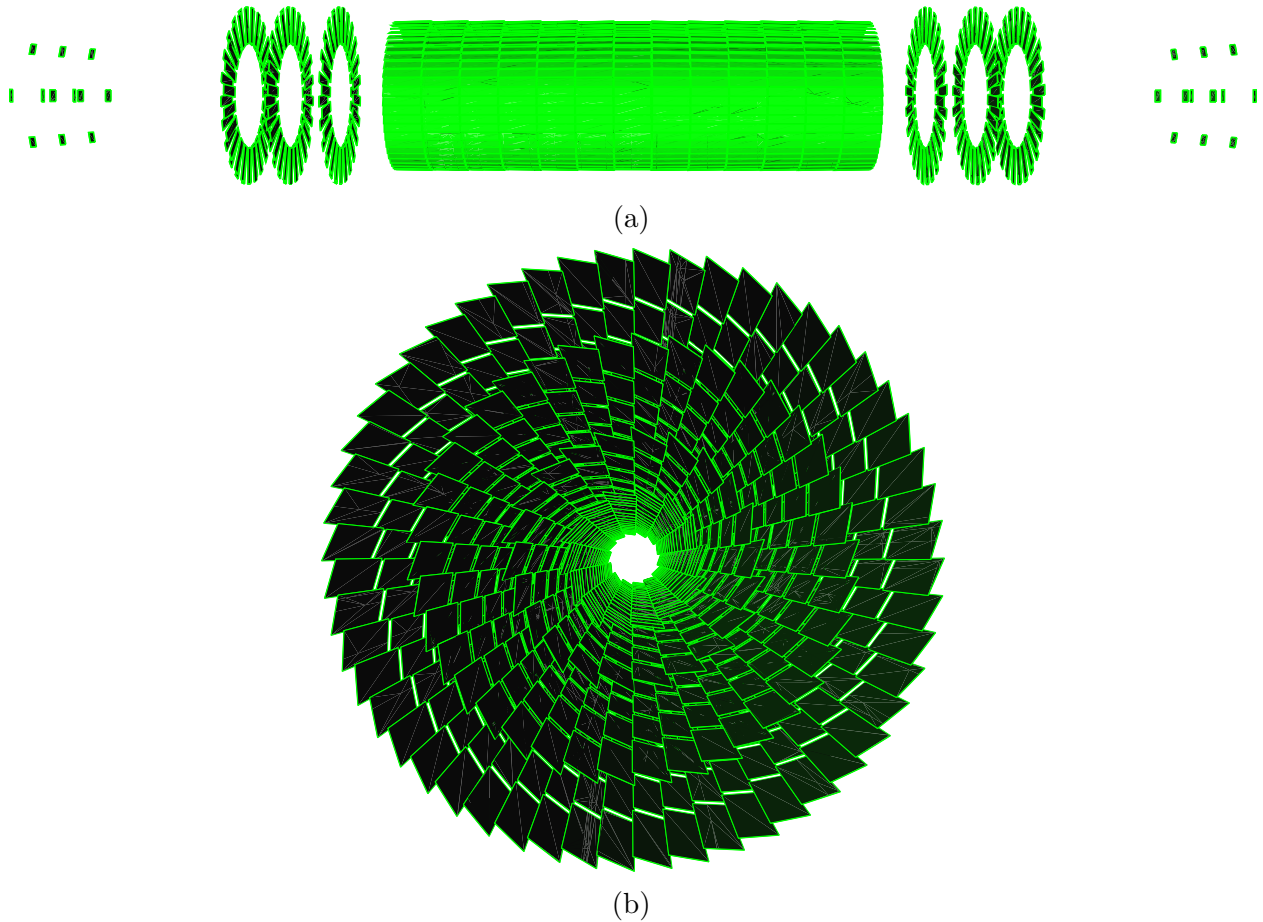


Figure 4.10: Renderings of the Pixel detector, showing (a) an exploded side view of the barrel and end-cap sections, and (b) a frontal view of the barrel section. Produced using the VP1 software package [108].

---

small but measurable mechanical sagging of the ATLAS detector, causing the interaction point to not be at the perfect center of the detector.

### 4.2.2.2 Semiconductor Tracker

The (aptly-named) SCT is, like the Pixel Detector, a silicon  $pn$  junction-based tracking detector. However, its silicon components are segmented as strips rather than pixels – which offer lower position resolution, but at a larger distance from the interaction point (where this has less impact on tracking precision). It consists of 4 barrel layers and 9 end-cap disks, with parameters outlined in Tables 4.2a and 4.2b. In the barrel region, each detector module consists of 4 single-sided silicon strip detectors, with a pitch of  $80\ \mu\text{m}$  and an active length of  $123.2\ \text{mm}$  [103]. Two of sets of strips run parallel to the  $z$ -axis, while two others are rotated with respect to it by  $40\ \text{mrad}$  as to allow for measurement in the  $z$ -direction. Figure 4.11 provides a cross-sectional view of the Pixel and SCT detectors.

Layer	$R$ [mm]
1	300.0
2	373.0
3	447.0
4	520.0

(a) SCT barrel parameters.

Layer	$z$ [mm]	$R_{\text{min}}$ [mm]
1	835.0	259
2	925.0	336
3	1072.0	259
4	1260.0	259
5	1460.0	259
6	1695.0	259
7	2135.0	336
8	2528.0	401
9	2788.0	440

(b) SCT end-cap parameters.

Table 4.2: Overview of the (a) barrel and (b) end-cap layers of the SCT. For the barrel layers, each has a half-length of  $746.7\ \text{mm}$  and a pitch of  $80\ \mu\text{m}$ . For the end-cap layers, strip pitches range from  $54.53\ \mu\text{m}$  to  $90.34\ \mu\text{m}$ , and each layer has a maximum radius of  $560\ \text{mm}$ . Taken from Ref. [103].

### 4.2.2.3 Transition Radiation Tracker

The TRT is a straw-tube tracker, consisting of Kapton and carbon-fiber tubes  $2\ \text{mm}$  in radius, filled with either a  $\text{Xe}:\text{CO}_2:\text{O}_2$  or argon-based<sup>[23]</sup> mixture [109, 110]. With the tube walls

---

23. While designed for use with a xenon-based mixture, the TRT gas was eventually replaced with argon as the system suffers from gas leaks, and xenon would be prohibitively expensive for the required replacement

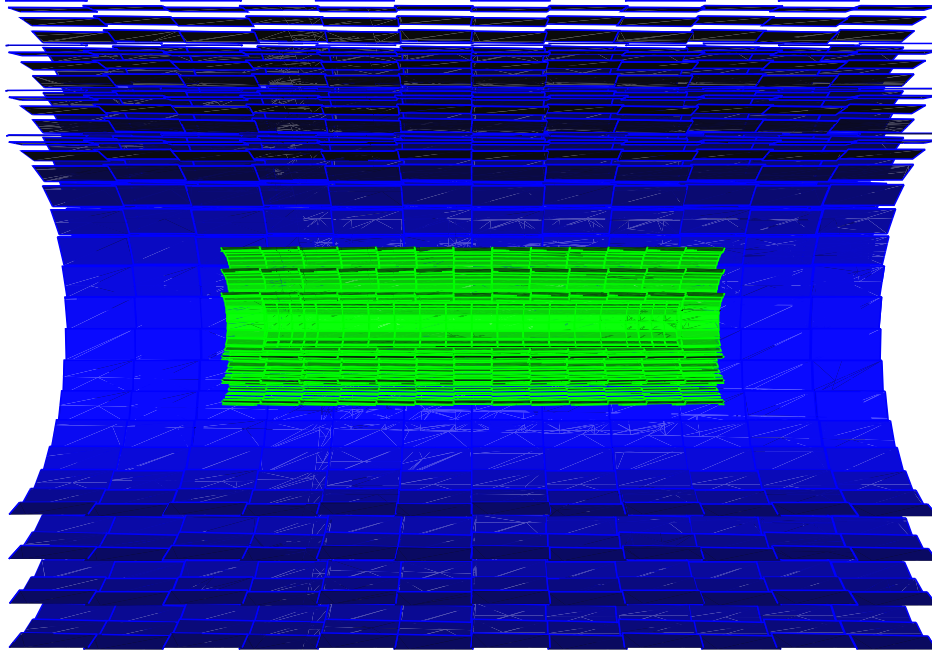


Figure 4.11: A cross-sectional diagram of the Pixel and SCT detectors. Produced using the VP1 software package [108].

kept at  $-1.5\text{ kV}$  and a  $15.5\text{ }\mu\text{m}$  Au–W cathode wire at the center of each tube, they act as proportional counters. The TRT gets its name from the spaces between the tubes, which is filled with polypropylene fibers and foil [111]: impinging, charged high-energy particles produce *transition radiation* [112, 113] as they cross the material boundaries of the polymer. The power emitted by the transition radiation is linearly proportional to the Lorentz factor  $\gamma = E/m$ , which (together with energy measurement) allows for determining the particle mass (and thus its identity). As the other subsystems, the TRT is divided into barrel and end-cap sections. Table 4.3 provides an overview of parameters for these two sections.

### 4.2.3 The ATLAS Magnet System

Although not a detector itself, the ATLAS magnet system plays a crucial role in measurements performed by the Inner Detector. Depicted in Figure 4.12, it consists of a central solenoid,  


---

 rate.

Parameter	Value
Number of straw tubes	52544
Radial coverage	(0.5 m, 1.1 m)
Pseudorapidity coverage	$ \eta  < 1$

(a) TRT barrel parameters.

Parameter	Value
Number of straw tubes	122880
$z$ coverage	(0.8 m, 2.7 m)
Pseudorapidity coverage	$1 <  \eta  < 2$

(b) TRT end-cap parameters.

Table 4.3: An overview of the design parameters of the Transition Radiation Tracker. Taken from Ref. [109].

as well as barrel and endcap toroid sections. The system produces strong magnetic fields parallel to the beam line [114], which serve to curve the trajectories of charged particles by applying a Lorentz force given by

$$\vec{F} = q\vec{v} \times \vec{B}. \quad (4.10)$$

- $\vec{F}$  is the Lorentz force,
- $q$  is the particle charge,
- $\vec{v}$  is the particle velocity,
- $\vec{B}$  is the magnetic field.

If the magnitudes of the magnetic field and particle charge are known<sup>[24]</sup>, the curvature of the particle trajectory (such as measured in the Inner Detector) can be used to measure the momentum-charge ratio  $p/m$ .

#### 4.2.3.1 Central Solenoid Magnet

The central solenoid consists of a wound NbTi conductor, encased in a Al support cylinder, and is located radially between the Inner Detector and the cryostat that houses the liquid argon calorimeter [114, 116]. As it sits before the calorimeter, its design is optimized so that the coil thickness is only approximately  $0.66X_0$  radiation lengths [117]. Table 4.4 provides an overview of the solenoid design parameters.

24. Note that as shown in Figure 2.1, all the charged particles have electric charges of  $\pm 1q$ . There are in fact BSM theories that include particles with effective fractional charges, such as those searched for in the MilliQan experiment [115].

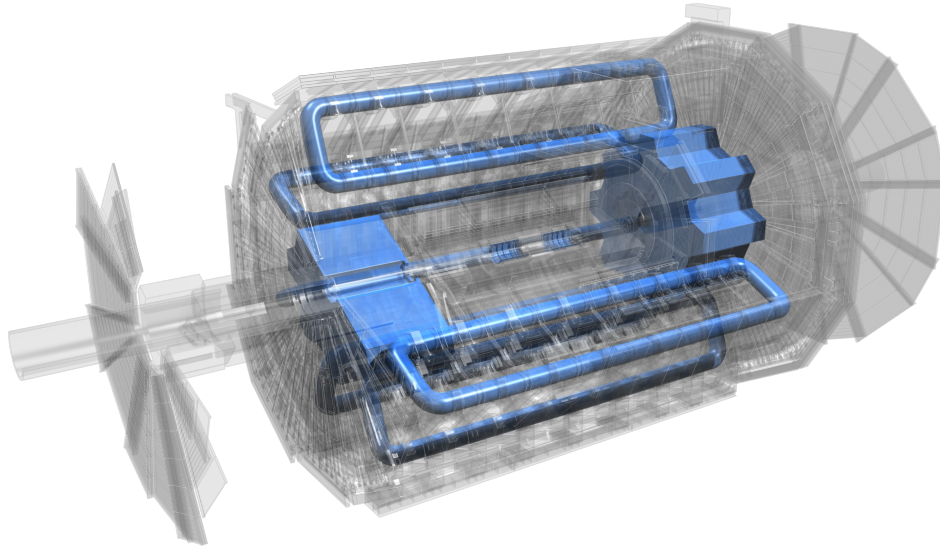


Figure 4.12: A highlight of the components of the ATLAS magnet system. Taken from Ref. [104].

Parameter	Value
Inner diameter	2.46 m
Outer diameter	2.56 m
Axial length	5.8 m
Number of turns	1154
Bore magnetic field	0.9-2.0 T

Table 4.4: An overview of the central solenoid design parameters. Taken from Ref. [117].

### 4.2.3.2 Toroid Magnets

The barrel and end-cap toroid magnets, like the central solenoid, use NbTi conductor. The barrel magnets consist of 8 “racetrack”-shaped vessels, containing the magnets inside a vacuum. The end-cap magnets consist of smaller sets of square and “keystone”-shaped coils located at either end of the detector, in the gear-shaped assemblies shown in Figure 4.12. Their primary function is to strengthen the magnetic field in the end-cap regions of the muon spectrometer. Table 4.5 provides an overview of the toroid magnet design parameters.

Parameter	Value
Inner diameter	9.4 m
Outer diameter	20.1 m
Axial length	25.3 m
Number of coils	8
Number of turns per coil	120
Bore magnetic field	0.2-2.5 T

(a) Toroid magnet barrel parameters.

Parameter	Value
Inner diameter	1.65 m
Outer diameter	10.7 m
Axial length	5.0 m
Number of coils	$2 \times 8$
Number of turns per coil	116
Bore magnetic field	0.2-3.5 T

(b) Toroid magnet end-cap parameters.

Table 4.5: An overview of the design parameters of the (a) barrel and (b) end-cap toroid magnets Taken from Ref. [116].

### 4.2.4 The ATLAS Calorimeters

The ATLAS electromagnetic (EM) and hadronic calorimeters surround the inner detector, consisting of two concentric cylinders and end-caps covering the radial region of approximately (1, 4) m. Their function is to precisely measure the energy deposited by electrons, photons and hadronic jets. Additionally, the calorimeter (in conjunction with the muon spectrometer) provides a measurement of the missing transverse energy (as discussed in Section 4.2.1.6). Aside from precision measurements, the calorimeters also provide input to the triggering and data acquisition system, in order to determine whether or not to save a given event.

The two calorimeters share some similar design principles. They fundamentally operate under the same basic principle of turning the ionization of their active media by impinging

high-energy particles into measurements of those particles' energies, and where those energies were deposited. Furthermore, both are examples of *sampling calorimeters*. These are calorimeters with their active media interleaved with non-instrumented *absorber* to encourage the more compact development of particle showers by packing in more radiation lengths than would be achieved otherwise<sup>[25]</sup>. However, the two calorimeters differ in the types of active media used, and are optimized for measuring the energy of different types of particle showers – electromagnetic and hadronic.

Figure 4.13 highlights the position of the ATLAS calorimeters in the detector.

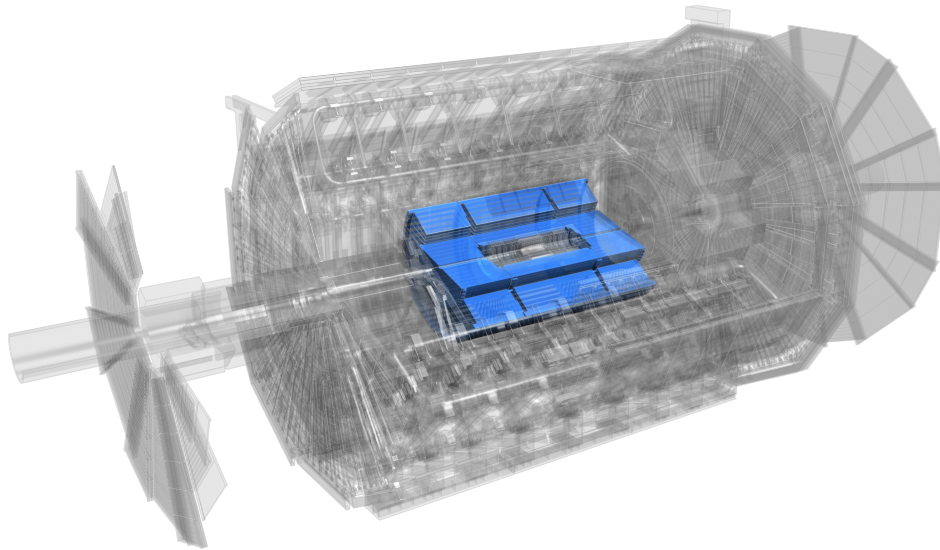


Figure 4.13: A highlight of the components of the ATLAS calorimeters. Taken from Ref. [104].

#### 4.2.4.1 Liquid Argon Calorimeter

The liquid argon (LAr) calorimeter is primarily an EM calorimeter, optimized to measure the energy of EM showers produced by electrons and photons, but also includes subsystems dedicated to measuring hadronic showers [118, 119]. Covering both the barrel of the detector and the end-caps, it consists of four sections as outlined in Table 4.6. Each section is

---

<sup>25</sup>. For details on sampling calorimeters, see Appendix F.1.

comprised of absorbers in an “accordion” configuration, interspersed with readout electrodes. The whole system is submerged in liquid argon – the active medium of the calorimeter – and is contained within a set of cryostats to maintain a temperature of approximately 89.3 K. A “presampler” system located before the beginning of the cryostat helps account for energy loss from particles’ interactions with the inner cryostat wall – as well as the solenoid magnet that separates the calorimeter from the inner detector. Figure 4.14 shows the design of the calorimeter in the barrel and end-cap regions, and Figure 4.15 shows the accordion structure of the absorber/electrode structure.

Name	Coverage	Absorber material
Electromagnetic barrel (EMB)	$ \eta  < 1.475$	Lead
Electromagnetic end-cap (EMEC)	$1.375 <  \eta  < 3.2$	Lead
Hadronic end-cap (HEC)	$1.5 <  \eta  < 3.2$	copper
Forward calorimeter (FCAL)	$3.1 <  \eta  < 4.9$	copper/tungsten

Table 4.6: An overview of the different sections of the LAr calorimeter. This includes both the electromagnetic calorimeter (EMB + EMEC), and parts of the hadronic calorimeter (HEC + FCAL).

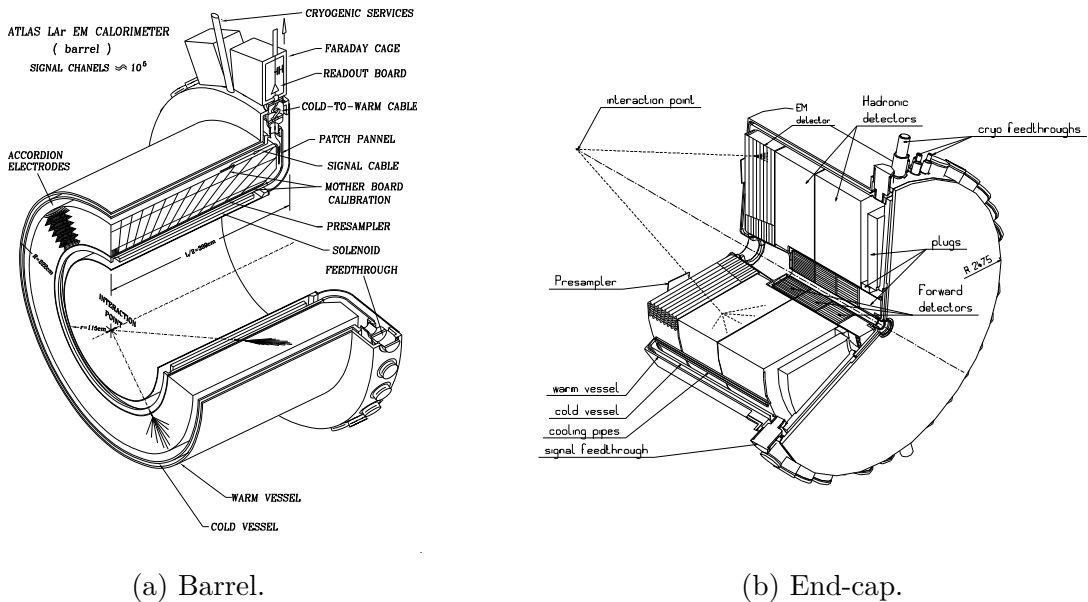


Figure 4.14: Diagrams showing the basic layout of the (a) barrel and (b) end-cap sections of the ATLAS liquid argon calorimeter. Taken from Ref [118].

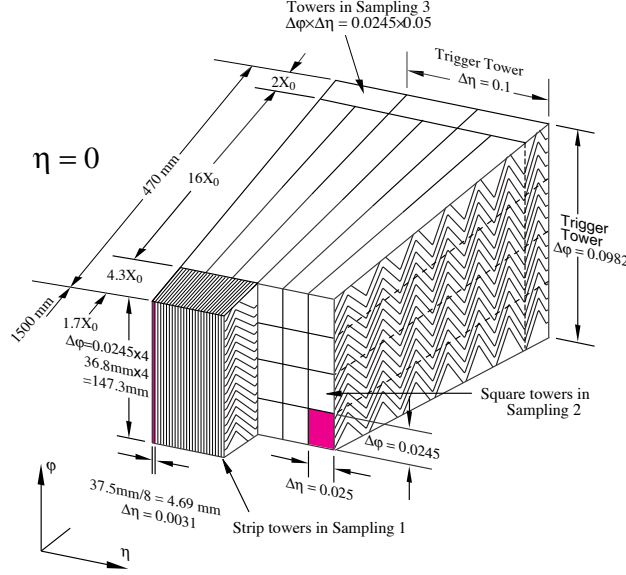


Figure 4.15: A schematic showing the structure of the ATLAS liquid argon calorimeter in the central barrel section. Note that the calorimeter consists of three concentric cylindrical structures with differing  $\eta$  granularity. Taken from Ref. [118].

As shown in Figure 4.15, the barrel of the calorimeter consists of different radial layers, referred to as *samplings*<sup>[26]</sup>, each with a different  $\eta$  granularity. Table 4.7 provides an overview of the granularity of the different samplings, for the EMB and EMEC.

Sampling	$ \eta  < 1.4$	$1.4 <  \eta  < 1.8$	$1.8 < \eta < 2.0$	$2.0 <  \eta  < 2.5$	$2.5 <  \eta  < 3.2$
Presampler	$0.025 \times 0.1$	$0.025 \times 0.1$			
Sampling 1	$0.003 \times 0.1$	$0.003 \times 0.1$	$0.004 \times 0.1$	$0.006 \times 0.1$	$0.1 \times 0.1$
Sampling 2	$0.025 \times 0.025$	$0.025 \times 0.025$	$0.025 \times 0.025$	$0.025 \times 0.025$	$0.1 \times 0.1$
Sampling 3	$0.050 \times 0.025$	$0.050 \times 0.025$	$0.050 \times 0.025$	$0.050 \times 0.025$	
Trigger	$0.1 \times 0.1$	$0.1 \times 0.1$	$0.1 \times 0.1$	$0.1 \times 0.1$	$0.2 \times 0.2$

Table 4.7: An overview of the different samplings of the ATLAS liquid argon calorimeter EMB and EMEC. Granularity is reported as  $(\Delta\eta, \Delta\phi)$ . Reproduced from Ref. [118].

26. This terminology may be a little confusing as the LAr calorimeter is a sampling calorimeter. This does *not* refer simply to full sections of instrumented material separated by sections of absorber, but rather to sections with differing  $\eta$  resolution.

#### 4.2.4.2 Tile Calorimeter

Like the HEC and FCAL subsystems of the LAr calorimeter, the Tile calorimeter (TileCal) serves as a hadronic calorimeter: it is optimized to measure the energy deposited by hadronic showers, those produced by hadrons (such as charged pions and kaons)<sup>[27]</sup>. These showers develop over larger distances – in terms of radiation lengths<sup>[28]</sup> – and so TileCal is accordingly made larger and is located outside of the LAr calorimeter, covering a radial region of approximately (2.3 m, 3.9 m). It consists of a periodic structure of modules, each of which is a laminate of scintillating plastic – transparent injection-molded polystyrene, containing paraterphenyl (PTP) and 1,4-bis(5-phenyloxazol-2-yl) benzene (POPOP) wavelength-shifting dyes – and steel absorber attached to a support girder [120]. Figure 4.16 shows the structure of a single module, and Figures 4.17 and 4.18 show the full TileCal layout, consisting of barrel and extended-barrel regions.

Readout is handled by wavelength-shifting fibers, that transmit signals from the scintillation photons produced in the plastic tiles, to photomultiplier tubes that convert these into voltage pulses<sup>[29]</sup>

#### 4.2.5 The ATLAS Muon Spectrometer

The muon spectrometer corresponds with the outermost layers of the ATLAS detector. Muons are leptonic particles like electrons, but with roughly 200 times the mass of an electron, they are not stopped as easily. Passing through the inner detector and the calorimeters, they deposit the majority of their momentum in the muon spectrometers' various subsystems. These subsystems, all of them gaseous particle detectors, consist of the following:

- Monitored Drift Tubes (MDTs),

---

27. For a discussion of electromagnetic and hadronic calorimeters – and the differences in calibrating these – see Appendix F.2.

28. See Appendix F.1.

29. For more details on photomultiplier tubes, see Appendix F.4.

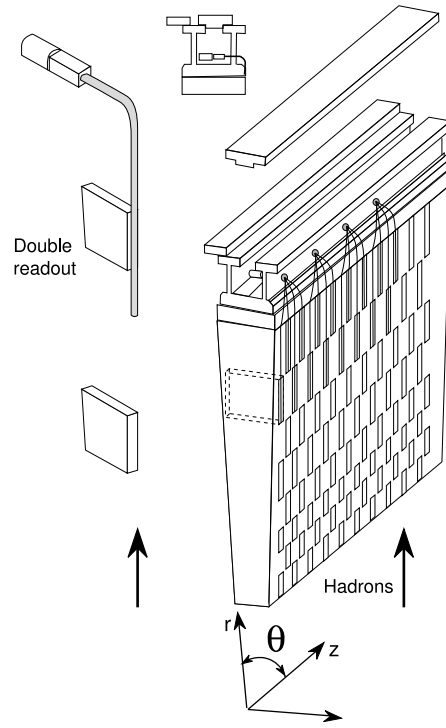


Figure 4.16: A schematic of a single TileCal module. Taken from Ref. [120].

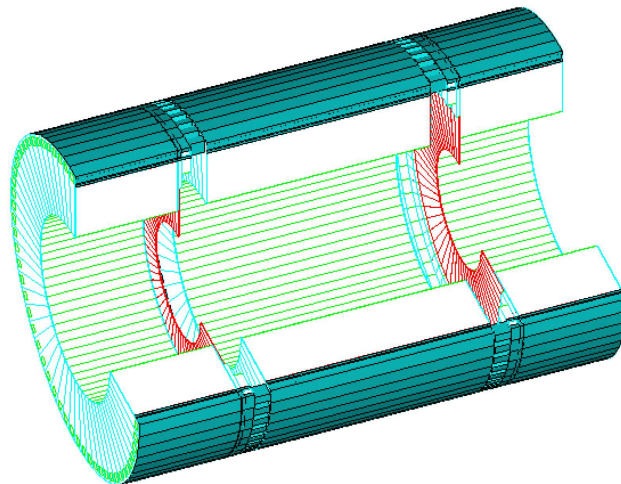


Figure 4.17: A rendering of the TileCal structure. Taken from Ref. [120].

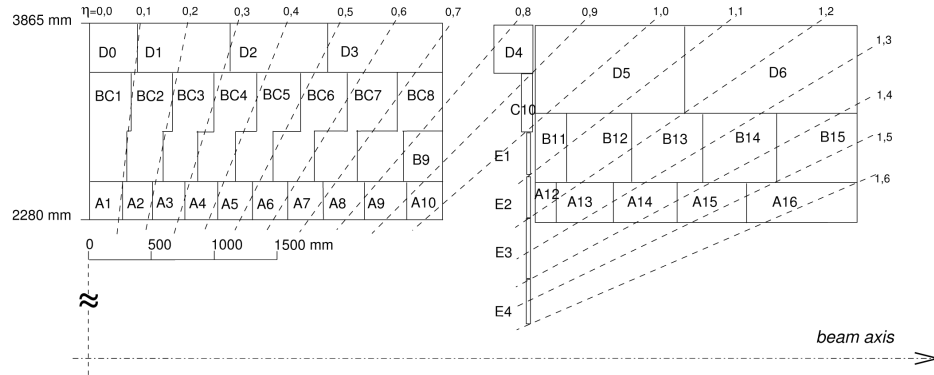


Figure 4.18: A schematic showing the division of TileCal into different towers. Taken from Ref. [121].

- Resistive Plate Chambers (RPCs),
- Thin Gap Chambers (TGCs),
- Cathode Strip Chambers (CSCs).

Figure 4.19 shows the position of the muon spectrometer components in the ATLAS detector, and Figure 4.20 shows the locations of the subsystems.

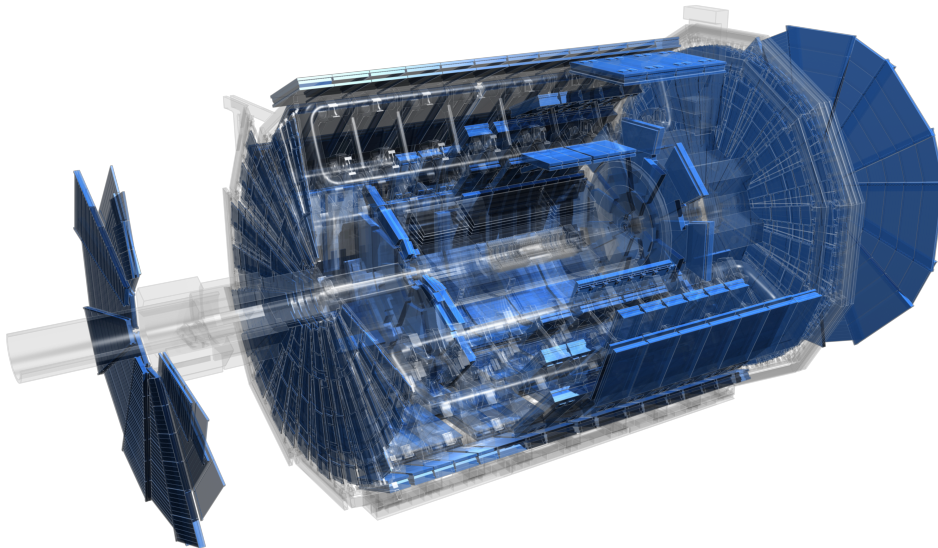


Figure 4.19: A highlight of the components of the ATLAS muon spectrometer. Taken from Ref. [104].

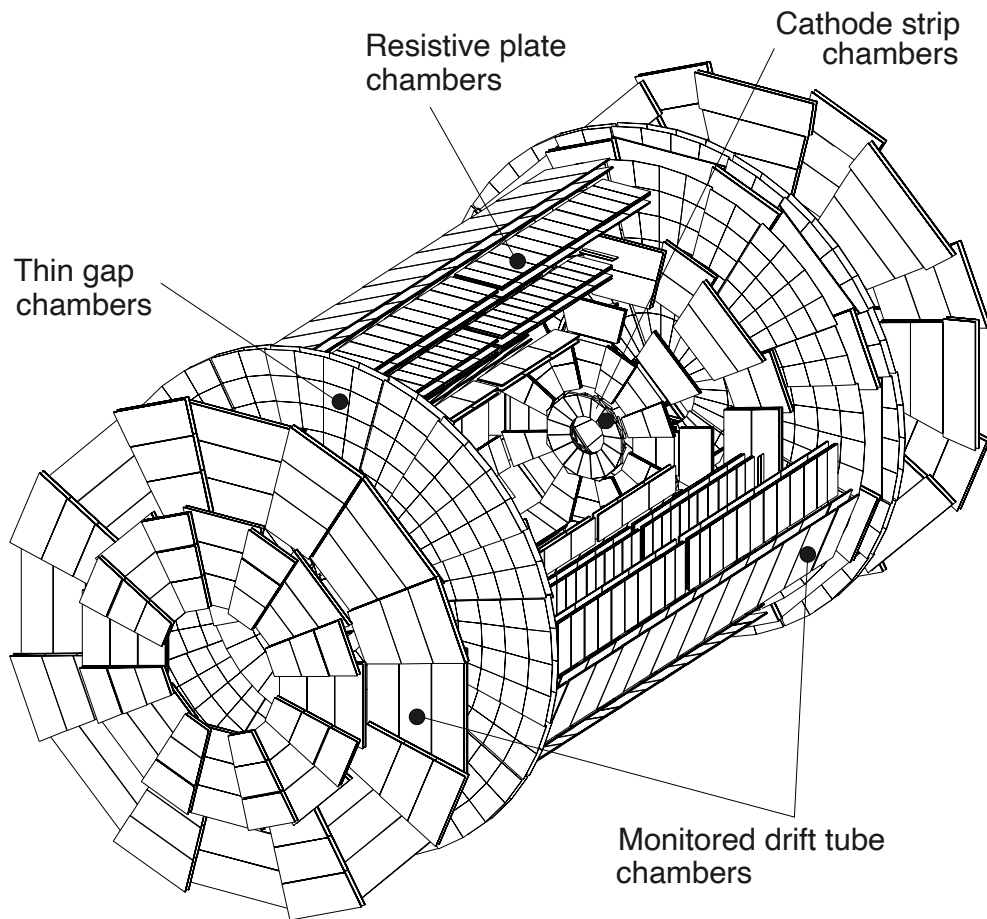


Figure 4.20: A schematic of the muon spectrometer layout. Taken from Ref. [122].

These different systems have trade-offs in terms of position, energy and timing measurement precision, and thus are used in concert – for collecting high-precision measurements for muon reconstruction, as well as fast timing information for triggering purposes. Although the muon spectrometer is perhaps the least relevant section of the detector for the physics analysis discussed in Chapter 5, it is an instructive example of how different types gaseous particle detectors can be employed in conjunction. In the following subsections we will review the basic design of each of the spectrometers’ subsystems, and conclude with a brief summary.

#### 4.2.5.1 Monitored Drift Tubes

The MDTs, which cover all the but the forward-most regions of the detector, are examples of *proportional counters*<sup>[30]</sup>. The anode consists of an aluminum tube 3 cm in diameter with 400  $\mu\text{m}$  wall thickness, filled with an Ar:N<sub>2</sub>:CH<sub>4</sub> mixture. The cathode is a W–Re axial wire at the center of the tube, which is kept at a relative potential of 3270 V [122]. The MDTs are arranged into bunches of parallel tubes, placed within boxes or “chambers”. These chambers are tiled around the barrel of the detector, as shown in Fig. 4.20, so that the MDTs are perpendicular to the beam axis. Any deformations owing to mechanical stress on the system are measured by an optical system, in order to be accounted for in detector operation, hence the moniker “monitored drift tube”.

Charged particles (such as muons) that pass through the MDT will ionize the gas, and the resulting electrons and ions will drift to the wire and tube. The location of where the muon ionized the gas – specifically its longitudinal and radial coordinates <sup>[31]</sup> – can be determined based on the system’s segmentation, as well as the ion-electron drift time: From the difference in times between the electrons and ions reaching their respective receptors, one can determine

---

30. See Appendix F.3.

31. Hypothetically one can attain some very rough azimuthal information, since each MDT covers some finite range in azimuth. However there are other systems that provide precision azimuthal measurements.

the distance of the ionization from the tube center. <sup>[32]</sup> Figure 4.21 provides a schematic of the MDT cross-section.

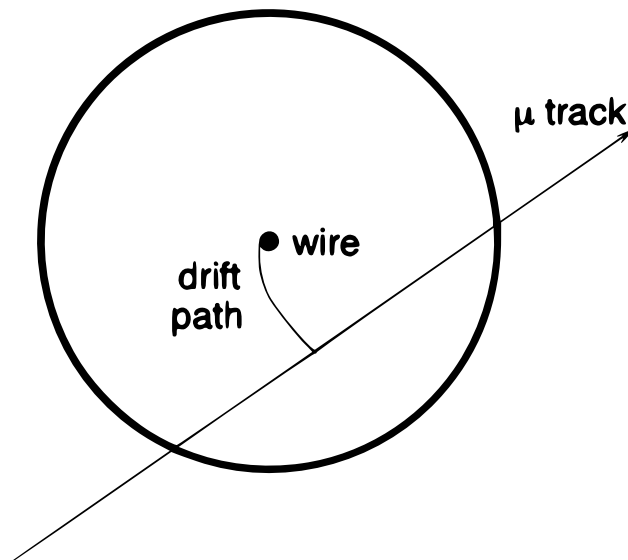


Figure 4.21: A cross-section of a Monitored Drift Tube in the ATLAS muon spectrometer. Note the curved drift path produced by the muon, which is a consequence of the MDT being located within the detector’s magnetic field. Taken from Ref. [122].

#### 4.2.5.2 Resistive Plate Chambers

The RPCs cover the central region as shown in Figure 4.20. They consist of sets of parallel Bakelite plates, with a spacing 2 mm, surrounded by insulating material as shown in Figure 4.22. The space between the plates is filled with a  $C_2H_2F_4:C_4H_{10}$  gas mixture, and a uniform electric field of  $4.5 \text{ kV mm}^{-1}$ . In analogue with the MDTs, muons ionize this gas, and the primary ionization electrons are multiplied by the electric field and accelerated into the plates for readout. Unlike the MDTs, the RPCs provide both azimuthal and longitudinal measurement of the position of the ionization, which is achieved by a set of readout wires along either direction. The RPCs also play a role in the trigger system, owing to their good

---

32. This position measurement is slightly more complicated by the fact that the MDTs are within the detector’s magnetic field, so that the electron/ion drift paths are curved. Thus the local magnetic field strength introduces a radially-dependent shift to the drift time. For details, see Ref. [122], Section 5.1.1.1.

timing resolution with an root-mean-square resolution of 1.5 ns.

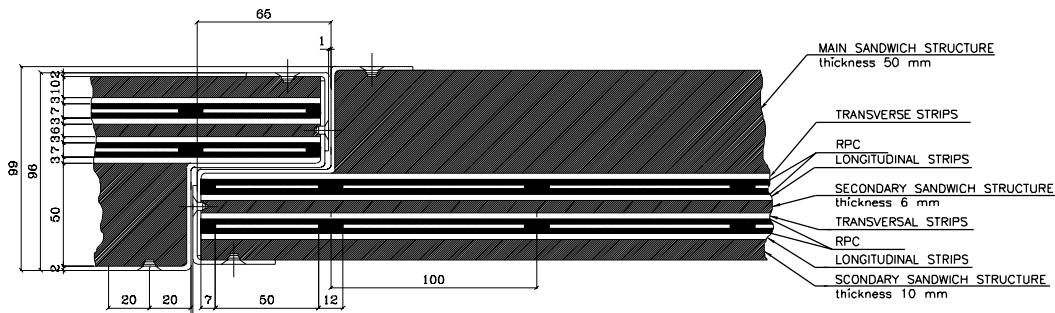


Figure 4.22: A schematic of a Resistive Plate Chamber in the ATLAS muon spectrometer, showing multiple units encased in the insulating “sandwich structure”. Taken from Ref. [122].

### 4.2.5.3 Thin Gap Chambers

The TGCs cover a forward region of  $|\eta| \in [1, 2.7]$ . They consist of sets of parallel graphite planes, spaced 2.8 mm apart. The gap between them is filled with a  $\text{CO}_2:n\text{-C}_5\text{H}_{12}$  gas mixture, with anode wires running parallel to the plates, equidistant from them and pitched 1.8 mm apart. Figure 4.23 shows the basic structure of the TGCs.

These detectors are similar in principle to the MDTs, but with a few key differences: Operating with an anode potential of 3.1 kV, the TGCs are in the so-called *saturation* mode. This causes them to operate as Geiger-Müller tubes rather than as proportional counters, and the combination of this high voltage and the small anode-cathode distance leads to low ionization electron drift times – and thus good timing resolution. The anode wires run parallel to those of the MDTs, but perpendicular Cu readout strips on the graphite planes allow for measuring the azimuthal coordinate as well. As with the RPCs, the TGCs are used as part of the triggering system.

### 4.2.5.4 Cathode Strip Chambers

The CSCs are multiwire proportional chambers, consisting of W–Re anode wires with a pitch of 2.54 mm in a volume of  $\text{Ar}:\text{CO}_2:\text{CF}_4$  gas. Cathode readout strips are located on planes

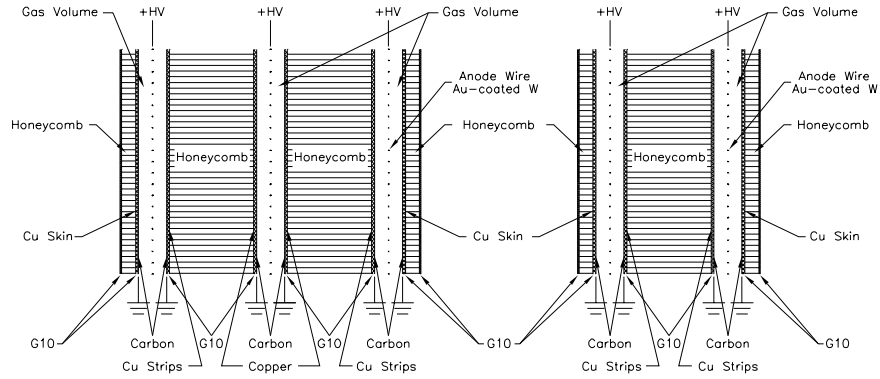


Figure 4.23: A schematic of Thin Gap Chambers in the ATLAS muon spectrometer, showing both “triplet” and “doublet” configurations with the TGCs spaced apart by paper honeycomb structures. Note that the gap sizes shown have been enlarged for detail. Taken from Ref. [122].

2.54 mm above and below the anode wire plane, with one set of strips running perpendicular to the anode wires and the other running parallel – thus providing measurements of both spatial coordinates. Figure 4.24 provides a schematic of the CSC design.

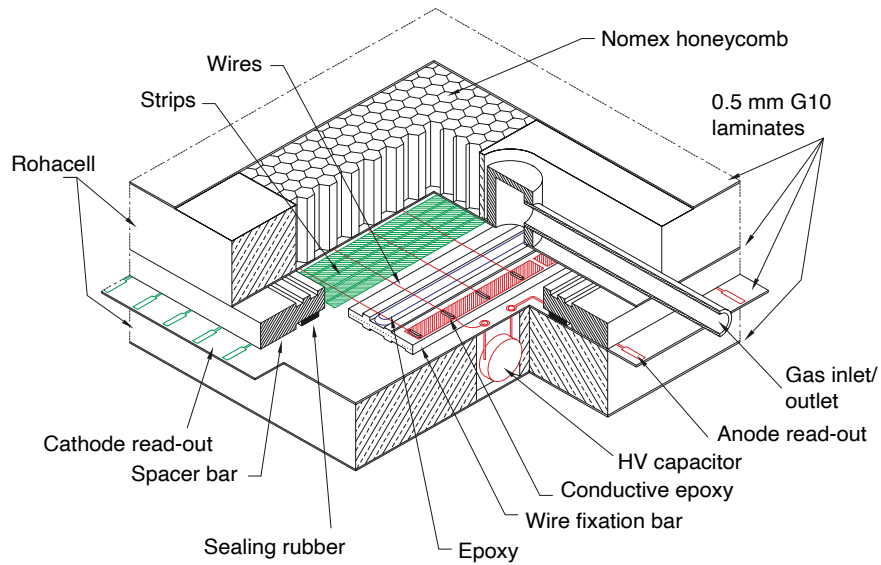


Figure 4.24: A schematic of a Cathode Strip Chamber in the ATLAS muon spectrometer. Taken from Ref. [122].

### 4.2.6 The ATLAS Triggering System

As discussed in Section 4.1.3, the LHC produces bunch crossings at a rate of 40 MHz, with multiple  $pp$  collisions occurring per bunch crossing. This produces far more data than can be saved to disk, in terms of both total volume and data rate, with each event consisting of approximately 1 MB of information [123]<sup>[33]</sup>. Furthermore, much of the information coming off of the detector corresponds with high-energy processes we are not interested in analyzing: Recall our discussion of cross-sections in Section 4.1.4. As shown in Figure 4.5, the largest cross-section corresponds with *jets*, which refers to the emission of light quarks and gluons<sup>[34]</sup>. These are plentiful QCD processes, and typically not ones of interest for many SM measurements and BSM searches. In fact, these processes often serve as “background” for other rarer ones that we wish to measure. Producing the rarer processes – and gathering enough of their events to make statistically-meaningful measurements – necessarily means producing a lot of this background as well. To mitigate this issue, ATLAS employs the triggering and data acquisition (TDAQ) system to determine whether or not to save a particular event, and cut down the recorded event rate to manageable levels. Crucially, the TDAQ system must make this determination extremely quickly to keep up with the event rate of 40 MHz (corresponding with one event every 25 ns). To accomplish this task, it is structured as a tiered system, consisting of “Level-1” trigger and “High-Level Trigger” (HLT) subsystems, as shown<sup>[35]</sup> in Figure 4.25.

---

33. For reference, in Run 3 a single event corresponds with about 3 MB of data, so that the raw data production rate is approximately  $1 \text{ PB s}^{-1}$ . This increase in event size is due to changes and upgrades to the underlying detector systems.

34. See Appendix E.

35. This is specifically the Run 2 layout of the TDAQ system. The layout has been modified for Run 3, as shown in Figure 4.29, although its general design as a tiered system is unchanged.

### 4.2.6.1 The Level-1 Trigger

The Level-1 trigger is the first tier of the TDAQ system, nearest the detector in terms of data flow. It uses only a subset of information collected by the detector – most notably omitting all tracking information from the Inner Detector – to make its decision. To process incoming data, it employs application-specific integrated circuits (ASICs) that are located near the detector sensors, rather than traditional computer processors, as to allow for fast and efficient data processing at the cost of the computational complexity and flexibility<sup>[36]</sup>. As shown in Figure 4.25, the *Level-1 Accept* decision is passed on to the HLT, as well as the detector read-out that furnishes the HLT (and final data readout) with more data, including richer readouts from the calorimeter and muon spectrometer systems, as well as information from the Inner Detector.

### 4.2.6.2 High-Level Trigger

The HLT consists of the second tier of the TDAQ system, taking as inputs the Level-1 Accept decision, as well as the full detector readout. This corresponds with much larger per-event data sizes than the coarser Level-1 inputs, but this size increase is facilitated by the event rate reduction achieved by the Level-1 subsystem. Unlike Level-1, the HLT is a software trigger, and runs on more traditional central processing units (CPUs) located in a “processing farm”. This allows for more flexibility in algorithm design, in terms of complexity and resource-sharing, as well as timing.

---

36. Unlike traditional central processing units (CPUs), ASICs are not programmable: the algorithm they execute is effectively baked into the design, thus not allowing for on-the-fly changes. This limitation is addressed by the inclusion of Field-Programmable Gate Arrays (FPGAs) in the TDAQ upgrade, as will be discussed in Section 4.2.8.2.

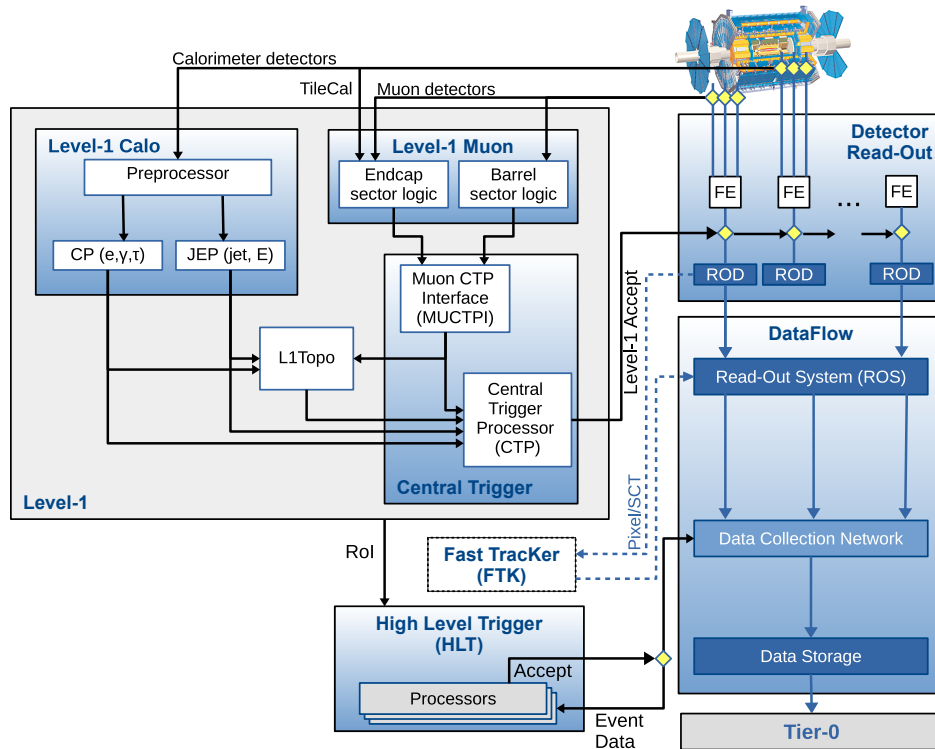


Figure 4.25: An overview of the ATLAS TDAQ system for Run 2. Note that this system has since been significantly updated for Run 3. Also note that the Fast TracKer (FTK) was not deployed – it was used only for testing purposes, and the project has since been deprecated. Taken from Ref. [124].

### 4.2.7 Phase-I Upgrade

The Phase-I upgrade of the ATLAS detector was performed before the start of Run 3, and consisted of upgrades to the muon spectrometer, the front-end electronics for the liquid argon calorimeter, as well as numerous upgrades to the TDAQ system. As these upgrades are not relevant to analysis discussed in Chapter 5 (which uses data collected from Run 2), nor do they relate to projects in which I participated, we will only briefly cover these topics.

#### 4.2.7.1 The New Small Wheel

A substantial part of the Phase-I upgrade was the addition of the New Small Wheel (NSW) [125, 126], a forward detector replacing part of the original end-cap sections of the muon spectrometer – this includes all of the CSCs (Section 4.2.5.4). Covering the forward region of  $1.3 < |\eta| < 2.7$ , the NSW uses two different detector technologies: “small-strip” TGCs (sTGCs) and “micro mesh gaseous structure” (MicroMegas) detectors.

The sTGCs have many of the same design parameters as the regular TGCs, but the readout strips have a much smaller pitch of 3.2 mm. Like the regular TGCs (Section 4.2.5.3), the sTGCs are used for triggering purposes due to their good timing resolution.

The MicroMegas detectors [127], are the precision-measurement counterpart to the sTGCs. Similar to the RPCs, they consist of a set of parallel plates – one of them a cathode and the other equipped with readout electrodes – with the space in between filled with a Ar:CO<sub>2</sub> gas mixture. In contrast with the RPC design, this space is divided into 5 mm “drift/conversion” and 128  $\mu\text{m}$  “amplification” gaps by a stainless steel mesh, as shown in Figure 4.26. The presence of this conducting mesh allows for applying different electric field strengths in the two regions:  $600 \text{ V m}^{-1}$  in the conversion gap, and a much stronger  $40 \text{ kV m}^{-1}$  in the small amplification gap right adjacent to the readout plane. Thus the MicroMegas detector operates as a proportional counter.

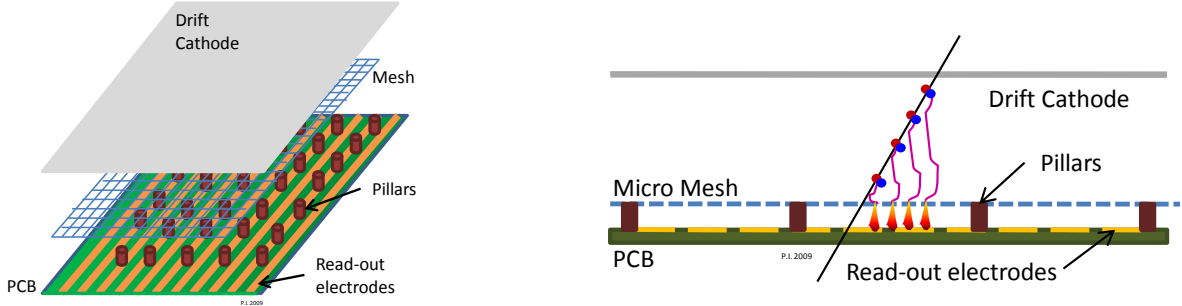


Figure 4.26: A schematic of the MicroMegas detectors. Taken from Ref. [126].

#### 4.2.7.2 Upgrades to the TDAQ System

The Phase-I upgrade also included significant updates to the TDAQ system, as shown in Figure 4.27. This includes the addition of so-called *feature extractor* (FEX) modules to the Level-1 Calorimeter Trigger, for electron (eFEX), jet (jFEX) and global (gFEX) features [128], respectively. These modules use Field-Programmable Gate Arrays (FPGAs), which are low-latency, low-power processors, to efficiently process data from the LAr and Tile calorimeters and attempt to identify certain types of physics objects<sup>[37]</sup> to be used in the trigger decision. We will reserve further discussion of FPGA-based trigger systems for our discussion of the Phase-II upgrade below.

#### 4.2.8 Phase-II Upgrade

The Phase-II upgrade of the ATLAS detector is being performed in anticipation of the high-luminosity LHC (HL-LHC) era, where the average number of simultaneous  $pp$  collisions will be increased – with the instantaneous luminosity increasing by a factor of 5 [131]. This will greatly increase the rate at which data can be collected – and at which SM processes can be measured and BSM processes searched for – but comes at the cost of greatly increased pile-up, and thus detector upgrades that can handle this more challenging environment.

<sup>37</sup>. For eFEX and jFEX, these objects correspond with electrons and small-radius jets. For gFEX, the “global” features it searches for correspond with large-radius jets and  $\cancel{E}_T$  [129].

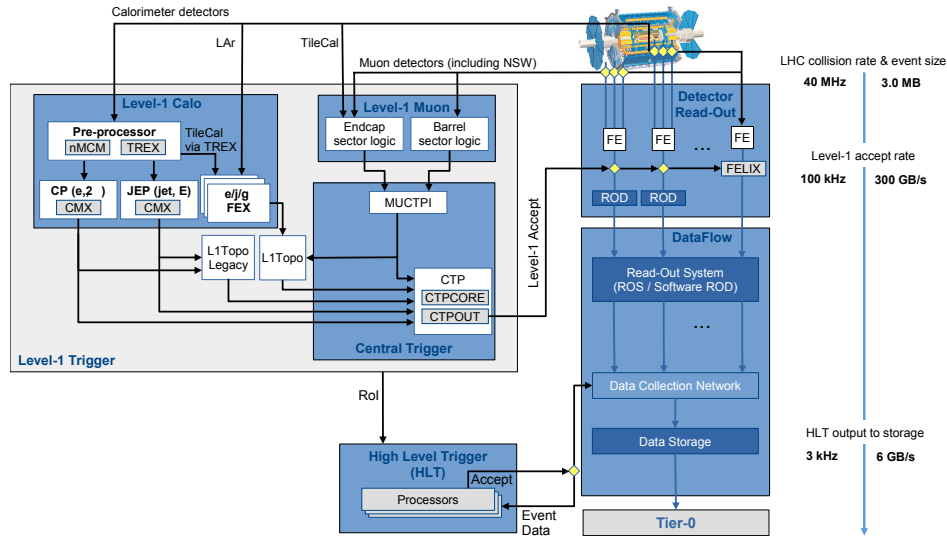


Figure 4.27: An overview of the ATLAS TDAQ system for Run 3. Taken from Ref. [130].

In the following subsections, I will briefly describe these upgrades, and highlight particular studies (related to calorimeter reconstruction) to which I directly contributed.

#### 4.2.8.1 Upgrades to the Inner Detector

The five-fold increase in instantaneous luminosity will result in an increase in the average number of interactions per crossing (and thus pileup), from approximately 34 to 200. This presents a significant challenge for the inner detector – nearest the interaction point, where hits from particles will become extremely dense. To deal with this challenge, the inner detector will be replaced with a new system known as the Inner Tracker or “ITk”. This system will use silicon pixel and strip technologies – as do the current Pixel and SCT detectors – but unlike the current system, it will *only* use these silicon trackers and forego a transition radiation tracker [132]. The ITk detector is complemented by the High-Granularity Timing Detector (HGTD), a silicon detector covering the  $2.4 < |\eta| < 4.0$  range [133]. Figure 4.28 provides a diagram showing the ITk and HGTD layout.

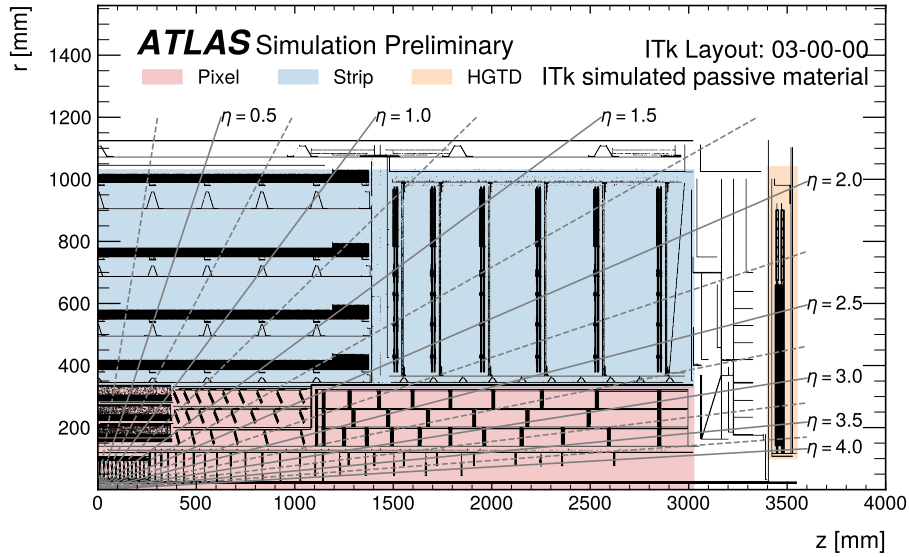


Figure 4.28: An overview of the ITk and HGTD layout. Taken from Ref. [134].

#### 4.2.8.2 Trigger upgrades and the Global Event Processor

The Phase-II upgrade involves significant modifications to the triggering system. It will consist of a “Level-0” (L0) hardware trigger using calorimeter and muon spectrometer information operating at 40 MHz – with an output rate up to 1 MHz – followed by an “Event Filter” that utilizes tracking information to further filter the L0-accepted events to a rate of 10 kHz [135, 136]e. The TDAQ system workflow is shown in Figure 4.29.

One component of this system is the “Global Event Processor” (GEP), which serves a similar purpose as the Event Filter – making a triggering decision based on a large set of event features (or high-level observables computed from these features), but as part of the L0 trigger<sup>[38]</sup> Figure 4.30 shows an overview of the GEP design.

In order to meet the L0 low-latency requirements, the GEP makes use FPGAs. As discussed in Section 4.2.7.2, these are specialized computational “accelerators” that perform low-latency, fixed-precision calculations<sup>[39]</sup>. Compared to ASICs, FPGAs have the advantage

38. In Figure 4.29, this is indicated as the “Event Processor” inside the “Global Trigger” block.

39. FPGAs, as computational accelerators, are sometimes compared to graphics processing units (GPUs), in that they are very fast and efficient in performing certain types of operations, but algorithms have to be

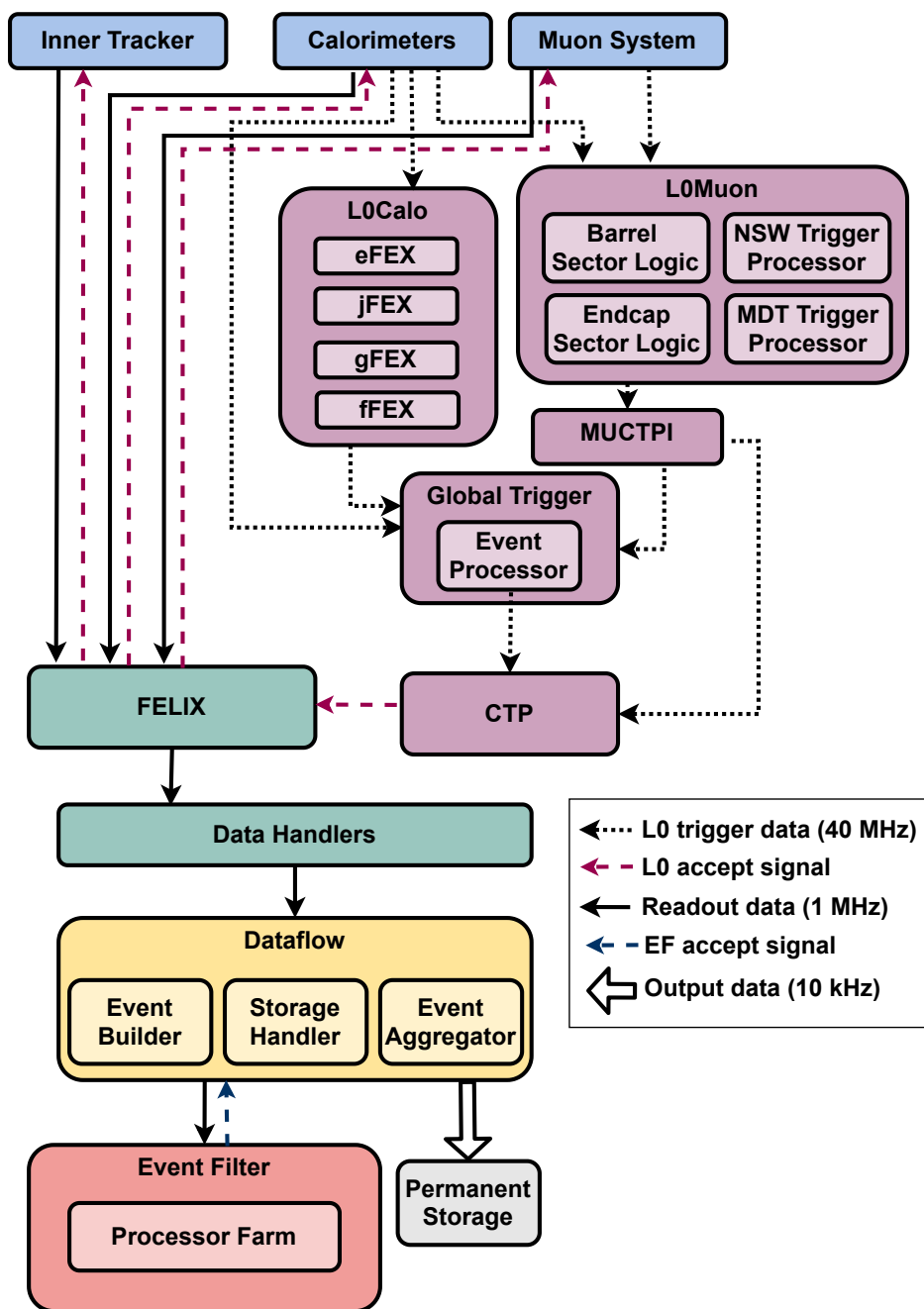


Figure 4.29: An overview of the ATLAS TDAQ system for the Phase-II upgrade. Taken from Ref. [136].

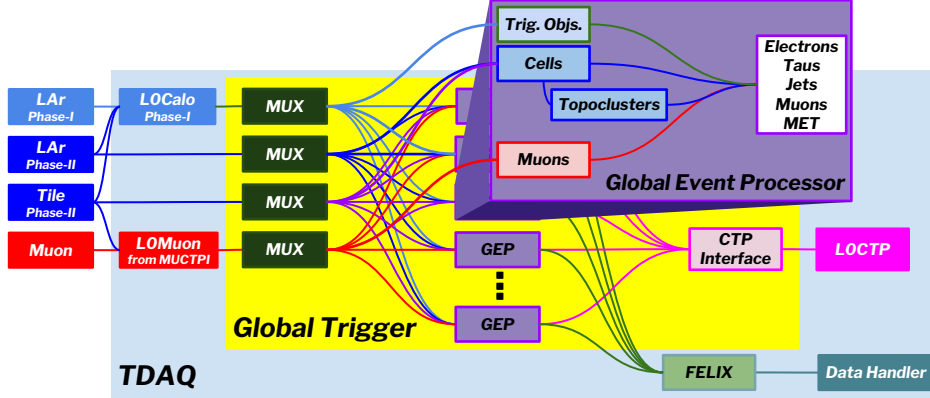


Figure 4.30: An overview of the Global Event Processor design. Taken from Ref. [135].

that they are (re)programmable – however their firmware must be written in a very different way than traditional CPU-based software, in order to handle fixed-precision calculations and the devices’ memory management systems.

As shown in Figure 4.30, one of the tasks of the GEP is to reconstruct jets from groups of energy deposits in the calorimeter known as *topological clusters* (or *topo-clusters* for short)<sup>[40]</sup>. This reconstruction also involves performing a *jet energy scale* (JES) calibration, whereby a calibration factor is applied to the reconstructed jet energy based on its (uncalibrated) energy and pseudo-rapidity<sup>[41]</sup>. As part of my work in Phase-II upgrade studies, I have derived a JES calibration specifically for the GEP under HL-LHC conditions. This involves using Monte Carlo (MC) simulations of QCD dijet processes – the production of light quark and gluon jets – to simulate the calorimeter energy response, from which a set of calibration functions can be derived. For this calibration, the “stand-in” trigger jet are formed using 4-2-2 topo-clusters, which are formed via the following algorithm [135]:

1. The topo-cluster is seeded by finding a calorimeter cell with an energy deposit signifi-

---

modified (or even custom-tailored) in order to run on them.

40. For a review of topological clustering, see Ref. [137]. Here, it suffices to say that these clusters are defined by grouping neighboring calorimeter cells. As described further below, the topo-cluster is seeded by finding a cell with energy above some noise significance threshold, and this is then iteratively joined with neighboring cells possibly meeting some different significance thresholds.

41. For some general details about jet energy scale calibrations, see Appendix E.2.4.

cance,  $\text{sig}(E_T) = |E_T|/\sigma_{E_T}$ , satisfying  $\text{sig}(E_T) > 4$ . Here,  $\sigma_{E_T}$  is the calorimeter cell energy resolution – so that cells with a higher  $\text{sig}(E_T)$  are less likely to be the product of electronics or instrumentation noise.

2. Neighboring cells (in 3D) are combined with the topo-cluster, if they satisfy  $\text{sig}(E_T) > 2$ .

Once formed, these topo-clusters are used as inputs<sup>[42]</sup> to clustering anti- $k_t$ ,  $R = 0.4$  jets<sup>[43]</sup>. Figure 4.31 shows the trigger jet mean  $E_T$  response before and after JES calibration, where the calibration function has been implemented as a set of energy-binned calibration factors<sup>[44]</sup>. Such an implementation allows it to be deployed as a lookup table (LUT) on a GEP FPGA, allowing for extremely fast application.

### 4.2.8.3 Calorimeter reconstruction: Algorithmic upgrades

In addition to physical upgrades to the detector systems and readout electronics, the Phase-II upgrade also involves a large set of algorithmic upgrades for reconstructing particle candidates – much of it owing to the significant increase in instantaneous luminosity and resulting pileup. One particular upgrade – in which I participated – is the development of neural network-based methods for energy calibration of topo-clusters constructed in the ATLAS calorimeters, to replace the current *local cell weighting* (LCW) method [140].

The purpose of this energy calibration is to account for the calorimeters’ different energy responses for electromagnetic and hadronic showers<sup>[45]</sup>. Thus, implicit in this calibration is a classification problem – to identify if a particular topo-cluster is electromagnetic or hadronic

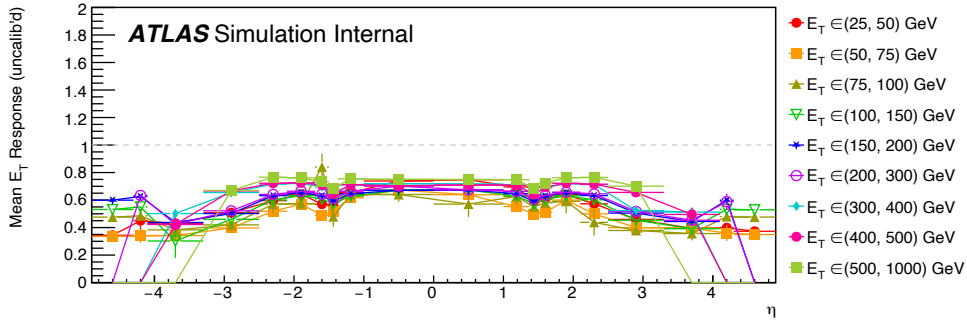
---

42. This is in contrast with offline jet clustering, which instead uses 4-2-0 topo-clusters from the calorimeters (possibly among other inputs). These topo-clusters are formed similarly to the 4-2-2 variety, except that the algorithm features an additional final step where all neighboring cells are combined with the topo-cluster.

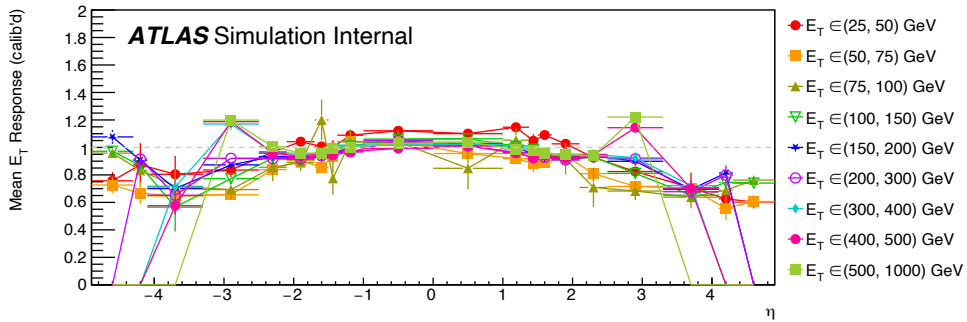
43. See Appendix E.2.

44. For details, see the software package in Ref. [138] for producing the JES calibration, and Ref. [139] for binning the resulting calibration functions. These are software repositories internal to the ATLAS collaboration.

45. See Appendix E.2 for a discussion of this phenomenon. Aside from the different responses, this calibration also implicitly corrects for energy losses in dead material.



(a)



(b)

Figure 4.31: The (a) uncalibrated and (b) calibrated trigger jet mean  $E_T$  response, as a function of jet  $\eta$  (and binned in jet  $E_T$ ). The calibration is evaluated in MC simulation with respect to EM-scale Particle Flow jets (which are first calibrated with respect to truth-level jets).

in origin. This effectively boils down to being able to identify topo-clusters produced in the LAr and Tile calorimeters by charged and neutral pions which constitute a significant fraction of the outputs of hadronic showers, and the latter of which almost always decays to photons via  $\pi^0 \rightarrow \gamma\gamma$  and thus serves to siphon off energy into electromagnetic showers. To perform this classification this, we can employ convolutional and graph neural networks (CNNs and GNNs, respectively), as well as deep fully-connected neural networks (DNNs), and treat topo-clusters as images in the  $(\eta, \phi)$  plane<sup>[46]</sup> with pixel intensities representing cell energy deposits, or as point clouds of energy deposits in 3D space. Figure 4.32 shows an example of how a CNN classifier is structured.

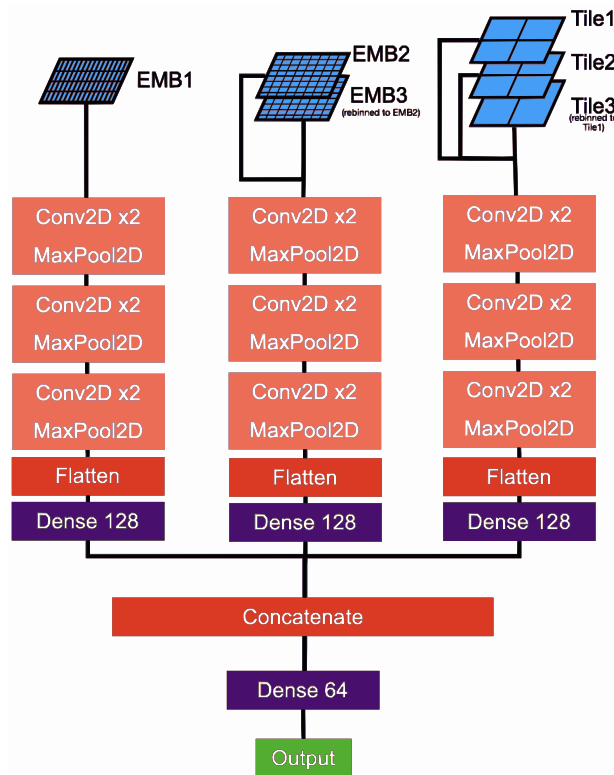


Figure 4.32: A CNN topo-cluster classifier network architecture, corresponding with “CNN (separated EMB1 layer)” in Figures 4.36 and 4.36. The “EMB” and “Tile” images correspond with samplings of the electromagnetic barrel and Tile calorimeters. Taken from Ref. [141].

46. For a thematically-similar discussion of treating calorimeter energy deposits as images for jet identification, see Section 6.1.

To study the performance of these classifiers, a set of DNNs and CNNs were trained on MC simulation consisting of single charged or neutral pions interacting with the ATLAS calorimeters as modeled via the `GEANT4` software package [142]. As shown in Figure 4.33, these samples were prepared such that the two species of pions had similar kinematics, and were limited to the central  $|\eta| < 1$  region as to focus on performance of the barrel calorimeter sections<sup>[47]</sup>.

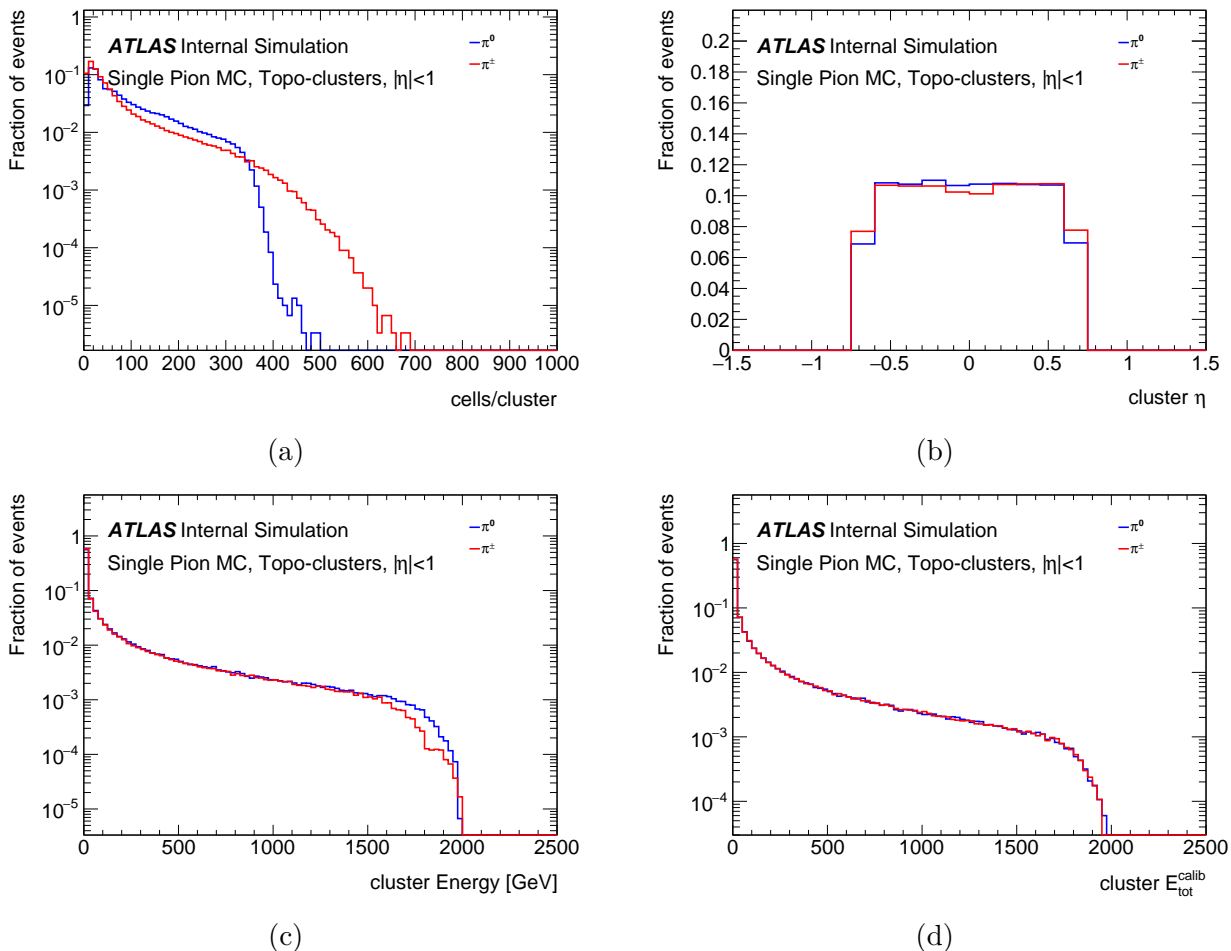


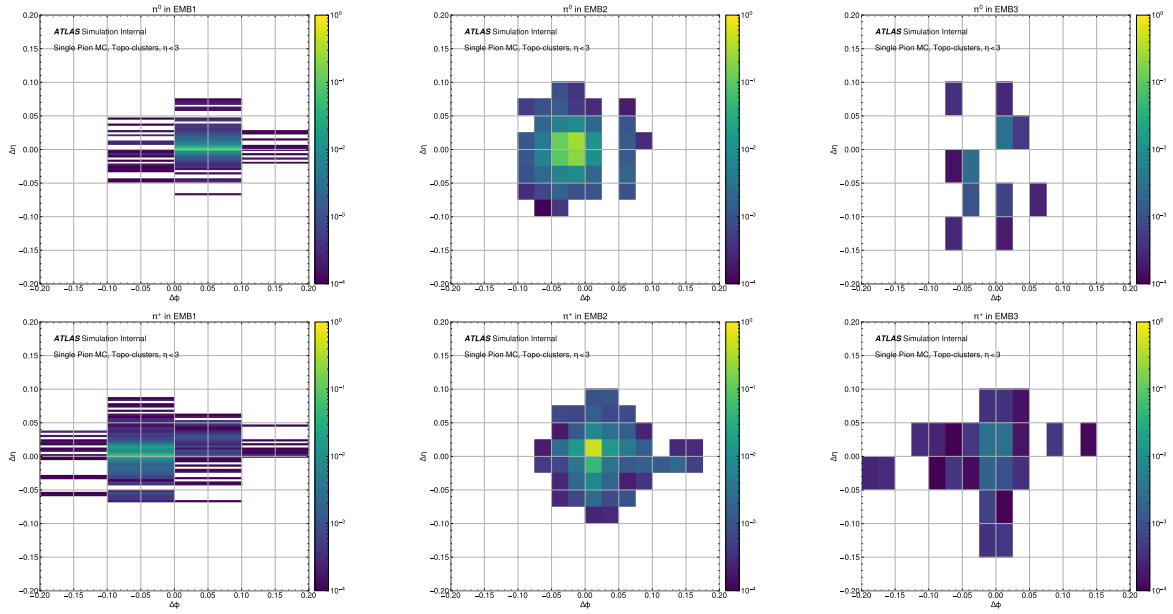
Figure 4.33: Topo-cluster kinematics for the MC simulation used to train and test the topo-cluster classifiers, showing the (a) number of cells per cluster, (b) uncalibrated cluster energy, (c) cluster  $\eta$ , and (d) truth cluster energies.

47. Of course, whatever calibration method(s) is used must ultimately handle the entire calorimeter. However, the central region is a natural starting point for studying new algorithm designs, as it features a regular geometry and thus eliminates  $\eta$ -dependent effects that may arise from inhomogeneity in the calorimeter structure.

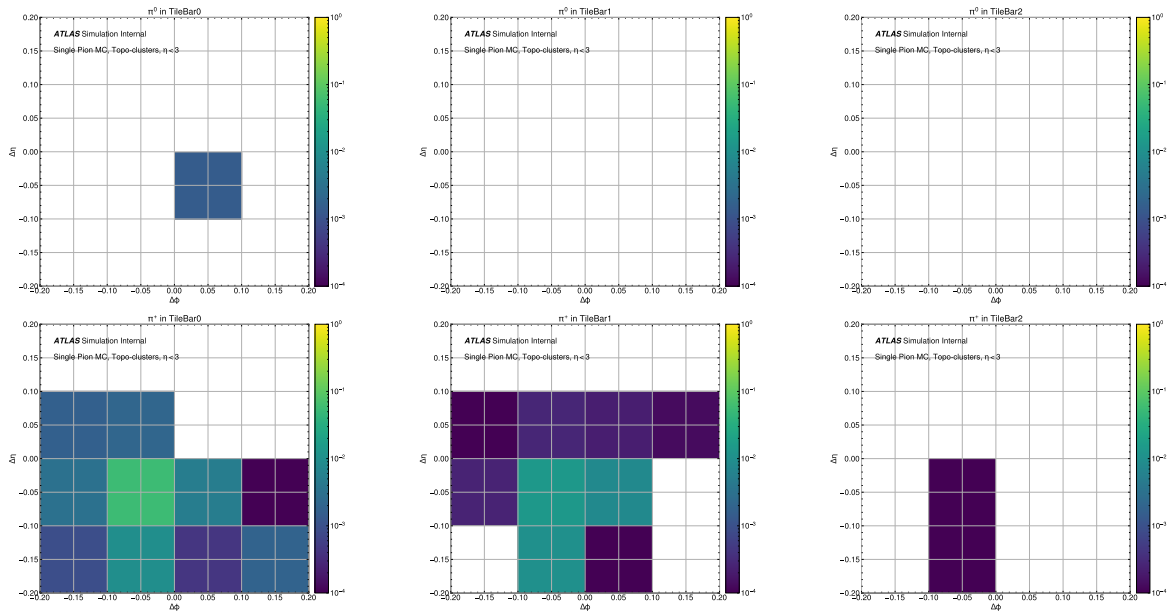
Figures 4.34 and 4.35 show example images produced from 3 electromagnetic barrel (EMB) and 3 TileCal (Tile) samplings, which together serve as 6 images of each pion topo-cluster used as network inputs. In many cases, each species of pion deposits nearly all its energy in only one of the two calorimeters, corresponding with the type of shower it produces. However as shown in Figure 4.35, the two species can also produce similar shower profiles in some cases – and it is here where leveraging the neural network-based methods makes a difference. Figure 4.36 shows the *receiver operating characteristics* (ROC) curves of a number of different image-based neural networks developed for this task, as well as of the LCW method, and Figure 4.37 shows a set of false positive classification rates extracted from these curves. For each classifier – and any general binary classification method – the ROC curve is produced in the following manner:

1. We scan over different thresholds in the classifier output, which is represented as some output score on the interval  $[0, 1]$  with higher scores indicating that the input is classified as more signal-like.
2. For each choice of threshold, the numbers of signal and background events that are classified as signal are recorded, and the resulting signal and background *efficiencies* can be computed.
3. Each pair of these efficiencies corresponds with a point on the ROC curve, and it quantifies how well the classifier discriminates between signal and background at a particular choice of score threshold.

In practice, the information communicated in a ROC curve is useful as the score threshold can always be adjusted to tune the classifier performance. For example, high background rejection may be more desirable than high signal efficiency in classification tasks where the background is much more plentiful – such as in the data filtering tasks of the ATLAS TDAQ system – and so the ROC curve indicates how efficiently the classifier will identify signal

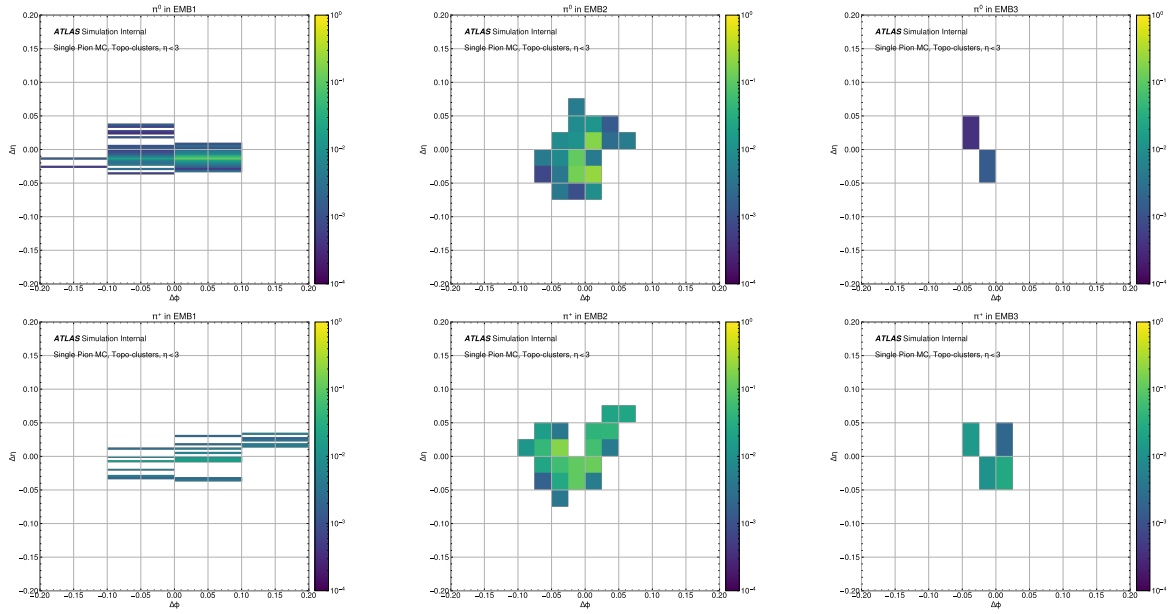


(a)

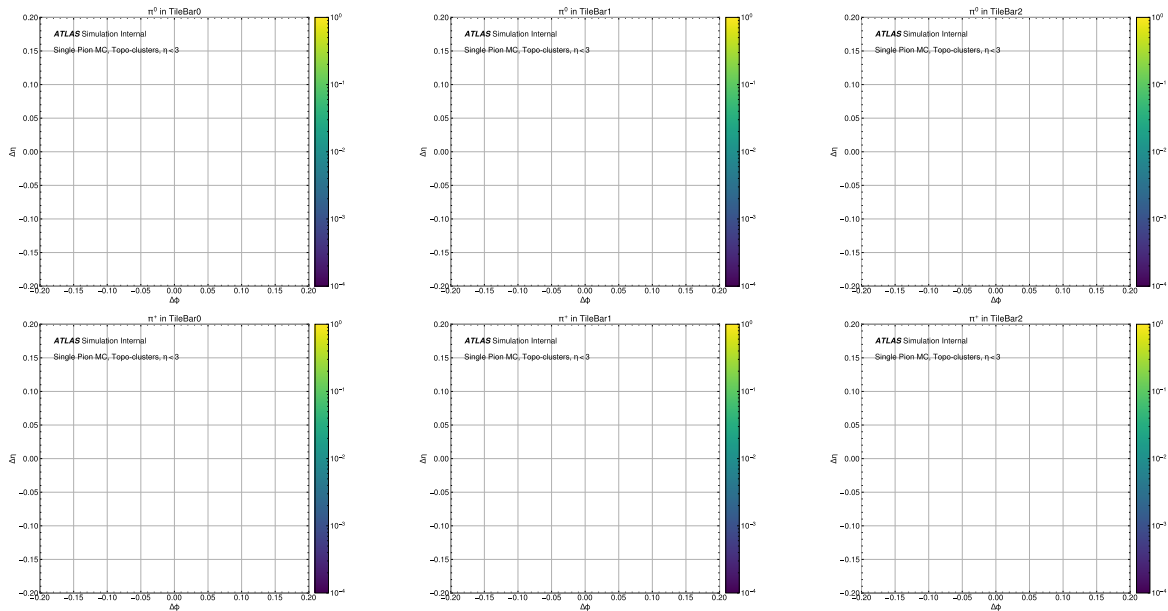


(b)

Figure 4.34: Topo-cluster images produced by a charged pion and a neutral pion in (a) the 3 EMB calorimeter samplings, and (b) the 3 TileCal samplings. Each pion has an energy of approximately 115 GeV, and  $\eta = 0.6$ .



(a)



(b)

Figure 4.35: Topo-cluster images produced by a charged pion and a neutral pion in (a) the 3 EMB calorimeter samplings, and (b) the 3 TileCal samplings. Each pion has an energy of approximately 13 GeV, and  $\eta = -0.7$ .

events at a given false positive rate.

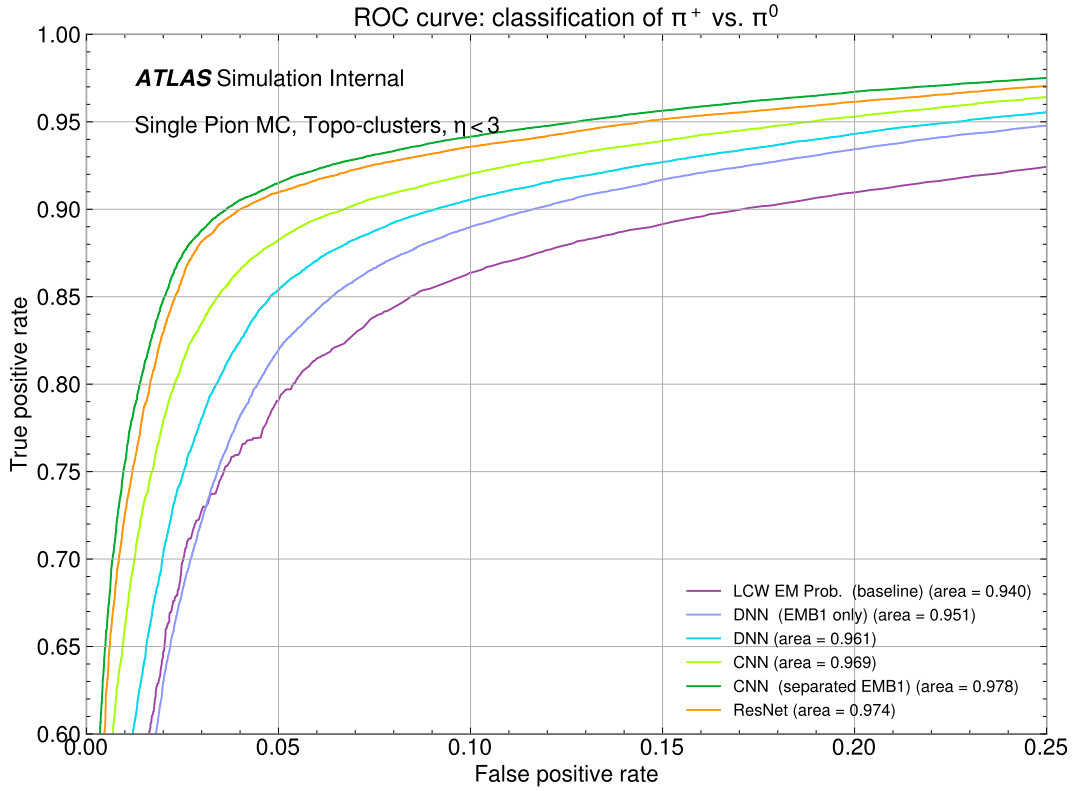


Figure 4.36: A set of ROC curves for various neural network methods developed for  $\pi^\pm/\pi^0$  classification in the ATLAS calorimeters. The existing LCW method is also shown for comparison.

As shown in the ROC curves in Figure 4.36, even simple neural networks leveraging only the first sampling of the EM barrel calorimeter (EMB1) can perform comparably to the LCW method – and more complex networks can significantly outperform it. The highest-performing image-based classifier, with the network architecture shown in Figure 4.32, is a CNN that leverages information from all available EMB and TileCal samplings, merging the images from each set of samplings but keeping the EMB1 sampling separate to leverage its particularly high angular resolution. While the results reported here correspond with fully-connected NNs and CNNs, state-of-the-art GNNs can achieve even higher performance [141], and possibly offer a more natural way of representing and operating on the data<sup>[48]</sup>.

48. For more discussion of how to “naturally” manipulate physics data in neural networks, see Chapter 6

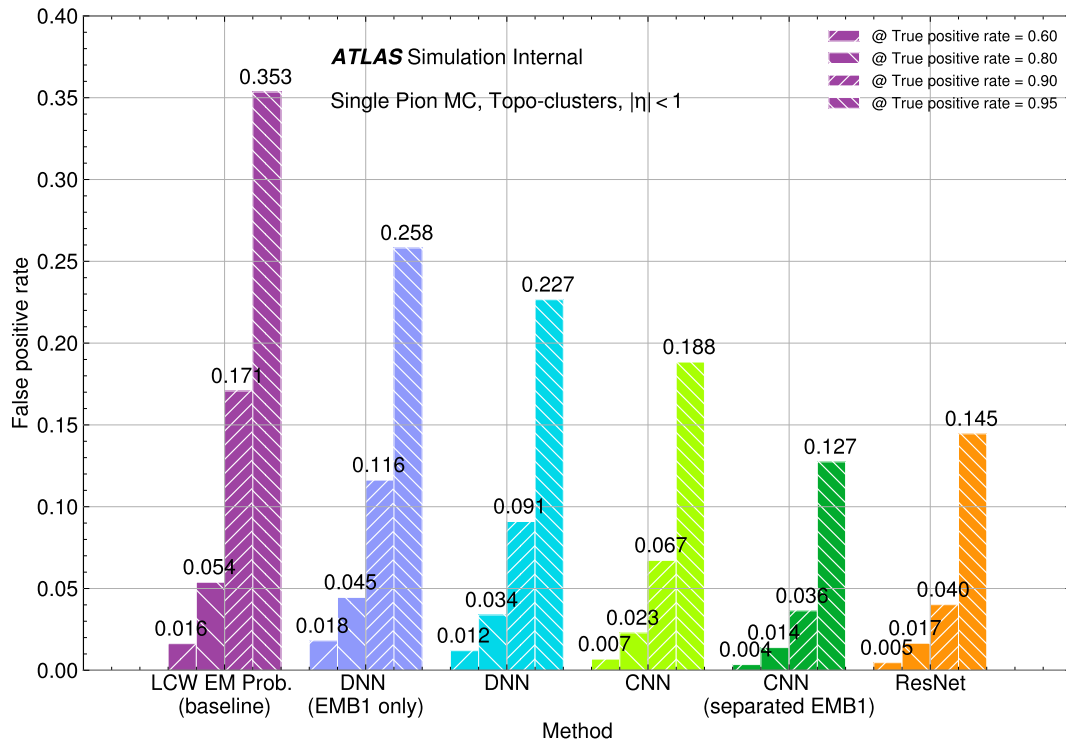


Figure 4.37: The false positive rate – the rate at which the classifier incorrectly identifies  $\pi^0$  topo-clusters as  $\pi^\pm$  topo-clusters – at a set of different fixed true positive rates, for the classifiers shown in Figure 4.36.

---

for a discussion of Lorentz-equivariant network architectures.

# CHAPTER 5

## SEARCHING FOR DISPLACED VERTICES AND MISSING TRANSVERSE ENERGY AT THE ATLAS EXPERIMENT

In this chapter, I will describe an analysis of data from the ATLAS experiment in which I participated, specifically a search for beyond-Standard Model (BSM) physics. Performed using data collected by the experiment during its “Run 2” – specifically during the years 2016 through 2018 – this analysis targeted a set of physics models in which non-Standard Model (SM) particles may be produced in proton-proton ( $pp$ ) collisions, and travel unseen partway through the inner detector before decaying into a combination of detectable and (directly) undetectable decay products. Such a process may produce a telltale signature of displaced particle production vertices together with an imbalance in the sum of the transverse momenta of all particles detected in the event.

I will describe the entire analysis process, but place an additional emphasis on some of the tasks and methods to which I directly contributed. A much more detailed description is provided by Ref. [143], which will be cited at a number of points<sup>[1]</sup>.

### 5.1 Introduction

Before delving into the details of this BSM search, let us briefly answer a basic but important question: What is an “ATLAS analysis”? In Section 4.2 we reviewed how the different components of the ATLAS detector record information from  $pp$  collisions. What do we actually do with this information?

---

1. This is an “internal note” for the ATLAS collaboration, and is unfortunately only available to collaborators via the CERN Document Server; at the time of writing this thesis, a paper is being written that will also summarize this analysis, under the working title “Search for displaced decays of long-lived, massive particles in events with missing transverse momentum in  $\sqrt{s} = 13$  TeV  $pp$  collisions with the ATLAS detector”. I should also note that while many of the tables in this chapter contain information taken from Ref. [143], this information is often presented or summarized differently here – in a way that I find potentially somewhat clearer.

### 5.1.1 *What is an analysis?*

The data from the ATLAS experiment are typically analyzed for two different purposes:

- Precision measurements of the SM. In other words, the data are analyzed to look for processes which are already described by our established theory of particle physics. The kinematics and cross-sections of these processes may depend on parameters of the SM, and so they provide a way of indirectly measuring these parameters themselves.
- Searches for BSM physics. In this case, the data are analyzed to look for processes which are *not* described by the SM.

On the surface, these two types of analyses may sound quite similar, the difference only being whether or not the particle interaction(s) being looked for in the data is part of the SM. However there are typically different methods employed, owing to the fact that the SM is a theory already supported by many decades of experiment: in precision measurements we look for processes that either have already been observed (in which case we seek to observe them more and improve our statistical analyzing power) or which we expect to be a direct consequence of properties of the SM already measured in some other way. By contrast, BSM searches almost by definition look for rare processes that we have not yet seen, and are typically ...

### 5.1.2 *Searching for long-lived particles: Some general comments*

As discussed in Section 3.2, a physics scenario combining SUSY with Peccei-Quinn theory may yield, for example, a long-lived SUSY particle that decays to an axino and a Higgs or  $Z$ -boson. By “long-lived”, here we mean a meta-stable particle with a lifetime such that after prompt production in a  $pp$  collision, it will decay within the ATLAS detector – and specifically within the inner detector, yielding a secondary vertex (as discussed in Section 4.2.1.4). As we will discuss below, there are in fact a number of BSM models (the majority of which do not

involve the axion) that may result in such displaced vertices. The advantage of using displaced vertices as a way to search for these processes is that, with a few caveats, they are a telltale sign of new physics: the SM yields only a handful of long-lived particles whose mean lifetimes and masses are known to a very high degree of precision, so these will not directly serve as a background when looking for the long-lived particles with masses of hundreds of GeV that are predicted by the models targeted in this search. As we will discuss in Section 5.5, there are still sources of background owing to SM particles’ interactions with the material of the ATLAS detector itself, and effects stemming from the complexity of reconstructing events where tracks may intersect or overlap. Nonetheless, long-lived particle searches are still relatively background-free when compared with their prompt decay counterparts.

## 5.2 Signal Models

While an analysis is designed around a particular detector signature, it is typically motivated by one or more physics models – that is to say, there is a particular kind of new physics that we are searching for<sup>[2]</sup>, which we expect to yield the targeted detector signature. The way in which some hypothetical particle produces this signature – how it interacts with the detector – is estimated via simulation. This involves performing Monte Carlo (MC) simulations to simulate the high-energy processes arising from  $pp$  collisions and subsequent particle decays, as well as simulation of the resulting (meta)stable particles’ interactions with the detector material, and how these interactions produce signals<sup>[3]</sup>. The ATLAS experiment leverages a number of MC event generators – as will be noted below – while detector simulation is

---

2. One can in principle also perform a model-agnostic search, such as looking for “forbidden signatures”, by which we mean those we do not expect to see as a result of any SM process. Another type of a model-agnostic search is “anomaly detection”, which has become increasingly popular as a machine learning-driven technique, where a neural network is tasked with finding events that look “anomalous” with respect to some training set (which consists of either simulation, or actual data). For a review of anomaly detection methods, see Ref [144].

3. In particle physics jargon, the MC simulation step is often referred to as “event generation”, with the term “simulation” referring specifically to the detector interactions. For a review of MC methods in particle physics, see Ref. [145–147]. For a review of detector simulation, see Ref. [148].

primarily handled via the `GEANT4` toolkit [142]<sup>[4]</sup>. In this analysis, we have four different signal models, which correspond with different new physics scenarios (most of which explicitly involve SUSY). In the following subsections, we will review each of these signal models. Particular focus will be given to an axino model, which is an interpretation of this search corresponding with the SUSY and axion physics discussed in Section 3.2, as I participated in implementing the simulator of this model.

### 5.2.1 Gluino $R$ -hadrons

In this signal model, we consider gluino production in a split SUSY [154, 155] model<sup>[5]</sup>, where the gluino forms a long-lived  $R$ -hadrons, a bound state of the gluino together with SM quarks or gluons. The  $R$ -hadrons decay to light quarks, and (invisible)  $\tilde{\chi}_1^0$  neutralinos, where we assume equal branching ratios for decays to the light quarks  $\{u, d, c, s\}$ . This process is shown in Figure 5.1. For this search, we consider gluino masses and ( $R$ -hadron) lifetimes, and gluino-neutralino mass splittings as given by Table 5.1.

Parameter	Range
$m_{\tilde{g}}$	400 GeV–3 TeV
$\tau_{\tilde{g}}$	0.01 ns–30 ns
$\Delta m_{\tilde{g}, \tilde{\chi}_1^0}$	{10 GeV, 100 GeV}

Table 5.1: An overview of the gluino  $R$ -hadron signal model parameters, over which we scan. For the gluino-neutralino mass difference, only two values are used (as shown).

---

4. It is worth noting that `GEANT4` is very computationally expensive, especially for large detectors like ATLAS with complex geometries. There has been considerable effort within the ATLAS experiment to move towards faster alternatives for simulating particle interactions with the different subsystems, such as the `FastCaloSim` project [149, 150]. There is also ongoing development outside of the calibration, to leverage machine learning methods for both tracking and calorimetry simulations [151–153]. However, the “classic” full simulation was used for all the models employed in this analysis, as the newer tools do not support some of the features necessary for handling long-lived particle decays.

5. Split SUSY refers to a family models where the scalar sparticles are heavy – at the SUSY symmetry-breaking energy scale – while the fermionic sparticles are lighter, typically around  $\sim 1$  TeV.

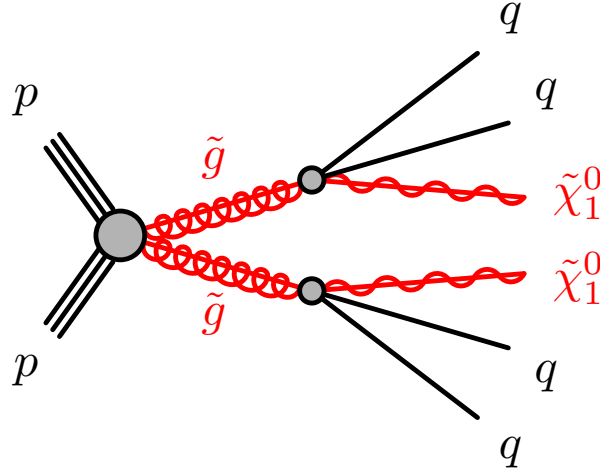


Figure 5.1: The “gluino  $R$ -hadron” process. Note that the hadronization of the gluino is not explicitly shown in the Feynman diagram, but is implied: the gluino decay vertices are displaced. Taken from Ref. [143].

### 5.2.2 Wino-Bino co-annihilation

In this signal model, we consider the co-annihilation of Wino- and Bino-like neutralinos [156, 157]<sup>[6]</sup>. Specifically, we consider neutralino-chargino production  $pp \rightarrow \tilde{\chi}_1^\pm \tilde{\chi}_2^0$ , where the  $\tilde{\chi}_1^\pm$  promptly decays to Bino-like  $\tilde{\chi}_1^0$  by off-shell  $W^\pm$  emission. The neutralino  $\tilde{\chi}_2^0$  is long-lived, and also decays to  $\tilde{\chi}_1^0$  via off-shell Higgs or  $Z$ -boson emission. We target the case where the Higgs boson decays to a bottom quark-antiquark pair<sup>[7]</sup>. A Feynman diagram of this process is shown in Figure 5.2. For this search, we consider Bino masses, Wino lifetimes and Wino-Bino mass splittings as given by Table 5.2.

6. As a reminder, by “Bino-like”, we refer to a neutralino that is mostly composed of a Bino.

7. We make the same choice for the axino model described below in Section 5.2.4. This is because the  $h \rightarrow b\bar{b}$  decay is the most probable Higgs decay, accounting for  $53 \pm 8\%$  of the Higgs decay branching [9]. Furthermore, the decay is one of those more easily identified, owing to the resulting  $B$ -mesons’ displacements (see Sections 2.1.2.4 and 4.2.1.4).

Parameter	Range
$m_{\tilde{W}}$	200 GeV–1.1 TeV
$\tau_{\tilde{W}}$	0.03 ns–3 ns
$\Delta m_{\tilde{W},\tilde{B}}$	20 GeV–50 GeV

Table 5.2: An overview of the Wino-Bino co-annihilation signal model parameters, over which we scan.

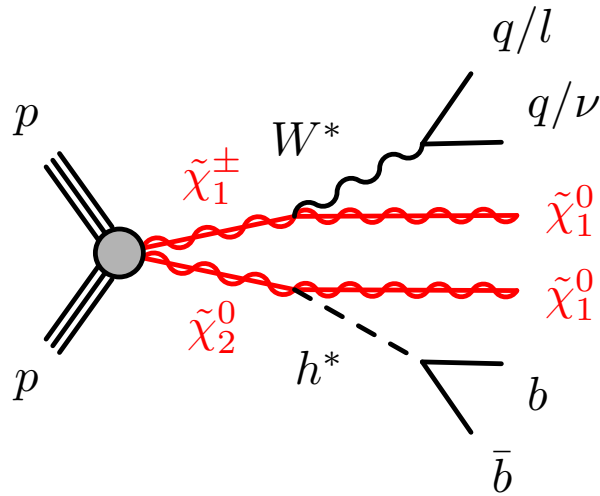


Figure 5.2: The “Wino-Bino co-annihilation ” process. Taken from Ref. [143].

### 5.2.3 Higgs Portal

In this signal model, we consider the decay of the Higgs boson to two heavy, long-lived scalars,  $h \rightarrow SS$ , each of which decays to bottom quarks<sup>[8]</sup>. Unlike the other models considered in this analysis, the Higgs Portal model is not strictly a SUSY model: one can more generally expect such decays in models with axions, or the Gelmini-Roncadelli model [159, 160] where the Higgs sector is expanded as a way of incorporating neutrino masses. An example Feynman diagram is provided in Figure 5.3, and the model parameters over which we search are provided in Table 5.3.

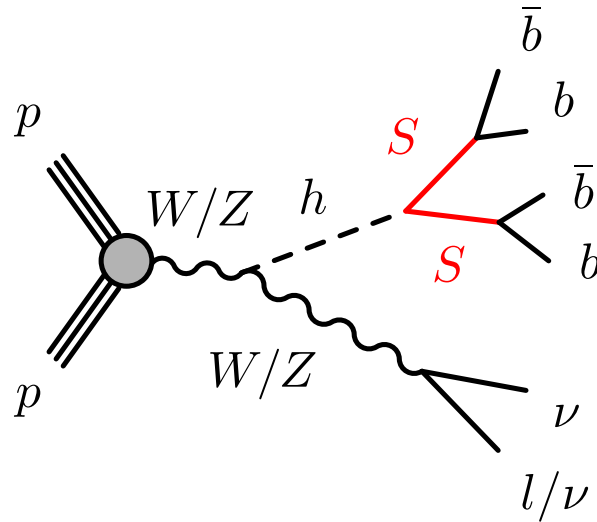


Figure 5.3: An example Higgs Portal process, where the Higgs boson is produced by gluon-gluon fusion. This analysis targets this Higgs production mechanism – production with an associated vector boson ( $VH$ ) – as well as production with associated top quarks ( $ttH$ ) and production via gluon-gluon fusion.

8. It is worth noting that this is not the first analysis of Run 2 data to search for a “Higgs Portal” model. This is a bit of an overloaded term, as some searches target models where the Higgs serves as a “portal” to stable dark matter, such as in Ref. [158] where the  $h \rightarrow \chi\chi$  process is targeted where  $\chi$  is a weakly-interacting massive particle (WIMP) and dark matter candidate. By contrast, this search targets a model where the Higgs decays to a pair of meta-stable scalars, each of which decays into a quark-antiquark pair.

Parameter	Range
$m_S$	5 GeV–55 GeV
$\tau_S$	0.0033 ns–3.3 ns

Table 5.3: An overview of the Higgs Portal signal model parameters, over which we scan.

### 5.2.4 Axinos

In this model, we consider the combination of Peccei-Quinn (Section 3.1) and MSSM (Section 2.3.1) models, as discussed in Section 3.2. We specifically consider the scenario where the neutralinos are Higgsino-like (and the charginos Wino- and Bino-like). We introduce a fifth neutralino  $\tilde{\chi}_5^0$ , which we take to be almost purely axino (with perturbative up- and down-type Higgsino contributions)<sup>[9]</sup>. Under this scenario, we consider the process of  $pp \rightarrow \tilde{\chi}_1^0 \tilde{\chi}_2^0$ , with subsequent  $\tilde{\chi}_2^0 \rightarrow Z^* \tilde{\chi}_1^0$  decay; here we assume the  $\tilde{\chi}_2^0$ - $\tilde{\chi}_1^0$  mass gap to be 2.5 GeV, so that the  $Z$ -boson is very off-shell, and its decay products will not be detectable as they will be very soft emissions<sup>[10]</sup>. We assume the neutralinos  $\tilde{\chi}_1^0$  and  $\tilde{\chi}_2^0$  to be Higgsino-like, and that they decay to a Higgs or  $Z$ -boson, together with an axino (which we assume to be the LSP). We focus on the  $h \rightarrow b\bar{b}$  and  $Z \rightarrow q\bar{q}$  decays for the two cases, respectively. Figure 5.4 shows an example Feynman diagram for this process. Table 5.4 provides an overview of the parameters we scan, and Figure 5.5 provides a visualization of the parameter grid.

---

9. Note that while it is conventional to number the neutralino states in order of increasing mass, we take  $\tilde{\chi}_5^0$  to be the lightest, to keep the meaning of  $\tilde{\chi}_1^0$  and  $\tilde{\chi}_2^0$  conceptually consistent with the other signal models under discussion.

10. The reason we consider this seemingly roundabout set of processes – production of  $\tilde{\chi}_2^0 \tilde{\chi}_1^0$  with prompt  $\tilde{\chi}_2^0 \rightarrow \tilde{\chi}_1^0$  decay, instead of  $\tilde{\chi}_1^0 \tilde{\chi}_1^0$  production – is because the former has a much larger cross-section. In fact, while we simulate neutralino production, we also implicitly include for the case of chargino production by using cross-sections computed by the CERN theory group, which cover combined Higgsino-like neutralino and chargino pair production processes [161, 162].

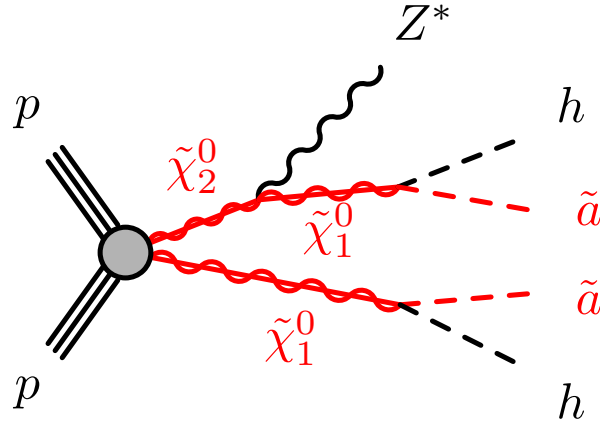


Figure 5.4: An example Feynman diagram of the axino process. The  $Z^*$  is very off-shell, and its decay products effectively invisible to the detector. Taken from Ref. [143].

Parameter	Range
$m_{\tilde{a}}$	0–500 GeV
$f_a$	$\{5 \times 10^9 \text{ GeV}, 5 \times 10^{10} \text{ GeV}\}$
$m_{\tilde{\chi}_1^0}$	200 GeV–1 TeV
$\tau_{\tilde{\chi}_1^0}$	0.0075 ns–3.5 ns

Table 5.4: An overview of the axino signal model parameters, over which we scan. The range in  $\tilde{\chi}_1^0$  lifetime  $\tau$  given here is derived using Eq. 3.9.

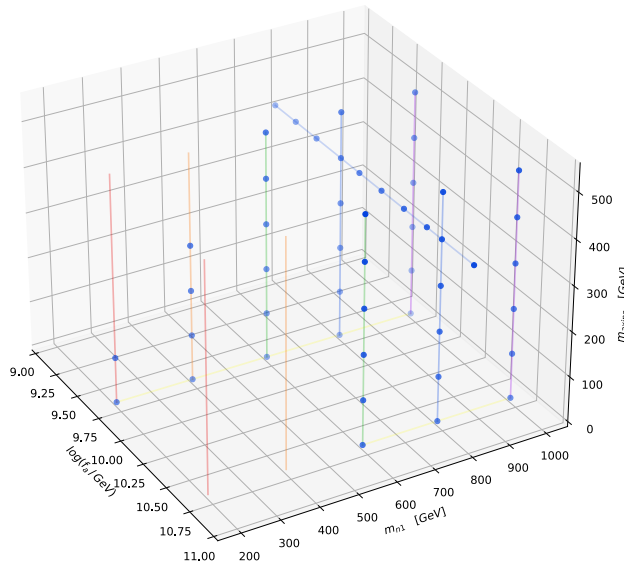


Figure 5.5: An overview of the parameter grid used to scan the axino model. Here,  $m_{n,1}$  refers to the  $\tilde{\chi}_1^0$  mass, and  $m_{\text{axino}}$  to the  $\tilde{\chi}_5^0$  mass (which is the same as the pure axino mass).

### 5.2.4.1 Producing a Monte Carlo sample: from theory to code

This analysis represents a milestone in the search for axino at ATLAS. It is *not* the first new physics search to feature an axino interpretation, as analyses such as Ref. [163] have probed (prompt) axino production. However, this is the first analysis to search for displaced axino production – and to use an explicit simulation of axino production processes. This was achieved via close collaboration with phenomenologist colleagues at the University of Chicago<sup>[11]</sup>, whereby an DFSZ axino model Lagrangian was formulated and corresponding model files produced via **SARAH** [164, 165] for use with the **MADGRAPH** [166] MC event generator<sup>[12]</sup>. The resulting model – after multiple iterations of testing and validation to ensure that truth-level kinematic distributions from MC generation matched expectations, and that it would properly interface with **GEANT4** – was merged into the centralized physics model repository for the ATLAS collaboration, allowing for future use in other analyses as well as better software preservation. It was then used in centralized ATLAS MC event generation and simulation, with the resulting samples used in this analysis.

## 5.3 Event Reconstruction

With the target models and processes defined, we need to determine how exactly we will reconstruct objects from the Run 2 data. In other words, how will we (for example) identify a  $b$ -quark in the data? How precisely will we reconstruct  $\cancel{E}_T$ ? Fortunately these are not entirely open-ended questions; ATLAS has a range of standardized algorithms for reconstructing “physics objects”<sup>[13]</sup>, from which we may choose. We will, however, introduce a new secondary

---

11. In particular, I would like to give special thanks to Gabe Hoshino and Keisuke Harigaya for their significant contributions to this work.

12. This is, to the best of my knowledge, the first example of a fully-fledged axino model implementation in MC generator software to be used in an experiment – though this requires special mention of an earlier study in Ref. [167, 168] that focused on the collider phenomenology of KSVZ  $\tilde{a}\tilde{g}g$  couplings.

13. These algorithms are developed and/or evaluated within the ATLAS collaboration by “combined performance” groups.

vertexing algorithm for this analysis, which will be useful for constructing displaced particle production vertices where the particles produced are themselves long-lived. In the following subsections, we will review how we reconstruct different objects – from low-level tracks and vertices to particle candidates.

Note that some of the details (especially regarding the particle candidate reconstruction in Section 5.3.2) are a little technical; they are included for completeness – and to emphasize that event reconstruction is complex – but are not all crucial to understanding the event selection or background estimate methods discussed in later sections. Nonetheless, in this and subsequent sections (along with the associated appendices), we will risk being verbose in outlining how objects are constructed and selected for the sake of precision. In particular, tables of object selection criteria will not only list the criteria but explicitly state how they are combined to define a selection: while this is straightforward in most cases, there are a few selections with somewhat complex Boolean logic<sup>[14]</sup>.

### 5.3.1 Inner Detector Reconstruction

As a search leveraging displaced vertices, the reconstruction of tracks and vertices in the ATLAS Inner Detector is crucial to this analysis. These objects’ reconstruction is relatively complex, as constructing a track requires relating a sequence of “hits” in the inner detector and typically in a very dense environment. For an abridged discussion of tracking, see Appendix A.1.

#### 5.3.1.1 Large-Radius Tracking

The standard ATLAS tracking algorithm places relatively stringent cuts on the track impact parameters  $d_0$  and  $z_0$ , which are generally useful for rejecting fake tracks that may have

---

<sup>14</sup>. For Boolean logic, we will be using the standard notation:  $A \wedge B = A \text{ and } B$ ,  $A \vee B = A \text{ or } B$ ,  $\bar{A} = \text{not } A$ .

been produced by incorrectly linking together hits. However, searching for displaced vertices may require identifying tracks with much larger impact parameters – namely those that originate from the displaced vertices. To this end, we additionally employ the *large-radius tracking* (LRT) algorithm [169], so that we have both standard and LRT tracks from which displaced vertices may be reconstructed. The differences between LRT and standard tracking are outlined in Table 5.5. For a discussion of tracking efficiency, see Appendix A.3.

Cut type	Cut description	Standard tracking	Large radius tracking
Forward tracking	Min. $p_T$	500 MeV	900 MeV
	Max. $ \eta $	2.7	5.0
	Max. $d_0$	10 mm	300 mm
	max. $z_0$	250 mm	1500 mm
Clustering	Min. Si hits, not shared	6	5
	Max. hits, shared	1	2
Back-tracking	Min. $p_T$	1000 MeV	-
	Max. $d_0$	100 mm	-

Table 5.5: A comparison of standard and large radius tracking parameters. Note in particular the much looser maximum  $d_0$  and  $z_0$  cuts among the “forward tracking” cuts. Taken from Ref. [143].

### 5.3.1.2 VSI Vertexing

As one of our secondary vertexing algorithms, we employ the standard `VrtSecInclusive` (VSI) algorithm [170, 171], which constructs point-like vertices. We shall refer to these simply as “VSI vertices”. For full details of the algorithm, see Ref. [170]. Here, we will provide a general outline<sup>[15]</sup>.

1. Tracks that are identified as *selected tracks* – if they pass the cuts outline in Table 5.6 –

---

<sup>15</sup> It is worth noting that the VSI algorithm is quite complex, and is very configurable. Its different configuration options are explained in detail in Ref. [170], and the parameter choices used for this analysis preserved in the ATLAS analysis code-base and specified by a file in Ref. [172]. Unfortunately Ref. [170] is a document internal to the ATLAS collaboration, and thus not necessarily accessible by all readers. However, many of the details it discusses are beyond the scope of our discussion here – we will cover a few only to understand that the algorithm performs a few steps to construct and refine its output vertices.

are merged into 2-track seed vertices, if each track satisfies  $|d_0| > 2$  mm. These 2-track seed vertices are required to satisfy  $\chi^2/N_{\text{DoF}} < 5$ .

2. The 2-track seeds are iteratively merged to form  $n$ -track vertices. This is done by determining which sets of seeds are incompatible, which means that merging them would create a vertex with too low quality.
3. As the seeds may be shared among multiple  $n$ -track vertices after merging, any ambiguity is resolved by detaching any shared tracks from vertices where they are worse-associated – those with fits with a  $\chi^2$  to which they contribute more<sup>[16]</sup>), or merging two vertices if they share at least 2 tracks or are within 1 mm of one another.
4. Once the seeds are no longer shared between vertices, additional lower-quality *associated tracks* – those passing the criteria in Table 5.7, looser than for the selected tracks – are attached to the vertices.
5. The vertex mass is nominally calculated by associating the charged pion mass  $m_{\pi^\pm}$  with each track<sup>[17]</sup>, and computing the tracks’ 4-momentum sum.

For a discussion of vertexing efficiency, see Appendix A.3.

---

16. As a reminder, we generally define the goodness-of-fit parameter  $\chi^2$  by the formula  $\chi^2 = \sum_i (O_i - E_i)^2 / E_i$ , where  $\{O_i\}$  are the observed values and  $\{E_i\}$  are the expected values. For fitting tracks, this corresponds with the observed tracker hits versus the positions in the tracker where the fitted track passes through – so each track has an associated  $\chi^2$ . Similarly, we can determine the goodness-of-fit of a vertex by the impact parameters of its tracks with respect to itself, or in other words how close each track is to the vertex. We can also then determine how much each track contributes to the vertex’s goodness-of-fit.

17. Recall that a track gives us a measurement of the momentum magnitude versus mass ratio  $p/m$ , as well as the momentum direction. It is only by assuming some mass (or deducing it separately) that we can reconstruct a full 4-momentum. Assigning  $m_{\pi^\pm}$  is a standard choice, as the jets produced in  $pp$  collisions will yield significant numbers of charged pions. Another common choice is to assume the tracks to be massless – while the particles that produced them are certainly not massless, this can be thought of as a “small-mass approximation” and is in practice not very different than assigning the relatively small  $m_{\pi^\pm} \approx 140$  MeV [9] when considering tracks with momenta on the order of GeV.

VSI Track Selection	
Index	Criterion
<i>A</i>	$p_T > 1 \text{ GeV}$
<i>B</i>	Not associated with any primary or pileup vertices
<i>C</i>	$N_{\text{SCT}} \geq 6$ if $N_{\text{Pix}} = 0$
<i>D</i>	$N_{\text{TRT}} \geq 7$ if $N_{\text{Pix}} < 2$
<i>E</i>	$N_{\text{SCT}} \geq 7$ if $p_T > 25 \text{ GeV}$
<i>F</i>	$N_{\text{TRT}} \geq 20$ if $((p_T < 25 \text{ GeV}) \wedge ( \eta  < 1.7))$
Selection = $A \wedge B \wedge C \wedge D \wedge E \wedge F$	

Table 5.6: Criteria for defining selected tracks for the VSI secondary vertexing algorithm. Taken from Ref. [143].

VSI Track Association	
Index	Criterion
<i>A</i>	$p_T > 1 \text{ GeV}$
<i>B</i>	$\chi^2/N_{\text{dof}} < 20$
<i>C</i>	Not associated with any secondary vertex
<i>D</i>	Require hit in adjacent outer tracker layer
<i>E</i>	$\text{sig}(\Delta d_0(\text{track}, \text{vertex})) < 5$
<i>F</i>	$\text{sig}(\Delta z_0(\text{track}, \text{vertex})) < 5$
Association = $A \wedge B \wedge C \wedge D \wedge E \wedge F$	

Table 5.7: Criteria for defining associated tracks for the VSI secondary vertexing algorithm. Here,  $\text{sig}(x) = x/\sigma_x$  is a measure of the significance of a quantity  $x$  with respect to its resolution  $\sigma_x$ .

### 5.3.1.3 Fuzzy vertexing

The VSI secondary vertices are effective in reconstructing displayed decays that produce short-lived particles. However, its efficiency may suffer when attempting to reconstruct displayed decays that produce (somewhat) long-lived particles, such as  $B$ -mesons – which is precisely the scenario considered in the Higgs portal model (Section 5.2.3), and one of the decay channels in the axino model (Section 5.2.4). Thus, we employ an alternative secondary vertexing algorithm, known as *fuzzy vertexing*, that constructs finite-volume “vertices” that may capture displaced decay products. We shall refer to these as “fuzzy vertices” (FVs). Importantly (and as discussed further below in Section 5.4), we do not mix our two secondary vertex algorithms: for a given event we construct both VSI and fuzzy vertices, but we shall not handle the two sets of vertices simultaneously when computing features of the event and determining whether or not it may represent a signal process<sup>[18]</sup>. The algorithm, described in Ref. [143], works as follows.

1. Tracks that are identified as *selected tracks* if they pass the selections in Table 5.8. This is similar to the VSI algorithm.
2. Before being merged into 2-track seeds, each pair of selected tracks is ranked by three boosted decision trees (BDTs)<sup>[19]</sup>, to determine how signal-like they are. Each BDT is trained on a combination of MC simulation and data, the former corresponding with a simulated Wino-Bino process (Section 5.2.2) with each using a sample with a different mean  $\tilde{\chi}_2^0$  lifetime. Table 5.9 provides an overview of the training data, Table 5.10

---

18. Of course, one could consider trying to reconstruct both types of DVs in the same event. However, this could lead to some ambiguities – as each vertexing algorithm is unaware of the other one – and so would require some additional tweaks in terms of reconstruction or event selection. For the purposes of this analysis, we find event selections defined only in terms of one vertexing algorithm or the other to be sufficient.

19. BDTs are machine learning algorithms, that produce a classification score (typically represented as some number between 0 and 1) based on a set of inputs. They consist of decision trees that are iteratively trained, with some “boosting” algorithm that re-weights events from one training iteration to the next. For a review of BDTs, see Ref. [173] for a general overview, and Ref. [174] for a review of their use in particle physics.

provides the variables used as BDT inputs, and Figure 5.6 shows the distribution of BDT scores for the samples upon which the BDTs were trained. All track pairs with one BDT output score greater than  $-0.05$  are considered for 2-track seed forming. The seed forming algorithm is identical to that in the VSI algorithm.

3. The 2-track seeds with BDT scores  $s_{\text{middle}} > 0.15$  or  $s_{\text{long}} > 0.15$  are identified as *primary seeds*. Seeds around the primary seed are merged into *seed groups*, if they meet the criteria in Table 5.11.
4. Seed groups are merged iteratively, until no seed groups sharing seeds are left. The resulting vertices are the FVs. Figure 5.7 shows an outline of this process.

As can be seen from the merging criteria in Table 5.11, the FVs have sizes on the order of a few millimeters across. For a discussion of vertexing efficiency, see Appendix A.3.

FV Track Selection	
Index	Criterion
$A$	$p_T > 1 \text{ GeV}$
$B$	Not associated with any primary or pileup vertices
$C$	$N_{\text{Si}} \geq 2$
Selection = $A \wedge B \wedge C$	

Table 5.8: Criteria for defining selected tracks for the fuzzy secondary vertexing algorithm. Here,  $N_{\text{Si}}$  refers to the number of silicon hits – which includes the Pixel and SCT detectors. Taken from Ref. [143].

### 5.3.2 High-Level Object Reconstruction

Together with our “low-level” inner detector objects reconstructed – tracks and secondary vertices – we can also reconstruct particle candidates, jets, and missing energy  $\cancel{E}_T$ . These objects will make use of measurements from all of the detector systems, as combining signals

Process	Category	$\tilde{\chi}_2^0$ mass [GeV]	$\tilde{\chi}_2^0$ lifetime [ns]	$\Delta m (\tilde{\chi}_1^0, \tilde{\chi}_2^0)$ [GeV]
MC, $pp \rightarrow \tilde{\chi}_2^0 \tilde{\chi}_1^\pm$ ,	Signal (long)	300-500	1	30
$\tilde{\chi}_2^0 \rightarrow \tilde{\chi}_1^0 h^*$ ,	Signal (middle)		0.1	
$h^* \rightarrow b\bar{b}$	Signal (short)		0.01	
Data, Run 364292	Background	-	-	-

Table 5.9: An overview of the samples used to train the 3 BDTs used in the fuzzy vertexing algorithm. Each BDT is trained with one of the three signal processes, targeting different lifetimes. Taken from Ref. [143].

Variables	Note
$\eta^1, \eta^2$	-
$d_0^1, d_0^2$	-
$\text{sig}(d_0^1), \text{sig}(d_0^2)$	$\text{sig}(d_0) = d_0/\sigma_{d_0}$ : $d_0$ significance
$z_0^1, z_0^2$	-
$z_0^1 - z_{\text{PV}}, z_0^2 - z_{\text{PV}}$	$z_{\text{PV}}$ : position of the hard-scatter PV
$\text{sig}(z_0^1), \text{sig}(z_0^2)$	$\text{sig}(z_0)$ : $z_0$ significance
innermost hit category of track #1, #2	0:IBL, 1:B-Layer, 2:{Layer-1,Layer-2}, 3:SCT
$\Delta\eta$ between track #1 and #2	-
$\Delta\phi$ between track #1 and #2	-
$(p_T^1 - p_T^2) / (p_T^1 + p_T^2)$	-
difference of the innermost hit category	-

Table 5.10: An overview of the input variables for the BDTs used in the fuzzy vertexing algorithm. Here,  $\text{sig}(x) = x/\sigma_x$  is a measure of the significance of a quantity  $x$  with respect to its resolution  $\sigma_x$ . One may notice a certain level of redundancy in the input variables – namely the use of  $\Delta\eta$  and the difference in innermost hit category, which will correlate with the individual  $\eta$  and hit category inputs. In practice, including these additional variables allows constructing a decision tree with additional granularity with respect to these properties, within a single “cycle” of the full list of input variables. Taken from Ref. [143].

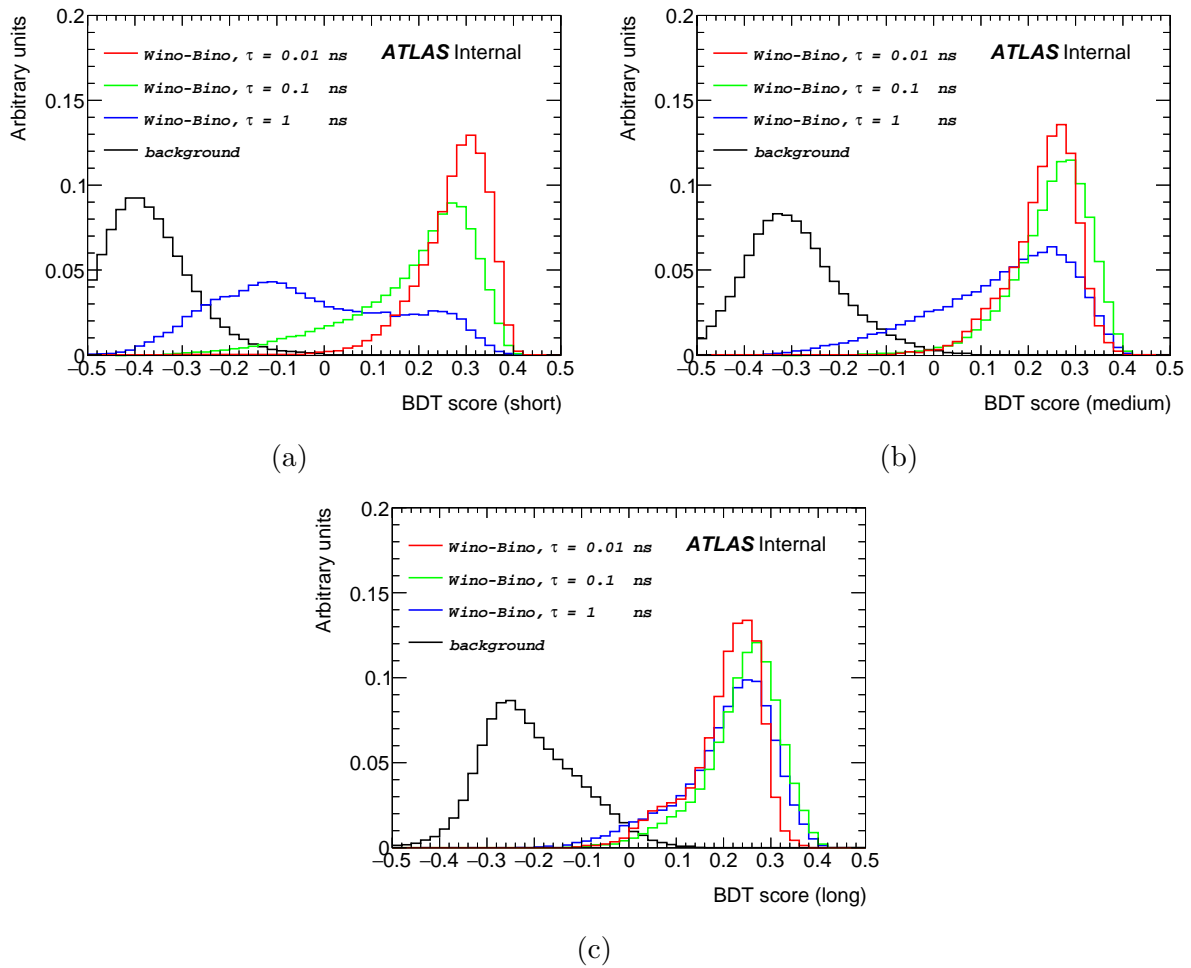


Figure 5.6: BDT scores for the 3 BDTs used by the fuzzy vertexing algorithm. Adapted from Ref. [143].

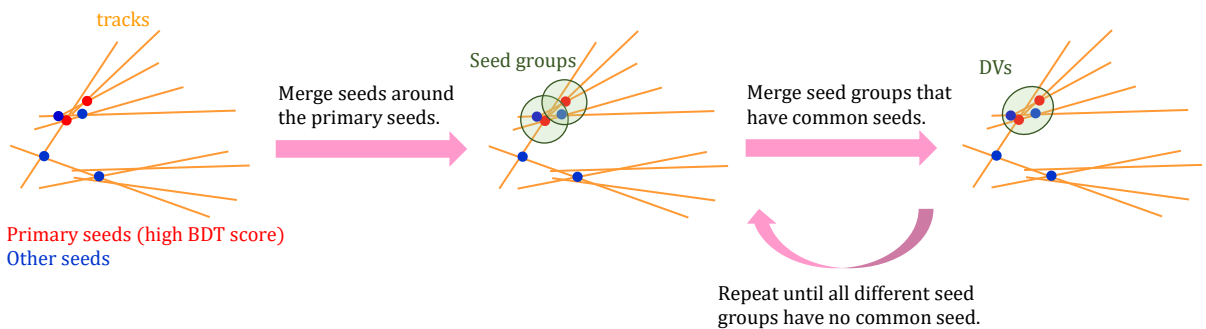


Figure 5.7: An overview of the production of seed collections and final vertex merging, in the fuzzy vertexing algorithm. Taken from Ref. [143].

FV Seed Merging	
Index	Criterion
$A$	$\{x, y, z\} < \begin{cases} 1 \text{ mm} & r_{\text{seed}} < 23.5 \text{ mm} \\ 3 \text{ mm} & 23.5 \text{ mm} \leq r_{\text{seed}} < 33.5 \text{ mm} \\ 5 \text{ mm} & 33.5 \text{ mm} \leq r_{\text{seed}} \end{cases}$
$B$	$\sum p_T^{\text{primary}} + \sum p_T^{\text{sub}} < 3 \times (\phi_{\text{max}} - \frac{\pi}{2} + 4)$
Merge = $A \wedge B$	

Table 5.11: Criteria for merging 2-track seeds into primary seeds in the fuzzy vertexing algorithm. Criterion  $A$  is applied separately to the  $x$ -,  $y$ - and  $z$ -components of the 2-track seeds. In criterion  $B$ ,  $\sum p_T^{\text{sub}}$  refers to the sum of the  $p_T$  of the two tracks associated with the seed being merged, and  $\phi_{\text{max}}$  is the maximum azimuthal angle between the tracks in the primary seed, and the tracks in the substitute seed. The last criteria is found to prevent the merging of large numbers of background seeds, particularly inside the beam-pipe region. Taken from Ref. [143].

from them help us identify what type of particle may have produced a particular set of signals via interaction with these different systems. In the following subsections, we will review the different objects we reconstruct. This is followed by *overlap removal*, the process of removing particle candidates of one kind that overlap with those of another, which is described in Appendix A.2.

### 5.3.2.1 Lepton and Photon Reconstruction

We reconstruct electrons and muons are part of the  $\cancel{E}_T$  calculation, as well as to perform overlap removal. We do not reconstruct hadronically-decaying tau leptons<sup>[20]</sup>. Tables 5.12 and 5.13 provide an overview of the parameters for electron and muon candidate reconstruction.

We also reconstruct photons as part of the  $\cancel{E}_T$  calculation and overlap removal, with

20. The leptonically-decaying tau leptons will produce electrons and muons (that we do reconstruct).

21. In general, “looser” and “tighter” particle ID working points refer to sets of cuts that particle candidates must pass: the tighter the cuts, the more stringent they are and the more likely the candidates are to be true particles (at the possible cost of reconstruction efficiency). The details of electron ID tagging for the ATLAS experiment in Run 2, and the various working points, are explained in Ref. [176], and this working point’s configuration in the ATLAS reconstruction software is specified in Ref. [177].

Baseline Electron Selection	
Index	Criterion
$A$	$p_T > 10 \text{ GeV}$
$B$	$ \eta  < 2.47$
$C$	Passing the <code>LooseAndBLayerLLH</code> electron ID working point <sup>[21]</sup>
Selection = $A \wedge B \wedge C$	

Table 5.12: An overview of electron candidate requirements. Note that this excludes any veto on the  $|\eta| \in [1.37, 1.52]$  “crack region”, a section of the calorimeter with 5-10 $X_0$  (radiation lengths) of material before the first calorimeter layer [175] which is thus often vetoed in electron identification. Taken from Ref. [143].

Baseline Muon Selection	
Index	Criterion
$A$	$p_T > 10 \text{ GeV}$
$B$	$ \eta  < 2.7$
$C$	Passing the Medium muon ID working point [178]
Selection = $A \wedge B \wedge C$	

Table 5.13: An overview of muon candidate requirements. Note that there is no track-to-vertex association requirement. Taken from Ref. [143].

baseline criteria given by Table 5.14. In addition, photons with  $p_T > 60 \text{ GeV}$  are used to veto DVs satisfying  $\Delta R(\text{DV}, \gamma) < 0.1$ .

Baseline Photon Selection	
Index	Criterion
$A$	$p_T > 25 \text{ GeV}$
$B$	$ \eta  < 2.37$
$C$	Passing the Tight photon ID working point [179]
Selection = $A \wedge B \wedge C$	

Table 5.14: An overview of photon candidate requirements. Taken from Ref. [143].

### 5.3.2.2 Jet Reconstruction

For this search we reconstruct jets, for use in the  $\cancel{E}_T$  calculation and background estimate, as well as overlap removal. Known as “EMTopo ” jets, they are reconstructed using the anti- $k_t$  algorithm [180] with a jet radius of  $R = 0.4$ , produced from calorimeter topoclusters [137] at the EM energy scale<sup>[22]</sup>. The selection requirements for these jets are outlined in Table 5.15, including working points for the “Jet Vertex Tagger” (JVT), a discriminant based on observables  $R_{p_T}$  and corrJVF [181], given by

$$R_{p_T} = \sum_k p_T^{\text{trk}_k}(\text{PV}_0) / p_T^{\text{jet}}, \quad (5.1)$$

$$\text{corrJVF} = \frac{\sum_k p_T^{\text{trk}_k}(\text{PV}_0)}{\sum_l p_T^{\text{trk}_l}(\text{PV}_0) + \sum_{n \geq 1} \sum_l p_T^{\text{trk}_l}(\text{PV}_n) / \left(k n_{\text{trk}}^{\text{PU}}\right)}, \quad (5.2)$$

---

22. The “EM scale” refers to energy as measured assuming electromagnetic interactions. Electromagnetic and hadronic showers have different energy responses in calorimeters, necessitating calibration. For details, see Section 4.2.8.3 for a discussion of neural network-based calibrations, and Appendix E.2 for a general discussion of measuring hadronic showers.

- $\sum_k p_T^{\text{trk}_k}(\text{PV}_j)$  is the (scalar)  $p_T$  sum of tracks associated with vertex  $j$ ,
- $\text{PV}_0$  is the primary vertex,
- $k = 0.01$ ,
- $n_{\text{trk}}^{\text{PU}}$  is the number of pileup tracks in the event.

which is used to estimate how likely a jet is to be associated with the primary vertex (versus being a pileup jet). We also employ the “forward JVT” (fJVT), a variant of this tagger specialized for jets in the  $|\eta| > 2.5$  region [182, 183].

Baseline EMTopo Jet Selection	
Index	Criterion
$A$	$p_T > 20 \text{ GeV}$
$B$	$ \eta  < 4.5$
$C$	JVT $< 0.64$ (Medium working point)
$D$	fJVT $< 0.4$ (Tight working point)
Selection = $A \wedge B \wedge C \wedge D$	

Table 5.15: An overview of anti- $k_t$ ,  $R = 0.4$  EMTopo jet candidate requirements. For the (f)JVT working point definitions, see Ref. [184]. Taken from Ref. [143].

We perform *b-tagging* on the EMTopo jets to gauge the likelihood of them being initiated by *b*-quarks<sup>[23]</sup>. This is done using the DL1 tagger, a deep neural network<sup>[24]</sup> that classifies jets as being initiated by *b*-quarks, *c*-quarks, or light quarks and gluons [185]. As inputs, DL1 uses jet kinematics ( $p_T, |\eta|$ ) as well as the outputs of lower-level taggers, including impact parameters taggers and algorithms which identify possibly secondary vertices associated with the jet. To be considered *b*-jet candidates, EMTopo jets must have  $p_T > 10 \text{ GeV}$ , and have a DL1 output score above its 77% tagging efficiency working point.

23. Although *b*-quark decays feature in a number of our signal models, we do not use this *b*-tagging information for any of our event selections (Section 5.4), but it is employed in the background estimation (Section 5.5).

24. DL1 is one of numerous examples of neural networks being utilized in the ATLAS experiment for reconstruction tasks, especially classification problems such as jet flavour-tagging. While well-performing, its fundamental architecture is not particularly specialized, consisting of fully-connected and “maxout” layers [185]. See Chapter 6 for a discussion of neural network architectures specialized for particle physics.

### 5.3.2.3 Missing Transverse Energy Reconstruction

Having briefly reviewed our reconstruction criteria for leptons, photons and jets, we can now turn our attention to the missing transverse energy  $\cancel{E}_T$ . As discussed in Section 4.2.1.6,  $\cancel{E}_T$  is defined as the negative vector sum of the  $p_T$  of all the particles reconstructed in an event – and thus in some way depends on how exactly those particles are reconstructed. Its components are given by

$$\cancel{E}_{x(y)} = \cancel{E}_{x(y)}^e + \cancel{E}_{x(y)}^\mu + \cancel{E}_{x(y)}^\tau + \cancel{E}_{x(y)}^\gamma + \cancel{E}_{x(y)}^{\text{jets}} + \cancel{E}_{x(y)}^{\text{soft}}, \quad (5.3)$$

- $\cancel{E}_{x(y)}^a$  is the  $x$ - or  $y$ -component of the  $\cancel{E}_T$  associated with particle/object species  $a$ ,

where  $\cancel{E}_{x(y)}^{\text{soft}}$  refers to the  $\cancel{E}_T$  components associated with *soft* energy depositions that are not explicitly a part of any of our particle candidates. An important subtlety of the  $\cancel{E}_T$  definition is that its different components – or rather the sets of reconstructed particle candidates with which they correspond – do not necessarily have to match the reconstructed particle candidates used elsewhere in the analysis: for example, we may reconstruct the reference electrons used for the  $\cancel{E}_T$  calculation differently than the electron candidates described in Section 5.3.2.1. Such is the case in this analysis, and in fact we reconstruct  $\cancel{E}_T$  in multiple distinct ways in this search. The first, which we shall refer to simply as  $\cancel{E}_T$ , is computed the “standard” way following ATLAS combined performance recommendations, where the  $\cancel{E}_T^{\text{soft}}$  term is computed using tracks. The second,  $\cancel{E}_T^{\text{LHT}}$ , is computed using topo-clusters with local weights<sup>[25]</sup>. In addition to these two *offline*  $\cancel{E}_T$  definitions, we will also impose a  $\cancel{E}_T$ -based trigger requirement on events, which involves reconstructing the *online*  $\cancel{E}_T$ . As discussed in Section 4.2.6, the TDAQ system performs online reconstruction under stringent timing constraints, and also performs this reconstruction using a limited amount of detector input. The online  $\cancel{E}_T$  is reconstructed without muon spectrometer input, and thus can be

---

25. This is the *local cell weighting* method discussed in Ref. [137, 140].

potentially offset by muons the event.

## 5.4 Event Selection, Region Definitions and Expected Yields

Having identified the reconstructed objects in our data – DVs, particle candidates, jets and  $\cancel{E}_T$  – we can now describe a physics event in terms of a collection of these objects. As our goal in this analysis is to search for the processes described in Section 5.2, we can attempt to identify signal events by studying the event kinematics – the multiplicity, positions and momenta of the events’ constituent objects. In the following subsections, we will review how events are identified as signal-like or not – and in a few different ways, which are tailored to the different signal models described in Section 5.2<sup>[26]</sup>. First, however, we will review the basic concepts of how we define event regions, and how data is handled during the analysis development process to avoid biasing the development process.

### 5.4.1 Defining event regions, and blinding

In particle physics analyses, we often speak about “regions” of our data, which are regions of the event phase space defined by some set of kinematic selections<sup>[27]</sup>. For example, we might define a particular region as events that have a certain number of jets, which have transverse momenta above some threshold. In a new physics search such as this analysis, we define one or more *signal regions* (SRs) where we expect to see an appreciable number of signal events, based on our study of the signal process kinematics in our MC simulations. We can similarly define regions where we do not expect to see signal events, which we can use to develop and validate a *background estimate* whereby we estimate the number of background events in a particular region. We ultimately extend this background estimate to the signal region, to

---

26. This section – like the preceding one – is a little technical, and it may be easy to get lost in some of the details. While at least a quick review of this section is helpful to understanding the following discussions of background estimation, it may also be useful to use simply as a reference when reading the following sections.

27. We sometimes colloquially refer to these selections as “cuts”.

determine how many events we expect that region to contain due to background processes: when we count the number of events in the signal region, based on the background estimate and a given signal model, we can assess the statistical significance of any excess as evidence of the model's existence (or a statistical limit on the model's existence).

Tightly interlinked with the above discussion is the concept of *blinding*, which is the process whereby certain regions of the data are not observed until the analysis method (in particular the background estimate) is fully complete<sup>[28]</sup>. This process is done to limit the effects of the experimenter's possible prior bias (in favor or against the existence of a particular model), and the possibility of introducing (unintentional) statistical biases through phenomena such as *p*-hacking [187]. We typically blind the signal region, as well as some regions where we expect only background (or, in practice, minimal signal contamination), which we refer to as *validation regions* (VRs). We develop our background estimate using non-blinded regions referred to as *control regions* (CRs). We may then gradually unblind the VRs to check the validity of the background estimate there – and by defining multiple VRs, we provide ourselves multiple independent tests of the background estimate (allowing for modification or refinement of the method along the way). Once the background estimation is finalized, the signal region can be unblinded and the final results can be determined. Importantly, the background estimate methods and region definitions should not be changed after unblinding: once the proverbial box is opened, it cannot be closed.

To summarize, the regions in an analysis will typically consist of:

- Signal regions, where we expect to see signal events (based on MC), and which are blinded,
- Validation regions, where we do not expect to see signal events, and which are initially blinded,

---

28. For a review of blinding analyses in high-energy and nuclear physics, see Ref. [186].

- Control regions, where we do not expect to see signal events, and which are not blinded.

It is important to note that blinding is only performed with respect to actual data: we do not blind the MC simulations, which are used to determine the amount of signal in each region (and which inform some elements of the background modeling strategy). This also means that MC simulations can generally be used as an extra guide during analysis development, at least to the extent that we trust their outputs.

#### 5.4.2 Common signal region definitions: the MTR

This search features 3 different SRs, which are differentiated by the number and types of DVs on which they impose requirements, and each of which has an associated set of VRs (imposing similar DV requirements). These different SRs are not all explicitly orthogonal to one another, so that an event can potentially fall into more than one of them. Specifically, the non-orthogonality exists between SRs that use different vertexing algorithms. To avoid complicating the statistical interpretation of results, we only use one vertexing algorithm per signal model – that corresponding to the SRs which provide the most statistically significant event yield<sup>[29]</sup>. We will, somewhat colloquially, refer to the three different sets of SRs and VRs as three different *analysis channels*.

Before describing each of the analysis channels, we will review some selections that are common to all of them. These are summarized in Tables 5.16 and 5.17. The former, our *event cleaning*, consists of selections that remove events where measurements may be distorted by unwanted beam or detector effects. The latter – which includes these cleanings – defines a region consisting of events that pass some minimum  $\cancel{E}_T$  thresholds (at both offline and trigger levels), which we refer to as the  $\cancel{E}_T$ -triggered region (MTR).

We also define the photon-triggered region (PTR) as events that are not in the MTR and that pass a photon trigger, as in Table 5.18, which is used to define our VRs. In the

---

29. In some sense, one can think of this analysis as two or three parallel (but highly-related) analyses.

Event Cleaning			
Index	Criterion	Short Description	Reference
<i>A</i>	General Event Cleaning	Reject corrupted/bad events	Section 5.4.2.1
<i>B</i>	Good Runs List	Reject low-quality events	Section 5.4.2.2
<i>C</i>	Primary vertex	Require 1 PV with ( $N_{\text{tracks}} \geq 2$ ) $\wedge$ ( $ z_{\text{PV}}  < 200$ mm)	-
<i>D</i>	Non-collision background veto	Reject beam-halo distortions of $\cancel{E}_T$	Section 5.4.2.3
<i>E</i>	Dead tile module veto	Reject dead TileCal module distortions of $\cancel{E}_T$	Section 5.4.2.4
Selection = $A \wedge B \wedge C \wedge D \wedge E$			

Table 5.16: An overview of the event-level selections that define our event cleaning. Taken from Ref. [143].

MTR Selection			
Index	Criterion	Short Description	Reference
<i>A</i>	Event cleaning	Pass event cleaning selections	Table 5.16
<i>B</i>	$\cancel{E}_T$ trigger	Minimum online $\cancel{E}_T$ threshold	Appendix A.4
<i>C</i>	Offline $\cancel{E}_T$	$(\cancel{E}_T^{\text{LHT}} > 180 \text{ GeV}) \wedge (\cancel{E}_T > 150 \text{ GeV})$	-
Selection = $A \wedge B \wedge C$			

Table 5.17: An overview of the event-level selections that define the MTR. This is common to all SRs. Taken from Ref. [143].

following subsections, we will expand on the definitions of the selections that define the event cleanings and the MTR.

PTR Selection			
Index	Criterion	Short Description	Reference
$A$	Event cleaning	Pass event cleaning selections	Table 5.16
$B$	$\notin$ MTR	Fail MTR selection	Table 5.17
$C$	Photon trigger	Require at least one photon at HLT, with $p_T > 140$ GeV	-
Selection = $A \wedge B \wedge C$			

Table 5.18: Selections that define the photon-triggered region (PTR). HLT refers to the High-Level Trigger (Section 4.2.6.2). Taken from Ref. [143].

#### 5.4.2.1 General Event Cleaning

Our general event cleaning selection removes events where data may have been corrupted, or the event reconstruction may have been affected by the restart of a detector subsystem. Specifically, we remove events with

- Noise bursts or data corruption from the LAr and Tile calorimeters,
- Effects from non-operational cells in the Tile and Hadronic End Cap calorimeters,
- Effects from the recovery procedure for single event upsets in the SCT – which are effects of particle interactions with the SCT readout electronics itself [188].

#### 5.4.2.2 Good Runs List (GRL)

The GRL is a list of all luminosity blocks – sets of collisions approximately spanning approximately 1 min – where all the data quality flags indicate optimal operation of the detector. This ensures that the data was properly and fully recorded [189], as any malfunction

in a detector system could lead to missing or incorrectly-reconstructed particle candidates in the data.

### 5.4.2.3 Non-collision background (NCB) veto

The non-collision background (NCB) corresponds with a number of processes, unrelated to the  $pp$  collisions that can produce signals in the detector and lead to incorrect event reconstruction, such as beam interactions with gas in the beam-pipe<sup>[30]</sup>, or a *beam halo* of muons produced by beam interaction with tertiary beam collimators located outside of the detector [190, 191]. These processes can produce an imbalance in the reconstructed  $\cancel{E}_T$ , and so we seek a way to veto this events – particularly for the inclusive background estimate described in Section 5.5.1, where the estimated probability of DV production (conditioned on jets or track density) may be influenced by NCB contamination<sup>[31]</sup>. Figure 5.8 shows the  $\cancel{E}_T$  distribution before applying an NCB veto. The presence of NCB can be seen in the peaks at  $\{0, \pm\pi\}$ , resulting from beam halo effects.

Following from studies in Ref. [192], we define the NCB veto via the selections in Table 5.19, based on the following jet variables:

- $f_{\max}$ : The maximum fraction of the jet energy deposited in any single layer of the calorimeter.
- $f_{\text{EM}}$ : The fraction of the jet energy deposited in the EM calorimeter<sup>[32]</sup>.
- **SuperLooseBadLLP**: A very loose jet cleaning working point meant to eliminate fake jets produced by calorimeter noise, described in Appendix A.7.

---

30. The vacuum pressure in the beam-pipe, in the interaction point regions, is on the order of  $1 \times 10^{-9}$  Pa [85]. This is a near-perfect vacuum, but nonetheless we may expect to see effects of protons scattering off of the remaining gas.

31. By contrast, the event yields in the SRs are not significantly affected by NCB contamination, due to the DV-level requirements that are imposed.

32. See Section F.2 for a discussion of this phenomenon.

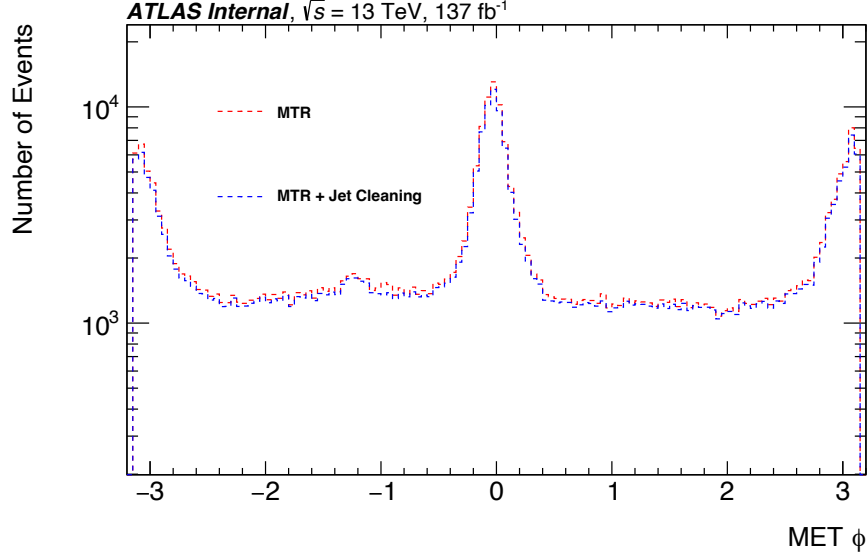


Figure 5.8: The distribution of the azimuthal direction of  $\vec{E}_T$  in the MTR, with and without a standard jet cleaning selection applied. The peaks correspond with NCB from beam halo effects, and the standard jet cleaning has practically no effect on the distribution – necessitating construction of a dedicated NCB veto. Taken from Ref. [143].

Note that the  $f_{\max}$  and  $f_{\text{EM}}$  selections are only applied to the leading (highest- $p_T$ ) jet in the event, while the `SuperLooseBadLLP` selection is applied to all jets in the event (so that the event fails the veto if any jet fails `SuperLooseBadLLP`). Figure 5.9 shows the effect of the NCB veto on the distribution of the azimuthal direction of  $\vec{E}_T$ .

NCB Veto	
Index	Criterion
$A$	$f_{\max} > 0.8$ (leading jet only)
$B$	$f_{\text{EM}} > 0.96$ (leading jet only)
$C$	fail <code>SuperLooseBadLLP</code> (any jet in event)
Pass Veto = $\overline{(A \wedge B)} \vee C$	

Table 5.19: An overview of the selections that define the NCB veto. Taken from Ref. [143].

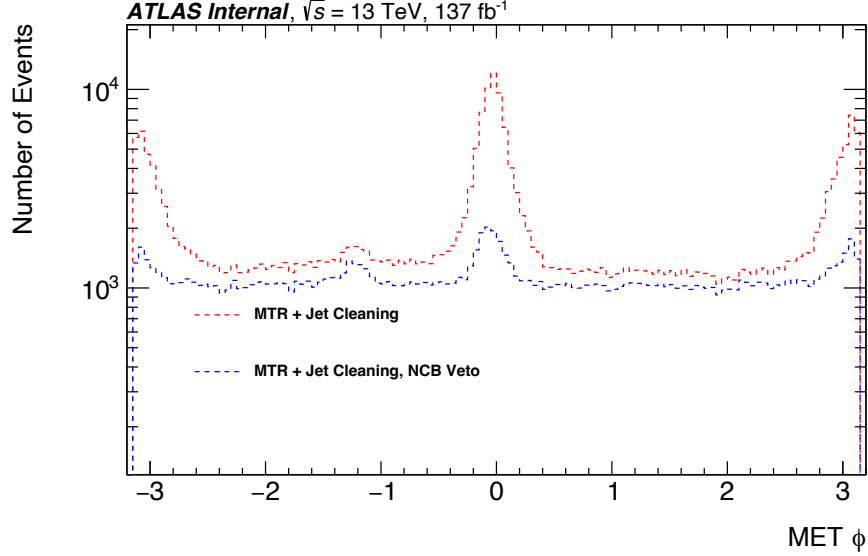


Figure 5.9: The distribution of the azimuthal direction of  $\vec{E}_T$  in the MTR, with and without the NCB veto applied. The veto significantly reduces the magnitude of the peaks in the distribution, bringing it closer to the expected flat shape<sup>[33]</sup>. Taken from Ref. [143].

#### 5.4.2.4 Dead tile module veto

Some events will have incorrectly-measured  $\vec{E}_T$ , due to dead (non-functioning) modules in TileCal, as can be seen by the spikes in Figure 5.10. To remove these events, we define a dead tile module veto based on the jet-level selections in Table 5.20. We reject an event that contains any EMTopo jets passing all these selections.

Dead Tile Module Veto	
Index	Criterion
$A$	jet on a dead tile module <sup>[34]</sup>
$B$	$p_T > 50 \text{ GeV}$
$C$	$\Delta\phi(\vec{E}_T, j) < 0.3$
Pass Veto = $\overline{A \wedge B \wedge C}$	

Table 5.20: The dead tile module veto is defined as an event containing an EMTopo jet that matches all criteria. Taken from Ref. [143].

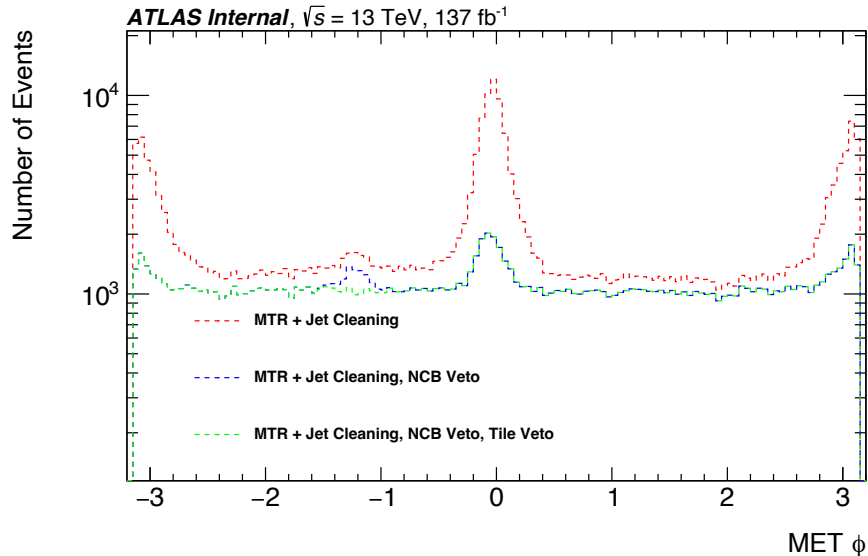


Figure 5.10: The distribution of the azimuthal direction of  $\vec{E}_T$ , in the MTR, with and without the dead tile module veto applied. For reference, the distribution with and without the NCB veto is also shown, as in Figure 5.9. On top of the NCB veto, the dead tile module further reduces the peaks (although less significantly). Taken from Ref. [143].

### 5.4.3 1 VSI DV Analysis Channel

The 1 VSI DV SR, as its name implies, targets events that produce at least one VSI DV that is determined to be signal-like. This SR is used to target the gluino  $R$ -hadron model (Section 5.2.1) – for which it is optimized – as well as the axino model (5.2.4), for which it is found to have the best sensitivity<sup>[35]</sup>. This SR is defined by the common selections in Section 5.4.2, as well as *track cleanings* and *DV-level selections* that we will detail in the following subsections.

33. In fact, even in the absence of any NCB, the distribution is not entirely flat but exhibits a very gentle sinusoidal shape, with a small excess in the  $-\phi$  region and deficit in the  $+\phi$  region. This is due to the very small but measurable mechanical sagging of the ATLAS detector, causing the interaction point to not be at the perfect center of the detector.

34. See Appendix A.8.

35. As the axino model was developed later than the other models in this analysis, none of the SR definitions were optimized to target it. Prior to its development, it was assumed that the Higgs decay channel would be best targeted by one of the FV SRs, as the FV algorithm is meant to target heavy-flavor decays such as the  $h \rightarrow b\bar{b}$  in this signal model. However, we ultimately found that the 1 VSI DV SR provided stronger constraints on this model for both its decay channels, and thus opted to use its results in that SR for final interpretation.

### 5.4.3.1 VSI Track Cleanings

The track cleanings correspond with a set of selections placed on the selected and attached tracks of VSI DVs (Section 5.3.1.2). Tracks that fail these selections are removed, and the DV mass (assigning  $m_{\pi^\pm}$  to the tracks) and track multiplicity are recalculated – other properties of the DV such as its position are left unchanged. The track cleanings are outlined in Table 5.21, using the following additional variable definitions:

- $\alpha(\vec{v}_1, \vec{v}_2)$ : The 3D angle between two 3-vectors,
- $\overrightarrow{\text{DV-PV}}$ : The 3-vector between a DV and the (hard-scatter) PV.

In general, the purposes of these cleanings is to remove tracks that are more likely to be produced by background processes – in particular, the  $\alpha(\vec{v}_1, \vec{v}_2)$  selections target tracks associated with hadronic interactions (Section 5.5.2.1) that typically produce highly-collimated sets of tracks, and *accidental crossing* of DVs by unrelated tracks (Section 5.5.2.3) that conversely may produce DV tracks with high crossing angles. Figure 5.11 shows the efficiency of the track cleanings for a range of gluino  $R$ -hadron signal models.

### 5.4.3.2 VSI DV Baseline Selections

After applying track cleanings, we finally perform a series of VSI DV selections – optimized for the gluino  $R$ -hadron model – to eliminate poorly-reconstructed or background-like DVs. We separate these selections into two groups, which we will refer to as the *baseline* and *signal* selections. The former defines the region in which our VRs and SR reside, with the latter separating between these two. These selections are indicated in Table 5.22, and we will discuss a few of the selections below (as indicated).

**5.4.3.2.1 DV - PV transverse distance** This selection serves to eliminate PVs that may be reconstructed as DVs, by requiring sufficient distance between the DVs and the

VSI DV Track Cleaning	
Index	Criterion
<i>A</i>	No hits with $R_{xy} < R_{xy, DV}$
<i>B</i>	$p_T > \begin{cases} 4 \text{ GeV} & \text{attached track, DV outside last Pixel layer} \\ 3 \text{ GeV} & \text{attached track, DV outside beam-pipe} \\ 2 \text{ GeV} & \text{otherwise} \end{cases}$
<i>C</i>	$\text{sig}(d_0) > \begin{cases} 15 & \text{attached track, DV within last Pixel layer} \\ 10 & \text{selected track, DV outside last Pixel layer} \\ 10 & \text{DV within beam-pipe} \end{cases}$
<i>D</i>	$\alpha(\text{track}, \overrightarrow{DV-PV}) < \pi/2$ attached tracks
<i>E</i>	$\alpha(\text{track}, \overrightarrow{DV-PV}) \begin{cases} > 0.2 & p_T < 4 \text{ GeV, DV outside beam-pipe} \\ > 0.02 & \text{otherwise} \end{cases}$
<i>F</i>	$\Delta\phi(\text{track}, \overrightarrow{DV-PV}) < 3$
<i>G</i>	Pass a hit pattern check (Appendix A.9)
Pass Cleaning = $A \wedge B \wedge C \wedge D \wedge E \wedge F \wedge G$	

Table 5.21: An overview of the 1 VSI DV track cleanings. Taken from Ref. [143].

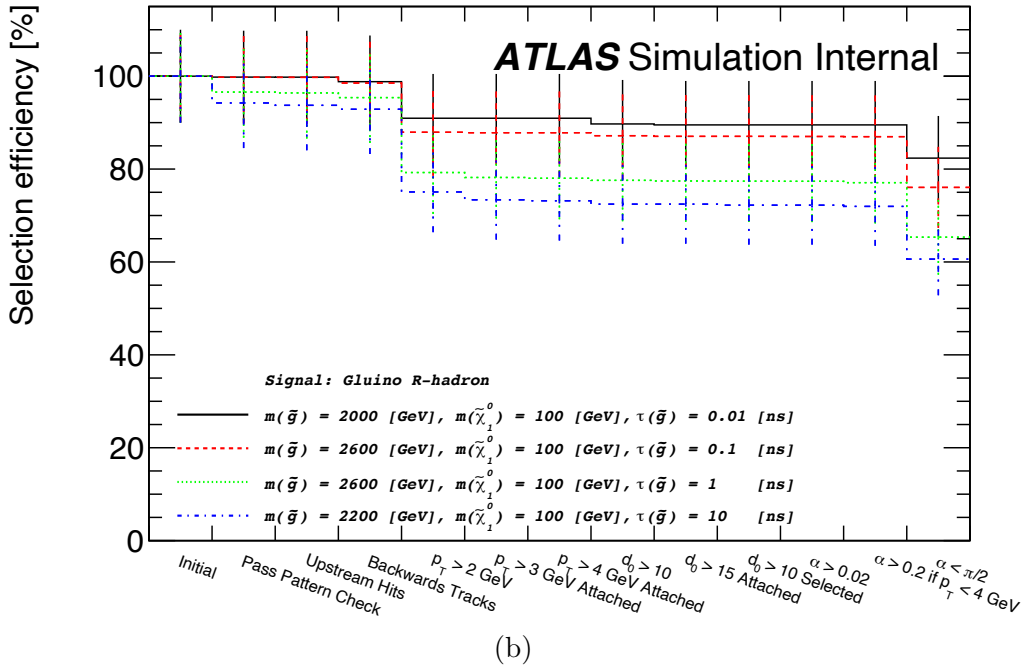
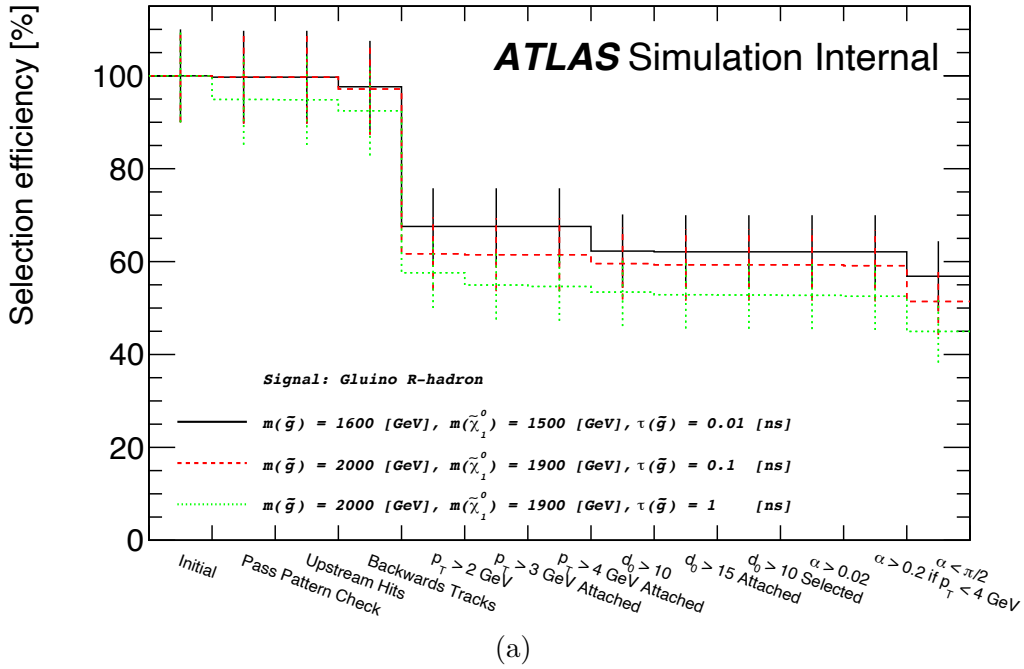


Figure 5.11: The track cleaning efficiency for a range of gluino  $R$ -hadron signal models, in the 1 VSI DV analysis channel. Studies of the effect of selections and cleanings on MC simulations of signal processes, like this one, are a crucial tool in designing an analysis. Taken from Ref. [143].

1 VSI DV-level Baseline Selection			
Index	Criterion	Short Description	Reference
<i>A</i>	Fiducial volume	$(R_{xy} < 300 \text{ mm}) \wedge ( z  < 300 \text{ mm})$	-
<i>B</i>	DV- PV transverse distance	$R_{xy}^{\text{DV-PV}} > 4 \text{ mm}$	Section 5.4.3.2.1
<i>C</i>	Vertex fit quality	$\chi^2/N_{\text{DoF}} < 5$	Section 5.4.3.2.3
<i>D</i>	Photon veto	$\Delta R(\text{DV}, \gamma) > 0.1$	Section 5.4.3.2.3
<i>E</i>	Material veto	Outside strict material map veto region	Appendix A.10
<i>F</i>	Max $p_T$ veto	$\max(p_T^{\text{track}}) / \sum_{\text{tracks}} p_T < 0.95$	-
Pass DV Baseline Selection = $A \wedge B \wedge C \wedge D \wedge E \wedge F$			

Table 5.22: An overview of the baseline VSI DV-level selections, which require an event to have at least 1 DV that passes all these selections. This is common to the 1 VSI DV VRs and SR, the latter having additional selections. Taken from Ref. [143].

hard-scatter PV. This also serves to suppress the background produced by heavy-flavor decays, such as  $B$ -mesons<sup>[36]</sup>.

**5.4.3.2.2 Vertex fit quality** This selection serves as a check on the vertex goodness-of-fit, requiring the reduced  $\chi^2$  statistic – as reported by the VSI fitting algorithm [170] – to be sufficiently small. This selection eliminates fake DVs, that are a product of the vertexing algorithm itself.

**5.4.3.2.3 Photon veto** As noted in Section 5.3.2.1, we use photons to veto DVs that satisfy  $\Delta R(\text{DV}, \gamma)$  if  $p_T^\gamma > 60 \text{ GeV}$ . This selection eliminates DVs that may be produced via photon conversions<sup>[37]</sup>, a potential SM background. It also helps make the CRs' kinematics

---

36. See Figure 2.4 in Section 2.1.2.4.

37. First documented in 1933 [193], photon conversion (or  $e^+e^-$  pair production) results from the interaction of a high-energy photon with matter.

more similar to those of the SR, the former being defined as the PTR in combination with these baseline-level DV selections.

**5.4.3.2.4 Max  $p_T$  veto** This selection eliminates DVs that may be reconstructed as signal-like due to errors in track reconstruction. Such errors may cause a particular track to be reconstructed with too large  $p_T$  and resulting in too large a DV mass.

### 5.4.3.3 Signal VSI DV Selections, and the Full Region Definitions

The preceding DV-level selections, in combination with the event-level selections that define the MTR, demarcate the region consisting of the SR and VRs. To separate between these two, the SR is defined by the further DV-level cuts provided in Table 5.23.

1 VSI DV-level Signal Selection		
Index	Criterion	Description
$A$	DV mass	$m_{\text{DV}} > 10 \text{ GeV}$
$B$	DV track multiplicity	$N_{\text{tracks}}^{\text{DV}} \geq 5$
$C$	DV selected track multiplicity	$N_{\text{sel. tracks}}^{\text{DV}} \geq 2$
Pass DV Signal Selection = $A \wedge B \wedge C$		

Table 5.23: An overview of the signal VSI DV-level selections, which require an event to have at least 1 DV that passes all these selections, in addition to the selections in Table 5.22. Here, “selected track” refers to DV tracks passing the VSI selection criteria in Table 5.6. Taken from Ref. [143].

With both our event-level and DV-level selections defined, as well as the track cleanings we apply to the DV tracks, we can now summarize (and visualize) the SR, VRs and CRs for the 1 VSI DV analysis channel. Table 5.24 summarizes the region definitions. Figure 5.12 shows the SR, VR and CRs in the  $(m_{\text{DV}}, N_{\text{tracks}}^{\text{DV}})$  plane, with two different choices of binning<sup>[38]</sup>, and Table 5.25 also outlines the VR and CR binnings.

---

38. The fact that there are different binning choices is a little bit of a historic quirk of the analysis

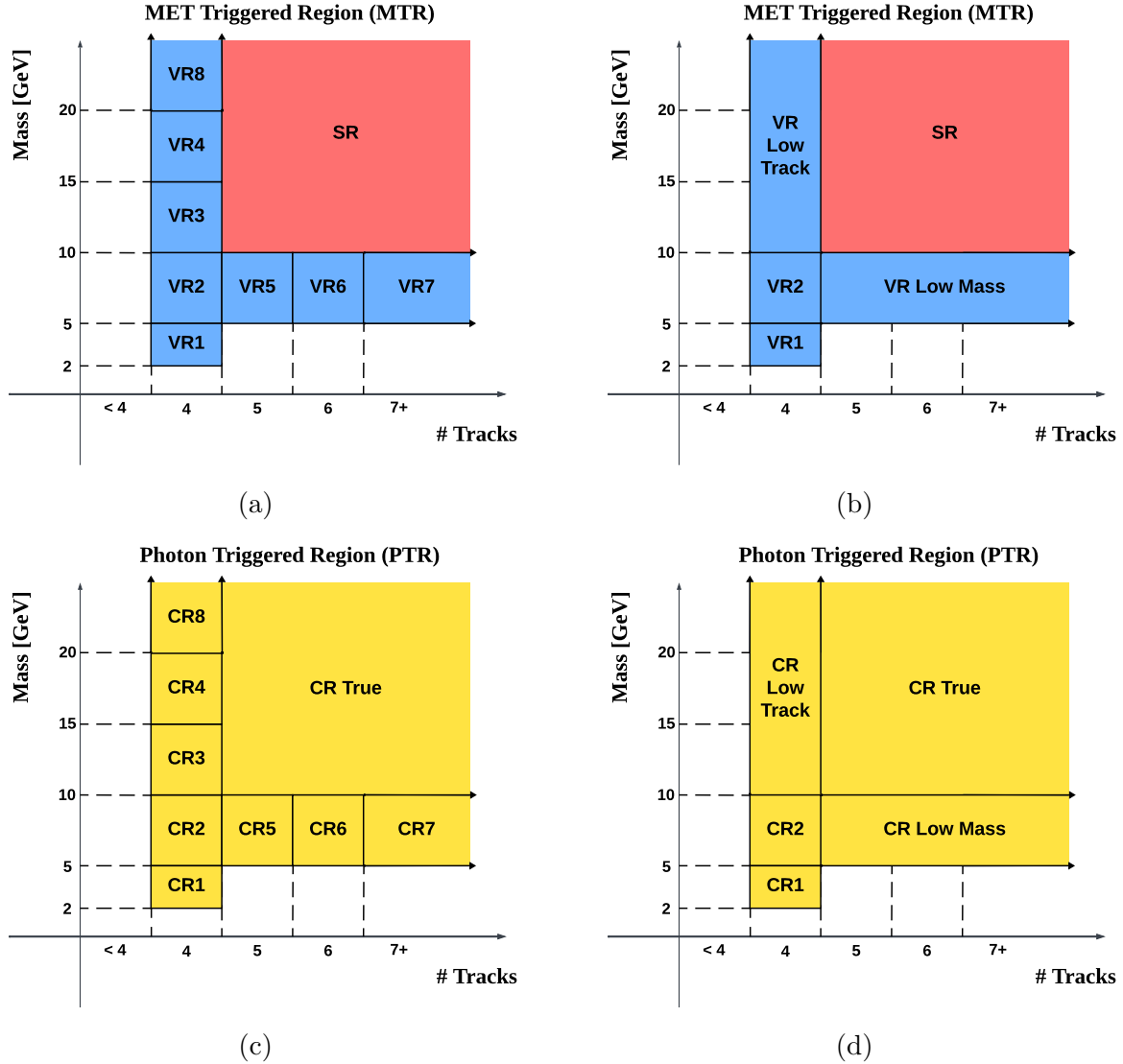


Figure 5.12: The signal, validation and control regions for the 1 VSI DV analysis channel, depicted in the  $(m_{DV}, N_{tracks}^{DV})$  plane, with (a,b) fine and (c,d) merged binning. The track cleanings and baseline DV-level selections (Tables 5.4.3.1 and 5.4.3.2) are implicit. Taken from Ref. [143].

1 VSI DV Channel: Region summary		
Shorthand	Criterion	Reference
-	MTR	Table 5.17
-	PTR	Table 5.18
DVB	1 VSI DV-level baseline	Table 5.22
DVS	1 VSI DV-level signal	Table 5.23
Signal Region = $MTR \wedge DVB \wedge DVS$ Validation Regions = $MTR \wedge DVB \wedge \overline{DVS}$ Control Regions = $PTR \wedge DVB$		

Table 5.24: An overview of the region definitions for the 1 VSI DV analysis channel. Note that the DVs used in the DV-level selections always have track cleanings applied, as outlined in Table 5.4.3.1. Taken from Ref. [143].

#### 5.4.4 1 FV Analysis Channel

The 1 FV SR is conceptually similar to the preceding 1 VSI DV SR, except that it uses FVs to identify displaced particle decays. This SR is used to target the Wino-Bino co-annihilation model (Section 5.2.2) – not only is the SR optimized for that model, but the FV algorithm itself was developed using a similar class of models for training its BDT (Section 5.3.1.3). Like its VSI counterpart, this SR is defined by a combination of event-level selections, track cleanings and DV-level selections.

##### 5.4.4.1 Event-Level Selections

Both FV SRs feature slightly extended event-level selections compared to the 1 VSI DV SR, featuring a stricter non-collision background veto. These selections are outline in Table 5.26.

---

development. Having more VRs provides more independent tests of background estimates, but at the cost of decreased statistics per bin (and thus possibly limited usefulness of each test).

1 VSI DV Channel: Validation Regions			
Region (merged)	Region (fine)	$m_{\text{DV}}$ [GeV]	$N_{\text{tracks}}^{\text{DV}}$
VR1 CR1		[ 2, 5]	4
VR2 CR2		[ 5, 10]	4
VR Low Track CR Low Track	VR3 CR3	[10, 15]	4
	VR4 CR4	[15, 20]	4
	VR8 CR8	> 20	4
VR Low Mass CR Low Mass	VR5 CR5	[ 5, 10]	5
	VR6 CR6	[ 5, 10]	6
	VR7 CR7	[ 5, 10]	$\geq 7$

Table 5.25: An overview of the binning of the VRs and CRs for the 1 VSI DV analysis channel, indicating both region binning systems. Taken from Ref. [143].

FV Region Event-level Selections			
Index	Criterion	Short Description	Reference
$A$	MTR	$\cancel{E}_T$ -triggered region	Table 5.17
$B$	Strict non-collision background veto	Reject beam-halo distortions of $\cancel{E}_T$	Section 5.4.2.3
Selection = $A \wedge B$			

Table 5.26: An overview of the event-level selections for the 1 and 2 FV SRs. Taken from Ref. [143].

**5.4.4.1.1 Strict NCB Veto** The strict NCB veto is similar to the standard one in Table 5.19, except that it also applies a condition on the leading jet’s  $f_{\text{ch}}$ , the ratio of the scalar sum of  $p_T$  of tracks associated to the jet (via ghost association) and the jet  $p_T$ <sup>[39]</sup>, and the veto is failed if any of its conditions are not met. Its definition is outlined in Table 5.27.

Strict NCB Veto	
Index	Criterion
$A$	$f_{\text{max}} > 0.8$ (leading jet only)
$B$	$f_{\text{EM}} > 0.96$ (leading jet only)
$C$	$f_{\text{ch}}/f_{\text{max}} < 0.1$ (leading jet only)
$D$	fail SuperLooseBadLLP (any jet in event)
Pass Veto = $\overline{A \vee B \vee C \vee D}$	

Table 5.27: An overview of the selections that define the strict NCB veto. Note that this is similar to the standard NCB veto (Table 5.19), except that it has an extra condition and requires all its conditions to be met for an event to pass. Taken from Ref. [143].

#### 5.4.4.2 FV Track Cleanings

Similar to VSI (Section 5.4.3.1), we apply a set of track cleanings to the tracks attached to the FVs, and any tracks that fail the cleanings are removed (and the FV mass and track multiplicity updated). These track cleanings, outlined in Table 5.28, are used for both the 1 and 2 FV SRs, and the efficiency is shown in Figure 5.13 for a range of Wino-Bino co-annihilation signal models as well as a  $Z \rightarrow \nu\bar{\nu} + \text{jets}$  MC background process. Note that while the track  $p_T$  cut in particular may appear a little fine-tuned, its purpose is to further reduce background tracks eliminated by the FV track selection criteria (Table 5.8) that impose a  $p_T < 1$  GeV requirement – the background track  $p_T$  distribution (in MC simulation) is found to exponentially fall as a function of increasing  $p_T$ , so slightly tightening

---

39. This is effectively a measure of the *charge fraction* of the jet, as associated tracks will correspond with charged particles. For details on the ghost association method, see Ref. [194, 195].

this selection criteria significantly reduces background. The signal and background track  $p_T$  distributions are shown in Figure 5.14.

FV Track Cleaning	
Index	Criterion
$A$	No hits with $R_{xy} < R_{xy, DV}$
$B$	$p_T > 1.1 \text{ GeV}$
$C$	$\text{sig}(d_0) > 5$
$D$	$\{\alpha(\text{track}, \overrightarrow{V-DV})\} > 0.15$ if $(R_{xy, DV} \leq 34 \text{ mm}) \wedge (\text{sig}(d_0) \leq 60)$
$E$	$\{\alpha(\text{track}, \overrightarrow{V-DV})\} > 0.15$ if $(34 \text{ mm} < R_{xy, DV} \leq 150 \text{ mm}) \wedge (\text{sig}(d_0) \leq 70)$
$F$	$\Delta\phi(\text{track}, \overrightarrow{DV-PV}) < 1.75$ if $R_{xy, DV} \leq 34 \text{ mm}$
$G$	$\Delta\phi(\text{track}, \overrightarrow{DV-PV}) < 1$ if $34 \text{ mm} < R_{xy, DV}$
Pass Cleaning = $A \wedge B \wedge C \wedge D \wedge E \wedge F \wedge G$	

Table 5.28: An overview of the FV track cleanings. In the selections above,  $\{\alpha(\text{track}, \overrightarrow{V-DV})\}$  is computed  $\forall V \in [\text{PV}, \{\text{PU}\}]$ , where  $\{\text{PU}\}$  refers to the set of pileup vertices in the event. Taken from Ref. [143].

#### 5.4.4.3 Baseline FV Selections

The baseline FV selections are outlined in Table 5.29. As in the 1 VSI DV analysis channel, these (together with the track cleanings) serve to isolate the DVs that, together with the corresponding event-level selections, define our SR, VRs and CRs<sup>[40]</sup>. In fact, these are mostly the same types of selections as are imposed on VSI DVs (Table 5.22), except that there is no

<sup>40</sup>. To be precise, these selections do not fully define the VRs for the FV analysis channels, as we shall discuss below.

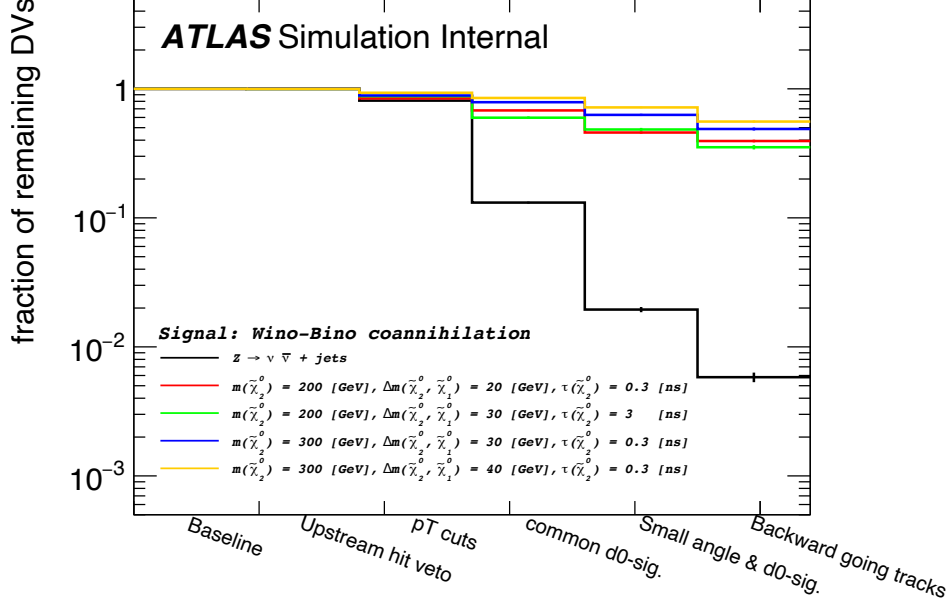


Figure 5.13: A test of the FV track cleaning efficiency for a set of Wino-Bino co-annihilation MC samples, as well as a background  $Z \rightarrow \nu\bar{\nu} + \text{jets}$  sample for reference. The track cleanings remove relatively few FVs from the signal samples, at least when compared with the significant elimination of background FVs – significantly improving the signal-to-background ratio. Taken from Ref. [143].

vertex fit quality selection<sup>[41]</sup>. We also apply a condition on the number of seeds in the FV, as described below.

**5.4.4.3.1  $N_{\text{seeds}}^{\text{DV}}$  Selection** Due to how the FV algorithm functions, FVs can have between 0 and<sup>[42]</sup>  $C(N_{\text{tracks}}^{\text{DV}}, 2)$  seeds, the former representing the case where all tracks in the FV belong to disconnected pairs, and the latter the case where tracks are maximally interconnected. This selection, optimized in MC simulation studies, is found to limit the contamination of background FVs still present at this stage of event selection.

41. The FVs are constructed in a fundamentally different algorithm (Section 5.3.1.3) employing a BDT, than their VSI counterparts (Section 5.3.1.2).

42. Here we are using the notation  $C(n, k) \equiv \binom{n}{k}$ .

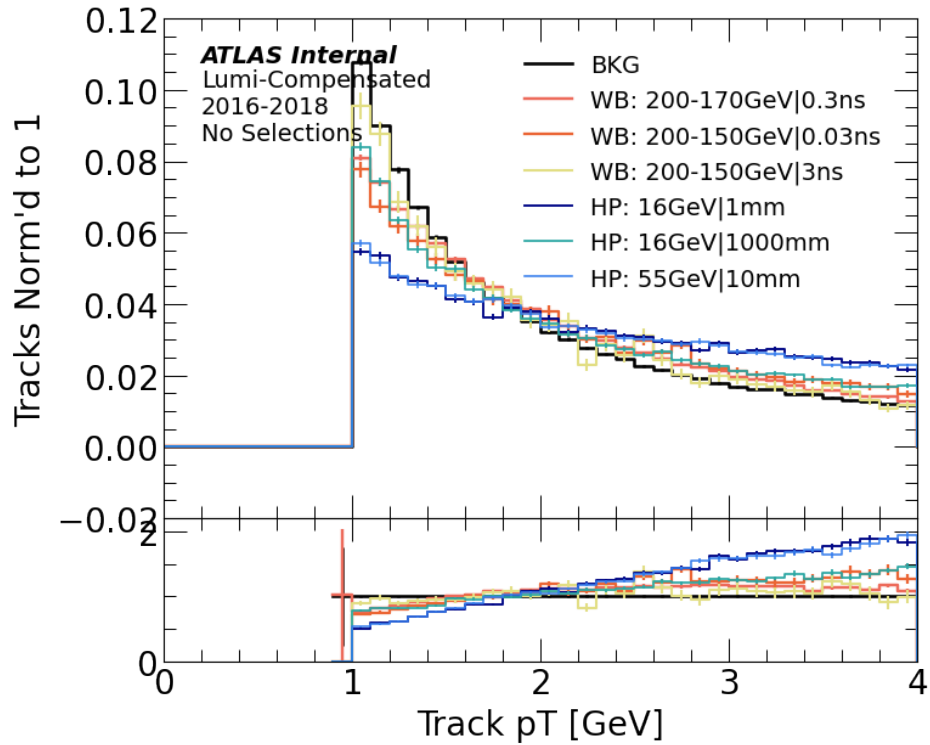


Figure 5.14: Track  $p_T$  distributions for a range of signal processes (“WB” = Wino-Bino co-annihilation, “HP” = Higgs Portal), as well as MC simulation background (“BKG” =  $Z \rightarrow \nu\bar{\nu} + \text{jets}$ ). For each signal model, the legend indicates the particle masses ( $(m_{\tilde{\chi}_2^0}, m_{\tilde{\chi}_1^0})$  for Wino-Bino co-annihilation,  $m_S$  for Higgs Portal), and the LLP mean lifetime/displacement. Taken from Ref. [143].

1 FV: FV-level Baseline Selection			
Index	Criterion	Short Description	Reference
<i>A</i>	Fiducial volume	$(R_{xy} < 300 \text{ mm}) \wedge ( z  < 300 \text{ mm})$	-
<i>B</i>	DV- PV transverse distance	$R_{xy}^{\text{DV-PV}} > 4 \text{ mm}$	Section 5.4.3.2.1
<i>C</i>	$N_{\text{seeds}}^{\text{DV}}$ Selection	$N_{\text{seeds}}^{\text{DV}} \geq N_{\text{tracks}}^{\text{DV}}! / (N_{\text{tracks}}^{\text{DV}} - 2)! / 2! - 1$	Section 5.4.4.3.1
<i>D</i>	Photon veto	$\Delta R(\text{DV}, \gamma) > 0.1$	Section 5.4.3.2.3
<i>E</i>	Material veto	Outside strict material map veto region	Appendix A.10
<i>F</i>	Max $p_T$ veto	$\max(p_T^{\text{track}}) / \sum_{\text{tracks}} p_T < 0.9$	-
Pass Baseline FV Selection = $A \wedge B \wedge C \wedge D \wedge E \wedge F$			

Table 5.29: An overview of the baseline FV-level selections, for the 1 FV analysis channel. Note that the  $N_{\text{seeds}}^{\text{DV}}$  and material veto conditions are lifted for some of our VR definitions, as will be discussed in Section 5.4.4.5. Taken from Ref. [143].

#### 5.4.4.4 Signal FV Selections

Finally, we have our signal FV selections, as outlined in Table 5.30. These are similar to the signal VSI DV selections, except that we also apply a track  $\Delta\eta$  selection as described below.

1 FV: FV-level Signal Selection			
Index	Criterion	Short Description	Reference
<i>A</i>	Material veto	Outside strict material map veto region	Appendix A.10
<i>B</i>	Max track $\Delta\eta$	$\Delta\eta_{\max} < 3.5$	Section 5.4.4.4.1
<i>C</i>	Track multiplicity	$N_{\text{tracks}}^{\text{DV}} \geq 5$	-
<i>D</i>	DV mass	$m_{\text{DV}} \geq 10 \text{ GeV}$	-
Pass FV Signal Selection = $A \wedge B \wedge C \wedge D$			

Table 5.30: An overview of FV-level SR selections, for the 1 FV SR. Taken from Ref. [143].

##### 5.4.4.4.1 $\Delta\eta_{\max}$ Selection

We apply a selection on

$$\Delta\eta_{\max} = \max \left( \{ \Delta\eta (\vec{p}_{\text{track}, i}, \vec{p}_{\text{total}} - \vec{p}_{\text{track}, i}) \} \right), \quad (5.4)$$

- $\vec{p}_{\text{track}, i}$  is the 3-momentum of the  $i$ 'th track attached to the FV,
- $\vec{p}_{\text{total}} = \sum_i \vec{p}_{\text{track}, i}$  is the vector sum of the 3-momentum of all tracks attached to the FV.

in order to eliminate FVs that may be produced by accidental crossings (Section 5.5.2.3), which are often characterized by large track- $\overrightarrow{\text{DV-PV}}$  crossing angles.

#### 5.4.4.5 Full Region Definitions

The full region definitions for the 1 FV analysis channel are structurally similar to those for the 1 VSI DV analysis channel (Table 5.24), with the appropriate substitution of selections in the event-level, baseline DV-level and signal DV-level categories. However, there are a couple distinct differences that affect the VR definitions:

- As noted earlier, the FV VRs include regions without the material map applied. They also include regions with the map applied.
- The FV VRs also include regions where we specifically lift the  $N_{\text{seeds}}^{\text{DV}}$  baseline FV-level selection.
- When imposing the material map and the  $N_{\text{seeds}}^{\text{DV}}$  conditions, we only use one VR which is the effective analogue of VR1 in the 1 VSI DV analysis channel (Figure 5.12).

This results in a larger number of VRs than for the 1 VSI DV analysis channel<sup>[43]</sup>. The VRs are summarized in Table 5.31.

### 5.4.5 2 FV Analysis Channel

This SR targets events that produce at least two FVs, as is expected in processes such as the Higgs Portal signal model for which it is optimized. As noted earlier, this analysis channel is made orthogonal to the 1 FV analysis channel by designing the latter to require strictly 1 FV— thus while the two FV-based SRs are optimized for different signal models, they are used in conjunction with one another. It is also subdivided differently than the 1 VSI DV and FV analysis channels, where there is close correspondence between the two channels’ VR and SR definitions. The event-level selections and track cleanings are identical to those in the 1 FV analysis channel (Sections 5.4.4.1 and 5.4.4.2 respectively).

#### 5.4.5.1 Baseline FV Selections

The baseline FV-level selections are the same as those in the 1 FV analysis channel (Table 5.29), except that the  $N_{\text{seeds}}^{\text{DV}}$  selections is different. At the risk of redundancy, we outline these selections in Table 5.32. Note that we require 2 FVs to pass these selections.

---

<sup>43</sup>. Having additional, independent opportunities for validation is useful in practice – particularly when using a new vertexing algorithm whose performance is less studied.

1 FV Analysis Channel: Validation Regions				
Region Name	$m_{\text{DV}}$ [GeV]	$N_{\text{tracks}}^{\text{DV}}$	$N_{\text{seeds}}^{\text{DV}}$ Requirement	Material Map Veto
VR1 <sub>inside</sub>	[ 2, 5]	4	Nominal	Fail
VR2 <sub>inside</sub>	[ 5, 10]	4		
VR3 <sub>inside</sub>	[10, 15]	4		
VR4 <sub>inside</sub>	[15, 20]	4		
VR5 <sub>inside</sub>	[ 5, 10]	5		
VR6 <sub>inside</sub>	[ 5, 10]	6		
VR7 <sub>inside</sub>	[ 5, 10]	$\geq 7$		
VR8 <sub>inside</sub>	> 20	4		
VR9 <sub>inside</sub>	> 10	$\geq 5$		
VR1 <sub><math>N^{\text{seeds}}</math></sub>	[ 2, 5]	4	[2,4]	Pass
VR2 <sub><math>N^{\text{seeds}}</math></sub>	[ 5, 10]	4	[2,4]	
VR3 <sub><math>N^{\text{seeds}}</math></sub>	[10, 15]	4	[2,4]	
VR4 <sub><math>N^{\text{seeds}}</math></sub>	[15, 20]	4	[2,4]	
VR5 <sub><math>N^{\text{seeds}}</math></sub>	[ 5, 10]	5	3	
VR6 <sub><math>N^{\text{seeds}}</math></sub>	[ 5, 10]	6	3	
VR8 <sub><math>N^{\text{seeds}}</math></sub>	> 20	4	[2,4]	
VR9 <sub><math>N^{\text{seeds}}</math></sub>	> 10	$\geq 5$	3	
VR1	[ 2, 5]	4	Nominal	

Table 5.31: An overview of the VR definitions used for the 1- and 2-FV analysis channels. Event-level selections are applied, as well as baseline FV selections (except as noted otherwise). The VR9<sub>inside</sub> and VR9 <sub>$N^{\text{seeds}}$</sub>  regions are similar to the SR, except for different material map and  $N_{\text{seeds}}^{\text{DV}}$  conditions. Taken from Ref. [143].

2 FV: FV-level Baseline Selection			
Index	Criterion	Short Description	Reference
$A$	Fiducial volume	$(R_{xy} < 300 \text{ mm}) \wedge ( z  < 300 \text{ mm})$	-
$B$	DV- PV transverse distance	$R_{xy}^{\text{DV-PV}} > 4 \text{ mm}$	Section 5.4.3.2.1
$C$	$N_{\text{seeds}}^{\text{DV}}$ Selection	$N_{\text{seeds}}^{\text{DV}} \geq N_{\text{tracks}}^{\text{DV}}$	-
$D$	Photon veto	$\Delta R(\text{DV}, \gamma) > 0.1$	Section 5.4.3.2.3
$E$	Material veto	Outside strict material map veto region	Appendix A.10
$F$	Max $p_T$ veto	$\max(p_T^{\text{track}}) / \sum_{\text{tracks}} p_T < 0.9$	-
Pass Baseline FV Selection = $A \wedge B \wedge C \wedge D \wedge E \wedge F$			

Table 5.32: An overview of the baseline FV-level selections, for the 2 FV analysis channel. Taken from Ref. [143].

#### 5.4.5.2 Signal FV Selections

The signal FV-level selections are modified with respect to the 1 FV SR, as shown in Table 5.33.

#### 5.4.5.3 Full Region Definitions

The 2 FV SR structure is similar to the other SRs – a set of event-level selections, track cleanings, and FV-level selections – except that at least two FVs must pass the FV selections. The VR and SR definitions are outlined in Table 5.34. Note that the material map veto and  $N_{\text{seeds}}^{\text{DV}}$  selections are changed for some of the VR definitions (Table 5.32).

#### 5.4.6 Expected Signal Yields

Having defined our various signal regions, we can now turn to the question of how many signal events we actually expect to see for each signal model, over the various ranges of

2 FV: FV-level Signal Selection			
Index	Criterion	Short Description	Reference
$A$	$\overrightarrow{DV-PV}$ Pseudo-rapidity	$ \eta_{DV-PV}  < 2.5$	-
$B$	Jet matching	$\Delta R(DV, j) < 0.4$	-
$C$	Track multiplicity	$N_{\text{tracks}}^{DV} \geq 4$	-
$D$	DV mass	$m_{DV} \geq 1.5 \text{ GeV}$	-
Pass FV Signal Selection = $A \wedge B \wedge C \wedge D$			

Table 5.33: An overview of FV-level SR selections, for the 2 FV SR. Note that the lower bound on the FV mass is much lower than in the 1 FV SR. Taken from Ref. [143].

parameters we are testing. We summarize the model sensitivities in a series of plots in the following subsections.

#### 5.4.6.1 Gluino $R$ -hadron Yields

Figure 5.15 shows the expected signal yield for the gluino  $R$ -hadron model, in the 1 VSI DV SR. As a reminder, this SR was developed specifically to optimize the gluino  $R$ -hadron yield, and as expected it provides a higher sensitivity to probing this model than the other SRs.

#### 5.4.6.2 Wino-Bino Co-annihilation Yields

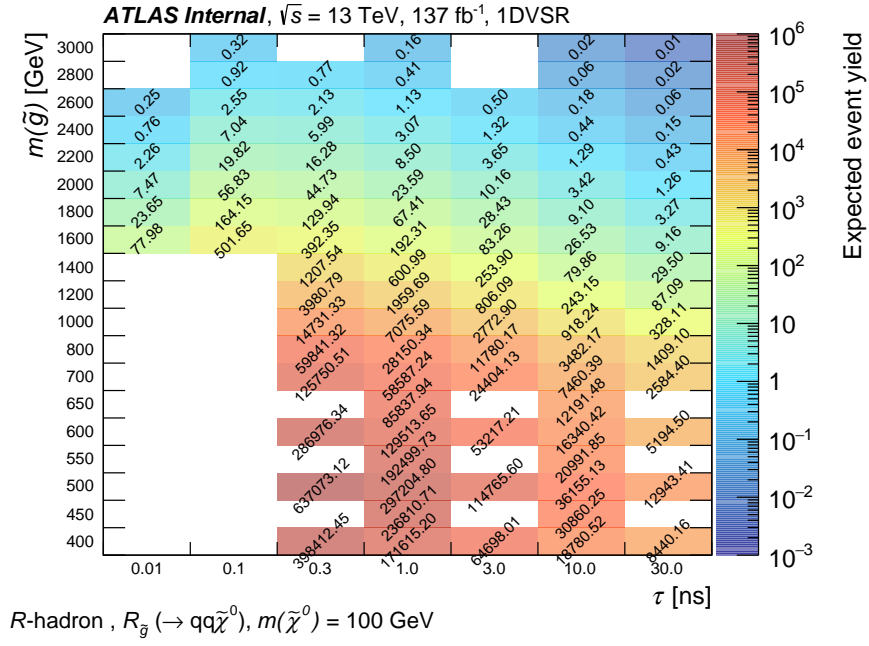
Figures 5.16 and 5.17 show the expected signal yield for the Wino-Bino co-annihilation model, in the 1 and 2 FV SRs (the former of which was optimized to target it).

#### 5.4.6.3 Higgs Portal Yields

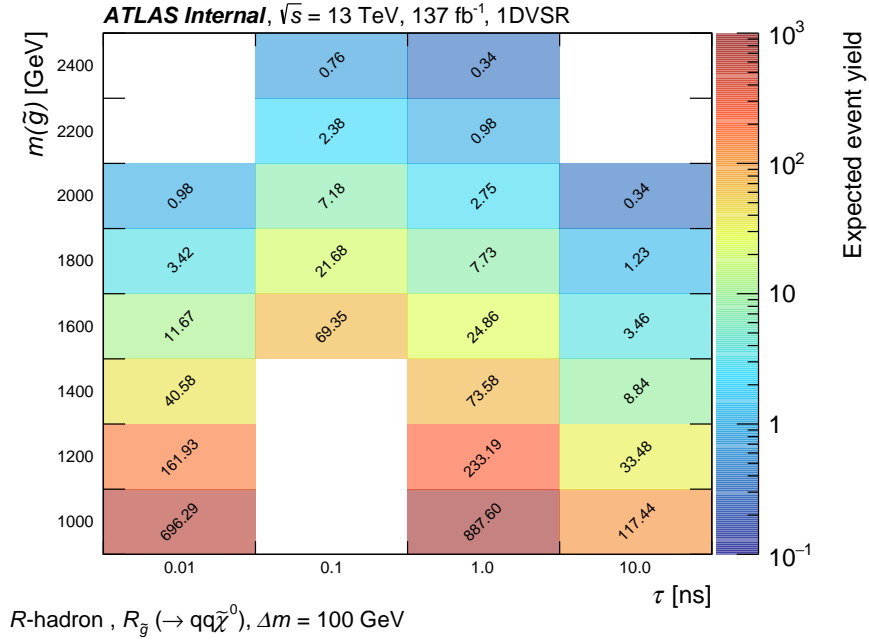
Figure 5.18 shows the expected signal yield for the Higgs Portal model, in the 1 and 2 FV SRs. Note that there is effectively no sensitivity for the case of a 5 GeV scalar  $S$ , which would

2 FV Analysis Channel: Validation and Signal Regions			
Region	$N_{\text{tracks}}^{\text{DV}}$	$N_{\text{seeds}}^{\text{DV}}$	Material Map Veto
VR1	3	$\geq N_{\text{tracks}}^{\text{DV}}$	Fail
VR2	3	$\in [2, N_{\text{tracks}}^{\text{DV}})$	
VR3	$\geq 4$	$\geq N_{\text{tracks}}^{\text{DV}}$	
VR4	$\geq 4$	$\in [2, N_{\text{tracks}}^{\text{DV}})$	
VR5	3	$\geq N_{\text{tracks}}^{\text{DV}}$	Pass
VR6	3	$\in [2, N_{\text{tracks}}^{\text{DV}})$	
VR8	$\geq 4$	$\in [2, N_{\text{tracks}}^{\text{DV}})$	
SR	$\geq 4$	$\geq N_{\text{tracks}}^{\text{DV}}$	

Table 5.34: An overview of the VR and SR definitions for the 2 FV analysis channel. Note that for VR8, the loose material veto is used as opposed to the standard strict one (Appendix A.10), and the  $m_{\text{DV}}$  condition is changed to  $m_{\text{DV}} > 0$  due to signal contamination. Taken from Ref. [143].

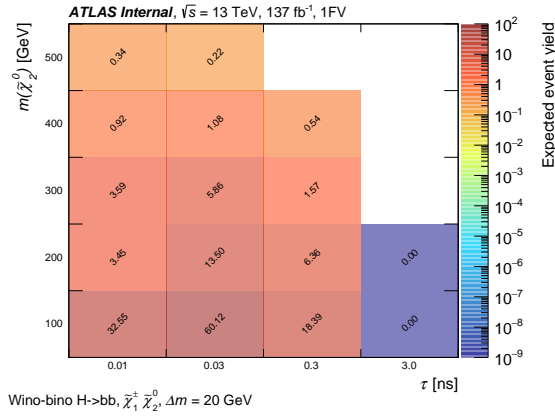


(a)

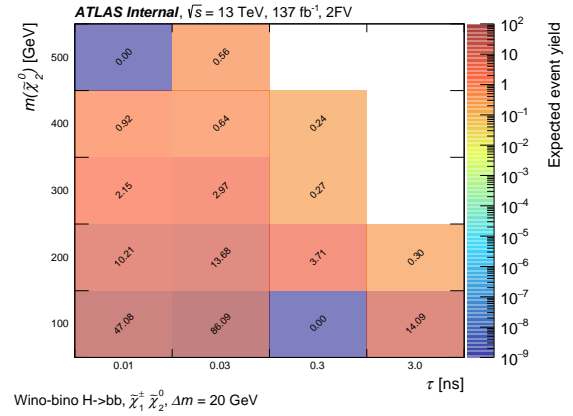


(b)

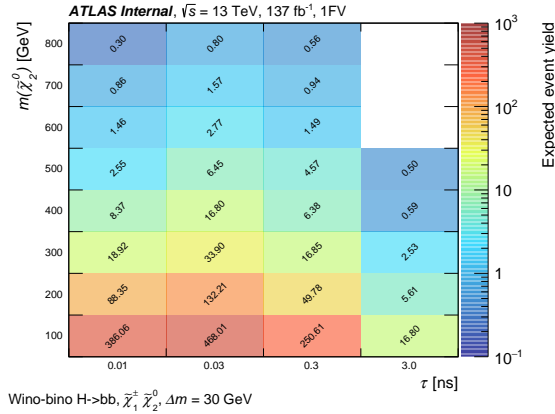
Figure 5.15: Expected signal yields for the gluino  $R$ -hadron signal model, for (a) fixed  $m(\tilde{\chi}_1^0) = 100$  GeV and (b) fixed  $\delta m(\tilde{g}, \tilde{\chi}_1^0) = 100$  GeV. Taken from Ref. [143].



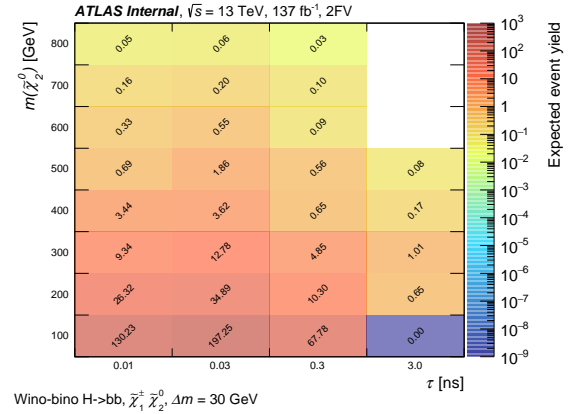
(a)



(b)

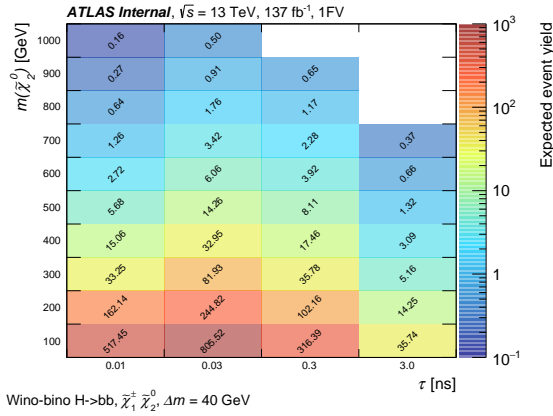


(c)

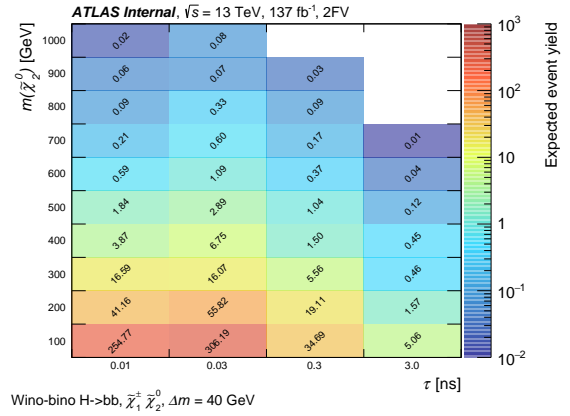


(d)

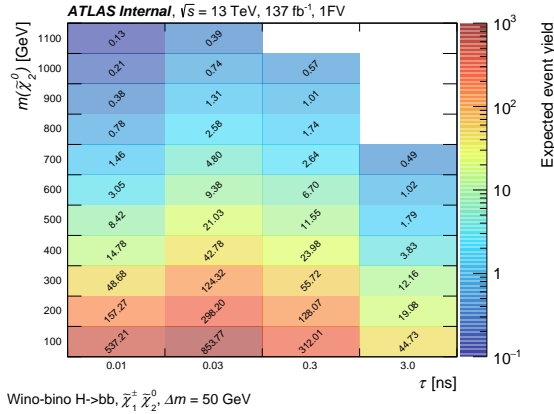
Figure 5.16: Expected signal yields for the Wino-Bino co-annihilation model, for (a,b)  $\Delta m(\tilde{\chi}_2^0, \tilde{\chi}_1^0) = 20$  GeV and (c,d)  $\Delta m(\tilde{\chi}_2^0, \tilde{\chi}_1^0) = 30$  GeV. Taken from Ref. [143].



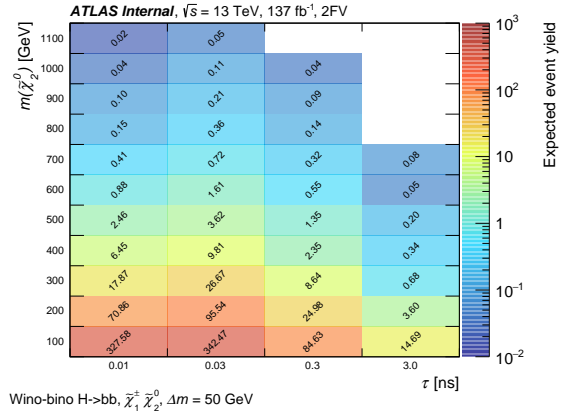
(a)



(b)



(c)



(d)

Figure 5.17: Expected signal yields for the Wino-Bino co-annihilation model, for (a,b)  $\Delta m(\tilde{\chi}_2^0, \tilde{\chi}_1^0) = 40$  GeV and (c,d)  $\Delta m(\tilde{\chi}_2^0, \tilde{\chi}_1^0) = 50$  GeV. Taken from Ref. [143].

correspond with decay to significantly off-shell  $b$ -quarks<sup>[44]</sup>

#### 5.4.6.4 Axino Yields

As mentioned in Section 5.2.4, the axino model did not benefit from the custom-tailoring of a specific SR, as did the other 3 models considered in this analysis. Prior to producing the full axino MC simulation samples, it was assumed that the axino processes involving a  $h \rightarrow b\bar{b}$  decay channel would achieve highest efficiency in one of the FV-based SRs, as the resulting long-lived  $B$ -mesons would be best identified as products of a single displaced decay by the FV algorithm. However, the 1 VSI DV SR provides the highest signal yield for both the  $h \rightarrow b\bar{b}$  and  $Z \rightarrow q\bar{q}$  axino channels, and so it is chosen for use with this model as well. Figure 5.19 shows the expected signal yield for the two decay channels of the axino model, and Appendix A.11 provides the yields for each of the SRs.

## 5.5 Background Estimation

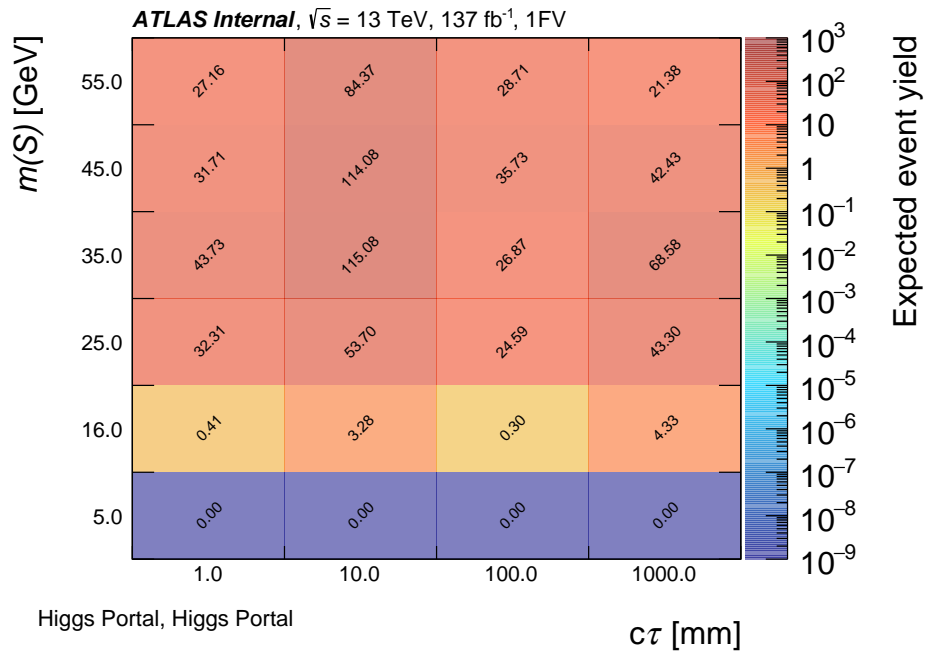
Our goal in this analysis is to count how many events fall into our SRs, and make a determination of the statistical significance of what we find: does it provide evidence of any of our signal models, or does it rule them out? And if so, how strongly? To do this, we will want to have a very good understanding of any background processes that contribute to this count – that is, anything that isn't the new physics we are looking for.

For this analysis, we use a data-driven background estimate strategy, whereby we model the background processes using real data in the (non-blinded) CRs, which we will extrapolate to the SRs<sup>[45]</sup>. This is in contrast to using a MC-based estimate, where we would estimate

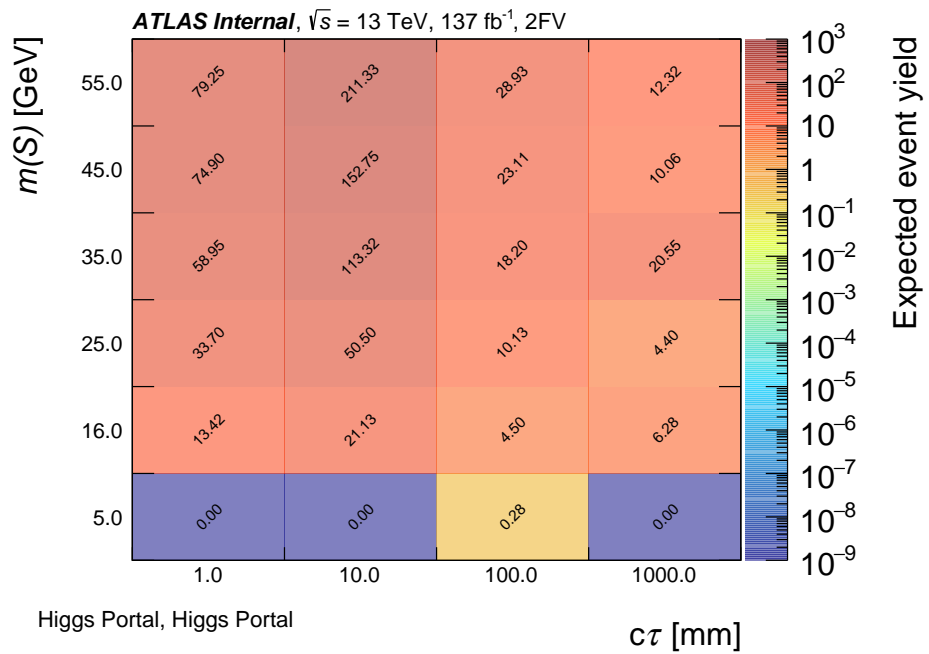
---

44. Beyond suppression of this process due to the off-shell  $b$ -quark production, such low-mass scalars are difficult to reconstruct as they are hard to distinguish from  $b$ -quarks.

45. To be a little more precise, we extrapolate the estimate to the VRs, which we sequentially unblind (to allow for continued refinement of the background estimate strategy, without immediately exhausting all opportunities for cross-checking the method). At this point, extending the estimate to the SR is something between and extrapolation and interpolation – the wording is perhaps a little tricky, as our VRs flank it in

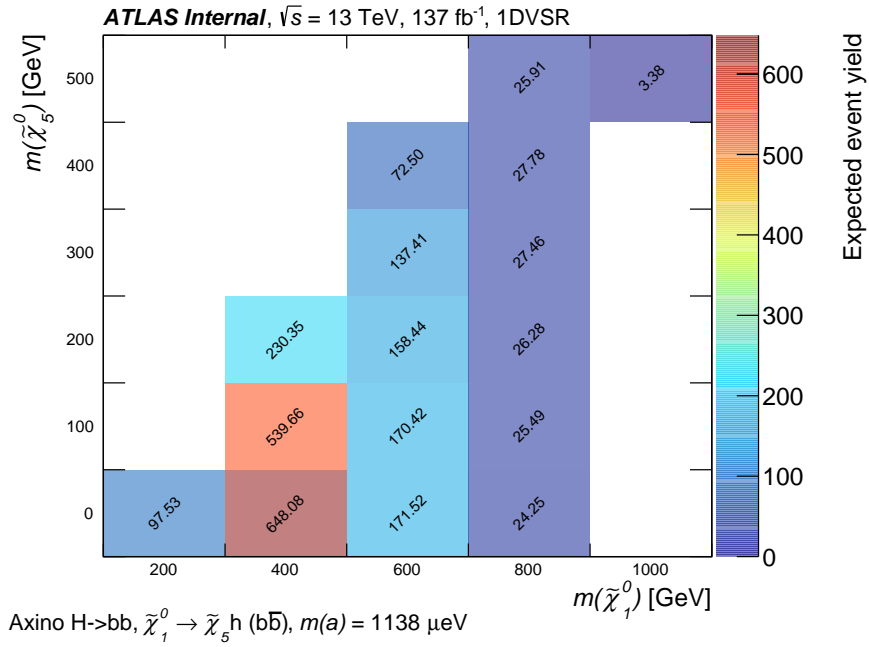


(a)

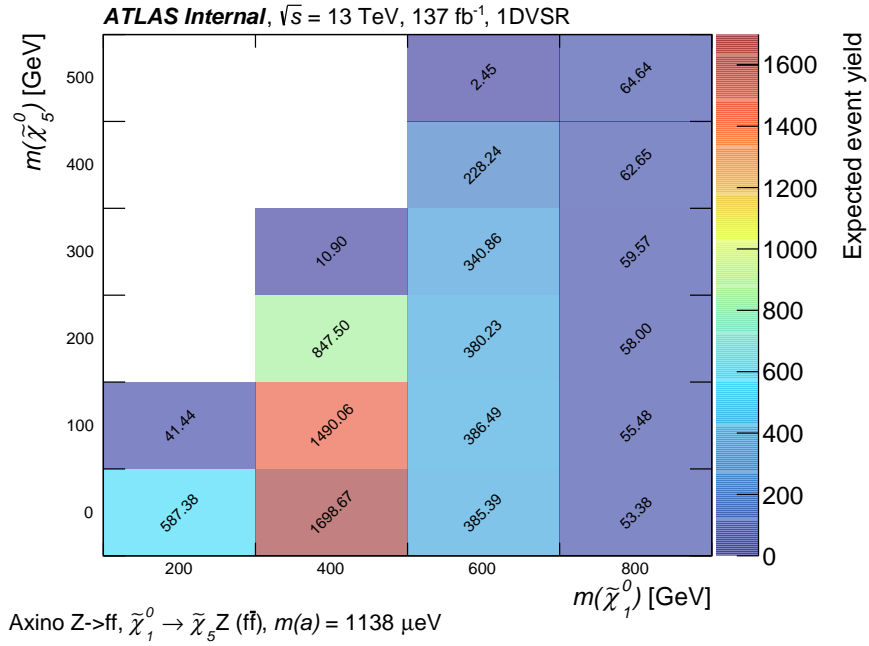


(b)

Figure 5.18: Expected event yields for the Higgs Portal signal model, in the (a) 1 and (b) 2 FV SRs. Taken from Ref. [143].



(a)



(b)

Figure 5.19: Expected signal yields for the axino signal model, for the (a)  $h \rightarrow b\bar{b}$  and (b)  $Z \rightarrow q\bar{q}$  channels. Note that these both correspond with  $m_a = 1138 \mu\text{eV}$ , which in turn corresponds with  $f_a = 5 \times 10^9$  GeV. None of the channels are appreciably sensitive to the other tested value of  $f_a = 5 \times 10^{10}$  GeV. Taken from Ref. [143].

the background level in the SRs based on MC simulations of SM processes. The strength of an MC-based estimate is that the analyzer nominally has a good understanding of precisely what processes are contributing to the background. However, this is only true in as much as the MC simulation is an accurate representation of reality. While these simulations are designed and tuned to match data, we know that they are inherently imperfect – and there are in fact multiple MC generators used by experiments in ATLAS, that implement different computational models of SM processes (such as hadronization), producing results that are not entirely consistent with one another.

One possible downside of the data-driven approach used here is that it is agnostic to the precise mechanisms that produce the background. To mitigate this issue – and serve as a cross-check of the background estimate – we perform a second, independent background estimate<sup>[46]</sup> comprised of three parts: each models a process that, based on physics principles and past analyses, we suspect will contribute to the background. We refer to these two methods as the *inclusive* and *combined* background estimates, respectively. In the following subsections we will review both methods, with particular emphasis given to the *accidental crossing* component of the combined background estimate, a component to which I significantly contributed.

### 5.5.1 *Inclusive Background Estimate: 1 DV Analysis Channels*

Our main background estimate method is referred to as the *track density* method, and its basic assumption is that the number of background DVs in a given region is correlated with the track density of the event<sup>[47]</sup>. We will outline this method below, before discussing its

---

the two-dimensional DV mass-multiplicity space as shown for example in Figure 5.12.

46. As will be discussed further below, this independent estimate is only performed for the 1 VSI DV SR. For the FV-based SRs, only the first background estimate method is performed.

47. We also develop a more complex version of this method, the aptly-named *hybrid method*, that uses an additional step of matching DVs to jets and parameterizes the background in a slightly more complex way. This method is only used as a validation check – in addition to the combined background estimate

application to the specific analysis channels.

In the track density method, we use the CRs to estimate an *event-DV probability* (EDP), which is computed as

$$\text{EDP (DV|Event}(x, y)) = \frac{\# \text{ of DVs in events with } (N_{b\text{-tag}} = x, N_{\text{tracks}}^{\text{event}} = y)}{\# \text{ of events with } (N_{b\text{-tag}} = x, N_{\text{tracks}}^{\text{event}} = y)}. \quad (5.5)$$

- $N_{b\text{-tag}}$  is the number of  $b$ -tagged EMTopo jets,
- $N_{\text{tracks}}^{\text{event}}$  is the number of tracks in the event.

In fact, omitted from Equation 5.5 is the fact that the EDP is calculated independently for different  $m_{\text{DV}}$  and  $N_{\text{tracks}}^{\text{DV}}$  ranges: we are interested in the probability of an event having a background DV that falls within a particular mass range and track multiplicity, as these are the variables that define our VRs and SR<sup>[48]</sup>. In practice, computing the EDP consists of producing histograms of the number of DVs as a function of their events'  $N_{b\text{-tag}}$  and  $N_{\text{tracks}}^{\text{event}}$ , as well as histograms of these events, and dividing one by the other as shown in Figure 5.20. Note that when constructing these histograms, we reweight their entries as to match the underlying pileup distributions between the CRs and VRs<sup>[49]</sup>. We treat the resulting quotient histogram as a model of the EDP, with which we can then compute the number of background events in a region as

$$N_{\text{background}} = \sum_{i=0}^{N_{\text{events}}} \text{EDP (DV|event}_i) , \quad (5.6)$$

where the EDP used is that corresponding to the desired DV mass range and track multiplicity.

---

(Section 5.5.2) – and is described in Appendix A.13. In fact, a third method is also discussed in Ref. [143], which was developed in the analysis discussed in Ref. [196]. However as it was only used to motivate the development of the other methods, we omit its discussion for the sake of clarity (and brevity).

48. In light of this, it would be perhaps more transparent to write the EDP as  $\text{EDP}_{m_{\text{DV}}}^{N_{\text{tracks}}}(\text{DV}(m_{\text{DV}}, N_{\text{tracks}}) | \text{Event}(x, y))$ . However this notation is cumbersome, so we will continue to suppress it with the understanding that computing the background for a particular region requires using the EDP for the associated  $m_{\text{DV}}$  range and  $N_{\text{tracks}}^{\text{DV}}$  value.

49. See Section 5.6.1.2.1.

One weakness of this approach is that it requires sufficient statistics in the data to build a reliable model. This is not always the case, which necessitates an extension of the method discussed in Appendix A.12.

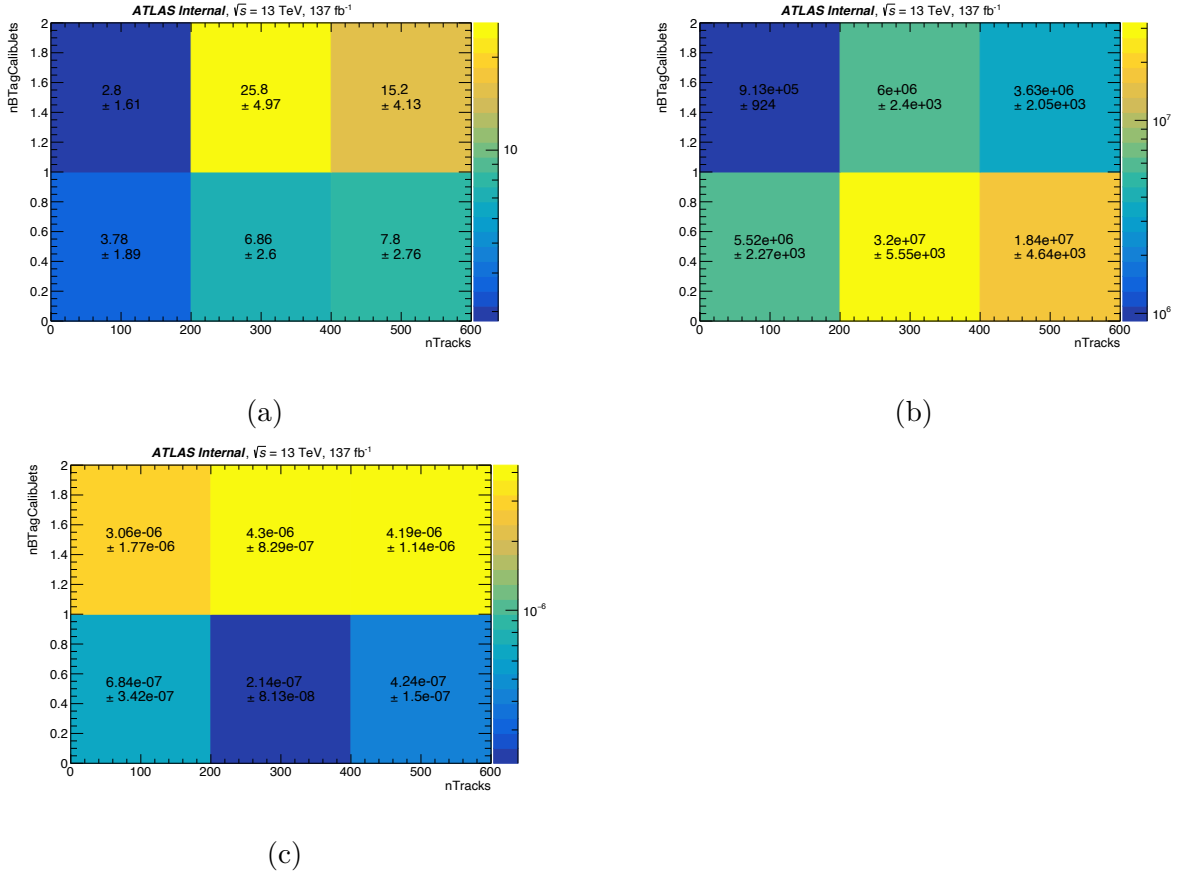


Figure 5.20: The track density estimation method, performed in the PTR with  $N_{\text{tracks}}^{\text{DV}} \geq 4$ ,  $m_{\text{DV}} > 5$  GeV, outside detector material, for the 1 VSI DV analysis channel. The histograms correspond with (a) the number of DVs, (b) the number of events, and (c) the resulting EDP. The non-integer counts are a consequence of pileup re-weighting, whereby PTR events are re-weighted so that the event pileup distribution matches that of the MTR. Taken from Ref. [143].

### 5.5.1.1 1 VSI DV Analysis Channel

The results for the inclusive background estimate are provided in Table 5.35. Note that VR8 was left blinded until unblinding of the SR, as it was found to have significant signal

contamination. It is thus omitted from the results of this analysis channel, being of relatively little use.

The largest discrepancy is seen in VR1, which (based on MC simulation studies) is likely due to contributions from  $B$ -meson decays and hadronic interactions not present in the other VRs<sup>[50]</sup>. As this background appears to be significantly different in nature than that in the SR, this discrepancy is not particularly concerning<sup>[51]</sup>.

Background Estimate: 1 VSI DV					
Region Name	$m_{DV}$ [GeV]	$N_{\text{tracks}}^{\text{DV}}$	Estimate	Validation (Hybrid method)	Observed Events
VR1	[ 2, 5]	4	$1228 \pm 203$	$1519 \pm 252$	1971
VR2	[ 5, 10]	4	$7.0 \pm 1.8$	$7.2 \pm 1.9$	9
VR3	[10, 15]	4	$0.52 \pm 0.39$	$0.50 \pm 0.38$	0
VR4	[15, 20]	4	$1.1 \pm 0.6$	$1.2 \pm 0.6$	2
VR5	[ 5, 10]	5	$2.2 \pm 0.9$	$2.3 \pm 0.9$	3
VR6	[ 5, 10]	6	$1.6 \pm 0.7$	$1.7 \pm 0.8$	1
VR7	[ 5, 10]	$\geq 7$	$1.6 \pm 0.7$	$1.6 \pm 0.8$	0
SR	$> 10$ GeV	$\geq 5$	$0.56 \pm 0.40$	$0.60 \pm 0.43$	—

Table 5.35: An overview of the 1 VSI DV background estimate results, as well as the observed number of events in the VRs. VR8 is omitted as it was ultimately not used during validation of this method. The hybrid method corresponds to an additional validation method described in Appendix A.13. Uncertainties are a combination of statistical uncertainties, as well as non-linearity and pileup systematic uncertainties (Section 5.6.1); the systematic uncertainties can be asymmetric but – with little loss in precision – we report symmetrized errors here for simplicity. Taken from Ref. [143].

---

50. A similar discrepancy was seen in the corresponding VR in the analysis described in Ref. [196].

51. It is worth noting that, if we did not observe any qualitative differences, this discrepancy would be notable: given a large set of VRs, from Gaussian statistics we might naïvely expect to see a  $> 2\sigma$  deviation in approximately 4% of the VRs, while we see it here in  $\sim 14\%$  of them here.

### 5.5.1.2 1 FV Analysis Channel

The results for the inclusive background estimate are provided in Table 5.36, for the FV VRs and SR.

### 5.5.2 Combined Background Estimate for the 1 VSI DV Analysis Channel

The combined background estimate serves as a cross-check for the inclusive background estimate, which we perform specifically in the 1 VSI DV analysis channel. As such, it is only used to derive a “non-closure” uncertainty for the inclusive background estimate results, given by the extent to which these estimates’ results diverge.

The combined background estimate method consists of three components:

- **Hadronic Interactions (HI):** This process corresponds with the interaction of SM particles with the detector material – both the sensors and the mechanical support structures – that may produce DVs with sufficient reconstructed mass and track multiplicity as to be signal-like.
- **Merged Vertices (MV):** This process is purely a reconstruction effect, where two (non-signal-like) DVs may in fact be reconstructed as a single, merged DV if they are sufficiently close to one another. This also may produce a DV with sufficient reconstructed mass and track multiplicity as to be signal-like.
- **Accidental Crossings (AX):** This process is, like MV, a reconstruction effect. In this case, we consider the process whereby a non-signal-like DV may be accidentally crossed (intercepted) by an spurious track (such as from pileup processes). This track is then treated as one of the DV tracks, and may result in a reconstructed mass and track multiplicity that promote the DV to signal-like status.

In the following subsections, we will describe the modeling of each of these processes.

Background Estimate: 1 FV					
Region Name	$m_{DV}$ [GeV]	$N_{\text{tracks}}^{DV}$	Estimate	Validation (Hybrid method)	Observed Events
VR1			$1057.9 \pm 20.24$	1013.92	1287
VR1 <sub>inside</sub>	[ 2, 5]	4	$17465.72 \pm 69.94$	15069.52	14669
VR1 <sub>Nseeds</sub>			$983.8 \pm 18.40$	906.72	850
VR2 <sub>inside</sub>	[ 5, 10]	4	$1028.31 \pm 16.11$	887.52	890
VR2 <sub>Nseeds</sub>			$356.2 \pm 11.33$	324.62	363
VR3 <sub>inside</sub>	[10, 15]	4	$72.14 \pm 4.34$	62.69	55
VR3 <sub>Nseeds</sub>			$100.25 \pm 5.72$	91.86	101
VR4 <sub>inside</sub>	[15, 20]	4	$18.26 \pm 2.02$	15.93	20
VR4 <sub>Nseeds</sub>			$26.81 \pm 2.61$	24.64	28
VR5 <sub>inside</sub>	[ 5, 10]	5	$603.16 \pm 11.45$	512.79	528
VR5 <sub>Nseeds</sub>			$17.86 \pm 2.66$	14.84	15
VR6 <sub>inside</sub>	[ 5, 10]	6	$369.56 \pm 8.84$	314.05	327
VR6 <sub>Nseeds</sub>			$3.55 \pm 1.06$	2.98	2
VR7 <sub>inside</sub>	[ 5, 10]	$\geq 7$	$303.58 \pm 7.89$	257.88	269
VR8 <sub>inside</sub>	$> 20$	4	$11.44 \pm 1.51$	10.01	17
VR8 <sub>Nseeds</sub>			$27.24 \pm 2.58$	24.84	40
VR9 <sub>inside</sub>	$> 10$	$\geq 5$	$45.63 \pm 3.02$	38.94	43
VR9 <sub>Nseeds</sub>			$10.97 \pm 1.64$	9.94	9
SR	$> 10$	$\geq 5$	$0.81 \pm 0.49$	-	-

Table 5.36: An overview of the 1 FV background estimate results, as well as the observed number of events in the VRs. Uncertainties are treated as in Table 5.35, and are omitted from the hybrid method validation for simplicity. For the various VR definitions, see Table 5.31. Taken from Ref. [143].

### 5.5.2.1 Hadronic Interactions (HI)

As briefly described above, the HI process primary corresponds with SM particles scattering off of the detector material’s constituent nuclei. It also includes – to a lesser extent – the scattering of SM particles off of lower-density materials such as gases<sup>[52]</sup>. The DV-level material map selection (Section 5.4.3.2) is meant to eliminate this source of background. While it does this quite effectively, it nonetheless may leave behind HI-induced DVs that will contaminate the SR, and so we want to model this background contamination.

To model the HI process, we examine DVs in events in the MTR (Section 5.4.2) that pass the baseline DV-level selections in Section 5.4.3.2. The DV track multiplicity distribution is fit with the function

$$N_{\text{tracks}}^{\text{DV}}(m) = \left( \frac{1}{C(m-b)} + \exp \frac{m-B}{l} \right)^{-1}, \quad (5.7)$$

- $N_{\text{tracks}}^{\text{DV}}$  is the DV track multiplicity,
- $m$  is the DV mass (reconstructed by assigning  $m_{\pi^\pm}$  to the tracks),
- $\{b, l, B, C\}$  are fitting parameters.

which – as validated in MC-based studies on  $Z \rightarrow \nu\bar{\nu} + \text{jets}$  samples<sup>[53]</sup> – models the multiplicity distribution of DVs produced by the HI process. This fit is performed in the VRs, and extrapolated to the (blinded) SR ( $m_{\text{DV}} \geq 10 \text{ GeV}$   $N_{\text{tracks}} \geq 5$ ) to estimate its HI contamination.

In data, where we do not have truth-level information by which we can validate our methods (as in MC simulation), we perform a *closure test* for this modeling by comparing it against a selection of  $\Delta R_{\text{max}} < 0.8$ , and verifying that the fit and the selection yield similar results. This selection, based on studies performed for the analysis described in Ref. [196],

---

52. These are in some way similar processes as the non-collision background described in Section 5.4.2.3, except that they are not induced by beam particles (and the corresponding energy distributions of the interactions may be quite different).

53. See Appendix A.14.

eliminates DVs that are more likely to be the products of accidental crossings (Section 5.5.2.3), where  $\Delta R_{\max}$  is the maximum  $\Delta R$  between a DV track and the vector sum over transverse momenta  $\sum_i \vec{p}_{T,i}$  of the other tracks attached to the DV. As an additional cross-check of this method (within both data and MC simulation), the fit is also performed in a similar region defined by the MTR and baseline DV-level selections, except that the material veto is lifted and the fit is extended to the  $m_{\text{DV}} \geq 10 \text{ GeV}$   $N_{\text{tracks}} \geq 5$  region. The HI fits – both for the estimate and for validation in data – are shown in Figure 5.21. The resulting contributions to the background estimate are provided in Table 5.37.

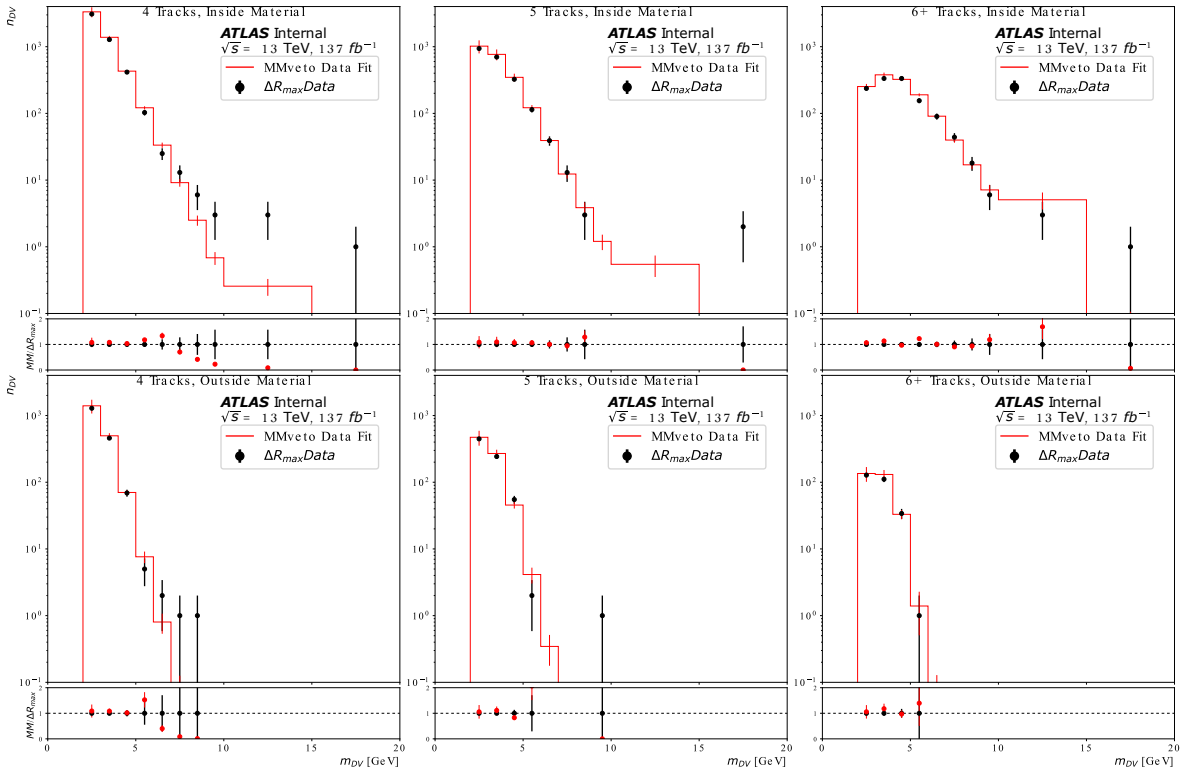


Figure 5.21: Fits performed to estimate the HI contribution to the background. Note that fits are performed in both the inside and outside material regions. For the latter, the SR is blinded. Modified from Ref. [143].

Region	Track Multiplicity	$m_{DV}$ [GeV]	Number of HI Events
VR1	4-track	[ 2, 5]	$(2.00 \pm 0.36) \times 10^3$
VR2	4-track	[ 5, 10]	$(8.5 \pm 2.0) \times 10^0$
VR3	4-track	[10, 15]	$(1.1 \pm 1.4) \times 10^{-4}$
VR4	4-track	[15, 20]	$(1.4 \pm 9.1) \times 10^{-9}$
VR5	5-track	[ 5, 10]	$4.5 \pm 1.3$
VR6	6-track	[ 5, 10]	$1.40 \pm 0.94$
VR7	> 6-track	[ 5, 10]	$0.0 \pm 0.0$
VR8	4-track	> 20	$(0.17 \pm 4.30) \times 10^{-13}$
SR	> 4-track	> 10	$(1.8 \pm 5.9) \times 10^{-5}$

Table 5.37: The HI background estimate results. Note that the expected numbers of events cover many orders of magnitude, depending on the region. Taken from Ref. [143].

### 5.5.2.2 Merged Vertices (MV)

In the VSI algorithm, two DVs may be merged into a single vertex if their distance measure,

$$S = \sqrt{(\vec{v}_1 - \vec{v}_2) (\text{cov}(\vec{v}_1) - \text{cov}(\vec{v}_2))^{-1} (\vec{v}_1 - \vec{v}_2)^T}, \quad (5.8)$$

- $S$  is the distance measure,
- $\vec{v}_i$  is the  $\overrightarrow{\text{DV-PV}}$  corresponding with the  $i$ 'th DV,
- $\text{cov}(\vec{v}_i)$  is the covariance matrix of the  $i$ 'th DV, from the VSI fitting algorithm.

satisfies  $S < 10$ , and one of the following conditions is satisfied [143, 170]:

1. **Re-assembling:** DVs with more tracks will have better position resolution than those with fewer, and so tracks of a lower-multiplicity DV are extrapolated to the higher-multiplicity DV. If these tracks all point towards the higher-multiplicity DV, the two DVs are merged.
2. **Suggested refitting:** The lower-multiplicity DV is refit, using the position of the higher-multiplicity DV as the starting point. If  $S < 4$  after this refitting procedure, the

two DVs are merged.

3. **Magnet merging:** Each track from the higher-multiplicity DV is iteratively associated with the lower-multiplicity DV, and the lower-multiplicity DV is refit. If  $S < 4$  after any of the refits, the two DVs are merged.
4. **Wild merging:** All tracks from both of the DVs undergo a single vertex fit, and if the resulting DV's position is within  $4\sigma$  of the higher-multiplicity DV, the two DVs are merged.

This merging process ensures that massive LLPs that produce multiple charged decay products will not be incorrectly reconstructed as clusters of low-mass, low-multiplicity DVs. As a consequence, however, it may merge background DVs to produce one that appears signal-like.

To model the MV background process, we use data from the VRs. The basic procedure is as follows:

1. We artificially overlay events, to produce a sample of *mixed events*.
2. In the mixed events, we merge pairs of DVs that satisfy  $S < 10$ , in order to produce *artificial* DVs. We expect these to have similar properties to the DVs produced by the MV process during reconstruction.
3. We use the artificial DVs to construct a *mass template* from the distribution of their masses, applying full DV track cleanings (Section 5.4.3.1) to them.
4. We use the mass template to estimate the number of MV events in the SR.

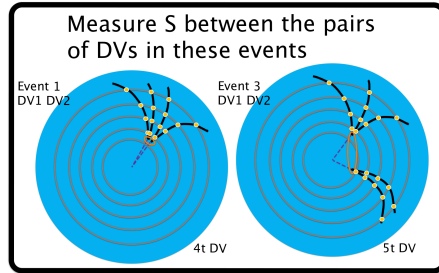
Multiple independent iterations of this procedure are performed, for treating the merging of  $m$ - and  $n$ -track DVs for different values of  $\{m, n\}$ . While this procedure is relatively simple, there are two important caveats regarding the production of the mass template:

- We have to account for the combinatoric effects of artificially overlaying events, which will produce more artificial DVs than there are DVs produced by the actual MV process. We will account for this by computing a *scale factor*.
- We also have to account for the fact that, based on the preceding discussion of merging conditions, the  $S < 10$  is a necessary but not sufficient condition for merging DVs. Thus in reality only some fraction of DV pairs with  $S < 10$  will be merged (although this is the only condition we apply when producing the artificial DVs). We will refer to this fraction as the *merging rate*, which we estimate by measuring the difference in DV pairs in the  $S < 10$  region, between those from the same event, and from artificially-overlaid events. Figure 5.22 provides a schematic of this procedure, and Figure 5.23 shows an example set of  $S^2$  distributions, for merging 2- and 3-track DVs.

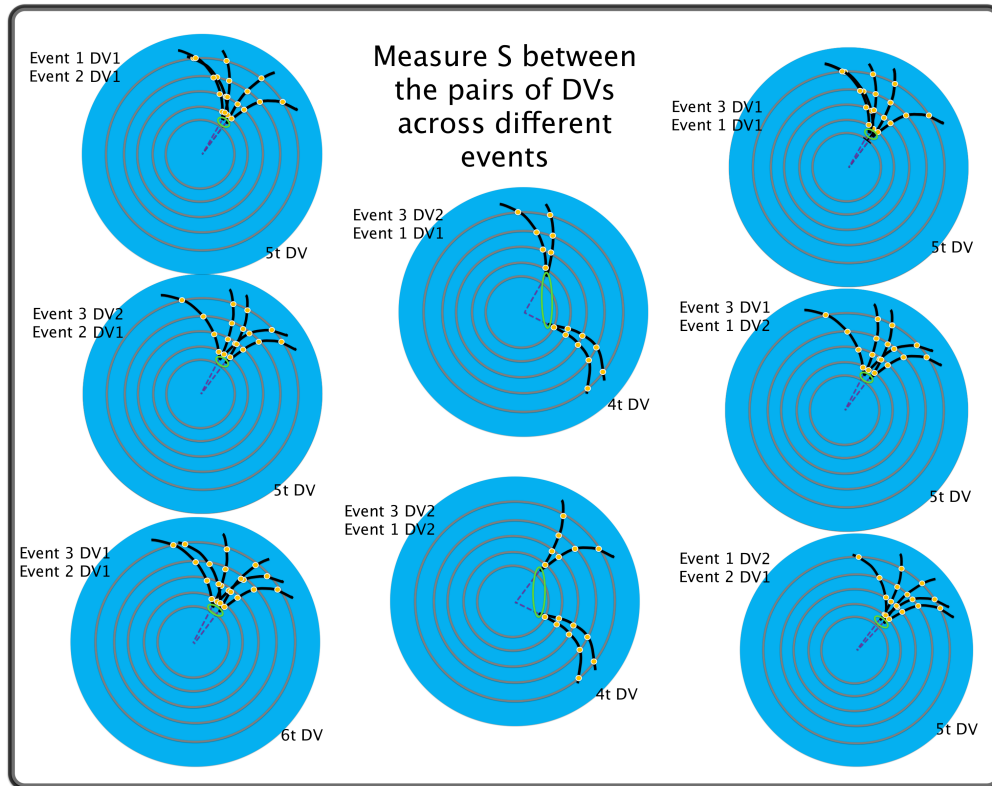
After production of the mass templates, we integrate the mass and multiplicity regions corresponding to the VRs and SR to estimate the contributions to the background in these regions. The results of this are provided in Table 5.38.

Region	Track Multiplicity	$m_{DV}$ [GeV]	Number of MV Events
VR1	4-track	[ 2, 5]	0.0065 $\pm$ 0.0032
VR2	4-track	[ 5, 10]	0.0690 $\pm$ 0.0093
VR3	4-track	[10, 15]	0.270 $\pm$ 0.018
VR4	4-track	[15, 20]	0.270 $\pm$ 0.019
VR5	5-track	[ 5, 10]	0.0098 $\pm$ 0.0044
VR6	6-track	[ 5, 10]	0.0063 $\pm$ 0.0037
VR7	> 6-track	[ 5, 10]	0.0042 $\pm$ 0.0030
VR8	4-track	> 20	0.730 $\pm$ 0.030
SR	> 4-track	> 10	0.183 $\pm$ 0.029

Table 5.38: The MV background estimate results. Taken from Ref. [143].



(a)



(b)

Figure 5.22: A schematic of measuring the distance in  $S$  between (a) same-event and (b) different-event DV pairs, for estimating the merging rate for the MV estimate method. Taken from Ref. [143].

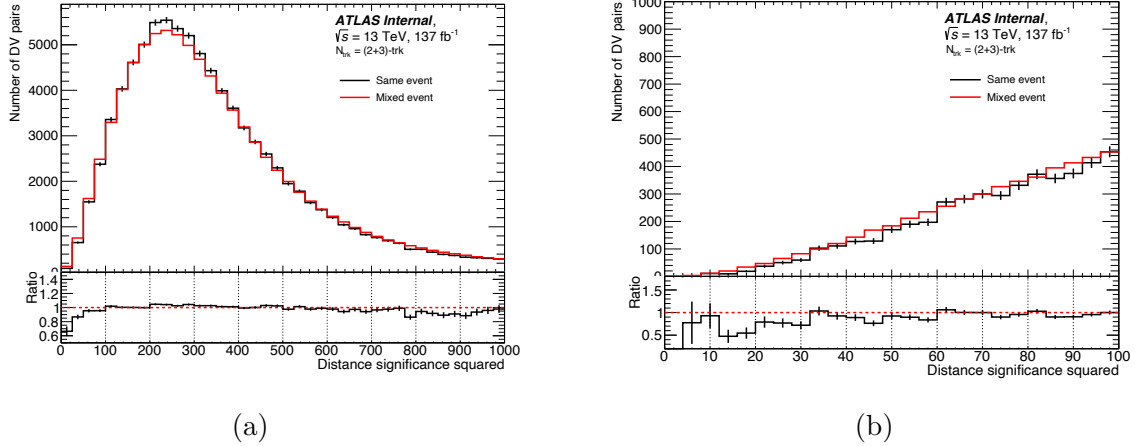


Figure 5.23: Example distributions of  $S^2$  for DVs within the same event, and within mixed events. The (a) full distributions show good agreement in the  $S > 10$  region (after application of the scale factor), while (b) the  $S < 10$  region shows a deficit in DV pairs in the same-event distribution, which is used to compute the  $S^2$ -dependent merging rate via the ratio between the two distributions: the merging rate is the difference of this ratio from unity. Taken from Ref. [143].

### 5.5.2.3 Accidental Crossings

The AX process corresponds with the scenario where a non-signal-like DV is “accidentally crossed” (or AX’ed, for short) by a spurious track originating from a different DV or PV. The AX’ing track becomes combined with this DV, increasing its track multiplicity  $N_{tracks}^{DV}$  as well as its computed mass  $m_{DV}$ , with this latter effect being particularly pronounced if the AX’ing track has a large opening angle with respect to the DV’s track 3-momentum vector sum. A number of the track cleanings and selections discussed in Section 5.4 are explicitly designed to eliminate AX’ing tracks, or DVs with the resulting misconstructed features; for example, the track cleaning requirement of rejecting tracks with hits that satisfy  $R_{xy} < R_{xy,DV}$  will remove tracks that may have originated from a different origin closer to the beam line. However, some amount of this background is expected to remain and contaminate the SRs, so we seek to model it as a means of validating the inclusive background estimate method (that implicitly covers it).

To model the AX process, we take the general approach outlined in Figure 5.24, which

works as follows:

1. We identify 2-track DVs in the data that correspond with  $K_S^0 \rightarrow \pi^- \pi^+$  decays.
2. We also identify 3-track DVs which are candidate AX'ed  $K_S^0$  decays, where 2 of the tracks are from the  $K_S^0 \rightarrow \pi^- \pi^+$  decay and the third is the AX'ing track.
3. Using the 2-track and 3-track  $K_S^0$  candidates, we estimate an *accidental crossing rate* (or “AX'ing rate”) as the ratio of 3-track  $K_S^0$  candidates versus all  $K_S^0$  candidates.
4. Using the 3-track  $K_S^0$  candidates, we identify which track is the likely AX'ing track, and save its kinematics to a *track database*. Specifically, we record its direction, as well as its opening angle with respect to the vector sum of the other DV tracks.
5. Using DVs in data – outside of our SR, and in or adjacent to our VRs in the  $(m_{\text{DV}}, N_{\text{tracks}}^{\text{DV}})$  plane – we produce artificially AX'ed DVs by randomly sampling our track database, and (artificially) attaching a track from it to a DV. We recompute the mass and track multiplicity of these AX'ed DVs, and use these to produce *mass templates*, which are distributions of these DVs' mass in a particular  $N_{\text{tracks}}^{\text{DV}}$  region. When adding a particular AX'ed DV's mass to a mass template, we scale its contribution by the appropriate AX'ing rate as to normalize it by the probability of the DV being AX'ed.
6. By integrating the mass templates over the corresponding  $m_{\text{DV}}$  and  $N_{\text{tracks}}^{\text{DV}}$  ranges, we produce estimates of the AX background in the VRs and SR.

Figure 5.25 shows an example mass template produced with the above method, and Table 5.39 provides the estimated AX background contribution in the VRs and SR. Appendix A.15 provides more details on the AX estimate method.

1. Find  $K_S^0$  candidates with an accidentally-crossing track.

2. Create a mass template of DVs with accidentally-crossing tracks.

3. Weight template by accidental crossing probability, estimated using  $K_S^0$  candidates.

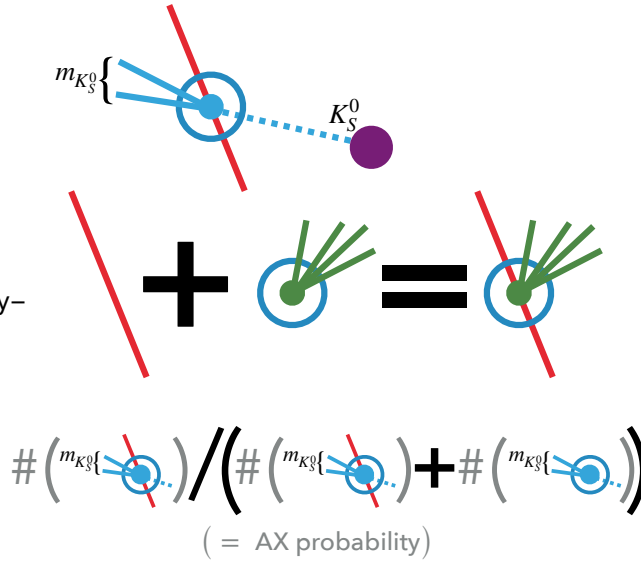


Figure 5.24: A schematic of the AX background estimate process, whereby we use  $K_S^0$  candidates identified in data to estimate and parameterize an AX'ing rate, and collect kinematics of likely AX'ing tracks. We use this information to model the AX background by attaching the AX'ing tracks to real DVs outside the SR. Taken from Ref. [143].

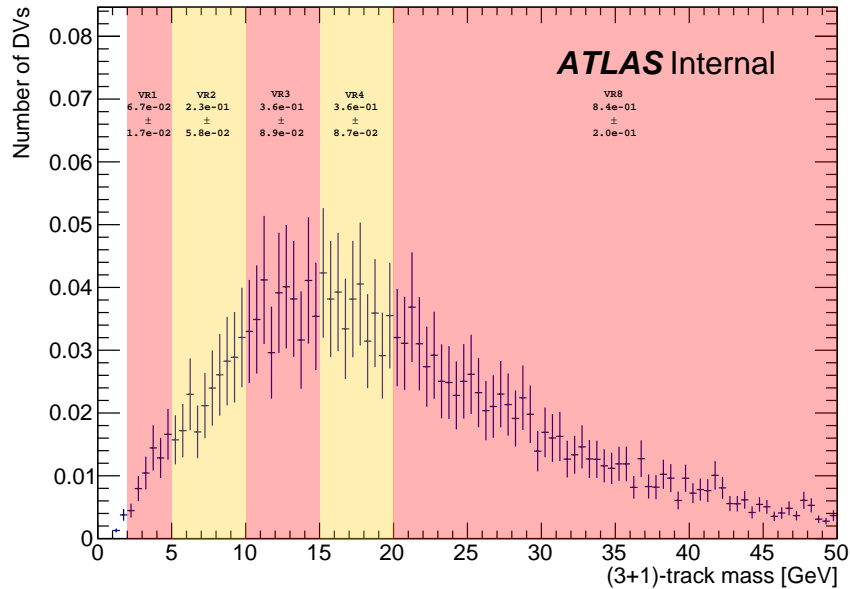


Figure 5.25: An example mass template produced as part of the AX background estimate, showing the integration of the different regions to produce estimated numbers of background events. Taken from Ref. [143].

Region	Track Multiplicity	$m_{DV}$ [GeV]	Number of AX Events
VR1	4-track	[ 2, 5]	0.067 $\pm$ 0.017
VR2	4-track	[ 5, 10]	0.230 $\pm$ 0.058
VR3	4-track	[10, 15]	0.360 $\pm$ 0.089
VR4	4-track	[15, 20]	0.360 $\pm$ 0.087
VR5	5-track	[ 5, 10]	0.061 $\pm$ 0.015
VR6	6-track	[ 5, 10]	0.0170 $\pm$ 0.0043
VR7	> 6-track	[ 5, 10]	0.0038 $\pm$ 0.0009
VR8	4-track	> 20	0.84 $\pm$ 0.20
SR	> 4-track	> 10	0.76 $\pm$ 0.14

Table 5.39: The AX background estimate results. Taken from Ref. [143].

#### 5.5.2.4 Combining results

With each of the combined background estimate’s components computed, we can combine them to produce our final combined background estimate – which serves as a validation check for the inclusive background estimate (Section 5.5.1) in the 1 VSI DV analysis channel. Figure 5.26 shows the combined estimate in the VRs and SR, and Table 5.40 provides a comparison of the inclusive and combined background estimates. We find that the nominal 1 VSI DV background estimate is in good agreement with the combined background estimate – as well as results from using the hybrid background estimate strategy – with the predicted number of background events falling within  $1\sigma$  of one another. Thus, we choose not to assign a *non-closure uncertainty* – a measure of limited confidence in the background estimate – when assessing the uncertainties in this analysis.

#### 5.5.3 Inclusive Background Estimate: 2 FV Analysis Channel

Owing to some of its structural differences with respect to the 1 DV analysis channels, the 2 FV analysis channel uses a somewhat different background estimation strategy. This involves

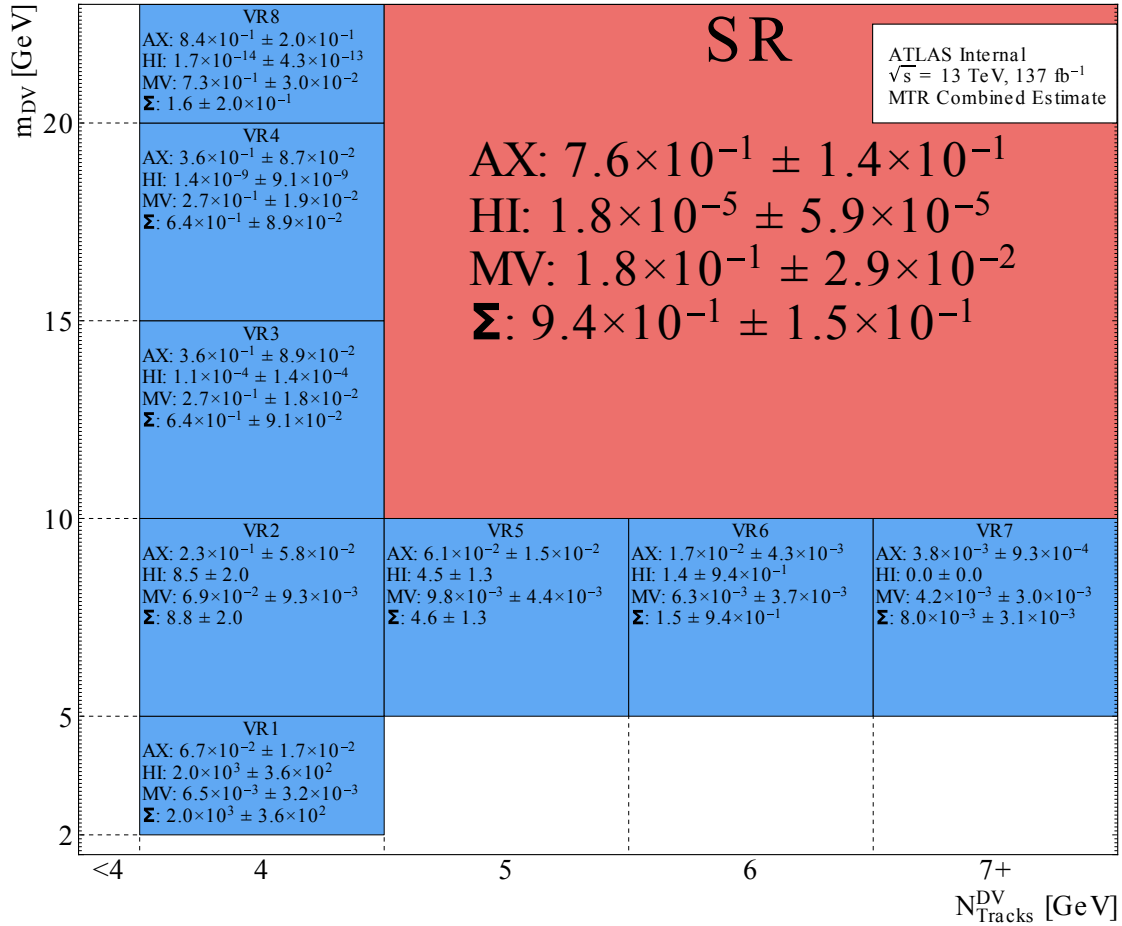


Figure 5.26: The combined background estimate, for the SR, as well as the fine-binned VRs. Taken from Ref. [143].

1 VSI DV Background Estimate Comparison	
Method	Estimate
Inclusive - Nominal	$0.56^{+0.40}_{-0.39}$
Inclusive - Hybrid	$0.60^{+0.44}_{-0.43}$
Combined	$0.94 \pm 0.15$

Table 5.40: A comparison of the background estimates for the 1 VSI DV analysis channel. Taken from Ref. [143].

the computation of a *jet-DV probability* (JDP), which parameterizes the likelihood of a background DV being produced in the presence of a jet with certain properties<sup>[54]</sup>. The basic procedure, performed in the CR, is as follows:

1. FVs are matched to jets if they satisfy  $\Delta R(\text{FV}, j) < 0.4$ , and the number of jet-matched DVs is parameterized as a function of the jet's  $p_T$  and  $b$ -tag. An FV may be matched with multiple jets; those matched with more than one jet are counted separately than those matched with only one. The jets are also counted and similarly parameterized<sup>[55]</sup>.
2. Using the two sets of matched jets and their events, we compute two JDP values, the  $\text{JDP}_{(1)}$  and  $\text{JDP}_{(\geq 2)}$ , the former using FVs with one jet match and the latter using those with multiple jet matches. Each is computed as

$$\text{JDP}_{(n)}(\text{FV}|\text{jet}(x, y)) = \frac{\# \text{ of FVs with } n \text{ matched jets with } (b_{\text{tag}} = x, p_T = y)}{\# \text{ of events with } (b_{\text{tag}} = x, p_T = y)}, \quad (5.9)$$

which is analogous to the EDP in Section 5.5.1.

3. With the two  $\text{JDP}_{(n)}$  definitions, we now predict the number of events with  $n$  background

---

54. Note that this concept also appears in the hybrid background estimate strategy discussed in Section A.13. However, the way that we define the JDP here is subtly different: As discussed below, we count the number of jet-matched FVs, as opposed to the number of DV-matched jets, allowing for multiple FVs to be matched to the same jet.

55. The parameterization is accomplished in practice by producing 2D histograms as in the track density method.

FVs, for  $n \in \{0, 1\}$  and the  $n \geq 2$  cases, as

$$N_{\text{background}}^{0 \text{ FV}} = \sum_{\text{events}} \prod_{\text{jets}} \left( 1 - \text{JDP}_{(1)} - \text{JDP}_{(\geq 2)} \right), \quad (5.10)$$

$$N_{\text{background}}^{1 \text{ FV}} = \sum_{\text{events}} \left( \prod_{\text{jets}} \left( 1 - \text{JDP}_{(1)} - \text{JDP}_{(\geq 2)} \right) \times \left( \sum_{\text{jets}} \frac{\text{JDP}_{(1)}}{1 - \text{JDP}_{(1)} - \text{JDP}_{(\geq 2)}} \right) \right), \quad (5.11)$$

$$N_{\text{background}}^{\geq 2 \text{ FV}} = N_{\text{events}} - N_{\text{background}}^{1 \text{ FV}} - N_{\text{background}}^{0 \text{ FV}}, \quad (5.12)$$

where the sums and products over jets are taken over each event.

The results of this background estimate are provided in Table 5.41.

Background Estimate: 2 FV						
Region Name	$m_{\text{DV}}$ [GeV]	$N_{\text{tracks}}^{\text{DV}}$	Material Map Veto	$N_{\text{seeds}}^{\text{DV}}$	Estimate	Observed Events
VR1	$\geq 1.5$	3	Fail	$\geq N_{\text{tracks}}^{\text{DV}}$	$158.81 \pm 12.93$	193
VR2	$\geq 1.5$	3	Fail	$\in [2, N_{\text{tracks}}^{\text{DV}})$	$108.09 \pm 4.25$	138
VR3	$\geq 1.5$	$\geq 4$	Fail	$\geq N_{\text{tracks}}^{\text{DV}}$	$80.68 \pm 5.02$	89
VR4	$\geq 1.5$	$\geq 4$	Fail	$\in [2, N_{\text{tracks}}^{\text{DV}})$	$47.52 \pm 3.04$	41
VR5	$\geq 1.5$	3	Pass	$\geq N_{\text{tracks}}^{\text{DV}}$	$4.55 \pm 1.04$	7
VR6	$\geq 1.5$	3	Pass	$\in [2, N_{\text{tracks}}^{\text{DV}})$	$42.20 \pm 3.08$	40
VR8	$> 0$	$\geq 4$	Pass (loose)	$\in [2, N_{\text{tracks}}^{\text{DV}})$	$36.55 \pm 3.09$	43
SR	$\geq 1.5$	$\geq 4$	Pass	$\geq N_{\text{tracks}}^{\text{DV}}$	$1.29 \pm 0.59$	–

Table 5.41: An overview of the background estimate results for the 2 FV analysis channel, for the VRs and SR. Uncertainties on the background estimates reported here are given as a combination of statistical, pileup and non-linearity uncertainties, treated as independent of one another. Taken from Ref. [143].

### 5.5.4 Summary of Background Estimates

To summarize the preceding sections, we have reviewed methods for producing data-driven background estimates for each of the analysis channels, as well as a set of cross-checks that validate these methods. By modeling the background through real data in CRs, these estimates have the advantage of not relying on the accuracy of MC simulations, and – particularly for the 1 DV analysis channels – we find good agreement between the estimation method and validation checks performed in data. Table 5.42 summarizes the final background estimates from above.

Background Estimate Summary	
Analysis Channel	Background Estimate
1 VSI DV	$0.56 \pm 0.40$
1 FV	$0.81 \pm 0.49$
2 FV	$1.29 \pm 0.59$

Table 5.42: A summary of the background estimates for the SRs of all analysis channels. Uncertainties are symmetrized for simplified reporting – the asymmetries are very small, as the uncertainty is dominated by the (symmetric) statistical component. Taken from Ref [143].

In the following sections, we will see how the background estimates – together with the observed numbers of events – translate into limits on the various signal models studied. First, however, we will review some important details regarding the treatment of uncertainties in the analysis.

## 5.6 Uncertainties

One of the most important steps in any physics analysis – and in fact, any data analysis in general – is assessing and quantifying the uncertainties associated with any measurements, both the *statistical* uncertainties stemming from the data statistics, as well as the *systematic* uncertainties introduced by the data reconstruction and analysis methods themselves. Simply

put, a measurement without an associated uncertainty is typically not meaningful.

In the following subsections, we will review how the dominant sources of uncertainty are modeled, in each part of the analysis<sup>[56]</sup>. Particular emphasis will be given to systematic uncertainties stemming from large-radius tracking (LRT), for which I developed a dedicated study to model its effects on signal yield uncertainties across the four different signal models.

### 5.6.1 Background Estimate Uncertainties

As a data-driven estimate, the inclusive background estimate methods described in Sections 5.5.1 and 5.5.3 are sensitive to statistical uncertainties in the underlying data they use, in addition to possible effects of mismodeling.

#### 5.6.1.1 Statistical Uncertainties

These uncertainties enter into the background estimates via the EDP and  $JDP_{(n)}$  calculations, which involve histogramming DVs, jets and events. For the latter two, the statistics are sufficient that they can safely be approximated as Gaussian<sup>[57]</sup>, with each histogram bin with count  $N_i$  being assigned an uncertainty of  $\sigma_i = \sqrt{N_i}$ . However, this is not a safe assumption to make for the DV histograms, which typically have too low counts and should be treated with Poisson statistics. To handle this, we perform the following method<sup>[58]</sup> to estimate the resulting uncertainties in the background estimate:

---

56. While we will discuss various sources of uncertainty, as well as the concept of *limit setting* in the following chapter, we will not have a formal discussion or review of the statistical methods themselves. For a relatively comprehensive review of statistical methods relevant to particle physics, see Ref. [197, 198] (with a slight emphasis on Bayesian methods), as well as Ref. [199] for a concise yet thorough overview targeting particle physics applications.

57. Note that all these objects obey Poisson (or “counting”) statistics. One can approximate a Poisson distribution as a Gaussian when the distribution mean is sufficiently high – a common rule-of-thumb is a threshold of approximately 20, at which point the difference between the distributions is at around the percent level [200].

58. Here we discuss the EDP. The same methods apply to the  $JDP_{(n)}$ ’s.

1. For each DV histogram, we run  $10^4$  pseudo-experiments using the extended-statistics variant of the method (Appendix A.12) whereby extended CRs are used to compute the EDP and the result is scaled by  $f = N_{\text{DV}}^{\text{target}}/N_{\text{DV}}^{\text{ext}}$  to account for the ratio of DVs in the original and extended regions.
2. In each experiment, the number of DVs in the (extended) CR is varied bin-by-bin by drawing a count for bin  $b_i$  from a Poisson distribution  $X \sim \text{Poisson}(N_i)$  where  $N_i$  is the original number of counts in  $b_i$ .
3. To vary the  $f$ -factor, a new value of  $N_{\text{DV}}^{\text{target}}$  is drawn from  $X \sim \text{Poisson}(N_{\text{DV}}^{\text{target}})$ .
4. The resulting background estimate is computed for each experiment, and the standard deviation of these results is taken as the final statistical uncertainty on the background.

Figure 5.27 shows the mean and standard deviation for each VR and SR in the 1 VSI DV analysis channel, from the above method.

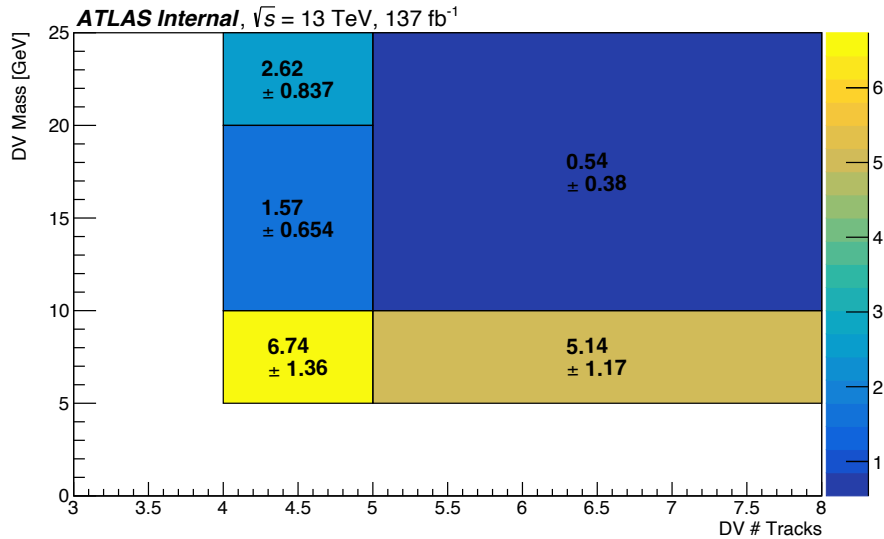


Figure 5.27: The mean and standard deviation for the background estimate for the 1 VSI DV analysis channel, computed using the pseudo-experiment method to simulate the effects of Poisson statistics, in the merged VR bins. VR1, which nominally has  $1228 \pm 203$  estimated background events, is excluded for better color scaling of the plot. Taken from Ref. [143].

### 5.6.1.2 Systematic Uncertainties

We evaluate a few different sources of systematic uncertainty in the background estimation<sup>[59]</sup> – which based on detailed studies of the method, are determined to be the dominant systematic uncertainties. For each background estimate, we will only report the two dominant systematic uncertainties. The two dominant systematic uncertainties are combined in quadrature, as they are assumed to be independent, and are then combined<sup>[60]</sup> in quadrature with the statistical uncertainty to yield the final background estimate uncertainty shown in Table 5.42. In practice, we find the systematic uncertainties to be dominated by the statistical uncertainty.

**5.6.1.2.1 Pileup Uncertainties** One systematic uncertainty that we model for the background is the pileup uncertainty, which accounts for differences in the pileup distributions of the PTR and MTR (and thus the CRs and VRs). As shown in Figure 5.28, the MTR has higher average pileup – which is to be expected, as pileup activity correlates with  $\cancel{E}_T$  triggers. In the background estimate (Section 5.5.1), we account for this by reweighting the events in the PTR and MTR to match the pileup distribution of the former with that of the latter. We take the difference between the nominal estimate and a non-pileup-reweighted version as the pileup systematic uncertainty, of approximately 5%. Due to the relatively simple modeling of this uncertainty, it is treated as symmetric.

---

59. Note that in Ref. [143], there is not a clear distinction made between statistical and systematic uncertainties – at least in terms of nomenclature (as they are treated correctly). In general, terms like “systematics” are used somewhat colloquially in the discussion of uncertainties in physics analyses. Here, we will make a clear distinction between uncertainties stemming entirely from counting statistics – which are of a statistical origin – and those which may stem from mismodeling effects and biases in the various estimation and reconstruction methods, which we shall refer to as systematic.

60. It is in fact typical to keep the reporting of statistical and systematic uncertainties separate, as the former is symmetric whereas the latter may be asymmetric. However, for simplicity we combine these uncertainties when reporting results here – a choice motivated partly by the fact that the statistical uncertainties are the dominant ones in this analysis, and also by the fact that owing to how we model the systematic uncertainties, we do report them as symmetric.

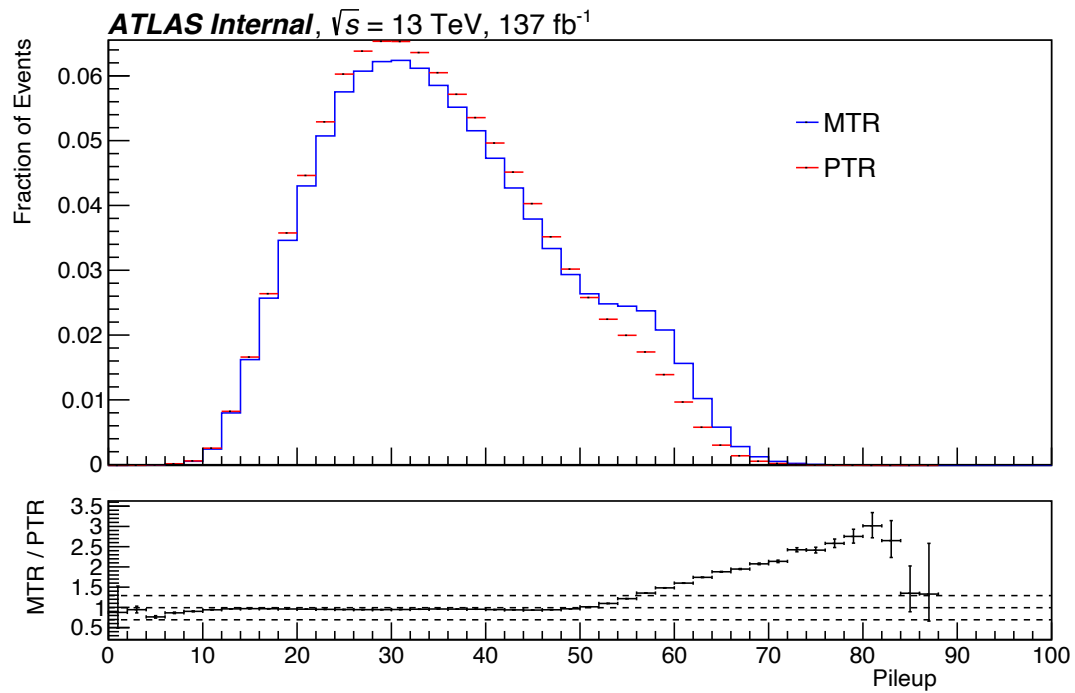


Figure 5.28: A comparison of the number of pileup vertices in the MTR and PTR. The lack of a bump in the 50-60 region of the PTR distribution is due to the enforced orthogonality of the MTR and PTR selections. Taken from Ref. [143].

**5.6.1.2.2 Non-closure Uncertainties** One last systematic uncertainty we will consider is *non-closure*, the discrepancy in background estimate validation. We have multiple types of background estimate validations in play – the combined estimate method for the 1 VSI DV analysis channel, the hybrid inclusive estimate method, and the validation tests performed using our VRs for each method. We define our non-closure uncertainty as the largest discrepancy between the nominal background estimate and any validation method, in any of the VRs or SR. As with the pileup uncertainty, we treat this as a symmetric uncertainty although it is assumed to be (partly) systematic in nature.

### 5.6.2 Summary of Background Uncertainties

In Table 5.43, we summarize the uncertainties on the background estimates. While the contributions from systematic uncertainties are non-negligible, we see that the statistical uncertainty is by far the largest – and as we treat these independent of one another (and thus add them in quadrature), it dominates in the total uncertainty we compute.

Background Uncertainty Summary					
Analysis Channel	Estimate	Statistical Uncertainty	Systematic Uncertainties		Total Uncertainty
1 VSI DV	0.56	$\pm 70\%$		Pileup $\pm 5\%$	$\pm 71\%$
1 FV	0.81	$\pm 57\%$	Non-closure $\pm 22\%$	Pileup $\pm 2\%$	$\pm 61\%$
2 FV	1.29	$\pm 45\%$	Non-closure $\pm 20\%$	Pileup $\pm 4\%$	$\pm 50\%$

Table 5.43: An overview of background estimate uncertainties for the three analysis channels. Note that the reported uncertainties for each analysis channel are not necessarily the same. Due to how the systematic uncertainties are modeled, only the uncertainty for the 1 VSI DV channel is reported as asymmetric, with the asymmetry being very small. Taken from Ref. [143].

### 5.6.3 *Signal Yield Uncertainties*

So far, we have seen how limited statistics and potential mismodeling effects contribute to uncertainties in the estimated number of background events in each SR. As we are ultimately counting some number of observed events, and comparing it to the combined estimated signal and background yield (the signal yield being different for each model and choice of model parameters), the only other place where uncertainties may reside is in the expected signal yield. The signal yields are estimated using MC simulations – there is not a “data-driven” approach available such as with the background estimation – and so we must contend with a host of uncertainties that originate from the theory inputs into the MC generators and the imperfections of their simulations. We must also consider the effects of detector reconstruction errors and inefficiencies, which will vary from one signal model to another as their different processes produce different kinds of signals (such as DVs with different masses and track multiplicities). In the following subsections, we will review the major sources of uncertainty in the signal yields. As noted earlier particular attention will be given to the systematic uncertainties associated with large-radius tracking – which is one of the leading sources of signal systematic uncertainties.

#### 5.6.3.1 Theory Uncertainties

The process of MC simulation for high-energy processes effectively consists of sampling high-dimensional probability distributions to statistically model the kinematics of particle interactions<sup>[61]</sup>. These probability distributions are constructed and scaled based on theory inputs, so that the MC generators are tuned to match theory predictions – and past measurements from experiments such as those at the LHC and Tevatron experiments, when possible. However these distributions all carry some associated uncertainties, stemming from

---

61. For a general review of MC methods – not specific to high-energy physics – see Ref. [201].

the limits of analytical theory calculations in estimating process cross-sections<sup>[62]</sup>. Handling of theory-based cross-sectional uncertainties is largely standardized across LHC experiments, and in practice is straightforward in its implementation (owing to common theory and software frameworks). While not specific to this analysis, we will briefly touch on a few specific sources of these uncertainties, if only to dispel possible mystery regarding their origins.

**5.6.3.1.1 General Cross-section Uncertainties** All the cross-sections used for the parton-level processes in the signal MC simulations are computed by the LHC theory group [203]. These include next-to-leading order (NLO) corrections, and resummation of soft gluon emissions to next-to-leading logarithmic (NLL) accuracy when possible<sup>[63]</sup>. Similarly, the theory group provides *factorization scheme* uncertainties, which relate to the computational process of QCD factorization that allows us to approximate parton interactions [205].

**5.6.3.1.2 Parton Distribution Function Uncertainties** The *parton distribution function*, closely related with the factorization scheme, is used to model how momentum is shared amongst partons in a proton. Modeling this momentum distribution is an important part of estimating  $pp$  collision cross-sections, as it determines the distribution of momenta of the interacting quarks – and the likelihood that an impinging particle will encounter a quark of a particular flavor, that carries a particular fraction of the full hadron momentum. PDFs cannot currently be determined by entirely analytic means, and are thus estimated via parameterized models that are fit to experimental data [206]. The PDF uncertainties are

---

62. As a reminder, a cross-section is the likelihood of a particular process. What precisely we mean by “process” here is context-dependent: we may simply refer to a parton-level process in a  $pp$  collision, or may also factor in subsequent particle interactions and decays (and processes such as hadronization). In practice, we typically distinguish between the parton-level process – the *matrix elements* of a process – and the subsequent hadronization, with separate models for each (with their associated uncertainties). For a discussion of these processes, and a review of efforts to combine them, see Ref. [202].

63. These corrections refer to dealing with divergences in perturbative treatments of QCD. For a brief review of this topic, see Ref. [204].

derived via differences between PDF models – and the precise handling of these uncertainties is standardized among LHC experiments [207].

**5.6.3.1.3 QCD Coupling Uncertainties** Another source of uncertainty in cross-section calculations is the strong coupling<sup>[64]</sup>  $\alpha_s$ . Something we have left out of our discussion of the SM in Section 2.1 are the dynamics of QCD. To touch on this briefly, the strong coupling is given by [6, 208, 209]

$$\begin{aligned}\alpha_s(Q^2) &= \frac{g_2^2(Q^2)}{4\pi} \\ &\approx \left(\beta_0 \ln(Q^2/\Lambda_{\text{QCD}}^2)\right)^{-1},\end{aligned}\tag{5.13}$$

- $Q^2$  is the momentum transfer factor,
- $\beta_0$  is a constant,
- $\Lambda_{\text{QCD}}$  is the location of the Landau pole in QCD, a boundary condition set by renormalization.

An interesting consequence of this is that the QCD strong force is weaker at higher energy scales (corresponding with smaller length scales). Conversely, it becomes stronger at long distances, and one consequence of this phenomenon is *color confinement*, the fact that we do not observe bare color-charged particles<sup>[65]</sup>. Figure 5.29 shows the most recent measurements of  $\alpha_s(m_Z^2)$ , the coupling strength at the scale of the  $Z$ -boson mass. As with PDF uncertainties, the handling of uncertainties on  $\alpha_s$  are standardized across LHC experiments [207].

---

64. This is often referred to as the *strong coupling constant*, and described as an effective constant. However – as with other effective constants in the SM – it is important to remember that, as an “effective” constant, this term is not a true constant as it depends on the momentum transfer factor  $Q^2$ .

65. Color confinement is why we see jets as opposed to free quarks or gluons. For some more discussion of its consequences, see Appendix E. For a more general overview of the running of the QCD coupling – a topic deeply interlinked with the renormalization group – see Ref. [210] and Chapter 26 of Ref. [6].

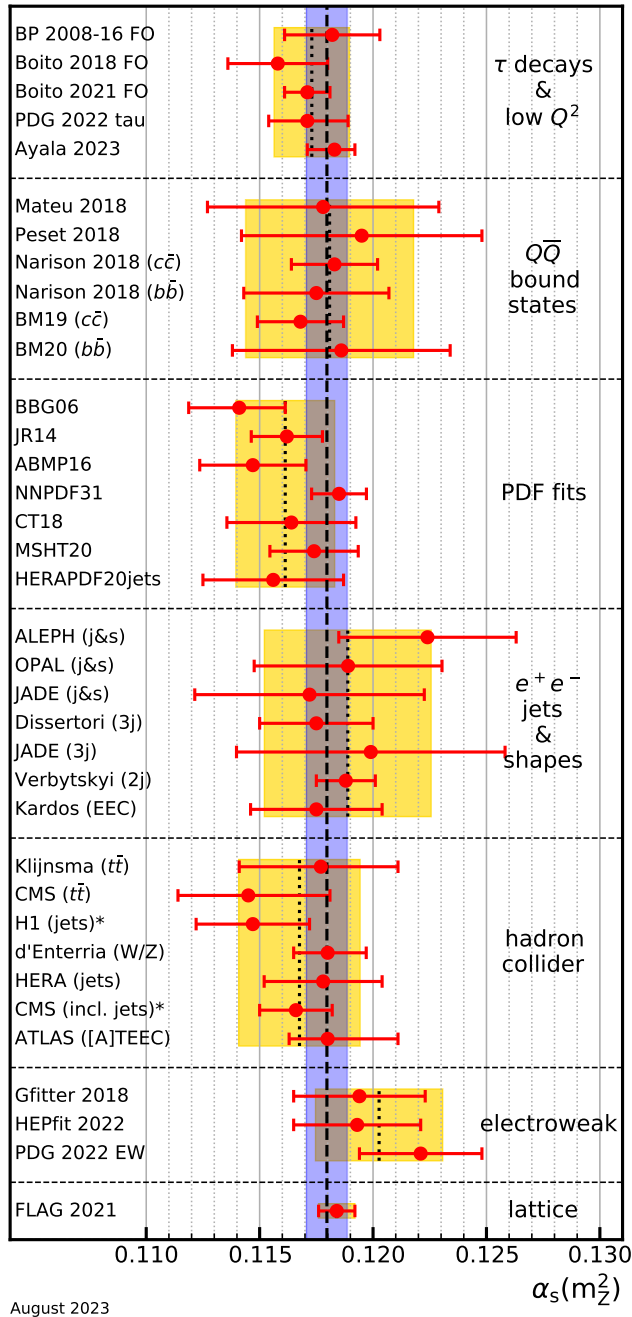


Figure 5.29: Various measurements of the strong coupling at the  $Z$ -boson mass scale. The Particle Data Group 2023 world average is  $\alpha_s(m_Z^2) = 0.1180 \pm 0.0009$ . Taken from Ref. [9].

### 5.6.3.2 Systematic Uncertainties

Aside from theory uncertainties, we also need to assess the systematic uncertainties that will affect our expected signal yields. These are, broadly speaking, related to how the physics of each model interacts with the ATLAS detector – and how our MC simulations may not fully capture particle-detector interactions or subsequent processing of that information to yield our final reconstructed objects.

**5.6.3.2.1 Jet and  $\cancel{E}_T$  Uncertainties** We assess the impact of systematic uncertainties stemming from jet and  $\cancel{E}_T$  reconstruction on the signal yields, following standard ATLAS prescriptions for handling jet energy scale<sup>[66]</sup> (JES) and jet energy resolution (JER) uncertainties [211], as well as uncertainties on the soft  $\cancel{E}_T$  component stemming from tracks not associated with any of our reconstructed objects. To do this, we recompute signal yields with these jet and  $\cancel{E}_T$ -related terms shifted within envelopes defined by their uncertainties. The standard deviation in the resulting signal yields is our final jet and  $\cancel{E}_T$  systematic uncertainty<sup>[67]</sup>.

**5.6.3.2.2  $\cancel{E}_T$  Trigger Uncertainties** The online  $\cancel{E}_T$  selection used by this analysis (Appendix A.4) is below the so-called *plateau* region where the  $\cancel{E}_T$  trigger efficiency nears 100% and is well-understood. By working in a lower-efficiency region, where a non-negligible fraction of events may be discarded due to online  $\cancel{E}_T$  mismeasurement, we need to account for the possibility of some resulting bias in our signal yields due to differences in how the trigger behaves in data and MC simulation.

---

66. This is related to the jet energy scale calibration briefly discussed in Section 4.2.8.2 and Appendix E.2.4.

67. As a technical note, we do not apply the full material map veto (Appendix A.10) to the signal yields when applying jet and  $\cancel{E}_T$  systematic variations, in order to lessen the computational cost. We instead apply a simpler veto, that operates the same way but lifts the check on the DV position uncertainty. This potentially shifts the nominal signal yield, but as the quantities being varied are not expected to strongly correlate with the uncertainty of DV positions, the resulting scale of the estimated errors is assumed to be comparable to what would be found with the full material map veto applied.

To account for this, we compare the trigger efficiencies in data and MC simulation. Of course, we cannot know the “efficiency” of the trigger in data in the classic sense, as we do not know the true  $\cancel{E}_T$  of a data event – and furthermore, we do not have information on an event if it did not pass any trigger (as we will not have saved it in the first place). Instead, we use a highly-efficient muon trigger as a *reference trigger*, and study the  $\cancel{E}_T$  trigger efficiency with respect to this muon trigger: does an event that activates the muon trigger also activate the  $\cancel{E}_T$  trigger? Our use of a muon trigger as a reference is apt as the online  $\cancel{E}_T$  is computed without muon spectrometer information – so muons will “look like”  $\cancel{E}_T$  to the  $\cancel{E}_T$  trigger algorithms.

In our comparison study<sup>[68]</sup>, we measure the  $\cancel{E}_T$  trigger efficiency as a function of  $\cancel{E}_T^{\mu}$ , the offline  $\cancel{E}_T$  computed where muons are treated as invisible as in the online  $\cancel{E}_T$ . An example of such a comparison plot is shown in Figure 5.30. We use the ratio of data and MC simulation trigger efficiencies to derive scale factors, with associated uncertainty determined by the data and MC simulation statistics. We apply these scale factors to the simulated samples, to account for any efficiency that they do not model.

**5.6.3.2.3 Systematic Tracking Uncertainties** Of particular interest, we must consider the systematic uncertainties stemming from imperfect tracking in our detector – in particular LRT reconstruction. To model this, we take an approach thematically similar to the accidental crossing (AX) background estimate (Section 5.5.2.3) and use  $K_S^0 \rightarrow \pi^+\pi^-$  candidate decays as a benchmark process. This time, we are interested in comparing the  $K_S^0$  yield in data and MC simulation:

1. We select 2-track DV  $K_S^0$  candidates, using the same general selection criteria as in the AX background estimate. As opposed to that estimate, we consider both VSI DV and

---

68. There are some additional technical details of our comparison study, that involve handling the different  $\cancel{E}_T$  triggers available during the various data-taking periods. We will omit some of these details from our discussion, as while important to the implementation of this study, they do not alter its underlying principle.

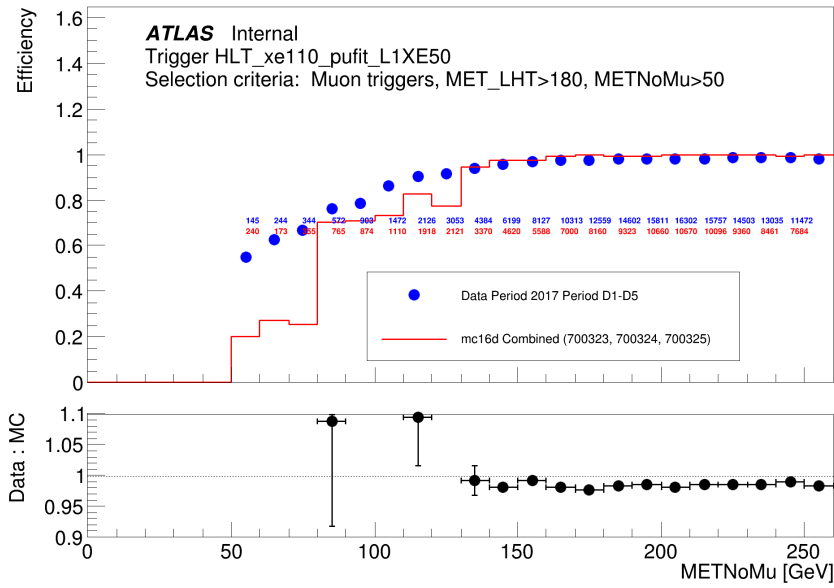


Figure 5.30: An example  $\cancel{E}_T$  trigger *turn-on* curve, showing the  $\cancel{E}_T$  trigger efficiency (with respect to a muon trigger) as a function of  $\cancel{E}_T^{hh}$ . As the  $\cancel{E}_T^{hh}$  increases, the trigger efficiency gradually reaches its plateau near 100% efficiency. The ratio of data versus MC simulation efficiency curves is used to determine the scale factor to apply to the MC simulation, and its uncertainty. Taken from Ref. [143].

FV cases, in order to model the tracking uncertainties for all analysis channels.

2. We compare the  $K_S^0$  yield in data and MC, as a function of  $R_{xy}$  as shown in Figure 5.31. The MC yield is normalized to data in the innermost detector region of  $R_{xy} \in (0, 38)$  mm where tracking efficiency is well-understood (from standard tracking algorithms).
3. We associate any excess in the MC simulation  $K_S^0$  yield with a tracking inefficiency that exists in data, but that is not being properly modeled in the MC simulation. In other words, the simulation is too optimistic in its modeling of track reconstruction. We combine the resulting estimated tracking inefficiency with a baseline value of 1.8% that is determined by the ATLAS tracking combined performance group, as shown in Figure 5.32.
4. We use the modeled inefficiency to perform a series of *track-killing* studies for each signal model, where tracks from DVs are randomly eliminated with a probability given by the tracking inefficiency and the resulting signal yield is recalculated.
5. The standard deviation of the signal yields from the track-killing studies are taken as the tracking systematic uncertainties for each model.

Figure 5.33 shows the tracking systematic uncertainties for a set of gluino  $R$ -hadron models, and Figure 5.34 shows these for a set of Wino-Bino co-annihilation models. In general, we find the tracking systematic uncertainty to be the largest of the signal systematic uncertainties, ranging from  $\mathcal{O}(1\%)$  -  $\mathcal{O}(10\%)$ . However, its significance in the statistical interpretation of our results is small compared to the statistical uncertainties. For more details on the tracking systematic uncertainties study, see Appendix A.16.

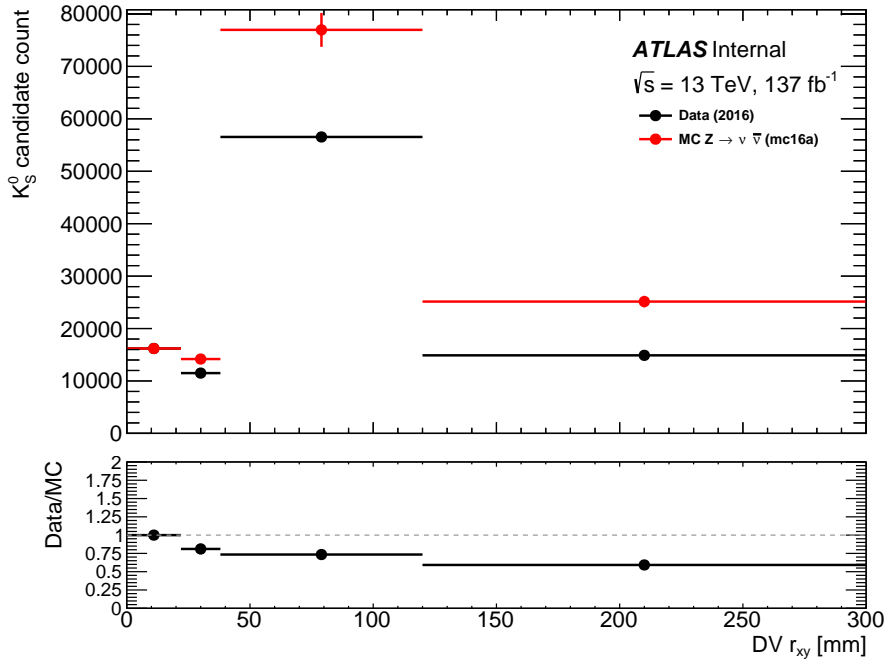


Figure 5.31: A comparison of data and MC simulation  $K_S^0$  yields, as a function of  $R_{xy}$ . Taken from Ref. [143].

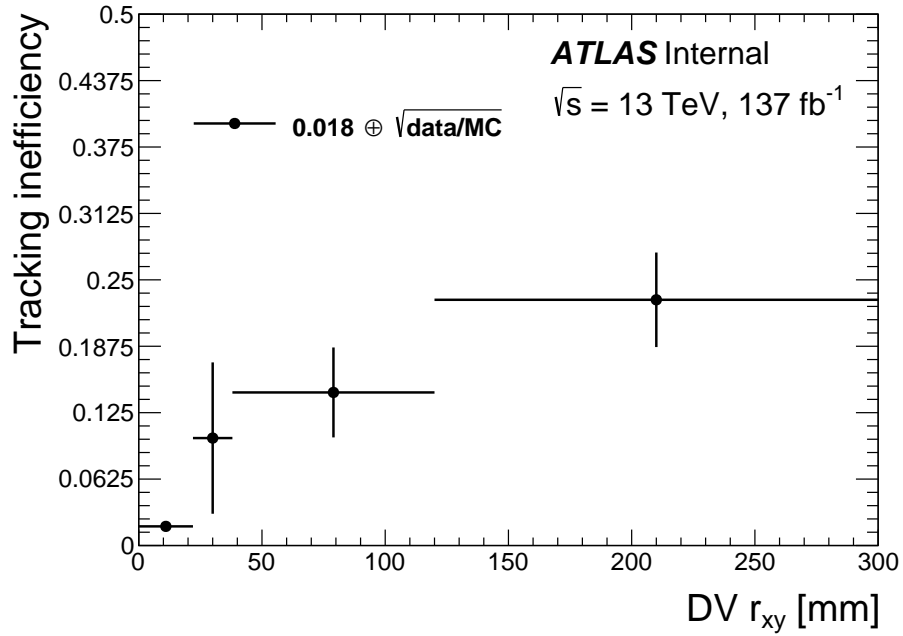
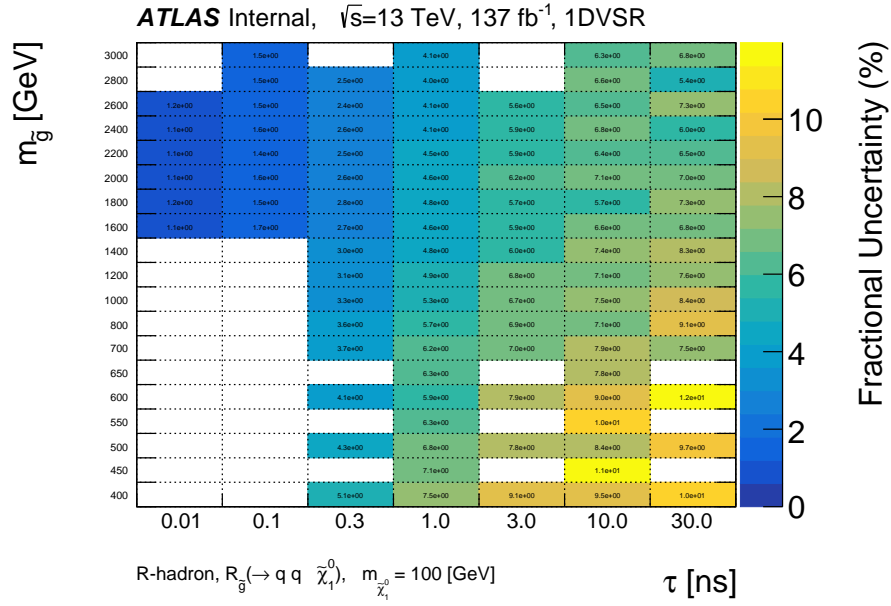
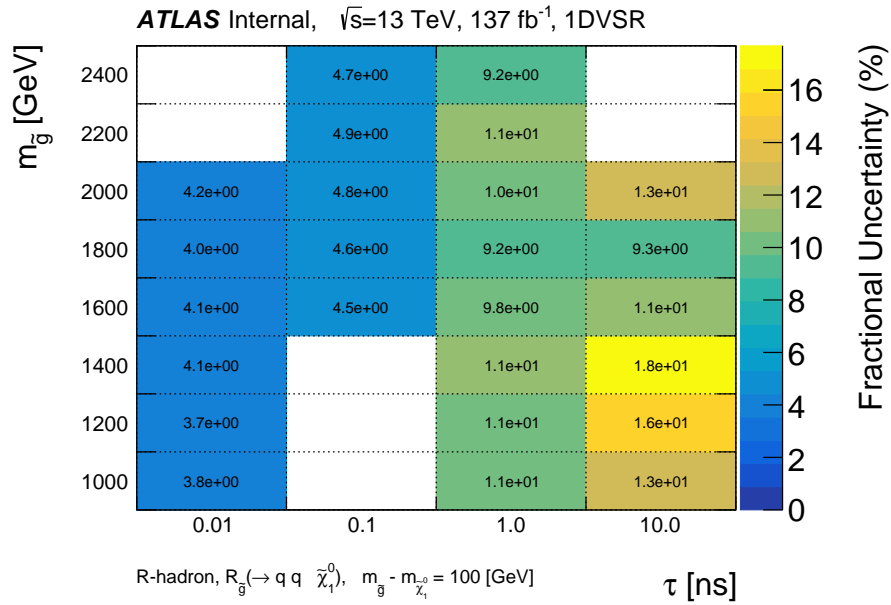


Figure 5.32: The estimated tracking inefficiency, as a function of  $R_{xy}$ . Taken from Ref. [143].



(a)



(b)

Figure 5.33: Tracking systematic uncertainties for the gluino  $R$ -hadron model, in the 1 VSI DV analysis channel, for fixed (a)  $m_{\tilde{\chi}_1^0} = 100$  GeV and (b)  $\Delta m(\tilde{\chi}_1^0, \tilde{g}) = 100$  GeV, corresponding with the signal yield shown in Figure 5.15.

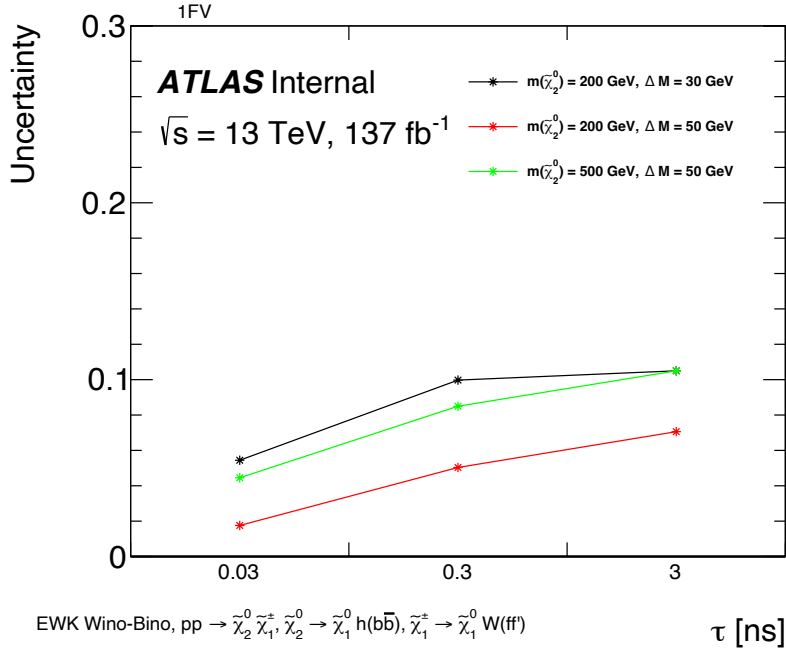


Figure 5.34: Tracking systematic uncertainties for the Wino-Bino co-annihilation model, in the 1 FV analysis channel. Taken from Ref. [143].

## 5.7 Results: Yields and Setting Limits

In the previous sections, we have outline the entire analysis method: what signal models we are looking for; how we reconstruct events and define signal regions (SRs); how we model our backgrounds; and lastly, how we model statistical and systematic uncertainties. With our analysis methods defined and all our estimates completed, the last step is to actually look at the data.

### 5.7.1 Event Yields

The estimated background yields in each SR are provided again in Table 5.44, this time together with the observed signal yields. Given the small number of observed events – and the uncertainties on our background estimate – we can already see that we (unfortunately)

have not discovered new physics<sup>[69]</sup>, as while we see an excess of events with respect to the mean counts we have estimated<sup>[70]</sup>, this excess is not statistically significant (as we will see below). Simply put, our results seem consistent with the Standard Model.

Another consequence of the small event yield in the SRs is that we can actually inspect the events individually. This is not how we will actually assess the significance of these results – which will require a statistical treatment, given the nature of the physics we are testing – but it is nonetheless instructive to actually study these events now that they are unblinded.

SR Event Yield Summary		
Analysis Channel	Background Estimate	Observed Events
1 VSI DV	$0.56 \pm 0.40$	1
1 FV	$0.81 \pm 0.49$	3
2 FV	$1.29 \pm 0.59$	2

Table 5.44: A summary of the background estimates and observed event yields in all the SRs. Taken from Ref. [143].

### 5.7.1.1 Visualizing an Event: The 1 VSI DV SR

We find a single event in the 1 VSI DV SR, which is visualized in Figure 5.35 using the VP1 software package [108]. Table 5.45 outlines some event-level observables, and Table 5.46 outlines the properties of the signal-like DV. While we can only speculate at the source of this DV, its positioning with respect to the  $b$ -tagged jets and the large crossing angle of its second track appear consistent with an accidentally-crossed  $B$ -meson decay.

---

69. It is important to emphasize that negative results are, while not necessarily exciting, nonetheless important. As we will discuss further on, such results allow us to place limits on the likelihood of a particular model, which is a statement about how confidently we can rule out its existence for a particular choice of model parameters.

70. Here, it is important to keep in mind that we are fundamentally dealing in statistical interpretations – the event yields that we have estimated are what we expect to see on average. To put things in context, we expected to see a total of 2.7 events across analysis channels, and observed a total of 6. From Poisson statistics, the probability of seeing 6 or more events when we expect 2.7 is approximately 5% (when ignoring the uncertainty on our expected event count).

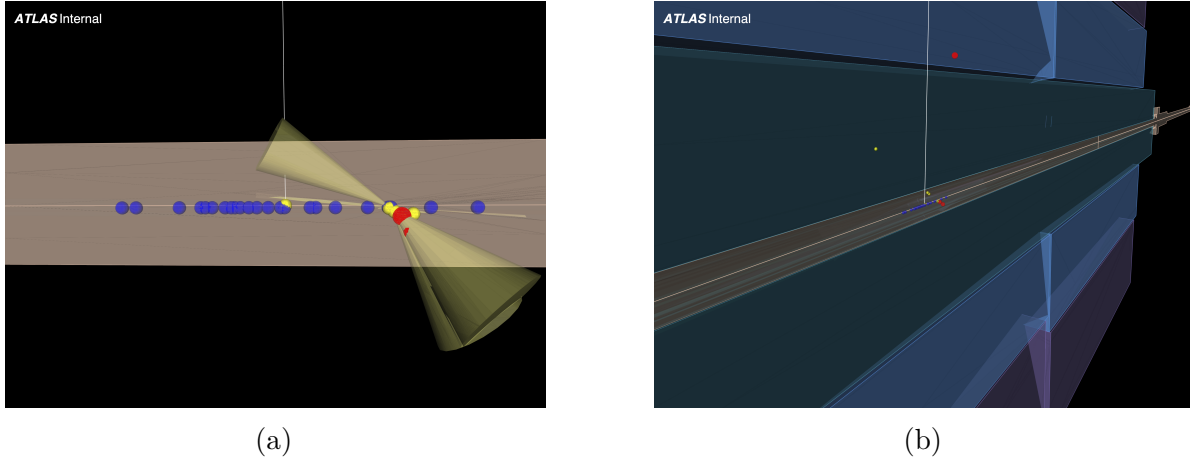


Figure 5.35: Two different visualizations of the single event in the 1 VSI DV SR. Primary vertices are shown in blue, with secondary  $b$ -tagging vertices in yellow and VSI vertices in red. Note that the actual tracks are not visualized. The two views show (a) a zoomed-in view of the beampipe, featuring EMTopo jets (yellow cones), and (b) a zoomed-out view, showing the cutaways of the Pixel, SCT and TRT sections of the inner detector, surrounding the beampipe. The signal-like DV is one of the two inside the beampipe, near the origin of the EMTopo jets.

1 VSI DV SR: Event-Level	
Variable	Value
Run Number	338897
Event Number	1534801244
$\cancel{E}_T$	211 GeV
$N_{\text{jets}}$	6
$N_{\text{b-tag}}$	2
Leading jet $p_T$	232 GeV
$N_{\text{tracks}}$	487
$N_{\text{pileup}}$	46

Table 5.45: An overview of event-level observables for the single event in the 1 VSI DV SR. The run and event numbers are unique indices used to identify this event in ATLAS data. Taken from Ref. [143].

1 VSI DV SR: DV-Level	
Variable	Value
$m_{\text{DV}}$	15.1 GeV
$N_{\text{tracks}}^{\text{DV}}$	5
$N_{\text{sel. tracks}}^{\text{DV}}$	3
$N_{\text{LRT tracks}}^{\text{DV}}$	0
$R_{xy}$	5.88 mm
$\eta$	2.84
$\phi$	-2.42
Track $p_T$ [GeV]	{ 5.80, 2.09, 4.67, 4.85, 4.53 }
Track $\eta$	{ 0.71, 2.34, 0.68, 0.67, 0.84 }
Track $\phi$	{ -2.54, -0.86, -2.55, -2.38, -2.40 }
Track Selection Status	{ 1 , 1 , 1 , 0 , 0 }

Table 5.46: An overview of properties of the signal-like DV in the 1 VSI DV SR. A track selection status of 1 corresponds with a selected track, and 0 with an associated track. Taken from Ref. [143].

## 5.7.2 Setting Limits: Constraining Our Signal Models

Fortunately, we do not have resort to pure speculation to interpret our results, and can instead turn (back) to statistical frameworks. Using our expected signal yields (Section 5.4.6), background estimate and observed yields, we can set limits on our signal models through the process of *maximum likelihood fitting*. Let us briefly review this method, before applying it to our results to produce our final signal model constraints<sup>[71]</sup>. Also note that the limits on signal models reported here correspond with preliminary analysis results, and may be subject to updates prior to publication of the final analysis paper<sup>[72]</sup>.

### 5.7.2.1 Maximum Likelihood Fitting: A Quick Review

In this process, we use the observed data to test our background-only hypothesis – that there is no new physics – against the hypothesis that there is. In a single-channel search<sup>[73]</sup>, we can express the probability of observing  $n$  events in the channel given data  $\{x_0, x_1, \dots, x_n\} = \{x\}_n$  as [212]

$$\begin{aligned} \mathcal{P}(\mathbf{x}, \mathbf{a} | \mu, \boldsymbol{\alpha}) &= \text{Poisson}(n | \mu S + B) \\ &\cdot \left[ \prod_{i=1}^n \frac{\mu S f_S(x_i; \alpha_S) + B f_B(x_i; \alpha_B)}{\mu S + B} \right] \\ &\cdot \prod_i f_{\alpha, i}(a_i | \alpha_i) , \end{aligned} \tag{5.14}$$

---

71. For a fuller review of this process – and its implementation in the software we use – see Ref. [212, 213]. We will only cover the basic method underpinning our limit-setting procedure.

72. In practice, updates may consist of reevaluation of the systematic uncertainties – which will likely have no significant impact given the outsize effect of the statistical uncertainties – as well as possible evaluation of additional points in parameter space to smooth the interpolated limit curves, some of which are currently quite rough.

73. Our search is in fact a multi-channel search. However we treat the 1 VSI DV analysis channel independently from the FV-based channels, so a model’s likelihood is only tested using the 1 VSI DV channel or the combination of FV-based channels. Without loss of generality, we will describe here the single-channel case: Our 1 VSI DV SR corresponds with a single-channel fit, whereas our FV SRs – which are treated together – correspond with a two-channel fit.

- $\mathbf{x}$  are the data,
- $\mu$  is the signal strength,
- $\{f_S, f_B\}$  are signal and background probability density functions of the discriminating variable  $x$  in the data,
- $\{S, B\}$  are the number of signal and background events,
- $\boldsymbol{\alpha} = \{\alpha_S, \alpha_B\}$  are *nuisance parameters* governing the shapes of  $\{f_S, f_B\}$ , such as uncertainties associated with the signal and background,
- $\mathbf{a}$  are measurements constraining the nuisance parameters,
- $f_{\alpha_i}$  is the probability distribution function of nuisance parameter  $\alpha_i$ .

where we have introduced a signal strength variable  $\mu$  such that  $\mu = 0$  corresponds with the background-only hypothesis, and  $\mu = 1$  with the original signal hypothesis so that our signal has its nominal predicted strength<sup>[74]</sup>. This probability, which folds in counting statistics (in the Poisson distribution) as well as signal and background probability density functions of the discriminating variable  $x$ , is formally referred to as the *likelihood function*  $\mathcal{L}(\mu; \boldsymbol{\alpha})$ , where we treat the data as fixed and vary  $\mu$  instead:

$$\mathcal{L}(\mu; \boldsymbol{\alpha}) \equiv \mathcal{P}(\{x_1, x_2, \dots, x_n\} | \mu, \boldsymbol{\alpha}) .$$

We often refer to constructing this likelihood function as *fitting*, since we are effectively fitting our model to the data. We can test the probability of a hypothesized value of  $\mu$  via the *likelihood ratio* [213], given by<sup>[75]</sup>

$$\lambda(\mu; \boldsymbol{\alpha}) = \frac{\mathcal{L}(\mu, \hat{\boldsymbol{\alpha}}(\mu))}{\mathcal{L}(\hat{\mu}, \hat{\boldsymbol{\alpha}})} . \quad (5.15)$$

- $\hat{\boldsymbol{\alpha}}(\mu)$  maximizes  $\mathcal{L}(\mu, \hat{\boldsymbol{\alpha}}(\mu))$ ,
- $\hat{\mu}, \hat{\boldsymbol{\alpha}}$  maximize  $\mathcal{L}(\hat{\mu}, \hat{\boldsymbol{\alpha}})$ .

74. At this point,  $\mu$  might seem like a very abstract parameter. We will ultimately understand it as a scaling on the full signal process cross-section, and it will allow us to place constraints on this cross-section.

75. Some of this notation is potentially a little cumbersome, but we will use it in order to closely match the expressions found in Ref. [213] and [212] for easier cross-reference.

What this likelihood ratio effectively does is that, given some hypothesized  $\mu$ , it tests that value paired with a choice of  $\alpha$  that maximizes its likelihood, against an *unconditional* likelihood function where both  $\mu$  and  $\alpha$  are “floated” so that they each take on whatever values – when combined – maximize the likelihood. In fact, this likelihood ratio formula is agnostic to the fact that we are considering models with an implicit  $\mu > 0$  constraint. Thus if we were to find  $\hat{\mu} < 0$ , the most consistent physical value of  $\mu$  would be  $\mu = 0$ . From this, we can define a modified likelihood ratio given by

$$\tilde{\lambda}(\mu; \boldsymbol{\alpha}) = \begin{cases} \frac{\mathcal{L}(\mu, \hat{\alpha}(\mu))}{\mathcal{L}(\hat{\mu}, \hat{\alpha})} & \hat{\mu} \geq 0 \\ \frac{\mathcal{L}(\mu, \hat{\alpha}(\mu))}{\mathcal{L}(0, \hat{\alpha})} & \hat{\mu} < 0 \end{cases}, \quad (5.16)$$

and from this modified likelihood ratio we construct a test statistic  $\tilde{q}_\mu$  given by [213]

$$\tilde{q}_\mu = \begin{cases} -2 \ln(\tilde{\lambda}(\mu)) & \hat{\mu} \leq \mu \\ 0 & \hat{\mu} > \mu \end{cases}. \quad (5.17)$$

From this test statistic, we can finally compute a  $p$ -value as

$$p_{\mu'} = \int_{\tilde{q}_\mu^{\text{obs}}}^{\infty} f(\tilde{q}_\mu | \mu') d\tilde{q}_\mu, \quad (5.18)$$

- $\tilde{q}_\mu^{\text{obs}}$  is the value of  $\tilde{q}_\mu$  we observe,
- $f(\tilde{q}_\mu | \mu')$  is the probability distribution function of  $\tilde{q}_\mu$ , under the hypothesis of  $\mu = \mu'$

where we leave some details on the test statistic probability distribution  $f(\tilde{q}_\mu | \mu')$  to Appendix A.17. In practice, we often refer to the *significance*  $Z$  of results, which is related to the  $p$ -value via [213]

$$Z = \Phi^{-1}(1 - p). \quad (5.19)$$

- $\Phi(\dots)$  is the Gaussian cumulative distribution function.

We also sometimes refer to a metric known as the  $CL_S$ , given by [214]

$$CL_S(\mu) = \frac{p_\mu}{2 - p_0}. \quad (5.20)$$

- $p_\mu$  is the  $p$ -value for some choice of  $\mu$ ,
- $p_0$  is the  $p$ -value for  $\mu = 0$ , the background-only hypothesis.

One important detail we have glossed over thus far is how we handle the constraints on our nuisance parameters  $\alpha$ . This is where we make use of our various uncertainty estimates. As expressed in Equation 5.14, we treat these estimates as drawn from external measurements – and thus sampled from their own respective probability distributions. As is the case in this search, we typically model the impact of the nuisance parameters on our likelihood function via Gaussian distributions<sup>[76]</sup> as

$$f_{\alpha,i}(a_i|\alpha_i, \sigma_i) = \frac{1}{\sqrt{2\pi\sigma_i^2}} \exp\left(-\frac{1}{2} \frac{(a_i - \alpha_i)^2}{\sigma_i^2}\right). \quad (5.21)$$

Note that, without loss of generality, we parameterize the  $\alpha_i$  such that<sup>[77]</sup> the nominal value corresponds with  $\alpha_i = 0$ , and  $\sigma_i = 1$ . As noted earlier, we float the values of these nuisance parameters, effectively allowing them to differ from their nominal value when determining the (modified) likelihood ratio<sup>[78]</sup>.

---

76. We are technically not limited to this assumption – and there are cases where other common distributions like the Poisson distribution are more appropriate (such as if handling a parameter estimated via counting of data). For nuisance parameters that should not be negative, we can also choose to use a Gaussian probability distribution but truncate and scale it accordingly to avoid non-physical regions. It is also worth noting how we choose to parameterize our uncertainties in the nuisance parameters – as shown in Section 5.6 some of our uncertainties are asymmetric. We can accommodate this by choosing our nuisance parameterization as to separately model the upwards and downwards shift effects on  $f_S$  or  $f_B$ , and we may also choose to abandon the prior of Gaussian probability distributions altogether. For details, see Ref. [212].

77. Consequently, our measured values of the nuisance parameters enter into the probability distributions  $f_S$  and  $f_B$ .

78. Keep in mind that it is not the  $\mathbf{a}$  but the  $\alpha$  that appear in  $f_S$  and  $f_B$ . Our measurements  $\mathbf{a}$  are used as

Using the above method, we fit the data and report an *observed limit* corresponding with  $CL_S = 0.05$  by convention. We also fit a so-called *Asimov dataset*<sup>[79]</sup>, to produce an associated Asimov fit. This is an artificial dataset constructed to be most consistent with the background-only hypothesis: In practice, this means that for whatever set of data  $\mathbf{x}$  is being fit, we define the Asimov dataset such that its probability distribution function(s) exactly match  $f_B$ . In other words, this is a dataset where the expected number of events is exactly the number of events we predict via our background estimate. From our Asimov fit, we derive an *expected limit*, again corresponding with  $CL_S = 0.05$ . This expected limit establishes how well we can exclude the signal hypothesis if we observe data maximally consistent with the background-only hypothesis. <sup>[80]</sup>.

In practice, we typically report these limits as curves, which we produce by scanning over the parameters of our model and evaluating the  $\mu$  at which we achieve  $CL_S = 0.05$  for each choice of model parameters. We can interpret the variable  $\mu$  as a scaling of our signal process cross-section – so that we are making an assessment about what magnitude of cross-sections we can rule out. With this (very) brief review of maximum likelihood fitting in hand, we are now ready to interpret the limits that we derive from the background estimate results and

---

constraints on the nuisance parameters; we have drawn them from some distribution (Gaussian) distributions, and claim these measurements are representative of their true values. The fit effectively tests this, and will return  $\alpha$  that are different from  $\mathbf{a}$  if the data are more consistent with these. Under such a scenario we might be tempted to simply use this result to constrain what the nuisance parameters ought to be – at which point we might as well throw out our measurements of the systematic uncertainties altogether and try to let the fit simply handle it. However, we would be constraining these uncertainties together with (or under constraint of) the signal model parameters which we originally set out to independently constrain. Thus finding our  $\alpha$  to significantly drift from  $\mathbf{a}$  is a strong sign that we have poorly modeled the systematic uncertainties – and that it is this modeling that should be fixed.

79. As noted in Ref. [213], where this nomenclature is adopted, this is a reference to Isaac Asimov’s short story *Franchise*, which depicts a society where elections are held by “selecting the single most representative voter to replace the entire electorate”. In a similar spirit, the concept of an Asimov dataset is one that is – by design – most representative of the background-only hypothesis.

80. Another practical function of the Asimov fit is that it serves as a test of our nuisance parameter modeling – where any effects of the presence of a signal in the data have been eliminated. If the fit results in these parameters drifting significantly from their nominal values, it is a likely sign of mismodeling. Of course, a more robust test of the nuisance parameter modeling is a full validation fit performed in data, however in practice this may be complicated by the potential need to adjust the parameter modeling to the validation region.

yields reported in Section 5.7.1.

### 5.7.2.2 Limits for the gluino $R$ -hadron model

Figure 5.36 provides limits on the gluino  $R$ -hadron model, in terms of contours in 2D model parameter space. To interpret these limits, we take the drawn contours to be representing the edge of an excluded region of parameter space: in the present case, this corresponds with the lower region of each plot<sup>[81]</sup>. As described in Section 5.7.2.1, our expected limits corresponds with the Asimov fit, which is fit to data maximally consistent with the background-only hypothesis. We see that our observed limits are less stringent, as they exclude a region that is slightly smaller. However, the observed limits fall within the  $\pm 1\sigma$  uncertainty bands of our expected limits, so there is not any significant tension between these two limits. In other words, our observations are highly consistent with there being no new physics. Had we found our observed limits to be far less stringent – leaving space between them and our expected limits – this might have been a sign of new physics, or at least that the data are consistent with the signal model hypothesis.

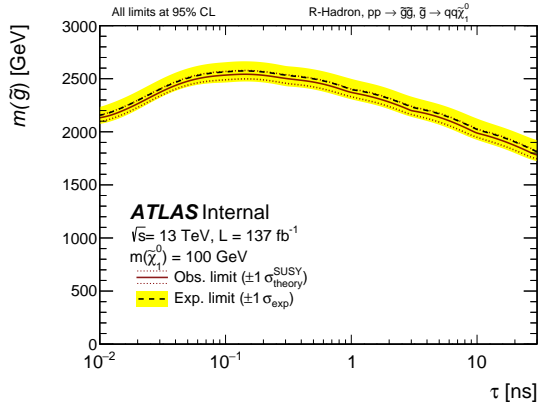
We also report cross-section limits as shown in Figure 5.37. Here the excluded regions correspond with where our observed limits are below the theory limit, which provides the nominal signal model cross-section. In some cases, we are able to set cross-section limits multiple orders of magnitude lower than the theory prediction – until we reach sufficiently high  $\tilde{g}$  or  $\tilde{\chi}_1^0$  masses where we start to run into the limitations of our  $pp$  collision energy.

### 5.7.2.3 Limits for the Wino-Bino co-annihilation model

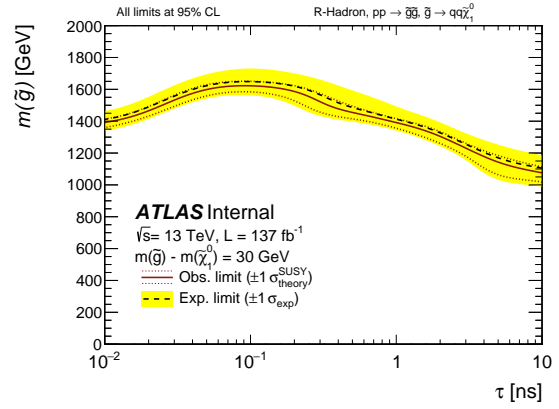
Figure 5.40 provides limits on the cross-section of this process. Figures 5.38 and 5.39 provide 2D limits on this model, in terms of  $\tilde{\chi}_2^0$  mass and lifetime, as well as in terms of the  $\tilde{\chi}_2^0$ - $\tilde{\chi}_1^0$

---

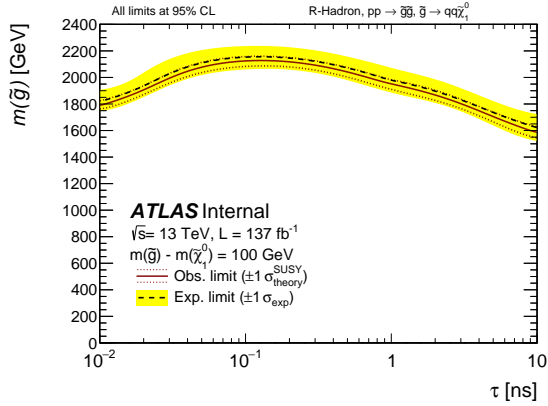
81. In practice, it is usually unambiguous as to which region is excluded. In this case, there is some upper limit to particle masses we can probe – imposed by the center-of-mass energy of our  $pp$  collisions – and so it is clear that we are excluding a range of lower particle masses.



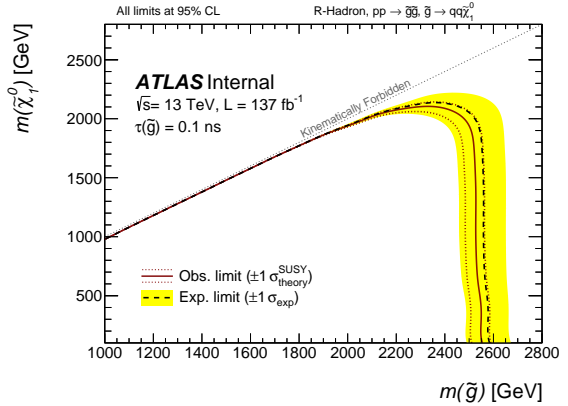
(a)



(b)

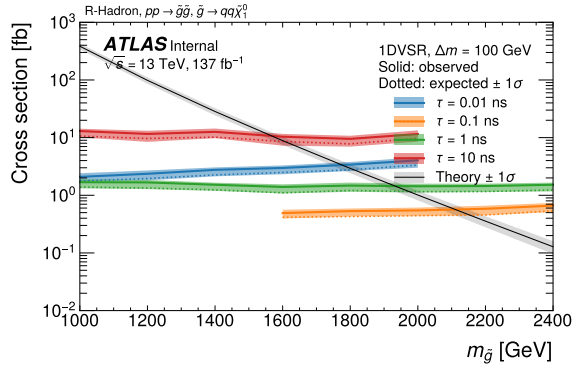


(c)

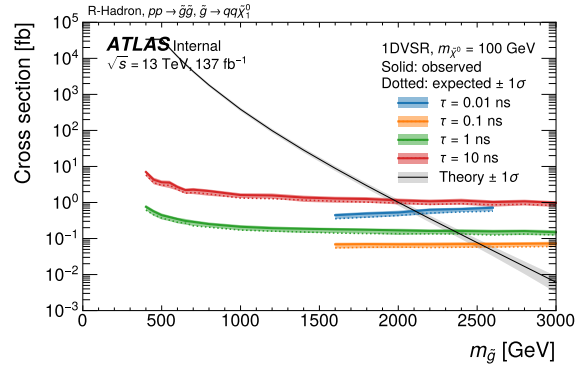


(d)

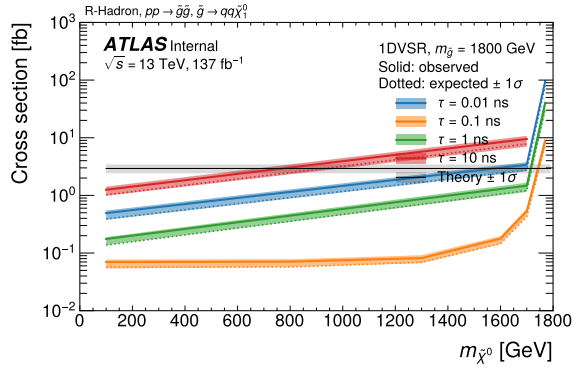
Figure 5.36: Preliminary limits on the gluino  $R$ -hadron model, in terms of (a-c)  $\tilde{g}$  mass and ( $R$ -hadron) lifetime, and (d)  $\tilde{g}$  and  $\tilde{\chi}_1^0$  mass. Taken from Ref. [143].



(a)



(b)



(c)

Figure 5.37: Preliminary limits on the gluino  $R$ -hadron model cross-section, as a function of  $\tilde{g}$  mass with (a) fixed  $\tilde{g}$ - $\tilde{\chi}_1^0$  mass splitting and (b) fixed  $\tilde{\chi}_1^0$  mass, and as a function of (c)  $\tilde{\chi}_1^0$  mass with fixed  $\tilde{g}$  mass. Uncertainty bands are set not using the asymptotic assumption described in Appendix A.17, but rather by modeling the test statistic probability distribution function via the Monte Carlo method with  $10^4$  pseudo-experiments. Taken from Ref. [143].

mass splitting. In these plots we see a slight difference between the observed and expected limits, with the two limits'  $\pm 1\sigma$  uncertainty bands just barely touching one another. This corresponds to a greater tension in the results than with the gluino  $R$ -hadron model – although with the observed limit less than  $2\sigma$  away from the expected limit (in terms of the theory uncertainties), this is still not what would be considered significant tension.

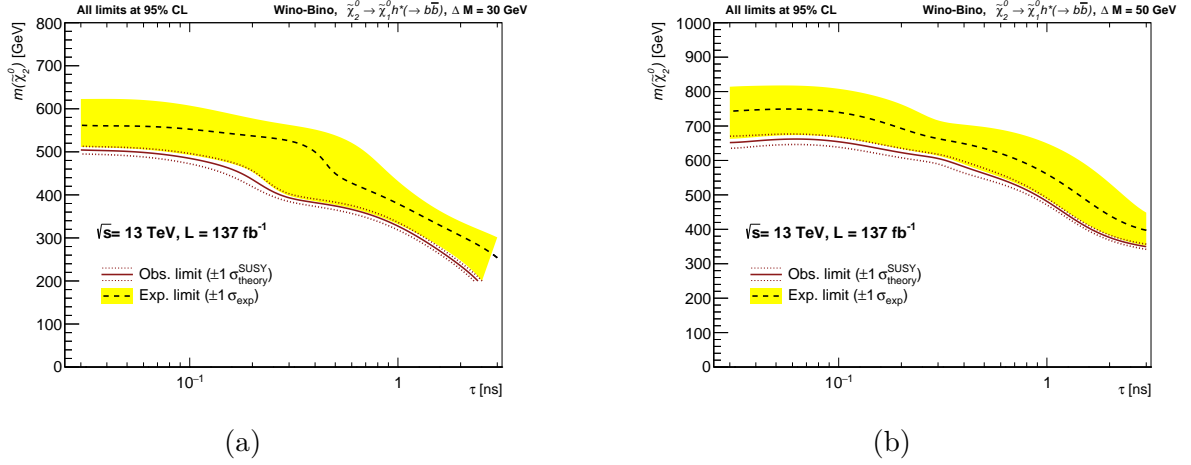


Figure 5.38: Preliminary limits on the Wino-Bino co-annihilation model, in terms of  $\tilde{\chi}_2^0$  mass and lifetime. Taken from Ref. [143].

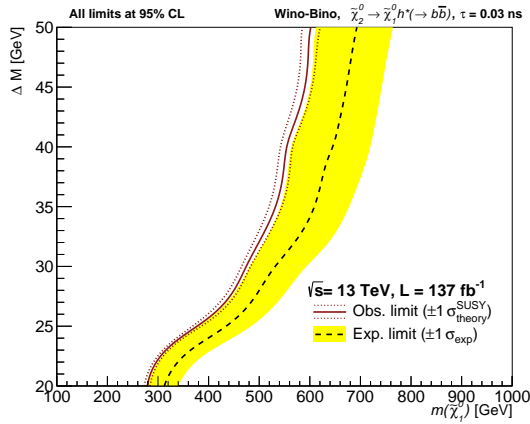
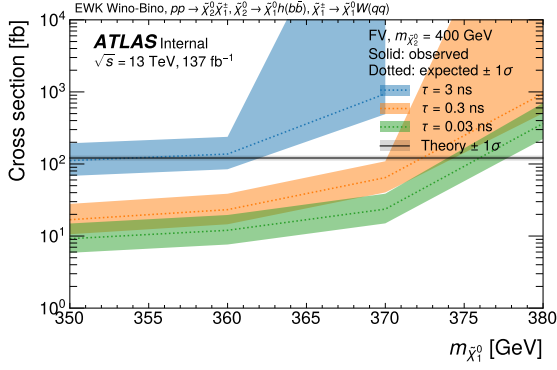
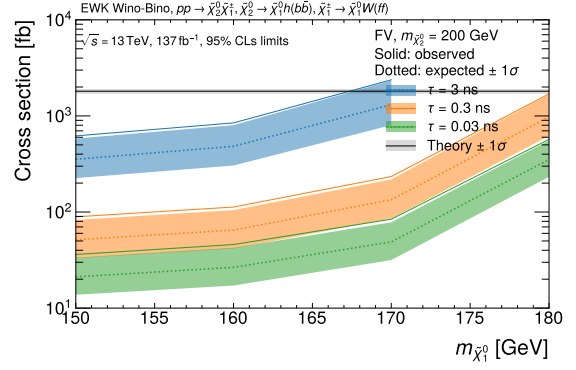


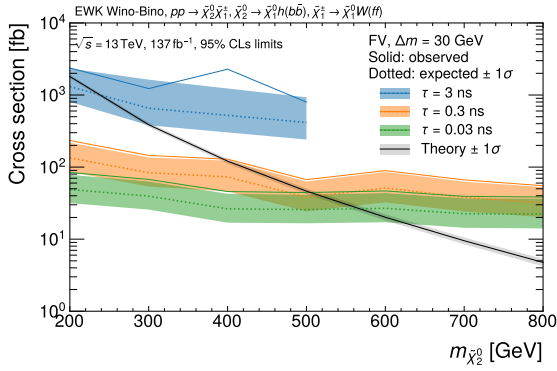
Figure 5.39: Preliminary limits on the Wino-Bino co-annihilation model, in terms of  $\Delta m(\tilde{\chi}_2^0, \tilde{\chi}_1^0)$  and  $\tilde{\chi}_2^0$  lifetime. Taken from Ref. [143].



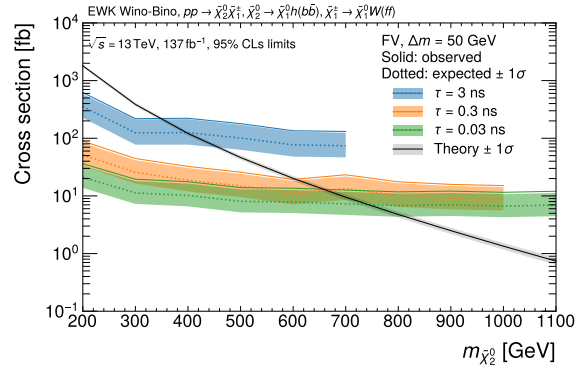
(a)



(b)



(c)



(d)

Figure 5.40: Preliminary limits on the Wino-Bino co-annihilation process cross-section. Taken from Ref. [143].

### 5.7.2.4 Limits for the Higgs Portal model

In Figure 5.41, we report the limits on the  $h \rightarrow SS$  branching ratio<sup>[82]</sup>.

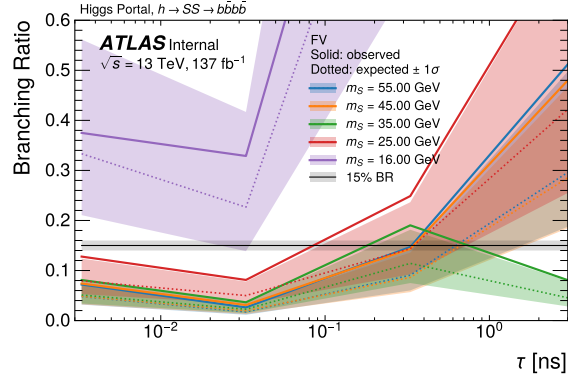
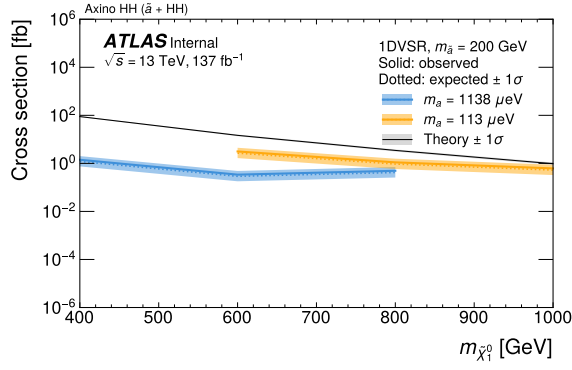


Figure 5.41: Preliminary limits on the Higgs Portal branching ratio, as a function of the scalar  $S$  lifetime. We suppress the observed limit uncertainties for improved legibility. Taken from Ref. [143].

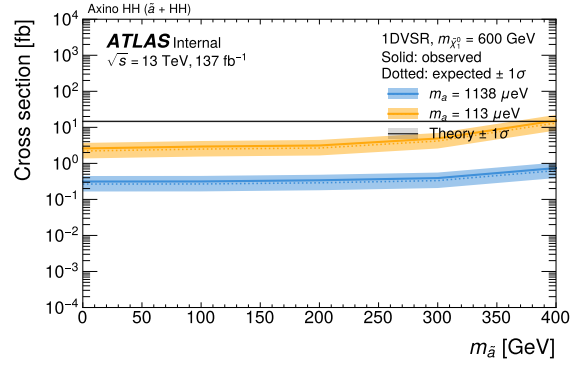
### 5.7.2.5 Limits for the axino model

Finally we arrive at the axino model – which is perhaps of the most interest to us, given the theory and phenomenology discussion of Chapter 3. To reiterate, while we may not have discovered the axino, setting limits is nonetheless an important exercise for constraining this particular model and understanding what regions of parameter space are (or aren't) thus excluded. In the case of axinos, this is also interesting insofar as we can relate these limits back to axions, akin to Figure 3.1. Of course any such limits we set are accompanied by a host of assumptions – namely that SUSY is real – but this simply a natural consequence of our bridging of the axion-collider divide. Figure 5.42 provides our cross-section limits in terms of the axino model parameters, as well as in terms of the axion mass.

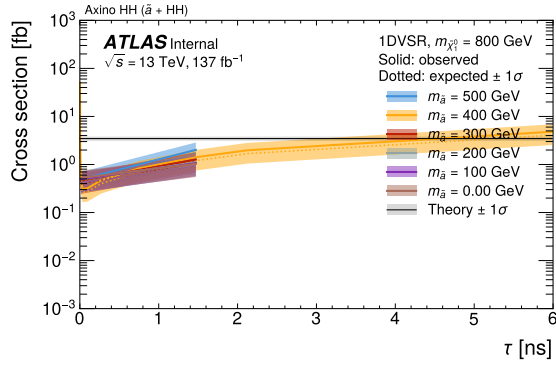
<sup>82</sup>. We report a branching ratio and not a cross-section, as we are explicitly probing a hypothetical Higgs-boson decay as opposed to some (possibly multi-process) production of a hypothetical particle.



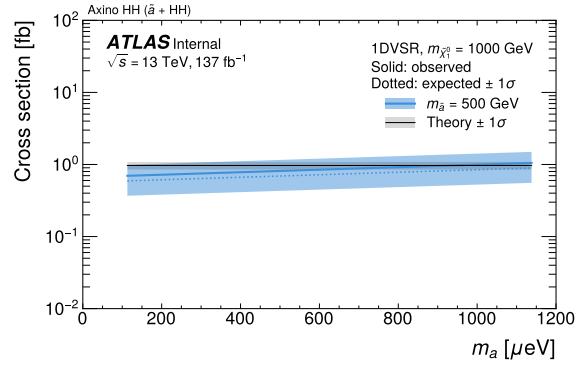
(a)



(b)



(c)



(d)

Figure 5.42: Preliminary limits on the axino model cross-section, in terms of (a)  $\tilde{\chi}_1^0$  mass, (b)  $\tilde{\chi}_5^0$  (axino) mass, (c)  $\tilde{\chi}_1^0$  lifetime, and (d) axion mass. Taken from Ref. [143].

### 5.7.3 *Final Remarks*

With limits established to constrain each of our signal models, we can take a moment to reflect on the analysis. With a multi-pronged estimate of background processes – ultimately a simple data-driven parameterization, but with multiple cross-checks – and a careful assessment of sources of uncertainty, we have constrained multiple beyond-Standard Model physics scenarios by searching for displaced vertices and  $\cancel{E}_T$ , an unusual event signature. Furthermore, we have done this using Run 2 data from the ATLAS experiment, collected in the previous decade. Just as this analysis has extended results from previous searches [192], we may expect an analysis of Run 3 data (which is currently being collected) to further improve our limits and resolve the few very small tensions we have found – or perhaps widen them.

## CHAPTER 6

### LORENTZ-EQUIVARIANT MACHINE LEARNING

In the previous chapters, we have reviewed a few different facets of particle physics: the Standard Model (SM) and some of its common hypothesized extensions; the basic design and operation of the ATLAS experiment; an analysis of ATLAS data conducted to search for beyond-SM (BSM) physics. Before concluding this thesis, we will turn our attention to the topic of data analysis algorithms for particle physics, and machine learning (ML) in particular. In fact, we have already touched upon some examples of ML in physics, such as the discussion of ATLAS calorimeter energy deposit calibrations in Section 4.2.8.3, as well as the description of the fuzzy vertexing method described in Section 5.3.1.3. These are but two of many examples of ML usage in ATLAS, where such techniques are applied to a host of detector operation and physics reconstruction tasks. As such tools only grow more ubiquitous in particle physics, we will turn our attention to a fundamental question: How should ML tools be designed for these tasks? We will posit one possible answer, from the relatively nascent but growing field of *equivariant* neural networks for particle physics, that may inform design principles for ML usage not only in ATLAS but across the broader field. To motivate these networks, we will begin our discussion outside of particle physics and on the topic of neural network image recognition.

#### 6.1 Computer vision: A motivational story

One of the more significant breakthroughs in ML research in the last two decades has been the development of convolutional neural networks (CNNs) for image recognition tasks [215, 216]. These neural networks (NNs) use two-dimensional convolutions to process images into a *feature map* as shown in Figure 6.1. The feature map is effectively some down-scaled image, and the convolution process can be repeated in tandem to produce increasingly abstract

features that combine information over larger areas of the image. In practice, this procedure is repeated a few times before the final feature maps are in some way averaged, and the results put through a standard multi-layer perceptron (MLP) as in a fully-connected NN<sup>[1]</sup>, as in Figure 6.2.

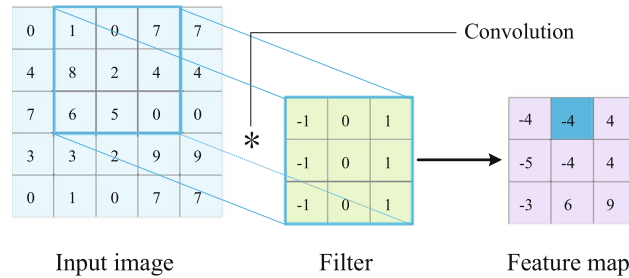


Figure 6.1: An schematic of a 2D convolution performed in a CNN. Taken from Ref. [216].

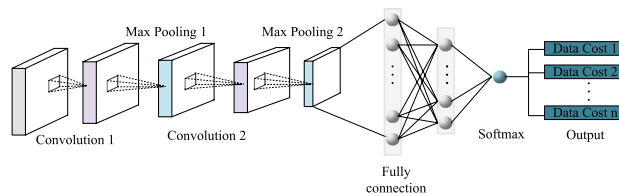


Figure 6.2: A schematic of a typical CNN architecture. Taken from Ref. [216].

Such a neural network can be trained to perform image recognition, a classification task. What makes CNNs particularly powerful tools for this problem, and more flexible than fully-connected NNs, is that their convolution layers exhibit *translational equivariance* by design. In the realm of image recognition, this means (for example) that a particular sub-image will produce the same output no matter where it is located: the convolution filter will scan over it regardless of its position. This translational symmetry in the network design is favorable, as this is a symmetry inherent to the problem of image recognition itself (and, somewhat abstractly, the space in which images reside). In practice, this equivariance leads not only to strong performance, but efficient training: to train a CNN image classifier to identify a particular object in an image, it does not need to see examples with the object in

1. For a historical review of MLPs, see Ref. [217].

every possible location. By contrast, a fully-connected NN will typically need some kind of training data augmentation to achieve similar performance – and possibly a larger network size in terms of its number of learnable parameters.

The success of CNNs in computer vision tasks was not unnoticed among particle physicists, and CNN-based methods have been developed for the task of jet flavor tagging<sup>[2]</sup>, which use “images” corresponding to energy deposits in a collider detector calorimeter [218–220], in the  $(\eta, \phi)$  plane, as shown in Figure 6.3. While these methods have shown success, they beg the question of whether or not a more specialized network architecture can be leveraged, that exploits the underlying symmetries inherent in particle physics processes.

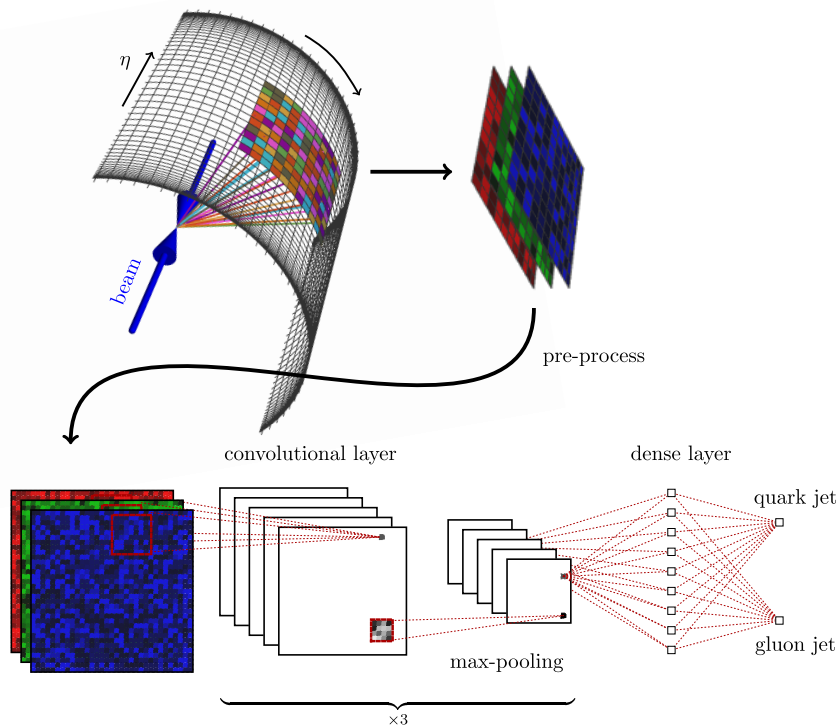


Figure 6.3: A schematic of “unfurling” a particle calorimeter to produce jet images in the  $(\eta, \phi)$  plane. These can be fed into a CNN to perform jet flavor tagging. Taken from Ref. [220].

---

2. See Appendix E for a short discussion of this topic, and jet reconstruction in general.

## 6.2 Equivariant Neural Networks, and PELICAN

In this section, we review the concept of equivariance as it relates to neural networks, and then discuss the PELICAN neural network architecture.

### 6.2.1 *Equivariant Network Architectures*

The basic concept of *equivariance*<sup>[3]</sup> is that for any object that transforms under representations of some group, there may exist a class of functions that preserve these transformations. Without delving into the details of representation theory, what we mean by this in the context of the Lorentz group is that the physical observables that we study in high-energy particle physics transform in a prescribed manner when acted upon by elements of the Lorentz group: particle masses and identities are invariant under Lorentz boosts or rotations; particle energies are conversely dependent on the choice of reference frame. This is analogous to how images transform under translations, except that we are dealing with a somewhat more complex group. Similar to how CNN architectures exhibit transformation invariance, we may wish to construct a neural network operating on measured particle 4-momenta which is Lorentz-equivariant<sup>[4]</sup>. This is not only interesting as a possible means of constructing a high-performance jet tagger or momentum regression network, but also as it may improve prospects of network interpretability: constructing a Lorentz-equivariant neural network requires designing an architecture where all the operations performed on the data themselves preserve Lorentz equivariance. This corresponds with preserving Lorentz symmetry – and as we have seen in Section 2, symmetries play an important role in how we model and analyze physical systems. If we think of a neural network as a computation graph, where we perform

---

3. For a very brief review of invariance and equivariance in the context of the Lorentz group, see Appendix B.3.

4. We may also consider a neural network architecture that is explicitly only Lorentz-invariant, but as we typically measure non-invariant quantities (such as energy) a more general Lorentz-equivariant formulation may address more possible use cases in particle physics data analysis.

a sequence of operations on our input data and eventually produce an output, enforcing Lorentz equivariance requires each node on the computation graph to correspond to a physical observable. Thus, we may be able to study the inner workings of a Lorentz-equivariant neural network, and interpret what observables it leverages in its operation<sup>[5]</sup>.

### 6.2.2 PELICAN

One way of implementing a Lorentz-equivariant neural network is the so-called “Permutation Equivariant and Lorentz Invariant or Covariant Aggregator Network” (PELICAN) [221, 222]<sup>[6]</sup>. Originally developed in the context of jet flavor tagging, this is a general architecture that operates on collections of 4-momenta as input, and can be trained to predict Lorentz-invariant or covariant quantities: the former may include particle masses or identities (such as in flavor tagging), and the latter may include quantities such as full particle 4-momenta. As the name implies, PELICAN preserves not only Lorentz but also permutation-equivariance: as it operates on collections of 4-momenta, there is typically not some notion of a natural ordering to these and we are most often interested in permutation-invariant quantities<sup>[7]</sup>. Figure 6.4 outlines the PELICAN architecture – which we can understand through the descriptions below of building in Lorentz permutation equivariance.

---

5. Whether or not this is a simple task is another matter – in practice we may construct arbitrarily complex functions that maintain Lorentz equivariance. However, interpretability of neural networks is a longstanding point of concern in their use throughout the physical sciences, and designing a network where its internal operations map to physically-meaningful operations is an important step in building generally interpretable systems.

6. PELICAN is not the first Lorentz-equivariant neural network architecture to have been developed – nor the first that I have helped develop, having previously worked on the Lorentz Group Network [223] with many of the same collaborators. It is also important to note that there have been efforts to incorporate elements of Lorentz symmetries into particle physics-oriented neural networks prior to my work, such as the Lorentz Layer [224] which explicitly computes a set of Lorentz-invariant quantities on 4-momenta, or the Lorentz Boost Network [225] which effectively reconstructs input 4-momenta in input-based rest frames.

7. Much like with Lorentz symmetry, we consider the more general case of encoding permutation *equivariance* in the network architecture – and typically project onto permutation invariant quantities (or *permutation scalars*) in the output layers of the network.

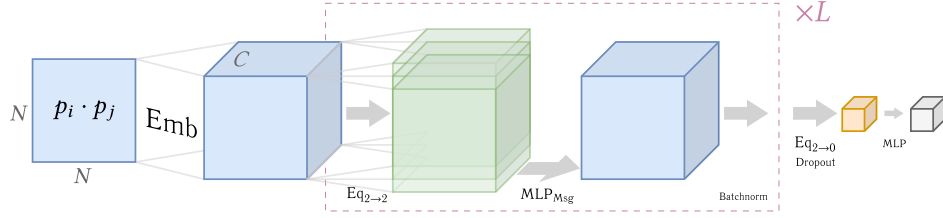


Figure 6.4: A schematic of the basic PELICAN architecture layout. Taken from Ref. [222].

### 6.2.2.1 Lorentz Equivariance in PELICAN

Encoding Lorentz equivariance turns out to be the easier of the two tasks. This is effectively accomplished by producing a rank-2 tensor consisting of all (Minkowski) inner products of the input four-momenta  $p_i \cdot p_j$ <sup>[8]</sup>. All totally symmetric Lorentz-invariant quantities that are functions of momenta can then be constructed from these inner products [221],

$$I(\{p_i\}) \equiv I(\{p_i \cdot p_j\}) . \quad (6.1)$$

- $I(\dots)$  is some arbitrary function,
- $p_i$  is the  $i$ 'th 4-momentum.

Here,  $I$  is some arbitrary function, which in practice can be an MLP. While the expression in Equation 6.1 is a way to construct Lorentz scalars, we can by extension produce all Lorentz-covariant quantities by employing these functions together with the input 4-momenta, as

$$F^\mu(\{p_i\}) = \sum_k I_k(\{p_i \cdot p_j\}) p_k^\mu . \quad (6.2)$$

What we are effectively doing is producing weighted sums of the input 4-momenta, where those weights are nothing other than functions of  $p_i \cdot p_j$  as in Equation 6.1.

<sup>8</sup>. In this section, we use notation  $p_i \cdot p_j \equiv p_i^\mu p_{\mu,j}$  and suppress the Greek indices for simplicity in this term.

### 6.2.2.2 Permutation Equivariance in PELICAN

The above ingredient gives us Lorentz equivariance, but simply producing any function of  $p_i \cdot p_j$  does not guarantee permutation equivariance – which turns out to be the more complicated symmetry to encode in the PELICAN architecture. To accomplish this we need a permutation-equivariant mapping between rank-2 tensors, specifically one that is equivariant under the simultaneous swapping of a row and column that corresponds to reordering the  $\{p_i\}$  in the  $\{p_i \cdot p_j\}$  tensor. We can write this mapping as [222]

$$T'_{ij}{}^a = S^a \left( \{T_{kl}|k, l : B_{ijkl}^a \neq 0\} \right) . \quad (6.3)$$

- $T_{ij}$  is a rank-2 tensor,
- $\{S^a\}$  are symmetric functions,
- $\{B_{ijkl}^a\}$  are rank-4 binary tensors.

Here, a set of output rank-2 tensors  $T'_{ij}{}^a$  are each given by some general symmetric function  $S$  – by which we mean permutation-invariant with respect to its inputs – acting on a set of components of the input rank-2  $T_{kl}$  that are selected by the binary rank-4 tensors  $\{B_{ijkl}^a\}$ <sup>[9]</sup>. It is these binary tensors that span the different permutation-equivariant mappings: these correspond with simple maps such as the identity and transpose, as well as maps which aggregate over rows, columns or the diagonal of the input tensor. There are 15 of these permutation-equivariant mappings in total<sup>[10]</sup>. These are depicted pictorially in Figure 6.5 for the case of a  $2 \times 2$  rank-2 tensor.

---

9. In practice, each of the  $\{S^a\}$  corresponds with an averaging of all its inputs, followed by a scaling by factor  $(N/\bar{N})^{\alpha_a}$  where  $N$  is the number of particles in the event,  $\bar{N}$  is a hyper-parameter representing the average number of particles in an event, and the  $\{\alpha_a\}$  are learnable parameters. In principle, the  $\{S^a\}$  could be chosen to be different functions for each  $a$  – such as some combination of averages, maximum and minimum functions – while still preserving total permutation equivariance.

10. Although 15 may seem like an odd and arbitrary size for this space of mappings, as explained in Ref. [226] it can be understood through the concept of partitioning sets: each  $B_{ijkl}$  is a rank-4 tensor, and there are 15 ways to partition a set of size 4. This number of possible partitions is known as a Bell number – and although the Bell numbers are named after Eric Temple Bell who wrote about them in the 1930s [227], their formal study can in fact be traced back at least to Edo-period Japan, with studies inspired by combinatoric symbols used to number the chapters of “The Tales of Genji” [228].

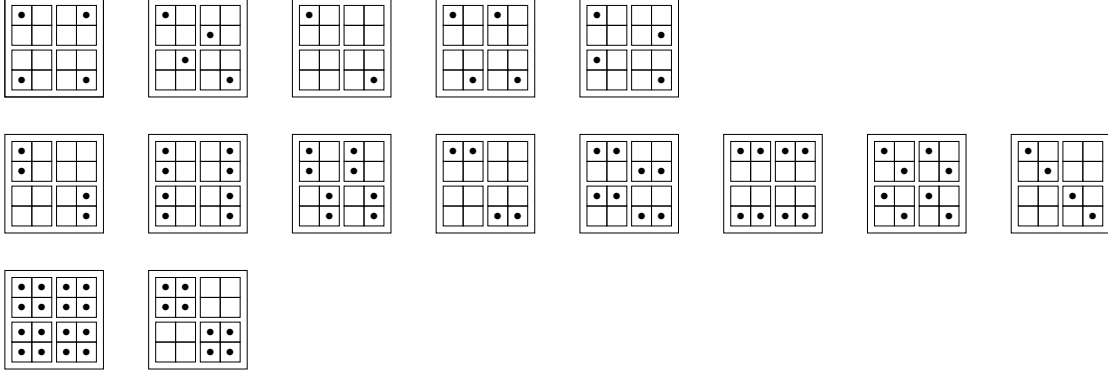


Figure 6.5: The 15 binary arrays of rank 4 that represent the basis elements of the permutation equivariant aggregators of PELICAN. Each  $2 \times 2$  square contains a smaller  $2 \times 2$  square in each position. The larger square represents the output tensor, with each smaller square representing the input tensor and the dots indicating which elements are aggregated from the input tensor and placed in this location of the output tensor. The first row consists of aggregators that are “rank-0” in terms of tensor dimension  $N$ , such as the identity mapping and trace. The second consists of “rank-1” aggregators that aggregate over rows, columns or the diagonal. The third consists of “rank-2” aggregators that aggregate over both rows and columns. Taken from Ref. [222].

### 6.3 Identifying hadronic top quark decays with PELICAN

As noted earlier, PELICAN was developed in the context of top quark tagging – the specific example of quark flavor tagging where we attempt to distinguish top quarks from other species. Top quark tagging is an task well-motivated by both Standard Model (SM) precision measurements [229–231], as well as searches for new physics that involve top quark signals [232–234]. It is also an interesting task from the perspective of the structure of top quark decays: the heaviest of the SM particles, the top quark decays before hadronization (Appendix E.1), almost always producing a  $W$ -boson and  $b$ -quark<sup>[11]</sup>. The  $W$ -boson may decay leptonically or hadronically, the latter via  $W \rightarrow qq'$ , and thus the full top quark decay may yield a set of multiple jets or a single large-radius jet with significant *substructure* owing to the different particle mass scales involved in the preceding decay chain. Top quark decays are therefore a

11. Other down-type quarks can be produced, with the branching ratios determined by the CKM matrix (Section 2.1.2.1). Owing to large differences in the sizes of the matrix elements, the branching ratio  $t \rightarrow Wb$  dominates.

strong motivation of – and playground for – jet substructure measurements, including both “classical” and ML-driven approaches [235, 236].

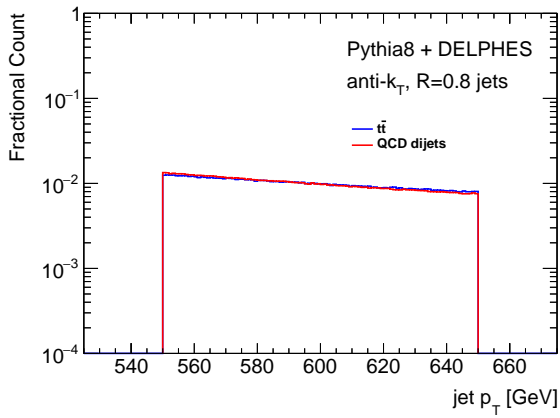
As a first benchmark of using PELICAN, we employ it on a top-quark tagging dataset in Ref. [237], on which a large set of other ML-based taggers – some of them also with theoretically-motivated designs – were tested [238]. This dataset corresponds with MC event simulation performed with the `PYTHIA` MC generator for parton-level simulation and hadronization [239], with fast detector pseudo-simulation performed via the `DELPHES` software package<sup>[12]</sup> [240]. Each “event” in the dataset corresponds with a single jet, chosen as the leading jet from either  $t\bar{t}$  production, or from a QCD dijet event (producing either light quark or gluon jets). The jets are clustered using `DELPHES` energy-flow information. Both sets of jets prepared so that their high-level kinematic distributions match closely as shown in Figure 6.6. Table 6.1 summarizes the performance of a number of top-tagging neural networks on this dataset, with ROC curves shown in Figure 6.7. We find that PELICAN achieves state-of-the-art performance in terms of accuracy, area under the ROC curve and background rejection. Furthermore, instances of PELICAN using only tens of thousands of learnable parameters perform comparably or even better than other networks with one or two orders of magnitude more – a consequence of the efficient parameterization generally afforded by equivariant neural network methods.

### 6.3.1 *Measuring momenta in top quark decays*

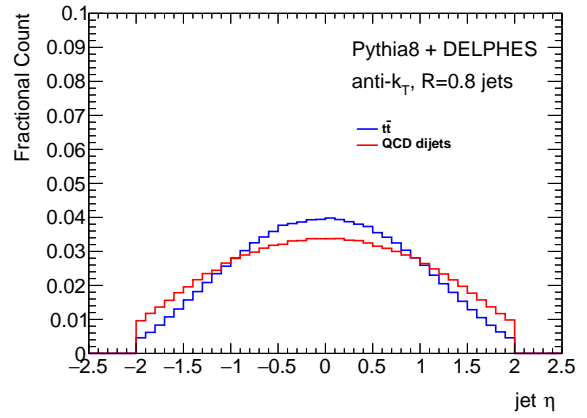
As noted in Section 6.2.2.1, the PELICAN architecture allows not only for predicting Lorentz-invariant quantities, but also predicting Lorentz-covariant quantities such as 4-momentum. This can be accomplished by changing the PELICAN output layer, from projecting onto

---

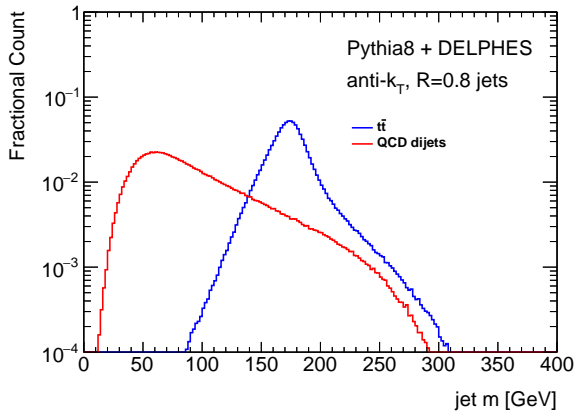
12. This pseudo-simulation corresponds with smearing of particle energies and angular distributions, as well as a series of parameterized reconstruction efficiencies, that emulate the effects of detector reconstruction. Tools like `DELPHES` are popular for phenomenology studies as these methods’ computational cost is vastly lower than full event simulation using libraries such as `GEANT4`, at the cost of realism. In addition, `DELPHES` is fully publicly-available, including its parameterization of the ATLAS detector (in contrast with the official ATLAS `GEANT4` geometry simulation, which is internal to the collaboration).



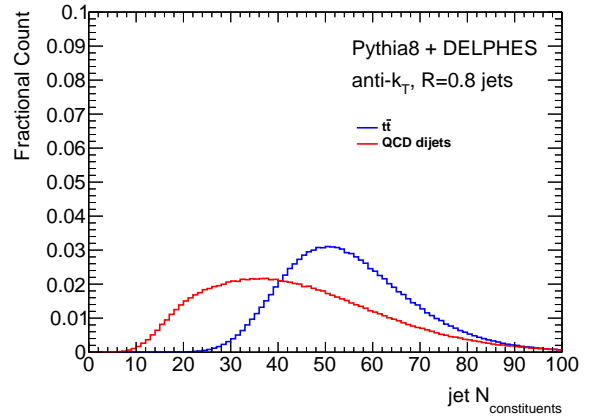
(a)



(b)



(c)



(d)

Figure 6.6: Jet kinematic distributions from the top-tagging benchmark dataset in Ref. [237].

Architecture	Accuracy	AUC	$1/\epsilon_B$ ( $\epsilon_S = 0.3$ )	# Params
TopoDNN [241]	0.916	0.972	$382 \pm 5$	59k
LGN [223]	0.929(1)	0.964(14)	$424 \pm 82$	4.5k
PFN [242]	0.932	0.982	$891 \pm 18$	82k
ResNeXt [238]	0.936	0.984	$1122 \pm 47$	1.46M
ParticleNet [243]	0.938	0.985	$1298 \pm 46$	498k
ParT [244]	0.940	0.9858	$1602 \pm 81$	2.1M
LorentzNet [245]	0.942	0.9868	$2195 \pm 173$	220k
PELICAN <sub>132/78</sub>	0.9426(2)	0.9870(1)	$2250 \pm 75$	208k
PELICAN <sub>60/35</sub>	0.9424(1)	0.9868(1)	$2148 \pm 125$	48k
PELICAN <sub>25/15</sub>	0.9410(3)	0.9858(4)	$1879 \pm 103$	11k

Table 6.1: An overview of a number of top-tagger metrics on the top-tagging benchmark: network accuracy (fraction of correctly classified results, using a score threshold of 50%), area under the ROC curve, background rejection (the inverse of background efficiency) at a fixed 30% signal efficiency, and the number of learnable parameters. The three different instances of PELICAN correspond with different configurations in terms of Reproduced from Ref. [222].

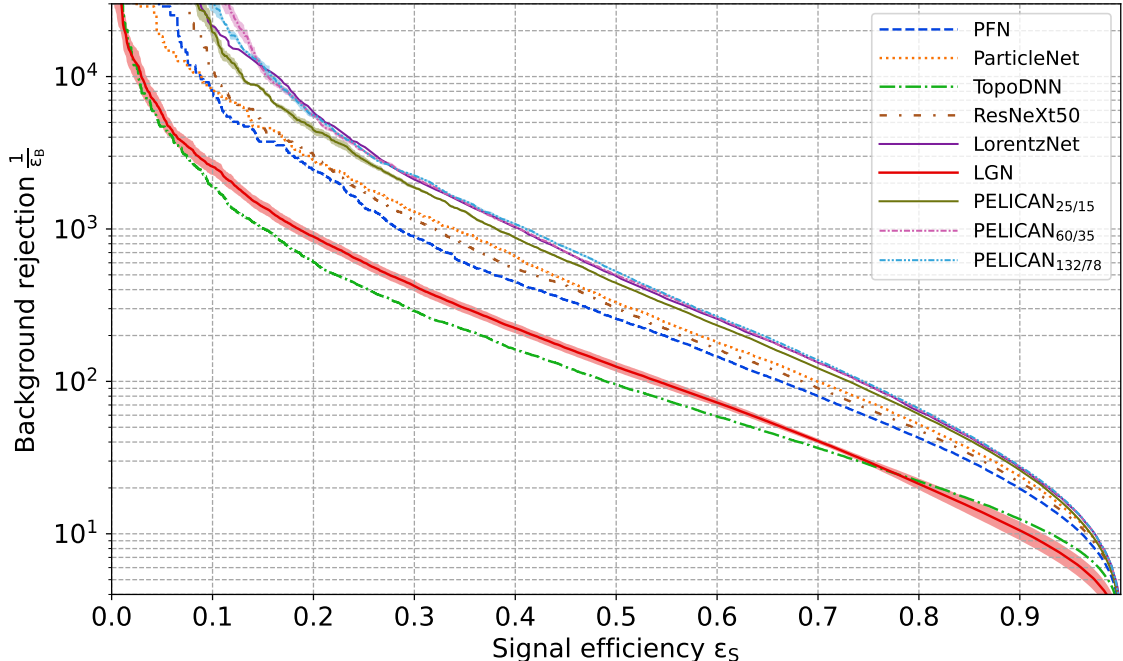


Figure 6.7: Receiver operating characteristic (ROC) curves for a set of top-tagging neural networks, evaluated on the top-tagging benchmark. These networks are also summarized in Table 6.1.

Lorentz invariants (as shown in Figure 6.4) to projecting onto Lorentz covariant quantities constructed as in Equation 6.2.

This also requires a new dataset – a mundane yet important problem, particularly for phenomenology studies performed outside of large collaborations such as ATLAS with access to centrally-produced MC simulations and dedicated software and computing infrastructure. To remedy this, we can use a custom-made dataset [246], produced using the `HEPDATA4ML` MC simulation interface for `PYTHIA` and `DELPHES` [247]<sup>[13]</sup>. Inspired by the top quark tagging benchmark, this dataset also consists of anti- $k_t$ ,  $R = 0.8$  jets corresponding with fully hadronic top quark decays. However, we make a few notable changes:

---

13. This package not only provides an easy Python-based interface for `PYTHIA`, but integrates `FASTJET` for jet clustering and `DELPHES` for (optional) fast detector simulation. In addition, it features tools for defining what truth-level and reconstruction-level particles are saved per event, as well as high-level features and observables (e.g. truth particle containment in jets, recording truth-level daughter particles of a particular decay) that can be used to decorate the resulting dataset. Importantly, the produced datasets contain metadata specifying the entire configuration and the version of the package that was used – to mitigate the simple yet common issue of simulation dataset reproducibility.

- Jets are clustered only using calorimeter information, from DELPHES “Tower” objects.
- Initial- and final-state radiation effects are not included. Including these effects would generally broaden jet mass distributions.
- We explicitly save information on the truth-level  $W$ -boson 4-momentum, as well as which stable decay products (at truth level) can be traced back to the  $W$ -boson decay. This allows us to use the  $W$ -boson 4-momentum as a regression target.
- We identify whether or not jets are *fully-contained* (FC), by which we mean whether or not the entire top quark decay is contained within the jet. To quantify this, we define jets as FC if the truth-level  $b$ -quark and the two light quarks from  $W \rightarrow qq'$  all satisfy  $\Delta R(\text{quark}, \text{jet}) < 0.8$ .

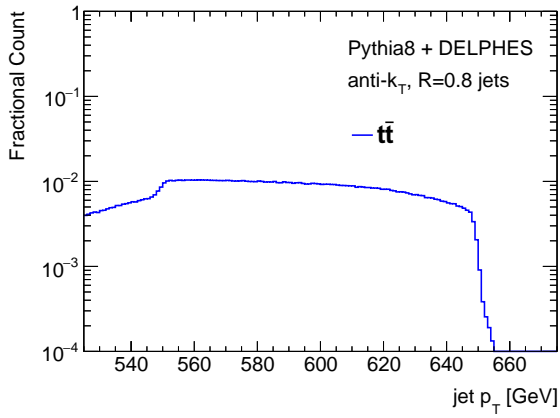
Figure 6.8 shows the jet-level kinematics of this dataset. Note that although we track whether a particular jet is contained, we do not explicitly remove uncontained jets from the dataset. Thus the mass distribution in Figure 6.8c looks notably different than that in Figure 6.8c, as we see a significant sub-population of jets that only contain the  $W$ -boson decay products – as well as a low-mass tail corresponding to jets only containing a fraction of these (or only the  $b$ -quark)<sup>[14]</sup>.

With this dataset, we can try to train PELICAN to reconstruct the truth-level  $W$ -boson 4-momentum – or we can target the *contained*  $W$ -boson 4-momentum,

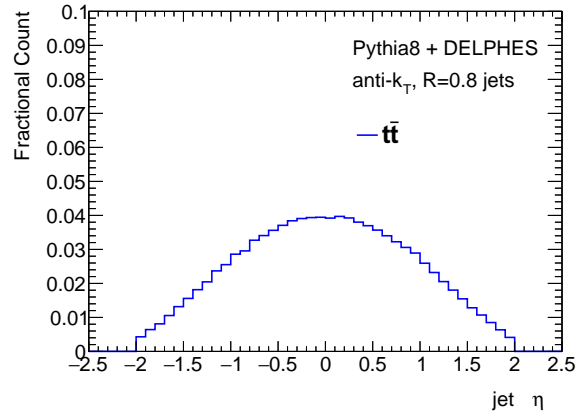
$$p_{W, \text{cont.}}^\mu = \sum_{i \in \text{contained}} p_i^\mu, \quad (6.4)$$

---

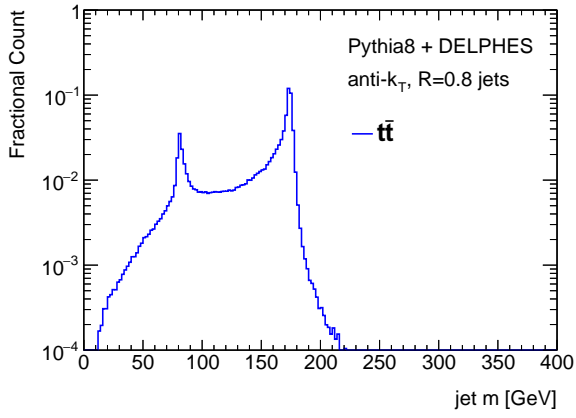
14. The jet  $p_T$  spectra are also notably different between the two datasets. This is because the former employed a jet  $p_T$  cut, with generation performed as to produce a relatively flat jet  $p_T$  distribution. By contrast, the latter involved producing events with a relatively flat distribution in the truth-level  $p_T$  of the leading top (anti)quark in  $t\bar{t}$  production. Each is a somewhat arbitrary but sensible choice for developing a benchmark – in either case it is important to keep track of these kinematics, particularly when comparing one dataset to another.



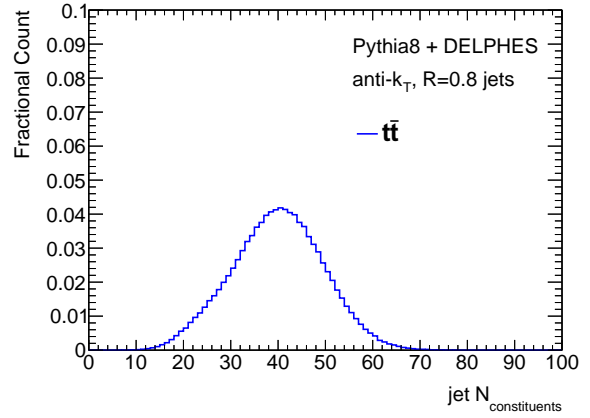
(a)



(b)



(c)



(d)

Figure 6.8: Jet kinematic distributions from the  $W$ -boson regression dataset [246].

as to attempt to reconstruct whatever fraction of the  $W$ -boson decay was captured by the jet<sup>[15]</sup>. As an algorithmic benchmark against which we can compare these regression results, we also record the  $W$ -boson 4-momentum as reconstructed by the Johns Hopkins (JH) top tagger [248], a (non-ML) top-tagging algorithm that reconstructs this momentum as part of its tagging procedure. Of particular note, the JH tagger does not reconstruct the 4-momentum for events that fail its tagging, and thus has a low reconstruction efficiency (albeit decent precision among the momenta it does reconstruct).

Tables 6.2 and 6.3 summarizes PELICAN and JH momentum reconstruction, in terms of the reconstructed  $W$ -boson mass,  $p_T$ , and its distance in the  $(\eta, \phi)$  plane from the true particle – for both choices of  $W$ -boson momentum regression target. The most direct comparison can be made between the JH results and “PELICAN|JH”, where the PELICAN regression has been evaluated only on jets that were successfully tagged as top quarks by JH: here, both algorithms are operating on the exact same set of events, and PELICAN achieves better  $p_T$ , mass and angular resolution. Nonetheless it is also interesting to note that PELICAN produces reconstructed  $W$ -bosons for all events, albeit with lower precision. On the surface, these predictions may not appear useful as they serve to worsen the general resolution<sup>[16]</sup>. However, as shown in Figure 6.9, the PELICAN momentum regression output can be leveraged to efficiently tag whether or not a particular jet contains a  $W$ -boson.

## 6.4 Conclusions, and further directions

As we have seen, equivariant neural networks perform well in benchmarks of standard particle physics classification tasks like jet flavor tagging – with PELICAN and the similarly Lorentz-

---

15. For a discussion of this task – and more general details on momentum and mass reconstruction – see Ref. [222].

16. Keep in mind that in Table 6.3, the resolution is still defined with respect to the true  $W$ -boson 4-momentum. Thus it is not surprising that the resolution – particularly the mass resolution – is very poor when PELICAN is evaluated on all jets in the dataset, as the network is not explicitly trying to reconstruct the true  $W$ -boson to begin with (but only the momentum of whatever fraction of its decay products are contained in the jet).

W-boson truth-level 4-momentum reconstruction				
Dataset Type	Method	$\sigma_{p_T}$ (%)	$\sigma_m$ (%)	$\sigma_{\Delta R}$ (crad)
Truth-level	JH	0.66	1.26	0.216
	PELICAN JH	0.26	0.57	0.113
	PELICAN FC	0.30	0.71	0.139
	PELICAN	0.79	1.12	0.473
DELPHES	JH	9.8	8.3	9.6
	PELICAN JH	3.5	2.6	2.8
	PELICAN FC	4.0	2.9	3.1
	PELICAN	5.1	3.0	4.7

Table 6.2:  $W$ -boson 4-momentum regression results. Here, “PELICAN|JH” refers to PELICAN applied only to JH-tagged jets, and similarly “PELICAN|FC” refers to PELICAN applied only to FC jets. Here we report PELICAN results for models trained to reconstruct the truth-level  $W$ -boson 4-momentum. Taken from Ref. [222].

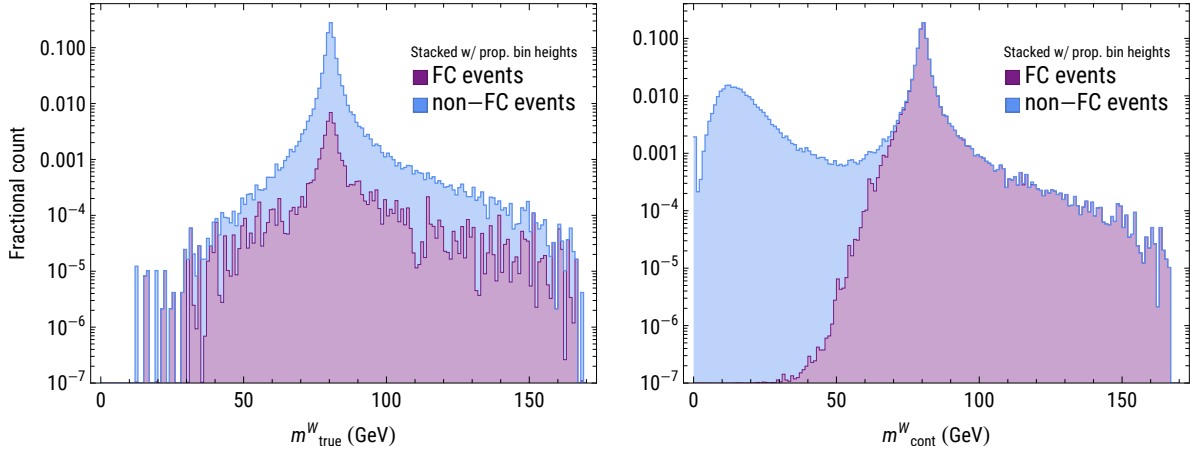


Figure 6.9:  $W$ -boson mass as predicted by PELICAN, targeting the (left) true and (right) contained  $W$ -boson 4-momentum. The distribution is separated into FC and non-FC jets, depicted with proportional bin heights – for each bin, the ratio of FC and non-FC jets is depicted by the (linear) ratio of the bins, with the combined distribution drawn on a logarithmic scale. Taken from Ref. [222].

<i>W</i> -boson jet-contained 4-momentum reconstruction				
Dataset Type	Method	$\sigma_{p_T}$ (%)	$\sigma_m$ (%)	$\sigma_{\Delta R}$ (crad)
Truth-level	JH	0.66	1.26	0.216
	PELICAN JH	0.27	0.62	0.113
	PELICAN FC	0.34	0.86	0.142
	PELICAN	2.37	38.93	0.681
DELPHES	JH	9.8	8.3	9.6
	PELICAN JH	3.6	2.8	3.1
	PELICAN FC	4.2	3.6	3.4
	PELICAN	6.2	39.6	5.6

Table 6.3: *W*-boson 4-momentum regression results. Here, “PELICAN|JH” refers to PELICAN applied only to JH-tagged jets, and similarly “PELICAN|FC” refers to PELICAN applied only to FC jets. Here we report PELICAN results for models trained to reconstruct the contained *W*-boson 4-momentum. Note that the resolutions are still computed with respect to the truth *W*-boson 4-momentum, and that the results for JH are repeated from Table 6.2 (as that method is independent of the PELICAN regression target). Taken from Ref. [222].

equivariant LorentzNet achieving state-of-the-art performance. Furthermore, networks like PELICAN can be naturally extended to full 4-momentum reconstruction. While we have investigated these tasks in the implicit context of physics analysis, where the methods operate on large amounts of precisely-reconstructed information, equivariant networks may also be useful for *online* tasks such as physics object reconstruction within the ATLAS TDAQ system (Section 4.2.6). Here equivariant methods may be particularly appealing because of their efficient parameterization, a necessity for operating on FPGAs onboard the TDAQ system with significant memory constraints [249]; with a high “performance-to-complexity” ratio, equivariant networks employing only a handful of learnable parameters can still achieve respectable performance [250] as shown in Figure 6.10. Another possible extension of the network could be expansion to the full Poincaré group, including position-level information. This may be leveraged in the existing jet classification tasks, where vertexing information associated with jets can assist in *b*-jet tagging<sup>[17]</sup>. This also opens up the possibility of using PELICAN or similar networks in track reconstruction – in collider experiments like ATLAS, or liquid argon TPC experiments where use of GNNs for object reconstruction is being actively investigated [251, 252].

---

17. See Appendix E.2.3.

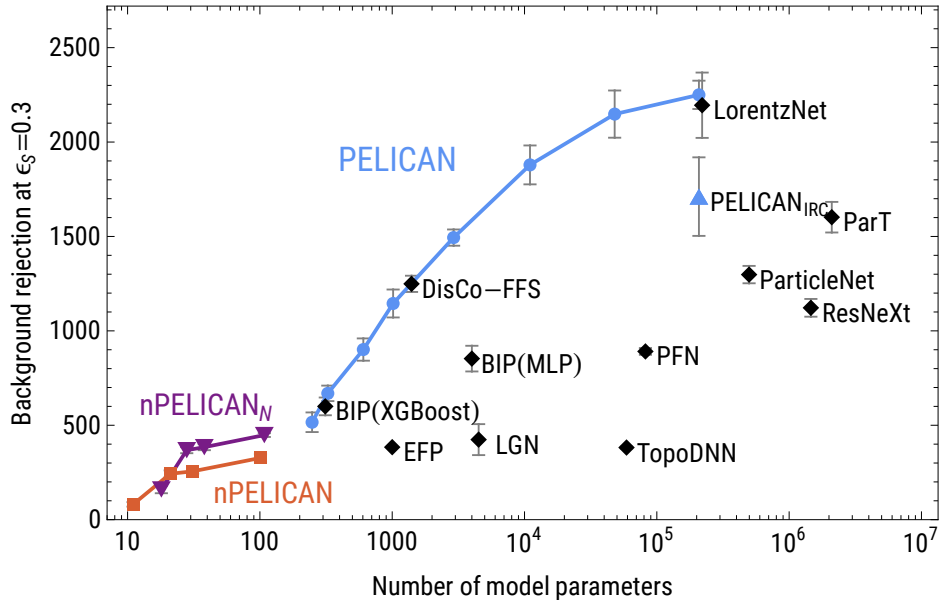


Figure 6.10: Top quark tagging background rejection (at 30% signal efficiency) as a function of number of network parameters, for neural networks evaluated on the dataset in Ref. [237]. Here, nPELICAN and nPELICAN<sub>N</sub> are low-parameter modifications of PELICAN which may be amenable to use in TDAQ systems – and PELICAN<sub>IRC</sub> is an infrared and colinearity-safe modification of the original network (Appendix E.2.2), discussed in Ref. [222]. In addition to the networks shown in Table 6.1, this plot also includes points corresponding with the Boost Invariant Polynomials [253] and DisCo-FFS [254]. Taken from Ref. [250].

## CHAPTER 7

### CONCLUSION

In this thesis, we have reviewed the method and results of a new physics search at ATLAS. Although we did not find strong evidence supporting the new physics models targeted, we have applied some of the tightest constraints to these models to-date, further squeezing the parameter space where new physics is likely to reside. We have also reviewed an emerging class of equivariant machine learning methods developed for particle physics, which appear to be promising tools for increasing our analytic power in particle physics experiments – and possibly even for reconstructing the low-level signals from particle detectors. With these two topics, we have seen examples of how high-energy physicists search for answers to open questions in our understanding of how the universe functions at the smallest scales, and how we may leverage our understanding of the fundamental symmetries of nature to improve the toolkit with which we try to answer these questions. We have also – in spite of hundreds of pages – only scratched the surface. Collider experiments like ATLAS are host to many parallel searches for new physics as well as precision measurements that test our current understanding, some using similar methods to what we have covered and others very different techniques. Nonetheless, even our single example of a new physics search conveys some of the most fundamental aspects of how we engage in experiments: a combination of highly precise apparatuses for recording our observations, and a very careful accounting for all the ways in which our data may be obscured or biased in the measurement process.

As the high-energy physics community embarks on long-term plans to build a successor to the LHC – and, to a certain extent, debates precisely what should be built – it is clear that there remains a whole host of studies we can perform on past and current LHC experiment data, if we wish to leave no stone unturned in the search for physics beyond the Standard Model – and perhaps more conclusively answer the questions we started with: What is the cosmos made of, and how does it behave?

# APPENDIX A

## DISPLACED VERTICES AND MISSING TRANSVERSE ENERGY SEARCH AT THE ATLAS EXPERIMENT: OVERFLOW

In this appendix, we will cover some details of the physics search discussed in Chapter 5, as well as some more general topics about ATLAS event reconstruction that were not covered prior to that chapter.

### A.1 Tracking in ATLAS: A brief review

While not specific to this particular analysis, it will be instructive to briefly review track reconstruction in ATLAS, and how the signals measured by the Inner Detector (Section 4.2.2) are turned into reconstructed charged particle tracks.

As described in Section 4.2.2, the inner detector consists of a set of silicon-based tracking detectors, as well as the Transition Radiation Tracker – a system that instead uses proportional counters and measurements of transition radiation, but which is also fundamentally a type of tracking detector. When a charged particle passes through these systems, its ionization of the silicon *pn* junctions and the gas of the TRT produces a set of *hits*, points in space (and time) where it passed. To produce a track, we must string together these hits – a task made complicated by the dense event environment and resulting high *occupancy* of the tracker<sup>[1]</sup> – in order to produce the helical paths along which charged particles travel in the detector’s magnetic field. The basic track reconstruction procedure consists of two steps: a *forward pass* starting from the Pixel and SCT detectors and working outwards, as well as a *backward pass* starting from the TRT. The forward pass procedure is as follows [255–257]<sup>[2]</sup>:

---

1. Simply put, there are a lot of hits – and thus many different ways in which we may (naïvely) combine them.

2. Note that Ref. [257] is hosted at a link which is not necessarily stable – during the course of writing

1. We construct points in 3D space called *space-points*, from clusters of Pixel and SCT sensors. Each space-point has an associated position uncertainty, which is determined based on the geometry and position of the sensors from which it is constructed.
2. Triplets of space-points in the Pixel or SCT detectors are combined into *track seeds*, and these seeds' approximate trajectories are computed.
3. *Search roads* are constructed, which consist of sets of modules along the track seeds' approximate trajectories. Seeds are extended along the search roads via a combinatorial Kalman filter (CKF), that adds additional space-points to the seed<sup>[3]</sup> to build track candidates.
4. Low-quality track candidates are filtered out, as are tracks that share too many hits. To resolve ambiguities, a neural network is used to determine the likelihood of multiple charged particles having contributed to a single cluster, and update these clusters' positions.
5. The track candidates are re-fit using the ATLAS global  $\chi^2$  fitting method [259], and are attempted to be extended into the TRT (following similar steps of building search roads and employing a CKF, followed by the global  $\chi^2$  fitter).

Figure A.1 shows a sketch of this process. The backward pass, which is used to increase the acceptance for non-prompt electrons produced by photon conversion in the detector, operates similarly to the forward-pass but starts from the TRT, and is seeded by energy deposits in the EM calorimeter that determine regions of interest where track-finding is performed [257].

Figure A.2 shows how tracks are typically parameterized, in terms of angles and their impact parameters (displacements) in transverse and  $z$  directions.

---

this thesis, it has changed at least once. A more stable albeit non-public version can be found in Ref. [258].

3. The benefit of using search roads is that it greatly reduces the combinatorial complexity of reconstruction at this stage.

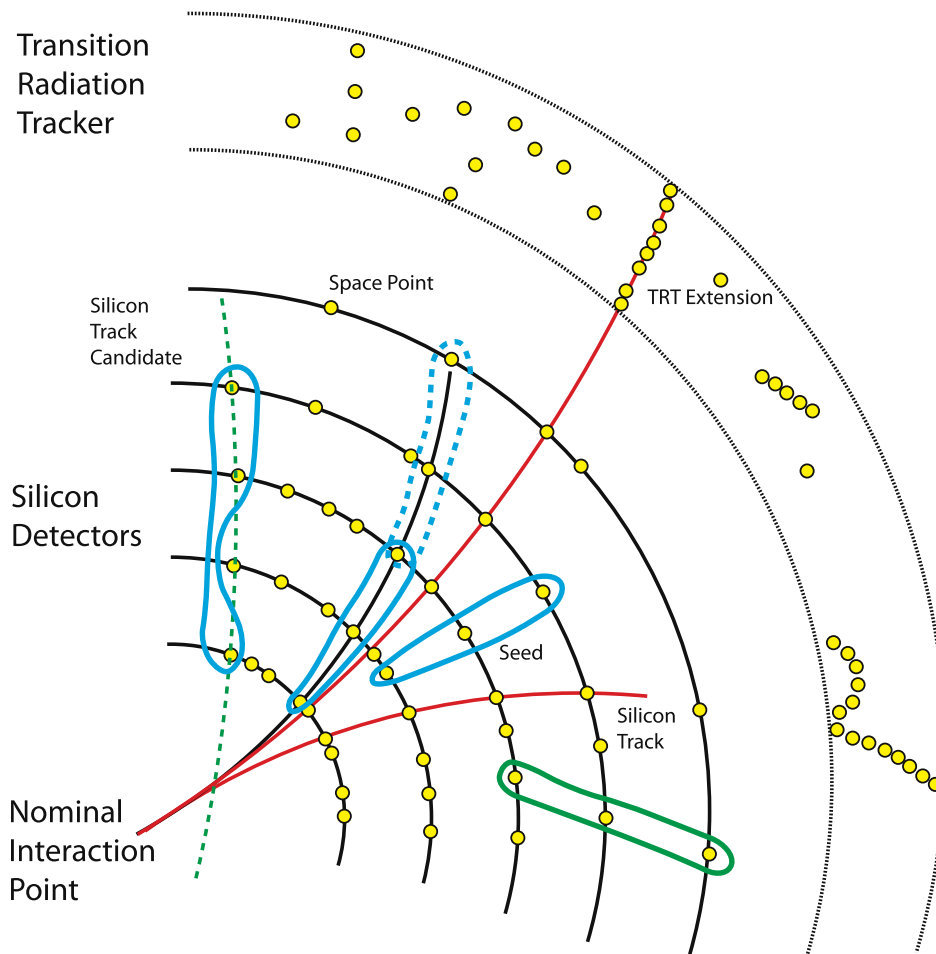


Figure A.1: An overview of track construction in the ATLAS inner detector, showing the construction of track seeds, candidates and final tracks. Taken from Ref. [260].

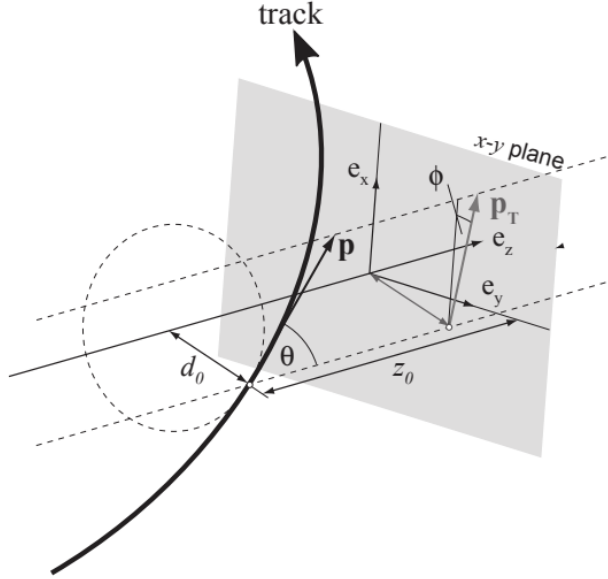


Figure A.2: An example of how tracks reconstructed in the ATLAS inner detector are parameterized in terms of angles  $(\theta, \phi)$ , impact parameters  $(d_0, z_0)$  and  $|\vec{p}|/m$ . Taken from Ref. [261].

## A.2 Overlap Removal

Overlap removal – the process of removing overlapping particle candidates – is another example of a method not specific to this particular analysis, but rather a general tool for resolving ambiguities and avoid double-counting of energy deposits in the detector. This is generally performed via a list of rules, where one type of particle candidate is removed if it is within some  $\Delta R$  of another candidate or shares tracks with it. For a general overview of overlap removal, see Ref. [262]<sup>[4]</sup>. For this analysis, the overlap removal algorithm proceeds as follows [143]:

1. **Electron-muon:** Electrons are removed if they share a track with a muon.
2. **Jet-electron:** Jets are removed if  $\Delta R(e, j) < 0.2$ , to remove jets originating from EM

---

4. This is an internal note. For a publicly-available source, see the Athena software package [263]. Although reading through the Athena algorithms is not particularly easy, it is potentially an effective way of understanding how precisely detector signals are reconstructed (as these are the very same algorithms as deployed in the experiment).

calorimeter showers initiated by electrons.

3. **Electron-jet:** Electrons are removed if  $\Delta R(e, j) < 0.4$ , to remove electrons originating from hadronic decays (which we instead treat as components of the jets).
4. **Jet-muon:** Jets with fewer than three associated tracks are removed if they have a muon with  $\Delta R(\mu, j) < 0.2$ <sup>[5]</sup>.
5. **Muon-jet:** Muons are removed if  $\Delta R(\mu, j) < 0.2$ .
6. **Photon-lepton:** Photons are removed if  $\Delta R(e, \gamma) < 0.4$  or  $\Delta R(\mu, \gamma) < 0.4$ .
7. **Jet-photon:** Jets are removed if  $\Delta R(j, \gamma) < 0.4$ .

### A.3 Tracking and Secondary Vertexing Efficiency

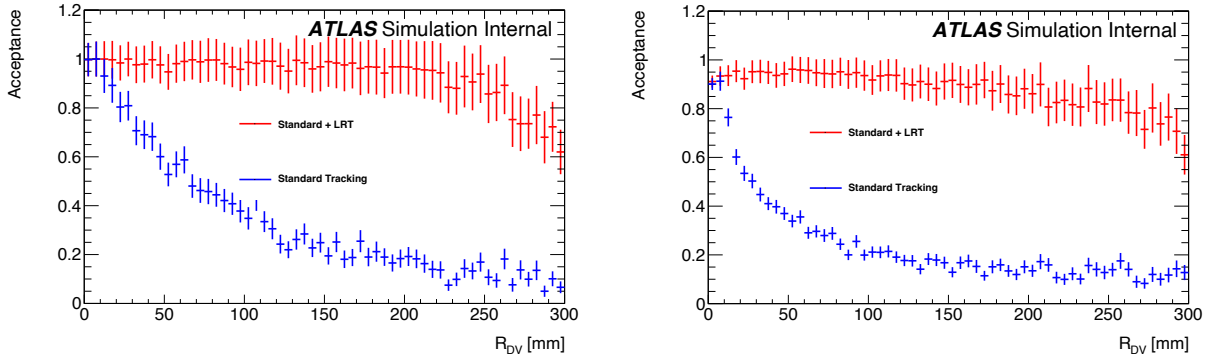
As a search looking for displaced vertices, this analysis is particularly sensitive to tracking (Section 5.3.1.1) and secondary vertexing (Sections 5.3.1.2 and 5.3.1.3) efficiencies: how well do we reconstruct these objects? We can study our reconstruction algorithms' efficiencies by using Monte Carlo (MC) samples, where we have access to both the reconstructed objects, and the MC truth-level information. Figure A.3 shows the tracking efficiency for two different signal MC samples; here we have defined the efficiency (or *acceptance*) as the ratio of true LLP decays for which at least two true charged particles are reconstructed, and the number of true LLP decays with at least two charged particles<sup>[6]</sup>, within the search fiducial volume ( $R_{xy} < 300$  mm and  $|z| < 300$  mm) with  $p_T > 1$  GeV and  $|\eta| < 5$  – and have parameterized this with respect to the  $R_{xy}$  of the LLP decay. As we can see, including LRT tracks greatly

---

5. This includes regular muon candidates, as well as *ghost-associated* muons, which are muons whose tracks are assigned an infinitesimal momentum, and are *associated* if their tracks are then clustered into the jet [195, 264].

6. With this definition, we are computing the tracking efficiency with respect to LLP decays – which is what we are interested in, as we want to understand how well we can reconstruct tracks associated with these decays.

improves the tracking efficiency, owing to its relatively loose cuts on track impact parameters (see Table 5.5). Note that this definition of efficiency is somewhat nuanced, as we are checking whether an LLP decay has at least two tracks reconstructed, and not necessarily that it has as many tracks reconstructed as it has produced charged particles<sup>[7]</sup> – thus this efficiency metric will exhibit correlation with the number of charged particles produced. We can see the effect of this correlation by comparing Figure A.3 with Figure A.4.



(a) An  $R$ -hadron sample with  $m_{\tilde{g}} = 2200$  GeV,  $m_{\tilde{\chi}_1^0} = 100$  GeV, and  $\tau_{\tilde{g}} = 10$  ns.

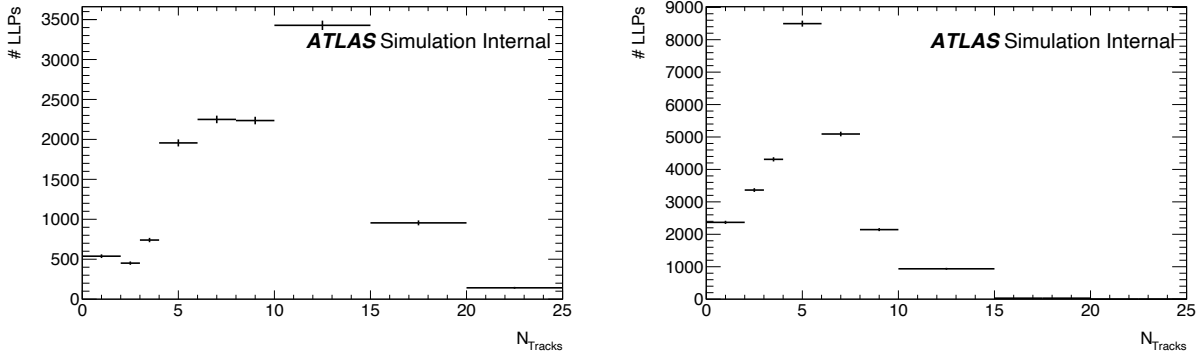
(b) A Wino-Bino sample with  $m_{\tilde{\chi}_2^0} = 200$  GeV,  $m_{\tilde{\chi}_1^0} = 170$  GeV and  $\tau_{\tilde{W}} = 3$  ns.

Figure A.3: LLP tracking efficiency with and without LRT tracking for (a)  $R$ -hadron sample and (b) a Wino-Bino sample, as a function of the DV radial position  $R_{xy}$ . The acceptance is defined as the ratio of number of true LLP decays for which two true reconstructed charged particles are reconstructed, and the number of true LLP decays within the fiducial volume with two charged particles with  $p_T > 1$  GeV and  $|\eta| < 5$ . Taken from Ref [143].

## A.4 Missing transverse energy triggers

The definition of the  $\cancel{E}_T$ -triggered region (Section 5.4.2) of the analysis includes the requirement that an event pass a  $\cancel{E}_T$ -based trigger. These triggers are part of the “derived raw” data format used by the  $R$ -parity and long-lived particles group, referred to as DRAW\_RPVLL in

7. To be clear, the number of charged particles “produced” is not necessarily those produced in the LLP’s immediate decay, but includes subsequent (prompt) processes – such as hadronization and showering in the case of decay to quarks. Thus while we are in principle only considering  $1 \rightarrow 2$  processes for the LLP decays, we may expect these decays to ultimately yield more than two charged particles.



(a) An  $R$ -hadron sample with  $m_{\tilde{g}} = 2200$  GeV,  $m_{\tilde{\chi}_1^0} = 100$  GeV, and  $\tau_{\tilde{g}} = 10$  ns.

(b) A Wino-Bino sample with  $m_{\tilde{\chi}_2^0} = 200$  GeV,  $m_{\tilde{\chi}_1^0} = 170$  GeV and  $\tau_{\tilde{W}} = 3$  ns.

Figure A.4: The number of tracks reconstructed per LLP for (a)  $R$ -hadron sample and (b) a Wino-Bino sample. The  $R$ -hadron sample has, on average, more tracks reconstructed per track, and thus is expected to have a higher estimated tracking efficiency than the Wino-Bino sample, as shown in Figure A.3. Taken from Ref [143].

Ref. [143]. These triggers are explicitly listed in Table A.1, where the algorithm for computed the High-Level Trigger (HLT)  $\cancel{E}_T$  is one of the following:

1. **cell**: The  $\cancel{E}_T$  is computed as the negative  $p_T$  vector sum of all calorimeter cells that pass a noise cut.
2. **mht**: The  $\cancel{E}_T$  is computed as the negative  $p_T$  vector sum of all anti- $k_t$ ,  $R = 0.4$  jets, with pileup subtraction and with the jet energy scale calibration (Section E.2.4) applied.
3. **pufit**: The  $\cancel{E}_T$  is computed as the negative  $p_T$  vector sum of all calorimeter topoclusters, with pileup subtraction.

Note that offline  $\cancel{E}_T$  – both at the L1 and HLT stages – is computed without information from the muon spectrometer.

Trigger $\cancel{E}_T$ algorithm	$\cancel{E}_T^{\text{HLT}}$ threshold [GeV]	$\cancel{E}_T^{\text{L1}}$ threshold [GeV]
cell	90	50
cell	100	50

(Table A.1 – continued on following page)

(continued from previous page)

Trigger $\cancel{E}_T$ algorithm	$\cancel{E}_T^{\text{HLT}}$ threshold [GeV]	$\cancel{E}_T^{\text{L1}}$ threshold [GeV]
cell	120	50
cell	90	55
cell	100	55
cell	120	55
cell	90	60
cell	100	60
cell	120	60
tc_lcw	90	50
tc_lcw	100	50
tc_lcw	120	50
tc_lcw	90	55
tc_lcw	100	55
tc_lcw	120	55
tc_lcw	90	60
tc_lcw	100	60
tc_lcw	120	60
mht	90	50
mht	100	50
mht	110	50
mht	120	50
mht	90	55
mht	100	55
mht	110	55

(Table A.1 – continued on following page)

(continued from previous page)

Trigger $\cancel{E}_T$ algorithm	$\cancel{E}_T^{\text{HLT}}$ threshold [GeV]	$\cancel{E}_T^{\text{L1}}$ threshold [GeV]
mht	120	55
mht	90	60
mht	100	60
mht	110	60
mht	120	60
mht	130	50
mht , cell	{110, 65}	50
mht , cell	{110, 70}	50
mht , cell	{110, 75}	50
mht , cell	{110, 80}	55
mht , cell	{110, 65}	55
mht , cell	{110, 70}	55
mht , cell	{110, 75}	55
mht , cell	{110, 80}	55
pufit	110	60
mht , cell	{120, 80}	60
pufit	110	50
pufit	110	55
pufit	120	70
pufit	120	60
mht , cell	{120, 80}	60
pufit , cell	{110, 70}	50
pufit , cell	{110, 65}	55

(Table A.1 – continued on following page)

(continued from previous page)

Trigger $\cancel{E}_T$ algorithm	$\cancel{E}_T^{\text{HLT}}$ threshold [GeV]	$\cancel{E}_T^{\text{L1}}$ threshold [GeV]
pufit , cell	{100, 75}	60
pufit , cell	{110, 65}	60

Table A.1: An overview of the  $\cancel{E}_T$  triggers. The  $\cancel{E}_T^{\text{HLT}}$  and  $\cancel{E}_T^{\text{L1}}$  refer to  $\cancel{E}_T$  as computed by the High-Level Trigger and Level-1 Trigger systems, respectively. The algorithm choice refers to the  $\cancel{E}_T^{\text{HLT}}$  computation.

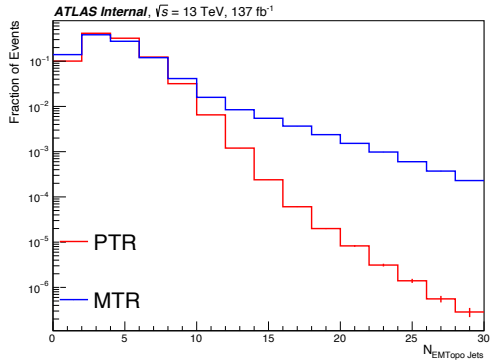
## A.5 Comparison of MTR and PTR Kinematics

In Figure A.5, we compare the kinematic and object multiplicity distributions of the MTR and PTR (Section 5.4.2). In addition to standard event-level variables (number of pileup interactions, and the sum of the scalar event  $p_T^2$ ) and objects defined in Section 5.3, we also compare the number of *track jets* in each region. The definition of these jets is given in Appendix A.6.

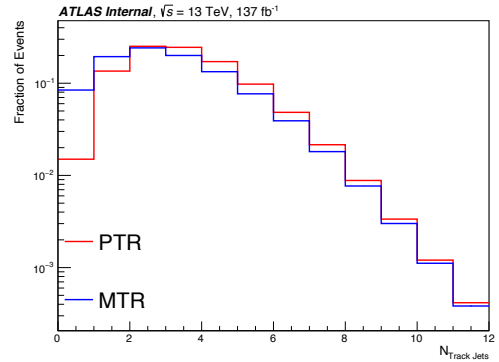
## A.6 Track Jets

In addition to the EMTopo jets (Section 5.3.2.2), we also reconstruct *track jets* that are not used for the background estimate directly, but which do play a role in modeling the systematic uncertainties. As their EMTopo counterparts, these jets are built using the anti- $k_t$  algorithm with  $R = 0.4$ . However, they are constructed not from calorimeter energy deposits, but rather from collections of tracks that pass the selections in Table A.2a and which are *associated* with the same PV. This track-PV association is determined via the following method:

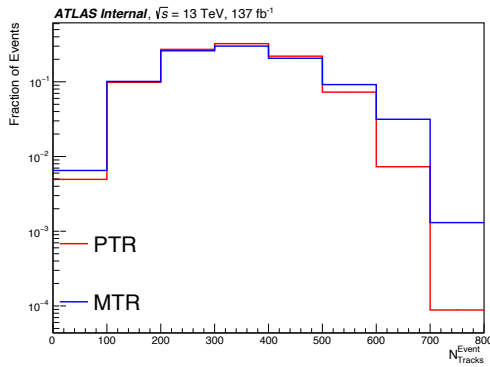
1. Tracks are associated with a PV if they are found to satisfy  $\text{sig}(z_0) < 3$ , where  $z_0$  is the impact parameter with respect to the PV and  $\text{sig}(x) = x/\sigma_x$  is the significance.



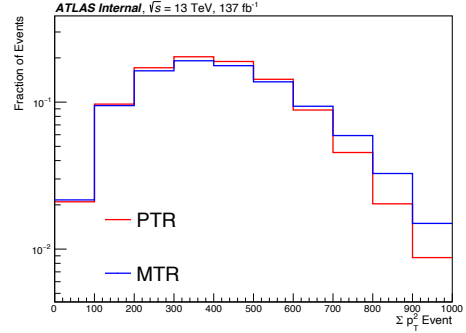
(a)



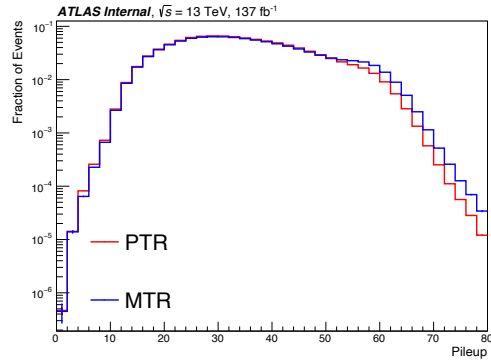
(b)



(c)



(d)



(e)

Figure A.5: A comparison of MTR and PTR, in terms of (a) number of EMTopo jets, (b) number of track jets, (c) number of PV-associated tracks, (d) scalar sum of  $p_T^2$  of all PV-associated tracks, and (e) number of pileup vertices. Taken from Ref. [143].

2. Remaining tracks are associated with a PV if they are found to satisfy  $|z_0| < 0.5$  mm with respect to the PV.
3. If a track is associated with multiple PVs, it is given to that with the highest  $\sum p_T^2$ .

The “Loose” track criteria in Table A.2a are provided in Table A.3. After clustering, track jets are required to meet the selection criteria in Table A.2b.

Baseline track jet track criteria
$p_T > 1$ GeV $ d_0  < 2$ mm
Passing the Loose track criteria

(a) Constituent track requirements.

Baseline track jet criteria
$p_T > 10$ GeV $N_{\text{tracks}}^{\text{jet}} \geq 2$

(b) Jet requirements.

Table A.2: Selection requirements for (a) track jet’s constituent tracks, and (b) track jets clustered from these tracks. Taken from Ref. [143].

Loose track criteria
$p_T > 400$ MeV $ \eta  < 2.5$ $N_{\text{Si}} \geq 7$ $N_{\text{shared}}^{\text{modules}} < 2$ $N_{\text{holes}} < 3$ $N_{\text{holes}}^{\text{Pixel}} < 2$

Table A.3: An overview of the “Loose” track criteria.  $N_{\text{Si}}$  refers to silicon hits (Pixel and SCT detectors),  $N_{\text{shared}}^{\text{modules}}$  to the number of modules shared with other tracks (1 module corresponds with 1 Pixel hit or 2 SCT hits).  $N_{\text{holes}}$  refer to *holes*, which are non-existing but expected measurement points for a given track, excluding disabled modules. Taken from Ref. [265].

## A.7 The SuperLooseBadLLP Jet Cleaning Working Point

The SuperLooseBadLLP jet cleaning working point is defined by the selections in Table A.4 whose definitions include the following additional variables [266]:

- $E_{\text{neg}}$ : The sum of all cells in the jet with negative reconstructed energy. Such cells can be produced in a real jet due to electronic and pile-up noise, but can also be a sign of noise activity that produces a fake jet.
- $f_{\text{HEC}}$ : The fraction of the jet energy deposited into the Hadronic End Cap (HEC) section of the LAr calorimeter.
- $Q_{\text{cell}}^{\text{LAr}}$ : This is the quadratic difference between actual and expected pulse shapes in the LAr calorimeter, with the latter produced via simulation of the calorimeter electronics response. A cell-level quantity, it is defined by

$$Q_{\text{cell}}^{\text{LAr}} = \sum_{j=i}^4 \left( s_j - A \cdot (g_j - \tau g'_j) \right)^2, \quad (\text{A.1})$$

- $A$  is the signal amplitude [267],
- $\tau$  is the signal time,
- $s_j$  is the amplitude of sample  $j$  (in analog-digital converter counts),
- $g_j$  is the normalized predicted ionization shape,
- $g'_j = dg_j/dt$  is the time derivative of  $g_j$ .

- $f_{\text{HEC}}^Q$ : The fraction of the jet energy deposited in HEC with poor signal shape quality, which is defined as  $Q_{\text{cell}}^{\text{LAr}} > 4000$ .
- $f_{\text{LAr}}^Q$ : The fraction of the jet energy deposited in LAr cells with poor signal shape quality.
- $\langle Q \rangle$ : The energy-squared weighted average of  $Q_{\text{cell}}^{\text{LAr}}$ . This quantity is normalized<sup>[8]</sup> so

---

8. Note that this normalization is not implicit in the variable definition used in Ref. [143], resulting in some differences between the formulae there and in Table A.4.

that  $\langle Q \rangle \in (0, 1)$ .

SuperLooseBadLLP jet flag	
Index	Criterion
<i>A</i>	$(f_{\max} > 0.99) \wedge ( \eta  < 2)$
<i>B</i>	$E_{\text{neg}} > 60 \text{ GeV}$
<i>C</i>	$(f_{\text{HEC}} > 0.5) \wedge (f_{\text{HEC}}^Q > 0.5) \wedge (\langle Q \rangle > 0.8)$
<i>D</i>	$(f_{\text{EM}} > 0.95) \wedge (f_{\text{Lar}}^Q > 0.8) \wedge ( \eta  < 2.8) \wedge (\langle Q \rangle > 0.8)$
pass SuperLooseBadLLP = $\overline{(A \vee B \vee C \vee D)}$	

Table A.4: An overview of the selections that define the SuperLooseBadLLP jet cleaning working point. Note that a jet that meets any of the criteria fails the jet cleaning. Taken from Ref. [143].

## A.8 Dead TileCal Modules

To determine whether or not a particular TileCal module is dead in a given event (Section 5.4.2.4), the modules are monitored to keep track of not only dead module locations but the times when these modules stopped functioning, as this changes during the course of detector operation. This information is indicated in Table A.5, per run and year.

Year	Run	Dead TileCal Module Region
2016	302053-311481	$0.0 < \eta < 0.9, -1.33 < \phi < -1.13$
2016	306988-311481	$-0.9 < \eta < 0.0, 0.34 < \phi < 0.54$
2017	325713-340453	$-0.9 < \eta < 0.0, -0.25 < \phi < -0.05$
2017	325713-340453	$0.8 < \eta < 1.7, 0.14 < \phi < 0.34$
2018	350310-352514	$0.0 < \eta < 0.9, 2.7 < \phi < 3.0$
2018	355261-364292	$0.0 < \eta < 0.9,  \phi  > 3.0$

Table A.5: Location of the dead TileCal modules. Taken from Ref. [268].

## A.9 VSI Track Hit Pattern Check

The hit pattern check – part of the VSI track cleanings described in Section 5.4.3.1 – is part of the VSI algorithm described in Ref. [170], which checks the constituent hits of selected and attached tracks for a DV. As configured in Ref. [172], we use the `ExtrapolationAssist` hit pattern check algorithm, which is an extension of the `Classical` algorithm. Thus it will be instructive to first explain the `Classical` algorithm, which functions as follows.

1. The algorithm identifies the  $R_{xy}$  region in which the DV is located. This determines what is considered the inner and adjacent outer tracker layers.
2. The track is rejected if it does not have a hit in the adjacent outer layer.
3. The track is rejected if it does have a hit in the inner layers.

This method is illustrated in Figure A.6. One downside of this algorithm is that it is agnostic to the presence of disabled tracker modules, which may cause it to reject tracks that should be associated with the DV if they pass through a disabled module (and thus fail to produce a hit on a certain layer). This issue is mitigated by the `ExtrapolationAssist` algorithm, which extrapolates the track to the end of the SCT and records any disabled modules through which it passes: the algorithm then behaves as the `Classical` algorithm, except that it operates on a combination of the hit pattern and disabled module pattern.

## A.10 Material Map Veto

In order to eliminate DVs produced not by the decay of LLPs produced in  $pp$  collisions but by scattering of SM particles off of the detector material nuclei, we apply a material map to veto DVs that are reconstructed inside the detector material. The material map – as its name implies – is a spatial map of the detector components, indicating what volumes are occupied by material. There are two material maps available, one produced by `GEANT4`

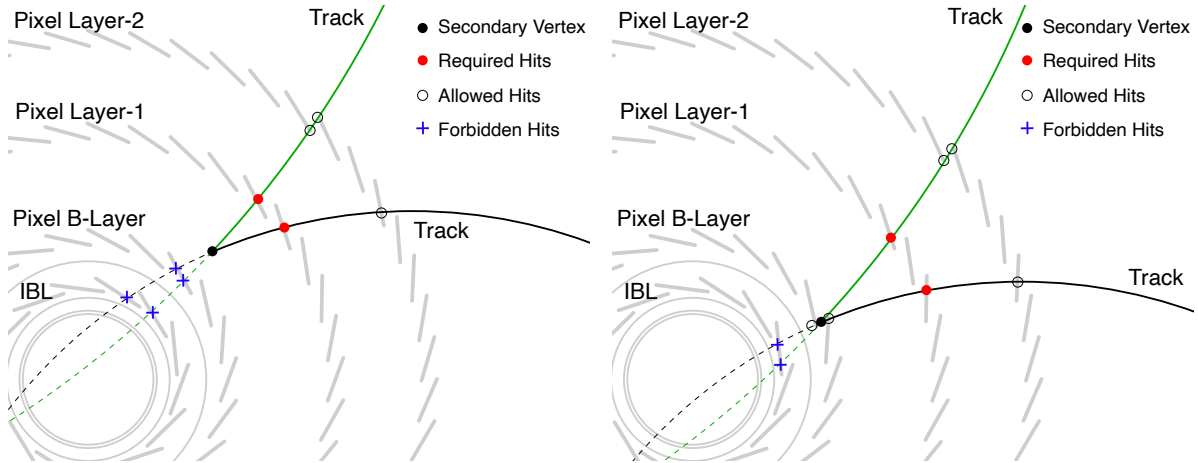


Figure A.6: An illustration of the Classical hit pattern check algorithm for the VSI secondary vertexing algorithm, for two DVs. Note that in the example on the right, the DV is located within the B-layer, and the required and forbidden hits are both located outside of this layer. Taken from Ref. [170].

(wherein the position of detector materials is assumed to be known), and one produced from data. We refer to the former as the *MC map*, as it is derived from the **GEANT4** models used in MC simulation. The latter, which we call the *data map*, is produced by a combination of two methods:

- For the Pixel detector, the detector components are effectively mapped out by tomography via tracking, by counting the density of low-mass, low-multiplicity tracks (that are deemed to not be  $K_S^0$  decays). These tracks are assumed to be the product of hadronic interactions (Section 5.5.2.1), and regions are marked as *inside material* if the track density passes a certain threshold.
- For the SCT, the low-mass and low-multiplicity tracks are of too low density for the same method to be used as in the Pixel detector. In this case, the map is derived using the MC map as a guide, augmented by track measurements in data [269].

Figure A.7 shows the material and data maps. While these would ideally be equivalent, there are noticeable visual differences between the two, as was discovered in the analysis discussed in Ref. [196]. To mitigate potential issues from these differences, we develop a set

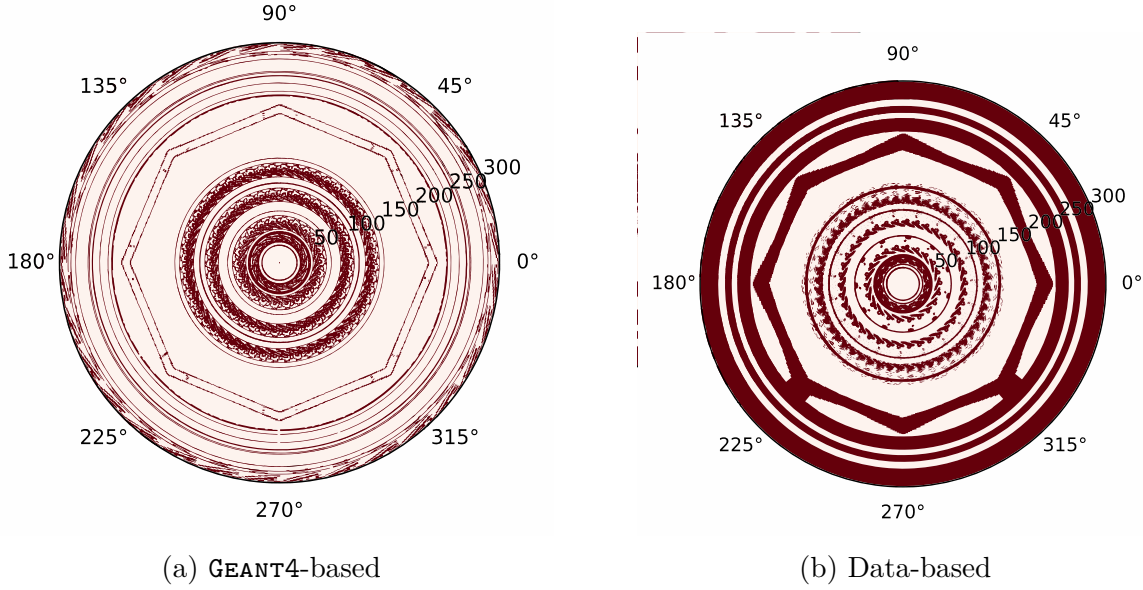


Figure A.7: The (a) **GEANT4**-based and (b) data-based material maps. The material map veto effectively removes DVs found to be inside the detector material. Taken from Ref. [143].

of vetoes based off of both maps. The first set of vetoes are referred to as the *loose* MC and data vetoes. These both use the data map, with the only difference being whether or not an offset to the Pixel layers (as measured in the data map) is applied<sup>[9]</sup>. From these loose vetoes, we also define strict vetoes, where we make the following additional corrections:

- For the map used in the veto, we add regions deemed to be inside material by the MC map. This is motivated by the fact that the MC map’s underlying **GEANT4** model is meant to accurately reflect the detector design (i.e. it should not contain material that is not actually present), and it is possible that the data map lacks certain regions due to limited statistics in the tomography method used to build it.
- The data map is divided into bins (as a consequence of its construction method), and so we also veto a DV if it is in a bin adjacent to one that is inside material. This is meant to mitigate edge effects from binning, whereby a bin considered outside material

---

9. In MC simulations, the detector is assumed to be perfectly centered in the ATLAS cavern. In reality, this centering is imperfect and can be measured (and incorporated into the data map). For the loose MC veto, this offset is explicitly not applied – it is effectively removed from the map in use.

may in reality contain some material from one of its neighbors.

- For each DV, a 3D ellipsoid is constructed from its covariance matrix. For VSI DVs, the covariance matrix is derived from the uncertainties in the DV position fit, whereas for FVs it is determined from the seed positions. The ellipsoid represents the  $1\sigma$  uncertainty on the DV position, and a DV is vetoed if this ellipsoid intersects an inside material region.

For this analysis, we use the strict vetoes for MC and data (as appropriate).

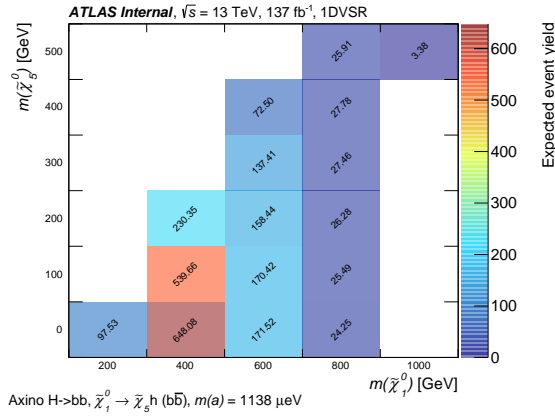
## A.11 Axino Signal Sensitivity

While the 1 VSI DV SR was ultimately chosen for targeting the axino model, the other SRs were tested in case they would have better sensitivity. Figures A.8 and A.9 provide an overview of each decay channel’s sensitivity in the three SRs, and Figure A.10 provides the sensitivity for the  $h \rightarrow b\bar{b}$  decay channel with  $f_a = 5 \times 10^{10}$  GeV in the 2 FV SR.

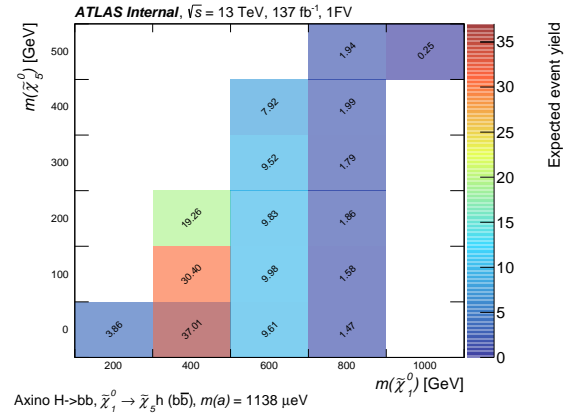
## A.12 Inclusive Background Estimate: Extended EDP

As discussed in Section 5.5.1, one potential weakness of the EDP estimation is that it requires sufficient statistics such that there are at least a few DVs per  $(m_{\text{DV}}, N_{\text{tracks}}^{\text{DV}}, N_{\text{b-tag}}, N_{\text{tracks}}^{\text{event}})$  bin. This is unfortunately not always the case, and following the standard estimation procedure would yield an EDP of zero in a number of the VRs. To mitigate this, we modify the method by extending the  $(m_{\text{DV}}, N_{\text{tracks}}^{\text{DV}})$  range used for computing each EDP, to produce an extended EDP<sub>ext</sub>. We then compute the background as

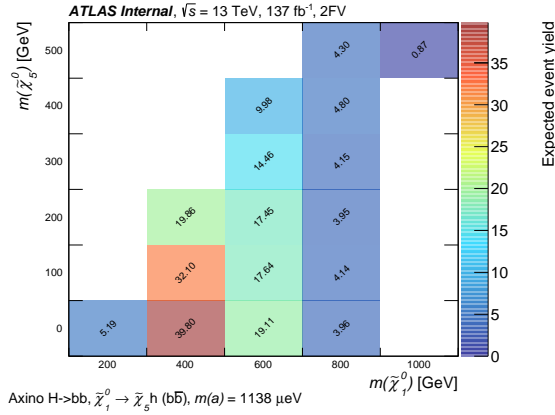
$$N_{\text{background}} = f \cdot \sum_{i=0}^{N_{\text{events}}} \text{EDP}_{\text{ext}}(\text{DV}|\text{event}_i) , \quad (\text{A.2})$$



(a)

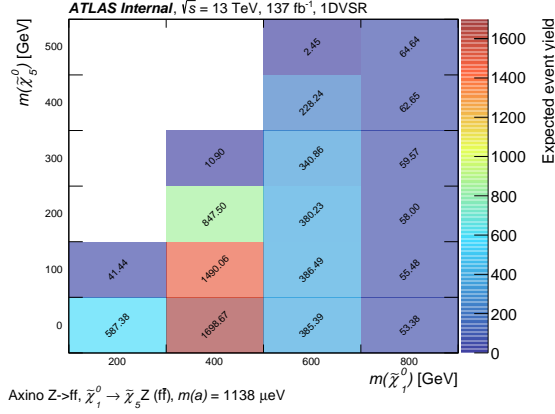


(b)

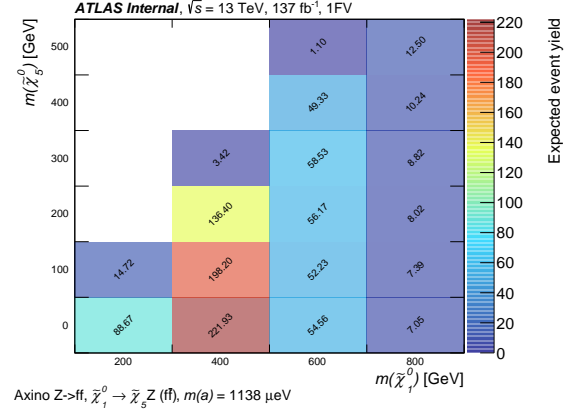


(c)

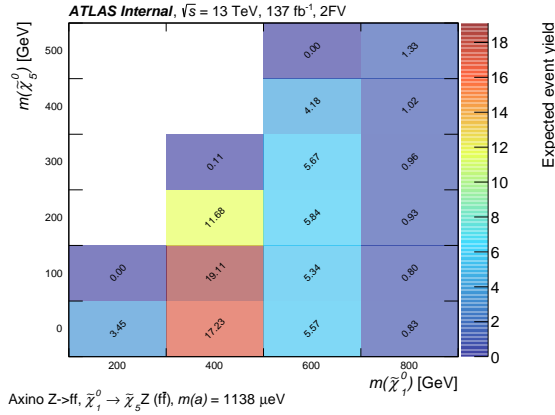
Figure A.8: Expected signal yields for the axino signal model with the  $h \rightarrow b\bar{b}$  decay channel, in the various SRs. Taken from Ref. [143].



(a)



(b)



(c)

Figure A.9: Expected signal yields for the axino signal model with the  $Z \rightarrow q\bar{q}$  decay channel, in the various SRs. Taken from Ref. [143].

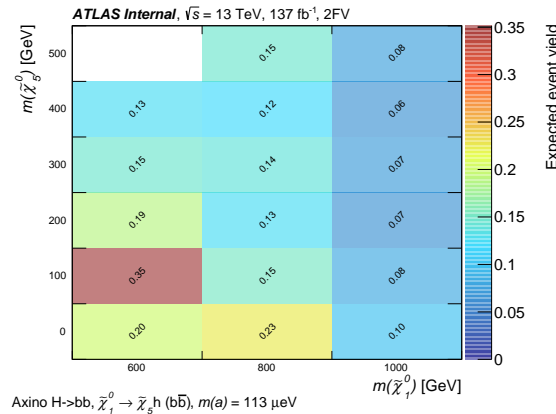


Figure A.10: Expected signal yields for the axino signal model with the  $h \rightarrow b\bar{b}$  decay channel, with  $f_a = 5 \times 10^{10} \text{ GeV}$ , in the 2 FV SR. Taken from Ref. [143].

where  $f = N_{\text{DV}}^{\text{target}}/N_{\text{DV}}^{\text{ext}}$  gives the ratio of DVs in the target and extended regions. The extended region definitions, used for the 1 VSI DV analysis channel, are provided in Table A.6.

Extended Regions for 1 VSI DV		
Region	$m_{\text{DV}}$ [GeV]	$N_{\text{tracks}}^{\text{DV}}$
VR Low Track CR Low Track	$> 10$	4
VR Low Track Mid Mass CR Low Track Mid Mass	[10,20]	4
VR Low Mass CR Low Mass	[ 5,10]	$\geq 5$
SR Extended CR Extended	$> 5$	$\geq 4$
SR CR	$> 10$	$\geq 5$

Table A.6: An overview of the extended regions used for the track density background estimate method, for the 1 VSI DV analysis channel. Note that these region definitions partly coincide with the merged bins in Table 5.25, and that these bins are not entirely independent of one another. Taken from Ref. [143].

### A.13 Inclusive Background Estimate: The Hybrid Method

As noted in Section 5.5.1, we developed a *hybrid background estimation method* in addition to the nominal inclusive method. This aptly-named method is based on matching DVs with EMTopo jets, with unmatched DVs being used to compute an EDP as in the track density method. The matched DVs are used to calculate a similar quantity referred to as the *jet-DV probability* (JDP). The estimation method, which is performed in the PTR, is as follows:

1. DVs are matched to the highest- $p_T$  jet that satisfies  $\Delta R(\text{DV}, j) < 0.4$ . Matched jets and DVs are set aside to compute the JDP, with unmatched DVs reserved for computing

an EDP.

2. The JDP is computed as

$$\text{JDP}(\text{DV}|\text{jet}(x, y)) = \frac{\# \text{ of jets with a matched DV, with } (b_{\text{tag}} = x, p_T = y)}{\# \text{ of jets with } (b_{\text{tag}} = x, p_T = y)}, \quad (\text{A.3})$$

which is similar to the EDP except computed over jets, and is parameterized in terms of the jet  $b$ -tag ( $b_{\text{tag}}$ ) and  $p_T$ . The EDP is computed using the unmatched DVs.

3. The number of background events is computed as

$$N_{\text{background}} = \sum_{i=0}^{N_{\text{events}}} \text{EDP}(\text{DV}|\text{event}_i) + \sum_{i=0}^{N_{\text{jet}}} \text{JDP}(\text{DV}|\text{jet}_i), \quad (\text{A.4})$$

where in practice the EDP and JDP can each be extended via the method discussed in Appendix A.12, in order to mitigate the issue of low statistics in their respective derivations.

## A.14 Hadronic Interactions Background Estimate Validation

The HI background estimate method (Section 5.5.2.1) is validated on a  $Z \rightarrow \nu\bar{\nu} + \text{jets}$  MC sample, where the results of the estimate can be compared to the MC truth-level information. The fits of the  $N_{\text{tracks}}^{\text{DV}}(m_{\text{DV}})$  distribution are shown in Figure A.11, and the results of this validation are shown in Table A.7, where the background estimate is in good agreement with the truth information.

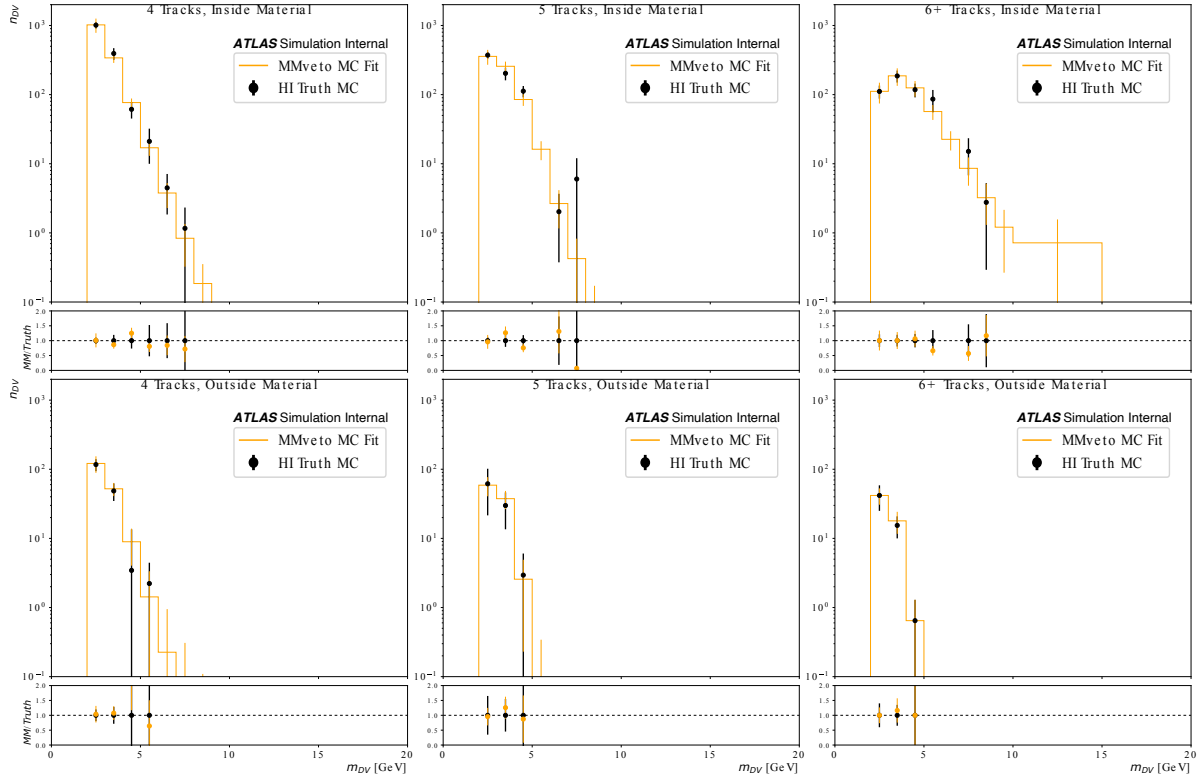


Figure A.11: Fits performed to estimate the HI contribution to the background, both the inside and outside material regions, on a  $Z \rightarrow \nu\bar{\nu} + \text{jets}$  MC simulation sample. Modified from Ref. [143].

MC Estimate Closure					
Region		Inside Material		Outside Material	
$N_{\text{tracks}}^{\text{DV}}$	$m_{\text{DV}}$ [GeV]	HI Estimate		Truth	
4	[ 2, 5]	1436.9 ± 232.5	1464.9 ± 133.9	182.4 ± 35.8	169.0 ± 28.7
4	[ 5, 10]	21.9 ± 5.0	26.7 ± 11.5	1.7 ± 2.0	2.2 ± 2.2
4	[10, 20]	0.0 ± 0.0	0.0 ± 0.0	0.0 ± 0.0	0.0 ± 0.0
5	[ 2, 5]	698.9 ± 95.6	687.8 ± 63.0	99.0 ± 27.1	94.5 ± 43.4
5	[ 5, 10]	19.4 ± 5.2	8.0 ± 6.2	0.0 ± 0.3	0.0 ± 0.0
5	[10, 20]	0.0 ± 0.0	0.0 ± 0.0	0.0 ± 0.0	0.0 ± 0.0
> 6	[ 2, 5]	423.7 ± 73.4	415.0 ± 51.1	60.4 ± 13.5	57.8 ± 17.6
> 6	[ 5, 10]	92.5 ± 16.2	103.9 ± 31.9	0.0 ± 0.1	0.0 ± 0.0
> 6	[10, 20]	0.7 ± 0.8	0.0 ± 0.0	0.0 ± 0.0	0.0 ± 0.0

Table A.7: Results from the MC closure tests for inside and outside material. DV counts from the material map fit are compared to the truth level selections.

## A.15 Accidental Crossing Background Estimate Details

Here, we will review a few details pertaining to the AX estimate method. The software used to perform this estimation is located in Ref. [270]<sup>[10]</sup>.

### A.15.1 Producing Mass Templates

As outlined in Section 5.5.2.3, the general procedure for estimating the AX background involves producing mass templates, which are how we model the contribution to the DV mass distribution that would be produced by DVs with AX'ing tracks. We create these mass templates by “artificially” producing AX'ed DVs, by attaching a single track to a  $n$ -track DV to produce a  $(n + 1)$ -track DV. These tracks are source from a track database, which

---

10. This is, unfortunately, another example of a source which is not publicly-accessible. However, for any reader with access to the CERN GitLab, I encourage referencing this software repository for understanding how the AX estimate method functions.

we source by identifying AX'ed  $K_S^0$  decay candidates in data, and saving the kinematic properties of the AX'ing track.

Identifying AX'ed  $K_S^0$  decay candidates corresponds to finding 3-track DVs, where a sum of two of the three tracks yields the  $K_S^0$  mass of approximately 498 MeV [9] when each track is assigned the  $\pi^\pm$  mass. We use DVs in events that pass MTR selections (Table 5.17), that pass baseline DV-level selections (Table 5.22), with the SR blinded<sup>[11]</sup>. For each 3-track DV passing these selections, we compute every combination of 2-track masses. If one of these is within 50 MeV of the  $K_S^0$  mass, we deem this a likely AX'ed  $K_S^0$  decay, and save the third unused track to our track database.

When producing mass templates, we randomly sample the track database to fetch a track to attach to a  $n$ -track DV, to promote it to a  $(n + 1)$ -track DV (thus simulating the AX process). To do this, we fetch a track that was attached to a DV in the same radial region, where we define our regions as<sup>[12]</sup>:

- $R_{xy} < 25$  mm: Inside the beam-pipe.
- $R_{xy} \in (25, 38]$  mm: Inside the Insertable B-layer.
- $R_{xy} \in (38, 120]$  mm: Inside Layer 2 of the Pixel Detector.
- $R_{xy} \in (120, 300]$  mm: Inside Layer 1 of the SCT.

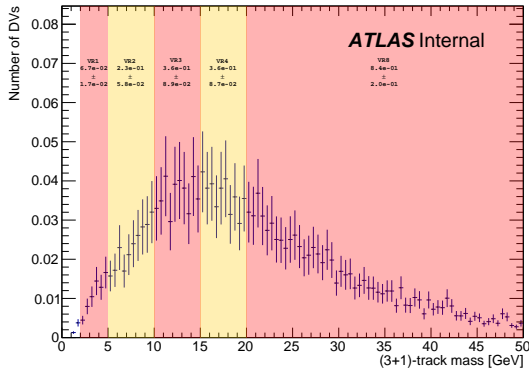
This binning is meant to limit the effects of any kinematic biases stemming from tracks being attached to DVs in regions distant from where they had originated – which could cause inaccuracies in the modeling of this process if the track kinematics correlate with  $R_{xy}$ . Figure A.12 provides the mass templates used to produce the AX estimate<sup>[13]</sup>.

---

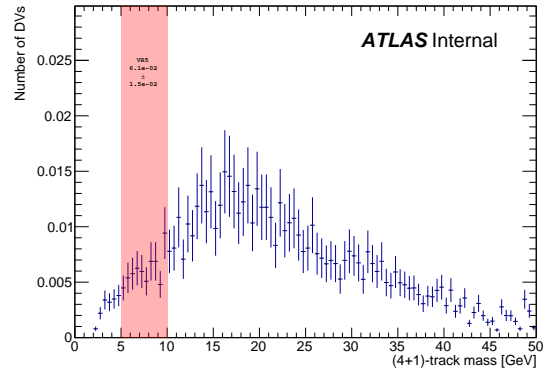
11. This yields DVs that are similar to those in the VRs, except that we do not impose the  $m_{DV}$  and  $N_{\text{tracks}}^{DV}$  selections as when looking for  $K_S^0$  candidates, we are looking for DVs that will explicitly fall outside of these.

12. These radial regions are chosen to roughly correspond with different elements of the Inner Detector (Section 4.2.2). Note that the layer radii given in Table 4.1 are *average* positions of sensitive elements.

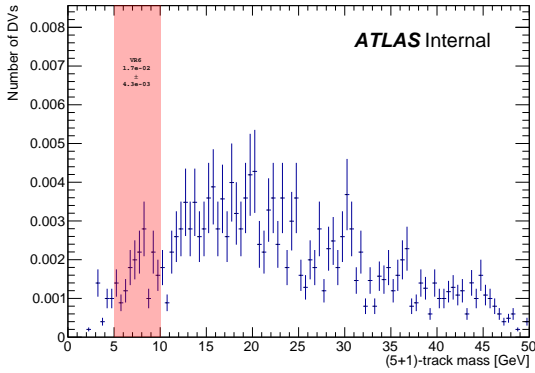
13. In principle, one can reduce the uncertainties in the template by performing this procedure multiple



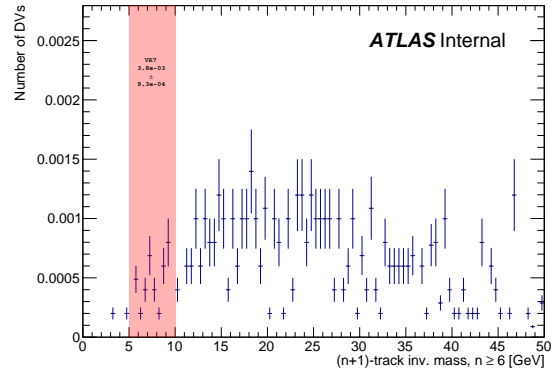
(a)



(b)



(c)



(d)

Figure A.12: Mass template used for the AX background estimate, showing the regions integrated for the different VRs. The integration for the SR covers the  $> 10$  GeV region for the  $(4 + 1)$ ,  $(5 + 1)$  and  $(6 + 1)$  templates.

### A.15.2 Estimating Accidental Crossing Rate

The AX'ing rate is computed by finding  $K_S^0 \rightarrow \pi^+\pi^-$  candidate DVs in data, and estimating the rate at which they are AX'ed by a third spurious track. As discussed in Section 5.5.2.3, this involves counting the number of 2- and 3-track  $K_S^0$  candidates, the latter consisting of the AX'ed candidates. We identify the 3-track  $K_S^0$  candidates through the method discussed in the preceding section, and we take the same approach for the 2-track  $K_S^0$  candidates, applying the same selections.

We identify the 2-track  $K_S^0$  candidates by constructing the mass spectrum of all DVs passing our baseline selections in Table 5.22, in events passing the MTR selections in Table 5.17. We apply the following additional selections to generate the final mass spectrum:

- We require the DV tracks to satisfy

$$\cos\left(\alpha\left(\overrightarrow{\text{DV}-\text{PV}}, \vec{p}_{\text{tot}}\right)\right) > 0.999, \quad (\text{A.5})$$

- $\overrightarrow{\text{DV}-\text{PV}}$  is the vector between the PV and DV,
- $\vec{p}_{\text{tot}}$  is the vector sum of the DV track momenta,
- $\alpha(\vec{v}_1, \vec{v}_2)$  is the 3D angle between vectors  $\vec{v}_1$  and  $\vec{v}_2$ ,

which eliminates background DVs by requiring the DV tracks to be nearly colinear with  $\overrightarrow{\text{DV}-\text{PV}}$ . This is particularly important when working in the low-mass region, as is necessary for the  $K_S^0$  with a mass of approximately 498 MeV [9].

- We also require that  $m_{\text{DV}, \lambda} > 1.125 \text{ GeV}$ . This “lambda mass” is the reconstructed 2-track DV mass where the higher- $p_T$  track is assigned the proton mass of approximately 938 MeV [9], and corresponds with the  $\lambda^0 \rightarrow p\pi^-$  decay – another SM decay that contributes to the 2-track DV spectrum. This selection eliminates the majority of likely

times – with different samplings of the track database – and averaging the results. However, such an approach was not taken for this analysis as the statistics of the track database were relatively limited, so that the results of multiple iterations of mass template production would be non-trivially correlated.

$\lambda^0$ 's, which have a mass of approximately 1.116 GeV [9], and which distort the mass spectrum if incorrectly reconstructed  $K_S^0$ 's.

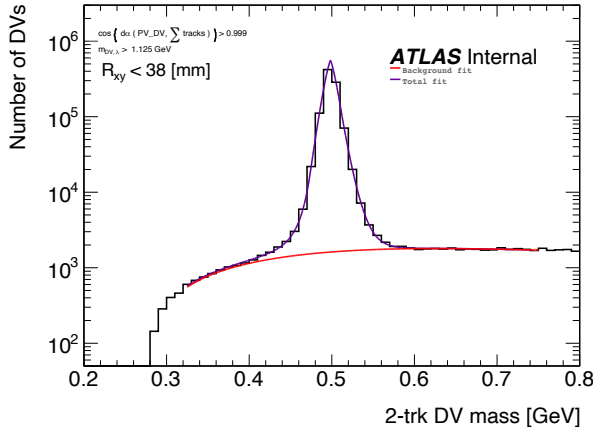
A similar approach is taken for 3-track  $K_S^0$  candidates, except that we reconstruct 2-track masses from them by trying each possible 2-track combination, and using that which yields a mass nearest the  $K_S^0$ . This will produce some combinatoric background, owing to incorrect combinations of tracks in addition to DVs that in fact are not a product of  $K_S^0$  decays in the first place. We manage these backgrounds by fitting the  $m_{\text{DV}}$  spectra to isolate the  $K_S^0$  mass peak, as shown in Figure A.13 for 2- and 3-track DVs for three different radial regions. This fitting procedure is an extension of the method used for a similar background estimate in Ref. [196]. Of particular note, the 2-track  $m_{\text{DV}}$  spectra are fit using a symmetric, generalized normal distribution [271] extension of the Crystal Ball function [272], given by

$$f(x) = \begin{cases} N_0 \cdot A \cdot (B - (\frac{x-\mu}{\sigma})^{-n}) & (x - \mu)/\sigma \leq -\alpha \\ N_0 \cdot \exp\left(-\frac{1}{2} \left|\frac{x-\mu}{\sigma}\right|^\gamma\right) & (x - \mu)/\sigma \in (-\alpha, \alpha) \\ N_0 \cdot A \cdot (B - (-\frac{x-\mu}{\sigma})^{-n}) & (x - \mu)/\sigma \geq \alpha \end{cases} \quad (\text{A.6})$$

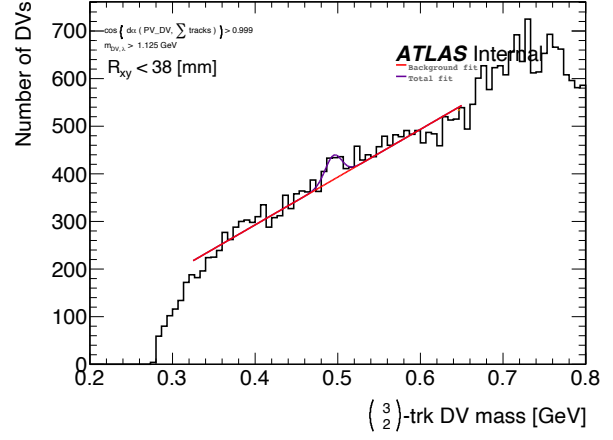
- $A = k^n \exp(-\frac{1}{2} |\alpha|^\gamma)$ ,
- $B = k - |\alpha|$ ,
- $k = 2n / (\gamma |\alpha|^{\gamma-1})$ ,
- $\{N_0, \mu, \sigma, \gamma, n, \alpha\}$  are fitting parameters.

## A.16 Tracking Systematic uncertainty Estimate Details

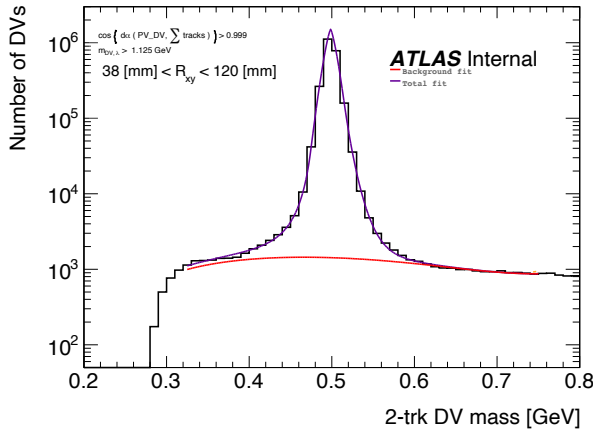
The systematic tracking uncertainty methods are implemented in the software in Ref. [273]. As discussed in Section 5.6.3.2.3, the basic structure of the study is a so-called “track-killing” study, whereby tracks are eliminated from DVs in signal MC simulation samples, to simulate tracking inefficiencies found not to be fully modeled in those samples. The tracking inefficiencies were modeled by comparing MC simulation and data  $K_S^0$  candidate



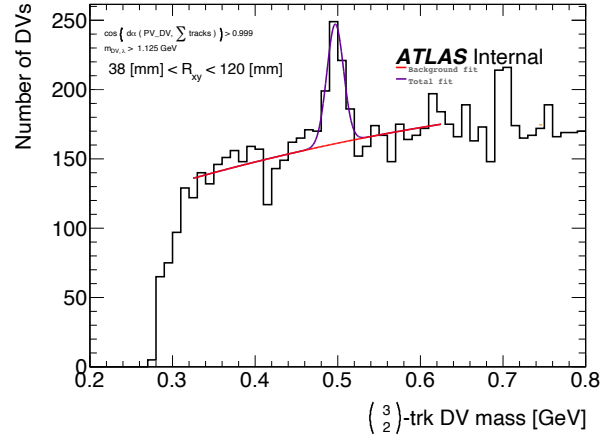
(a)  $R_{xy} < 38$  mm



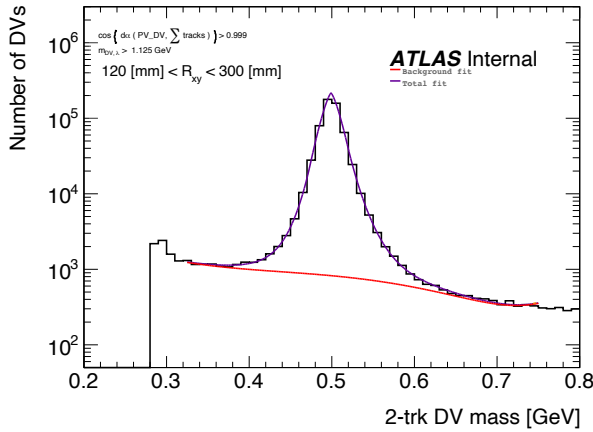
(b)  $R_{xy} < 38$  mm



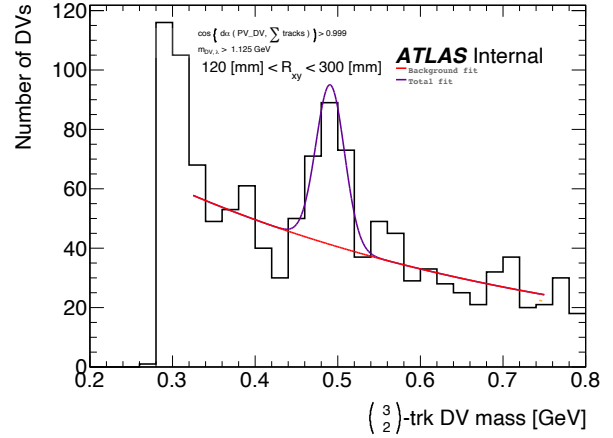
(c)  $R_{xy} \in (38, 120)$  [mm]



(d)  $R_{xy} \in (38, 120)$  [mm]



(e)  $R_{xy} \in (120, 300)$  [mm]



(f)  $R_{xy} \in (120, 300)$  [mm]

Figure A.13: DV mass distributions, for 2- and 3-track DVs, for three different radial regions. For the 3-track DVs, we reconstruct 2-track masses for each choice of 2-tracks, which produces a combinatorial background. We fit all of these peaks to extract the number of  $K_S^0$  candidates, which we use for the AX'ing rate estimation. Taken from Ref [143].

yields. For the 1 VSI DV analysis channel, this process was performed separately for each year of data as to account for possible year-to-year variations in the inefficiency (either in the data or the MC simulation). The  $K_S^0$  yield plots and estimated tracking inefficiencies are shown in Figure A.14. As the year-to-year variations were found to be very small, a single set of tracking inefficiencies was estimated for the FV algorithm, using data and MC simulation from all three years combined. Figure A.15 shows the  $K_S^0$  candidate yield and resulting tracking inefficiency estimate. In each case, the same  $R_{xy}$  binning was used as in the accidental crossing background estimate (Section 5.5.2.3 and Appendix A.15), except that the innermost bin was separated into beam-pipe ( $R_{xy} \in [0, 25)$  mm) and Insertable B-Layer ( $R_{xy} \in [25, 38)$  mm) regions, as the MC simulation  $K_S^0$  yield was normalized to match that in data for the beam-pipe region – as tracking uncertainties for tracks connected to DVs located in the beam-pipe region are assumed to be well-modeled.

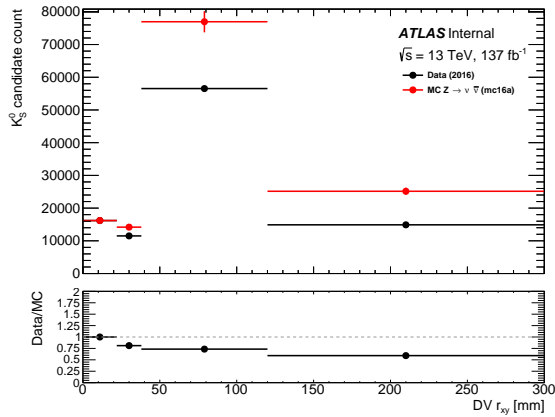
## A.17 Asymptotic Likelihood Test Statistic

Here, we provide some useful details regarding the likelihood test method discussed in Section 5.7.2.1. Note that this information can be found in Ref. [213], and we will not derive these results – they are simply summarized here for completeness.

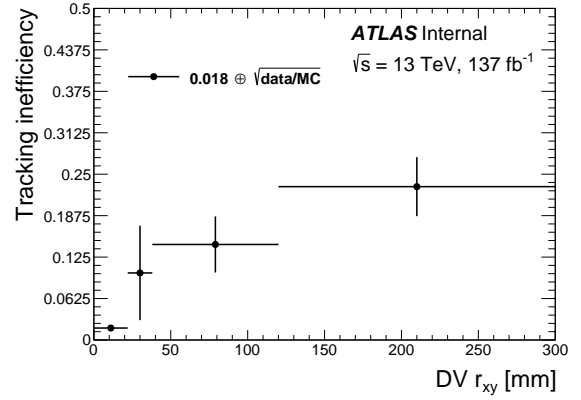
The probability distribution function of the test statistic  $\tilde{q}_\mu$  from Equation 5.18 can be approximated as

$$f(\tilde{q}_\mu|\mu') = \Phi\left(\frac{\mu' - \mu}{\sigma}\right) \delta(\tilde{q}_\mu) + \frac{1}{2\sqrt{2}\pi} \begin{cases} \frac{1}{\sqrt{\tilde{q}_\mu}} \exp\left(-\frac{1}{2}\left(\sqrt{\tilde{q}_\mu} - \frac{\mu - \mu'}{\sigma}\right)^2\right) & 0 < \tilde{q}_\mu \leq \mu^2/\sigma^2 \\ \frac{1}{\mu/\sigma} \exp\left(-\frac{1}{2}\frac{(\tilde{q}_\mu - (\mu^2 - 2\mu\mu')/\sigma^2)^2}{(2\mu/\sigma)^2}\right) & \tilde{q}_\mu > \mu^2/\sigma^2 \end{cases} \quad (\text{A.7})$$

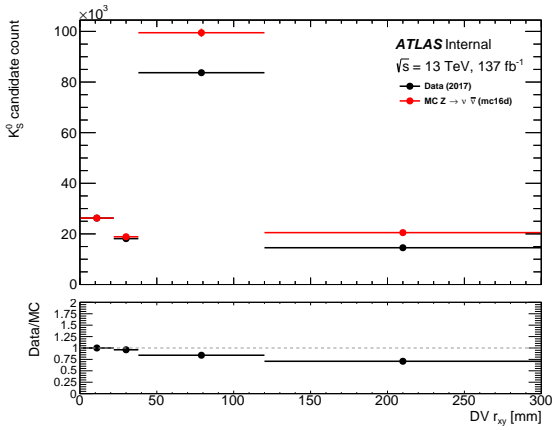
- $\Phi(\dots)$  is the Gaussian cumulative distribution function,
- $\delta(\dots)$  is the Dirac delta function.



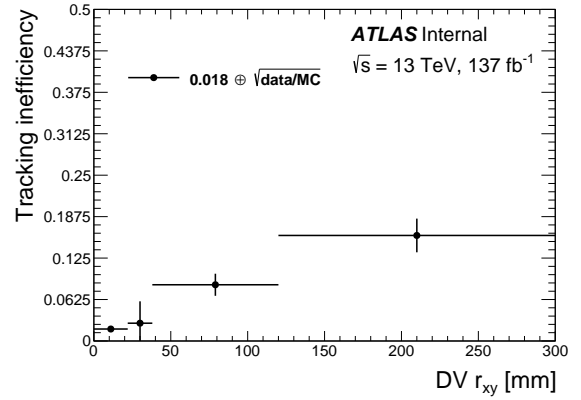
(a)



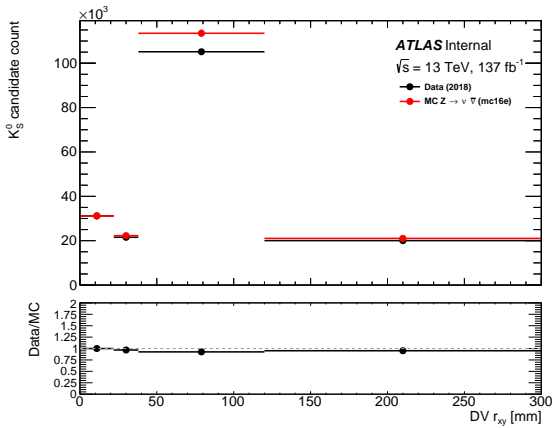
(b)



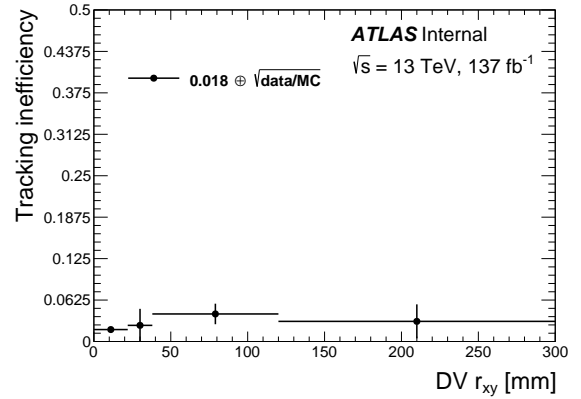
(c)



(d)



(e)



(f)

Figure A.14: The (a,c,e) comparison of  $K_S^0$  candidate yields in MC simulation and data, and (b,d,f) the resulting estimated tracking uncertainties for VSI DVs, separated by year. Taken from Ref [143].

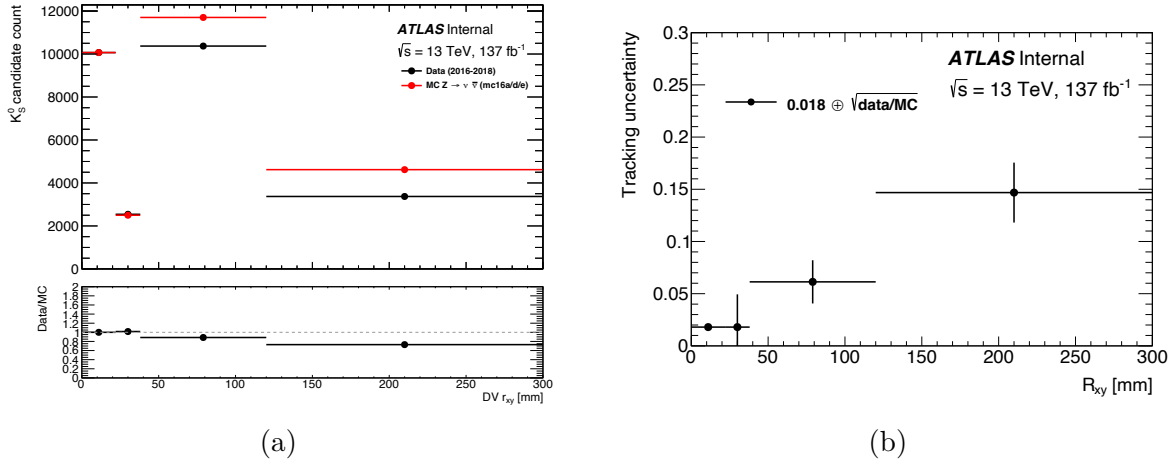


Figure A.15: The (a) comparison of  $K_S^0$  candidate yields in MC simulation and data, and (b) the resulting estimated tracking uncertainties for FVs. Taken from Ref [143].

This is known as a non-central  $\chi^2$  distribution, and it is a valid approximation when the dataset size is large. This is often referred to as the *asymptotic limit*, with corresponding fits thus referred to as asymptotic fits. When this approximation cannot be made, we can instead model  $f(\tilde{q}_\mu|\mu')$  using a Monte Carlo approach to generate datasets with different corresponding values of  $\tilde{q}_\mu$ . However, this can be quite computationally expensive – requiring possibly many thousands of fits – and thus in practice is avoided unless strictly necessary.

## APPENDIX B

### SPECIAL RELATIVITY AND THE LORENTZ GROUP

Here we will review some key concepts related to the theory of special relativity, namely the geometry of spacetime and transformations between different reference frames. This is but a very brief review – for more detail and mathematical rigor, including a general discussion of group theory, see Ref. [274], as well as Chapter 1 of Ref. [275] for a more rigorous review of the concepts we will touch on below.

#### B.1 Metrics and Minkowski Space

In  $\mathbb{R}^3$ , one typically defines the length of a vector  $\vec{v}$  (or its *norm*) via inner product:

$$\begin{aligned} \|\vec{v}\| &= \sqrt{\vec{v} \cdot \vec{v}} \\ &= \sqrt{v_x^2 + v_y^2 + v_z^2}. \end{aligned} \tag{B.1}$$

This is specifically the *Euclidean* norm – the Euclidean distance between the start and end-points of the vector, which is perhaps the most common definition of distance given its relevance in many fields of physics (and beyond) that operate in the  $\mathbb{R}^3$  vector space. However, this is not necessarily the only way to define distance.

To generalize things, every vector space  $V$  is equipped with some bilinear form  $f$ , that maps vectors in  $V$  to a field  $K$ ,  $f : V \times V \rightarrow K$ , where the elements of  $K$  are scalars [276]. We typically refer to action by this form as the *inner product*. In the case of  $\mathbb{R}^3$ , this is the familiar *dot product* as in Eq. B.1. One can generally write the inner product of two vectors

as the multiplication of them with a tensor that we call the *metric* of the space, like<sup>[1]</sup>

$$\langle \mathbf{v}, \mathbf{k} \rangle = v^\mu g_{\mu\nu} k^\nu, \quad (\text{B.2})$$

- $\mathbf{v}, \mathbf{k}$  are vectors,
- $\langle \dots \rangle$  denotes the inner product,
- $g_{\mu\nu}$  is the metric tensor.

where on the left-hand side we have used angle brackets to indicate the inner product. The raising and lowering of indices –  $v^\mu$  versus  $v_\mu$  – corresponds with whether a vector lives in  $V$  or its dual space<sup>[2]</sup>  $V^*$ , with elements of the dual space  $v^* \in V^*$  mapping vectors to scalars,  $v^* : V \rightarrow K$ .

In the case of special relativity, we describe spacetime as a *Minkowski* space. This is a 4-dimensional space, equipped with the  $4 \times 4$  Minkowski metric tensor given by<sup>[3]</sup>

$$\eta^{\mu\nu} = \begin{bmatrix} 1 & & & \\ & -1 & & \\ & & -1 & \\ & & & -1 \end{bmatrix} \equiv \text{Diag}(1, -1, -1, -1). \quad (\text{B.3})$$

With this metric tensor in hand, we can define the Minkowski norm of a 4-vector  $v^\mu$  as

$$\begin{aligned} \|\mathbf{v}\| &= \sqrt{v^\mu v_\mu} \\ &= \sqrt{v^\mu \eta_{\mu\nu} v^\nu} = \sqrt{v_0^2 - (v_1^2 + v_2^2 + v_3^2)}, \end{aligned} \quad (\text{B.4})$$

---

1. As a reminder, we use Einstein summation notation throughout: repeated indices are summed over.

2. One can think of this as “column” versus “row” vectors, or more formally vectors versus covectors. For a review of tensor math, see Ref. [277].

3. This metric is often indicated in shorthand as “ $(+, -, -, -)$ ”, and is known as the *West Coast* metric. This is in contrast to the *East Coast* metric of  $(-, +, +, +)$ , which has all the signs flipped in  $\eta^{\mu\nu}$ . The choice of which metric to use is a convention: computations using either will yield the same result, although it can make it tricky to compare derivations of formulae that use differing metrics. In particle physics, it is most conventional to use the  $(+, -, -, -)$  metric.

or if we write the 4-vector as  $v^\mu = (v_0, \vec{v})$  with  $\vec{v} \in \mathbb{R}^3$ , as<sup>[4]</sup>

$$\|\mathbf{v}\| = \sqrt{v_0^2 - \vec{v} \cdot \vec{v}}. \quad (\text{B.5})$$

In position space, the Minkowski norm is a notion of spacetime distance. In *momentum space*, where we express momentum 4-vectors as  $p^\mu = (E, \vec{p})$ , we can identify the Minkowski norm as the mass

$$\begin{aligned} m &= \sqrt{p^\mu p_\mu} \\ &= \sqrt{E^2 - \vec{p} \cdot \vec{p}}. \end{aligned} \quad (\text{B.6})$$

Due to the conservation of energy-momentum, this norm is a conserved quantity. This does not mean that a particle cannot decay into less massive particles, but rather that in any interaction, the Minkowski norm of the sum of all 4-momenta is preserved. This does, in fact, prevent particles from producing *more* massive decay products.

## B.2 Lorentz Transformations

A Lorentz transformation can be formally defined as a transformation of a spacetime vector by a member of the *Lorentz group* – in fact, a member of the restricted Lorentz group  $\text{SO}^+(1, 3)$ , which consists of transformations that preserve the orientation of space and the direction of time. Importantly, these transformations (and all those corresponding with the *full* Lorentz group) preserve the Minkowski norm, which is thus referred to as a *Lorentz-invariant* quantity. They correspond with 3 spatial rotations, as well as 3 *boosts*: transformations from one reference frame to another that moves with some constant velocity with respect to the former.

---

4. As we shall see, this convention of writing the first (or “zeroth”) component separately from the other three is handy notation given how spacetime is constructed: the zeroth component is time, and the other 3 are spatial so it makes sense to group them together as a position vector in  $\mathbb{R}^3$  when writing a 4-position.

In spacetime coordinates, the 3 spatial rotation matrices can be written as [278]

$$R_x(\theta) = \begin{bmatrix} 1 & 0 & 0 & 0 \\ 0 & 1 & 0 & 0 \\ 0 & 0 & \cos \theta & -\sin \theta \\ 0 & 0 & \sin \theta & \cos \theta \end{bmatrix}, \quad (\text{B.7})$$

$$R_y(\theta) = \begin{bmatrix} 1 & 0 & 0 & 0 \\ 0 & \cos \theta & 0 & \sin \theta \\ 0 & 0 & 1 & 0 \\ 0 & -\sin \theta & 0 & \cos \theta \end{bmatrix}, \quad (\text{B.8})$$

$$R_z(\theta) = \begin{bmatrix} 1 & 0 & 0 & 0 \\ 0 & \cos \theta & -\sin \theta & 0 \\ 0 & \sin \theta & \cos \theta & 0 \\ 0 & 0 & 0 & 1 \end{bmatrix}, \quad (\text{B.9})$$

from which all rotations can be composed – though it is important to remember that they are not commutative. From the above matrices structure, we see that they mix spatial components with one another, but not with time components. Conversely, we do see such

mixing in Lorentz boosts. We can represent them as matrices

$$\Lambda_x(\beta) = \begin{bmatrix} \gamma & -\gamma\beta_x & 0 & 0 \\ -\gamma\beta_x & \gamma & 0 & 0 \\ 0 & 0 & 1 & 0 \\ 0 & 0 & 0 & 1 \end{bmatrix}, \quad (\text{B.10})$$

$$\Lambda_y(\beta) = \begin{bmatrix} \gamma & 0 & -\gamma\beta_y & 0 \\ 0 & 1 & 0 & 0 \\ -\gamma\beta_y & 0 & \gamma & 0 \\ 0 & 0 & 0 & 1 \end{bmatrix}, \quad (\text{B.11})$$

$$\Lambda_z(\beta) = \begin{bmatrix} \gamma & 0 & 0 & -\gamma\beta_z \\ 0 & 1 & 0 & 0 \\ 0 & 0 & 1 & 0 \\ -\gamma\beta_z & 0 & 0 & \gamma \end{bmatrix}. \quad (\text{B.12})$$

- $\beta = v/c_0$  is the boost frame velocity, as a fraction of the speed of light in vacuum,
- $\gamma = (\sqrt{1 - \beta^2})^{-1}$  is the *Lorentz factor*.

In practice, we may be interested in rotations and boosts along arbitrary axes. We can more compactly write rotation and boost matrices in block form as [279]

$$R(\theta, \hat{u}) = \begin{bmatrix} 1 & 0 \\ 0 & \cos\theta I + \sin\theta[\hat{u}]_{\times} + (1 - \cos\theta)(\hat{u} \otimes \hat{u}) \end{bmatrix}, \quad (\text{B.13})$$

$$\Lambda(\vec{\beta}) = \begin{bmatrix} \gamma & -\gamma\vec{\beta}^T \\ -\gamma\vec{\beta} & I + (\gamma - 1)\vec{\beta}\vec{\beta}^T/\beta^2 \end{bmatrix}. \quad (\text{B.14})$$

- $\hat{u}$  is a unit 3-vector representing the rotation axis,
- $\vec{\beta}$  is the boost frame velocity 3-vector,
- $[\cdots]_{\times}$  is the cross product matrix operator, such that  $[\vec{v}_1]_{\times}\vec{v}_2 \equiv \vec{v}_1 \times \vec{v}_2$ .

### B.3 Invariance, Covariance, and Equivariance

When studying Lorentz transformations – or transformations performed by action of elements of any group – it is often instructive to classify how different types of quantities transform under these actions. As mentioned in Section B.1, quantities such as mass are invariant under Lorentz transformations. We refer to these aptly as Lorentz-invariant quantities, or *Lorentz scalars*<sup>[5]</sup>. Another class of quantities are those that are *Lorentz-covariant* – by which we typically refer to components of Lorentz vectors. These vector quantities are not invariant under Lorentz transformations, and transform under boosts and rotations as prescribed by the structure of the matrices in Section B.2 with their space- and time-like components mixing accordingly. Many of the quantities we deal with in high-energy physics, such as energy, are components of these Lorentz vectors, and are thus not Lorentz invariant: the values of these quantities depend upon the reference frame in which they are measured. As with their invariant counterparts, we can say that these quantities transform under representations of the Lorentz group.

When referring to how these quantities are acted upon by functions, and how these functions act under Lorentz transformations, we can turn to the concept of Lorentz *equivariance*. To borrow the definitions put forth in Ref. [280], we say that a function  $f : X \rightarrow Y$  is *invariant* with respect to a group  $G$  that acts on  $X$  and  $Y$  as  $\star$  if

$$f(g \star x) = f(x) , \tag{B.15}$$

- $x \in X$ ,
- $g \in G$ ,
- $\star$  is the action of group  $G$  on  $X$  and  $Y$ , which may be different for each.

---

5. Aside from the Minkowski norms of our vectors – which are Lorentz invariant by definition of how the Lorentz group is constructed – other examples include particle charges, or particle flavor: a top quark will remain a top quark after any rotation or Lorentz boost. In general, any quantities that commute with Lorentz transformations are Lorentz scalars.

and it is *equivariant* with respect to  $G$  if

$$f(g \star x) = g \star f(x) , \tag{B.16}$$

where we should emphasize that the action of  $G$  on  $X$  and  $Y$  is not necessarily the same. From these definitions it becomes clearer that the category of invariant functions is in fact a subset of equivariant functions, specifically those satisfying  $g \star f(x) = f(x)$ .

Turning back to particle physics interpretation, the way in which different objects transform under the Lorentz group may have consequences for how we analyze them – and what kinds of derivative quantities are physically meaningful. For example, the  $x$ -component of a particle’s 4-momentum is a Lorentz-covariant quantity, and has some physical meaning in describing the dynamics of that particle. By contrast, the sum of the particle’s  $x$ - and  $y$ -components of its 4-momentum – or some similarly arbitrary mix of vectors components – is not Lorentz-equivariant. It is also not an easily interpretable quantity, as it is the sum of two quantities that transform differently under boosts and rotations. The theories that we study are typically written down in terms of Lorentz-equivariant quantities, and so it is often helpful to analyze them through operators and observables that similarly respect Lorentz group symmetries<sup>[6]</sup>.

---

6. For a concrete example, see Chapter 6, where we discuss a Lorentz group-equivariant neural network.

# APPENDIX C

## THE HIGGS BOSON HIERARCHY PROBLEM

In quantum field theory, there is a difference between *bare* and *physical* masses. The bare mass refers to a free parameter that appears in a mass term in the theory’s Lagrangian. In the case of the SM Higgs boson this looks like

$$\mathcal{L}_{\text{SM}} = \dots + \underbrace{(m_H^0)^2 H^\dagger H}_{\text{Higgs mass term}} + \dots \quad (\text{C.1})$$

In any experiment, however, what we measure the physical mass  $m_H$ . This is related to the bare mass  $m_H^0$  by

$$m_H^2 = (m_H^0)^2 + \delta(m_H^2), \quad (\text{C.2})$$

where  $\delta(m_H^2)$  is computed as the sum of contributions to the Higgs boson self-energy – which are corrections to the Higgs propagator in the effective field theory [14]. In the SM, the corrections to this self-energy are given by the diagrams in Fig. C.1. Simply put, the physical mass of the Higgs boson receives “corrections” corresponding to its interactions with other particles in the theory, which causes it to differ from the bare mass.

To understand how this works, let us explicitly evaluate the first diagram in Fig. C.1 (the others will follow similar steps).

$$-i\Sigma_H(p^2) = n_f \int \frac{d^4k}{(2\pi)^4} (-1) \text{Tr} \left[ \left( -\frac{1}{\sqrt{2}} i\lambda_f \right) \frac{i}{\not{k} - m_f} \left( -\frac{1}{\sqrt{2}} i\lambda_f \right) \frac{i}{\not{p} + \not{k} - m_f} \right], \quad (\text{C.3})$$

where  $n_f$  is the number of fermions, and  $\lambda_f$  and  $m_f$  give their couplings to the Higgs

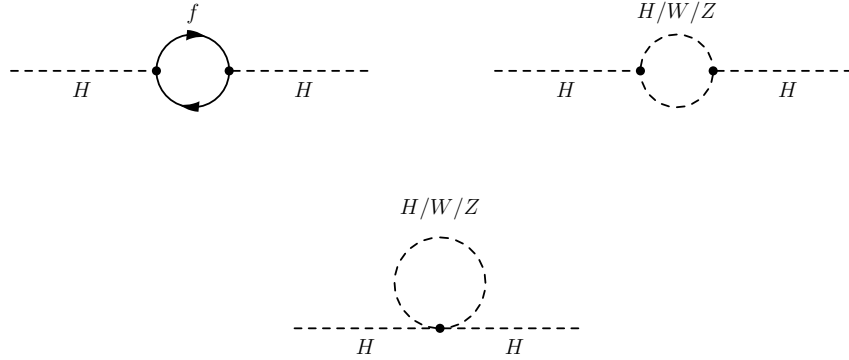


Figure C.1: Diagrams contributing to the correction to the Higgs self-energy.

(within some constant factors) and masses. Using the fact that

$$\frac{i}{\not{k} - m_f} = \frac{i\not{k} + m_f}{k^2 - m_f^2},$$

we can compute the trace in the integrand as

$$\begin{aligned} & \text{Tr} [(\not{k} + m_f)(\not{p} + \not{k} + m_f)] \\ &= \text{Tr} \left[ \not{k}\not{p} + \not{k}^2 + \underbrace{2m_f\not{k} + m_f\not{p}}_{\text{Vanishes in the trace}} + m_f^2 \right] = 4(k^2 + kp + m_f^2). \end{aligned}$$

Now, let's consider the limiting case of  $p^2 = 0$ . This corresponds with  $m_H = 0$ , or alternatively the limit where  $m_f \gg m_H$  (these are the bare masses). This will simplify the results – though importantly, the takeaways will hold for the more general case.

$$\Rightarrow -i\Sigma_H(p^2 = 0) = -n_f \frac{\lambda_f^2}{2} \int \frac{d^4k}{(2\pi)^4} \cdot 4 \frac{k^2 + kp + m_f^2}{(k^2 - m_f^2)(p^2 + 2kp - m_f^2)}. \quad (\text{C.4})$$

Employing the “usual” QFT tricks of introducing Feynman parameters and a UV cutoff for the momentum loop integral [281],

$$\begin{aligned}\Sigma_H(p^2 = 0) &= 2n_f \lambda_f^2 \frac{1}{16\pi^2} \int_0^1 dx \int_0^{\Lambda^2} dy \frac{y(-y + m_f^2)}{(y + m_f^2)^2}. \quad (\text{C.5}) \\ \int dy \frac{y(-y + m_f^2)}{(y + m_f^2)^2} &= \left( -y + 3m_f^2 \ln(m_f^2 + y) + \frac{2m_f^4}{m_f^2 + y} \right) + \text{const.} .\end{aligned}$$

With  $\Lambda \gg m_f$ , we find

$$\Sigma_H(P^2 = 0) = 2n_f \lambda_f^2 \frac{1}{16\pi^2} \left[ -\Lambda^2 + 6m_f^2 \ln\left(\frac{\Lambda}{m_f}\right) - 2m_f^2 + \mathcal{O}\left(\frac{1}{\Lambda^2}\right) \right]. \quad (\text{C.6})$$

From the above expression, which gives  $\delta(m_H^2)$ , we see that our correction to the Higgs square mass has a quadratic divergence in  $\Lambda$ . Furthermore, this is not a problem that we can resolve simply by introducing a regularization scheme such as dimensional regularization [281].

Accounting for the additional diagrams in Fig. C.1, we find

$$\delta(m_H^2) \propto \left[ \frac{3}{4} (m_W^2 + m_Z^2 + m_H^2) - \Sigma m_f^2 \right] \frac{\Lambda^2}{m_W^2}. \quad (\text{C.7})$$

From Eq. C.7, it appears that we can simply adjust the bare mass  $m_H$  to completely remove the divergence from  $m_H^2$  by canceling out the sum of boson and fermion masses, but this will not work if we look beyond 1-loop order. Thus, taking  $\Lambda \sim m_{\text{Planck}} \approx 1.2 \times 10^{19} \text{GeV}$ , we are left with the choice of fine-tuning some counterterm correction to  $\delta(m_H^2)$  to cancel around 30 orders of magnitude, unless we allow for some BSM phenomenon to resolve the quadratic divergence.

## APPENDIX D

### THE NEUTRON ELECTRIC DIPOLE MOMENT

Here, we will review the concept of the neutron electric dipole moment  $d_n$ , and its relevance to the issue of  $CP$  violation.

#### D.1 Charge, parity and time reversal transformations

Before discussing  $CP$  violation, it is helpful to first define charge, parity and time reversal transformations:

- A charge transformation (Section 2.1.1.3) flips the sign of all the quantum numbers of a particle (such as electric charge), taking the particles to antiparticles as  $\mathcal{C} |\Psi\rangle = |\bar{\Psi}\rangle$ .
- A parity transformation (Section 2.1.1.4) flips a spatial coordinate,  $(t, \vec{x}) \rightarrow (t, -\vec{x})$ . The consequences of this transformation are different for scalar, vectors and spinors<sup>[1]</sup>.
- Time reversal, as its name implies, flips the direction of time.

The combination of all three of these transformations,  $CPT$ , is understood to be an exact symmetry of nature according to the (aptly-named)  $CPT$  theorem [282–284]. In other words, all physical observables in the Standard Model (and their corresponding *operators* in the mathematical formulation) should be  $CPT$ -even. They are not all necessarily  $C$ -,  $P$ - or  $T$ -even, and in practice we can leverage the constraint of  $CPT$ -evenness to deduce a particular operator’s symmetry under one of these transformations, given its symmetry under the others.

---

1. For details, see Section 11.5 of Ref. [6]

## D.2 Connecting the neutron electric dipole moment to CP violation

For a fuller overview of this topic, see Ref. [285]. Given some kind of spatial charge distribution  $\rho(\vec{x})$ , the corresponding dipole moment is defined as

$$\vec{d} = \int d^3x \rho(\vec{x})\vec{x}. \quad (\text{D.1})$$

The neutron is a baryon, a particle composed of one up- and two down-type quarks. Up quarks have electric charge  $+\frac{2}{3}e$ , while down quarks have charge  $-\frac{1}{3}e$ , so that the neutron is neutrally-charged. However, it could have a non-zero electric dipole moment (EDM) if these charges are arranged in a way that is not isotropically symmetric.

The electric and magnetic dipole moments of elementary particles like the neutron are assumed to be proportional to their spin,  $\vec{d} \parallel \vec{S}$ , as this is the only intrinsic vector quantity that they are known to have [285]. The connection between  $d_n \neq 0$  and  $CP$  violation can be illustrated by considering how the operator  $\vec{S} \cdot \vec{E}$ <sup>[2]</sup> transforms under time reversal operator  $T$ . For a particle with  $\vec{E} \parallel \vec{S}$ , the time reversal operator will operate as<sup>[3]</sup>

$$\begin{aligned} T(\vec{E}) &\rightarrow \vec{E}, \\ T(\vec{S}) &\rightarrow -\vec{S}. \end{aligned} \quad (\text{D.2})$$

Thus the operator  $\vec{S} \cdot \vec{E}$  is  $T$ -odd, and since it is  $CPT$ -even, it must be  $CP$ -odd. As the EDM is the moment corresponding with this interaction – it governs the strength of the interaction between a particle’s spin and the electric field – it implies a  $CP$ -violating term in

---

2. Here,  $\vec{S}$  is a stand-in for  $\vec{d}$ , as we assume them to be parallel.

3. Recall that  $\vec{S}$  is odd under time reversal. One easy way to remember this is to consider how Feynman diagrams work: A fermion propagating forwards in time is equivalent with an anti-fermion propagating backwards in time.

the Lagrangian describing the particle’s dynamics if it is non-zero.

So far, we have seen that a non-zero neutron EDM corresponds with  $CP$  violation. To understand how it specifically connects to *strong*  $CP$  violation, see Section 1.4 of Ref. [285]. It is important to note that  $CP$  violation in the weak sector – which has been measured via the  $K_L^0 \rightarrow \pi^- \pi^+$  decay [286] – also contributes to the neutron EDM. However, this measurement only corresponds with  $d_n \sim 10^{-32} \text{e} \cdot \text{cm}$  [285], which is well below current experimental upper bounds.

### D.3 Measuring the nEDM

For a historical overview of nEDM measurements, see Ref. [287]. The limit on the nEDM of  $d_n = (0.0 \pm 1.1_{\text{stat}} \pm 0.2_{\text{sys}}) \times 10^{-26} \text{e} \cdot \text{cm}$  provided in Section 3.1 is the result of measurements performed by an experiment at the Paul Scherrer Institute, using an ultra-cold neutron source which produces neutrons via spallation of a Pb–Zr target by protons from a 590 MeV proton cyclotron, followed by cooling by  $\text{D}_{20}$  to energies below 300 neV [288, 289]. These neutrons are then spin-polarized via a 5 T superconducting solenoid, and directed into a precession chamber in the apparatus shown in Figure D.1. In the precession chamber, the neutron Larmor precession is measured under applied electric and magnetic fields, with the precession given by

$$f_n = \frac{1}{\pi \hbar} |\mu_n \vec{B}_0 + d_n \vec{E}_0|, \quad (\text{D.3})$$

- |  |
|--|
| <ul style="list-style-type: none"> <li>• <math>f_n</math> is the Larmor precession of the neutron,</li> <li>• <math>\mu_n</math> is the neutron magnetic moment,</li> <li>• <math>\vec{B}_0</math> is the applied magnetic field,</li> <li>• <math>d_n</math> is the neutron electric dipole moment,</li> <li>• <math>\vec{E}</math> is the applied electric field.</li> </ul> |
|--|

where  $\vec{E} \parallel \vec{B}_0$ , with  $|\vec{E}| = 11 \text{ kV cm}^{-1}$  and  $|\vec{B}_0| = 1036 \text{ nT}$  [58]. The electric field is then

varied and any changes in  $f_n$  measured<sup>[4]</sup>.

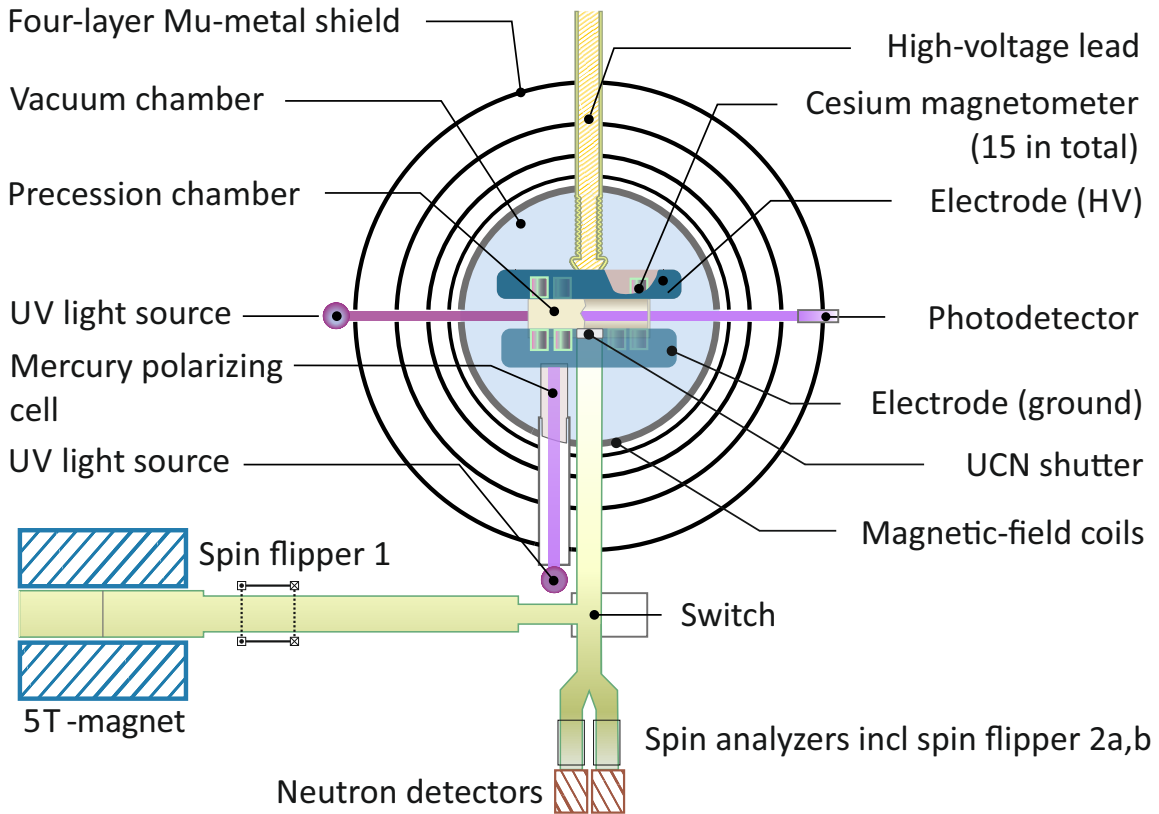


Figure D.1: A schematic of the spin chamber used to measure the nEDM via Larmor precession. Taken from Ref. [58].

4. The details of the procedure for how the fields are shifted, as well as the use of a  $^{199}\text{Hg}$  vapor “co-magnetometer”, are given in Ref. [58], and follow the Ramsey method of separate oscillating fields for molecular beam resonance measurements [290].

# APPENDIX E

## HADRONIC JETS

Here, we will review some of the theoretical background for hadronic jets, as well as some details about jet reconstruction algorithms. For a relatively comprehensive review of jets, see Ref. [291]. For a review of (non)perturbative QCD – the theory and methods that underpin the study of jets – see Ref. [292, 293].

### E.1 Color confinement: Why are jets necessary?

In a collider experiment like ATLAS, we are able to observe “bare” leptons like electrons, or bosons like the  $W$ - and  $Z$ -bosons (however brief their lifetimes). However, this does not hold true for particles that carry color charge: we do not observe bare quarks or gluons, but rather *hadrons*, composite particles that are bound states of multiple quarks. To be clear, we do observe processes that correspond with the interactions of single quarks: We collide protons in the Large Hadron Collider, so in fact all the processes we observe start with the interaction between two gluons, a quark and gluon, or two quarks. Furthermore, some of these processes – some of the most common ones – also result in the production or scattering of quarks and gluons, such as those represented by the Feynman diagrams in Figure E.1. But in the place of outgoing quarks or gluons, we instead observe collimated streams of hadrons. This phenomenon is a manifestation of the *color confinement hypothesis*, which is the general statement that only color-singlet states can exist as free particles<sup>[1]</sup>.

To understand how this phenomenon comes about, we can consider the fragmentation model described in Ref. [294] whereby there are two mechanisms that contribute to the showering and *hadronization* of quarks:

---

1. An equivalent formulation of this hypothesis is that color SU(3) is an exact symmetry of nature: As color-singlet states, all free particles are invariant under SU(3) color transformations.

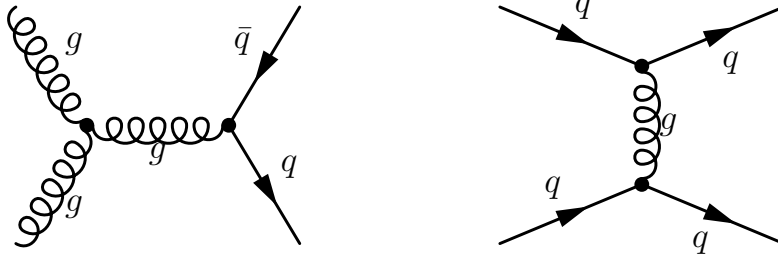


Figure E.1: Two examples of QCD processes that we may observe in proton-proton collisions. The left diagram corresponds to scattering of gluons to quarks (an  $s$ -channel process), and the right with the scattering of quarks to quarks (a  $t$ -channel process).

- **Radiation:** Quarks that are accelerated to high energies will radiate gluons<sup>[2]</sup>. These gluons will split into more gluons or quarks, which split further. This ultimately yields a large number of quarks with low relative energies, which join together to form hadrons (we refer to this process as hadronization).
- **Gluon tube:** As a quark-antiquark pair is separated by the quarks' relative accelerations, a narrow *flux tube* of gluons forms between them (the gluons being the carrier of the strong force that holds the quarks together). As the separation between the quarks increases, it becomes energetically favorable to “cut” this tube, pulling a new quark-antiquark pair from the vacuum. This process repeats as the new quark-antiquark pairs continue to separate, until eventually there are many quarks and antiquarks with low relative momenta that hadronize.

The consequence of these mechanisms is that we observe a cluster of hadrons in place of a naked quark. Thus we can identify the production of a quark<sup>[3]</sup> if we can correctly identify the hadrons corresponding to this cluster. By momentum conservation, the sum of their 4-momenta will give the quark's 4-momentum, and we may have an additional handle for

---

2. It is important to note that this process is phenomenologically very different than bremsstrahlung of electromagnetically-charged particles. When we describe the “radiation” of photons it is understood that these can travel off to infinity, as quantum electrodynamics (QED) does not exhibit the confinement of QCD that we are discussing here. This can be understood as a consequence of the difference between the force carriers in the theories: QED is Abelian and its force carrier does not carry charge, in the way that the gluon of QCD does.

3. Similar arguments to the above hold for gluons.

determining the type of quark (flavor and generation) by identifying the species of hadrons produced. We often refer to these clusters of hadrons as jets; however one should be careful to distinguish between the notion of a cluster of hadrons produced by a quark or gluon emission, and a cluster of hadrons *that we reconstruct*, as will be described in the following section<sup>[4]</sup>.

One caveat regarding the hadronization mechanisms discussed above is that the top quark – which is the heaviest of the quarks, with a mass of  $\sim 175$  GeV – decays before hadronization. This produces a  $W$ -boson, together with a down-type quark: owing to the parameters of the CKM matrix (Section 2.1.2.2), this is almost always a bottom quark. The  $W$ -boson may decay hadronically as  $W \rightarrow qq'$ , or leptonically as  $W \rightarrow l\nu$ . Thus the top quark decay may result in a one or multiple jets (possibly with some internal substructure), and possibly a charged lepton and neutrino.

## E.2 Reconstructing jets: Inputs and Algorithms

Having established that quark and gluon emission from events results in clusters of hadrons, we need some kind of *jet clustering algorithm* to reconstruct such clusters in data (or simulation). We also need to decide exactly what information is used in jet clustering, as in an experiment like ATLAS we may potentially use measurements from both the calorimeter and the inner detector (tracker).

There is a wide variety of algorithms one can use for clustering jets: these have been developed over decades as collider experiments have evolved<sup>[5]</sup>. For a historical review of jet

---

4. While this may seem like a simple distinction to make – the true set of hadrons associated with one quark or gluon emission, versus the set we cluster together in some experimental reconstruction – it is easy to confuse these concepts when discussing Monte Carlo simulations of particle collisions. In such settings it is typical for terms like “truth jets” to refer to jets that were clustered, using algorithms like in Section E.2, from truth-level information (the “true” particles output by the Monte Carlo generator, as opposed to the reconstruction from the simulated detector interaction). While these jets are free from all the inefficiencies and imperfections of detector reconstruction, they may still fall victim to the challenges of clustering itself – for example, hadrons from two overlapping clusters produced from two quarks or gluons emitted near one another, may not be assigned to the correct shower.

5. This includes both the detectors, as well as the types of collisions being studied –  $e^+e^-$  and  $pp$  collisions

algorithms developed before the LHC era, see Ref. [295]. Here, we will focus discussion on the so-called anti- $k_T$  algorithm [180], which is the jet clustering algorithm predominantly used in ATLAS and relevant to the work described in this thesis (the jet energy scale calibrations discussed in Section 4.2.8.2 and below in Appendix E.2.4, as well as the analysis in Chapter 5 and the discussion of machine learning for jet tagging and regression in Chapter 6).

### E.2.1 The anti- $k_t$ algorithm

The anti- $k_T$  jet clustering algorithm works by building jets from reconstructed particles' 4-momenta<sup>[6]</sup>. It operates iteratively, by calculating the distances between each pair of 4-momenta (or *pseudojets*)  $d_{ij}$ , and the distance between each pseudojet and the beam  $d_{iB}$  as [180]

$$d_{ij} = \min \left( p_{T,i}^{2\alpha}, p_{T,j}^{2\alpha} \right) \frac{(\Delta R_{ij})^2}{R^2}, \quad (\text{E.1})$$

$$d_{iB} = p_{T,i}^{2\alpha}. \quad (\text{E.2})$$

- $p_{T,i}$  is the transverse momentum of the  $i$ 'th pseudojet
- $\alpha = -1$ ,
- $\Delta R_{ij} = \sqrt{(\Delta y_{ij})^2 + (\Delta \phi_{ij})^2}$  is the distance between the  $i$ 'th and  $j$ 'th pseudojets in the rapidity-azimuthal angle plane,
- $R$  is the jet radius (a quantity without units, as a distance in rapidity-azimuthal angle).

If the smallest distance is a  $d_{ij}$  then the corresponding pseudojets are joined together, and if it is a  $d_{iB}$  then the  $i$ 'th pseudojet is discarded. The distances are then recalculated and the process repeated, until there are no more pseudojets to combine. The resulting clusters are anti- $k_t$  jets. In practice, we often apply post-processing algorithms or *grooming* algorithms

---

produce very different event characteristics

6. For the moment, we will defer the question of how exactly these momenta are reconstructed – and how we choose which ones are inputs to jet clustering (we don't want to include particles that were *not* produced from the showering and hadronization of quarks or gluons).

to these jets<sup>[7]</sup>, to remove jet constituents resulting from pileup or overlap of objects not originating from the jet’s initiating quark or gluon.

Note that Equation E.1 generalizes for different distance formulae, with different choices of  $\alpha$ . The choice of  $\alpha = 1$  corresponds with the  $k_t$  algorithm [304], and  $\alpha = 0$  with the Cambridge/Aachen algorithm [305, 306]. These three different jet clustering algorithms are demonstrated in Figure E.2, where we see the effects of the different distance metrics in how softer (lower- $p_T$ ) pseudojets are shared among the harder ones.

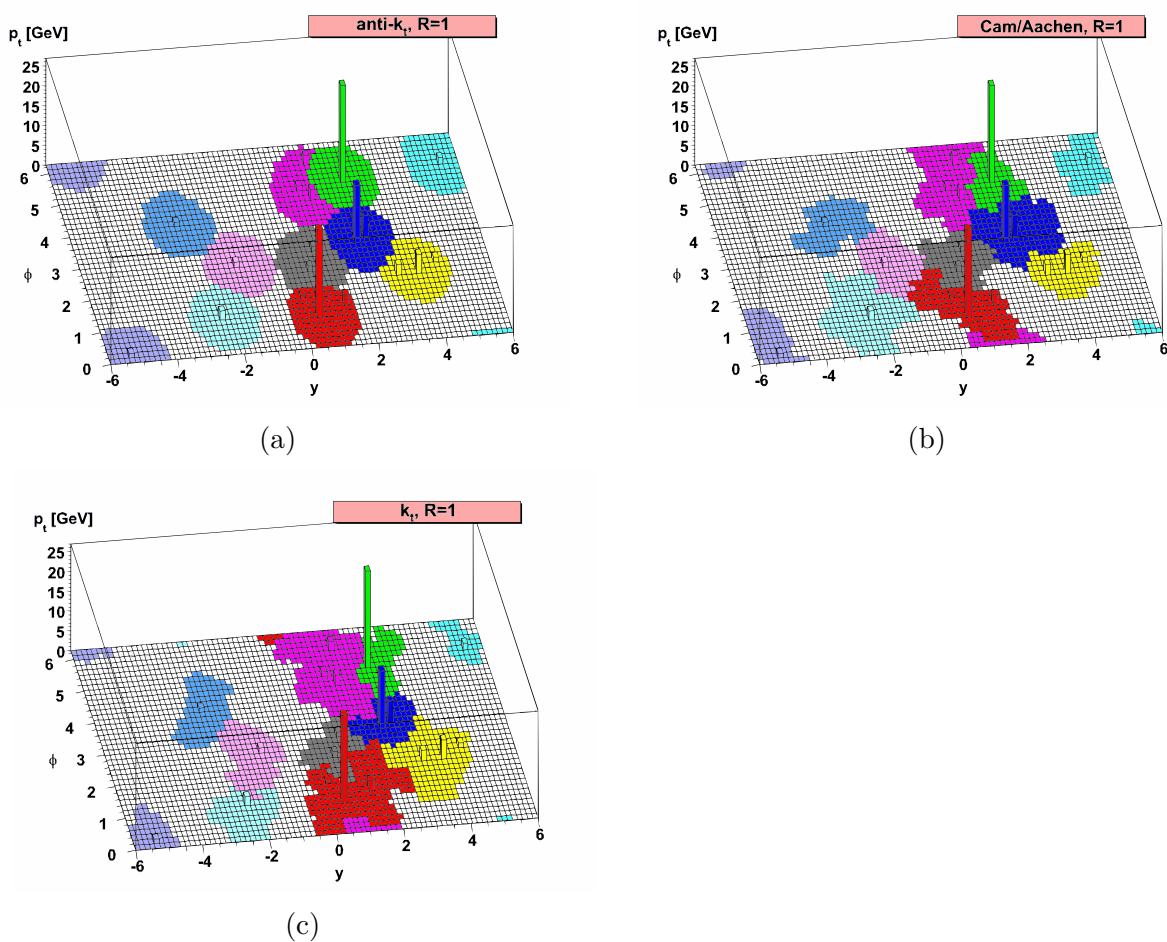


Figure E.2: Clustering of the same set of pseudojets (energy deposits) by the (a) anti- $k_t$ , (b) Cambridge-Aachen, and (c)  $k_t$  algorithms. Modified from Ref. [180].

7. For an overview of some common jet grooming techniques – of which there are many – see Ref. [296–303]. These range from very simple rule-based algorithms to machine learning approaches.

### E.2.2 Infrared and Colinearity Safety

One important consideration for jet clustering algorithms is that of infrared and colinearity (IRC) safety, which is a statement about a particular algorithm's sensitivity to infinitesimally low-momentum and colinear gluon emissions by a quark or gluon that initiates a jet [291]. While these two concepts – infrared (IR) and colinearity (C) – are typically treated together, we can formally define each [222]. We may define an IR-safe observable  $f^{(N)}$  computed on a set of  $N$  particle momenta as one with the feature

$$\lim_{\epsilon \rightarrow 0} f^{(N+1)}(p_1, \dots, p_N, \epsilon p) = f^{(N)}(p_1, \dots, p_N) , \quad (\text{E.3})$$

- $f^{(N)}$  is an IR-safe observable, as a function of  $N$  momenta,
- $p_i$  is the  $i$ 'th particle 4-momentum,

so that it is insensitive to the addition of a small momentum (tuned by  $\epsilon$ ). Similarly, we may define a C-safe observable  $f(p_1, \dots, p_N)$  so that whenever two massless 4-momenta  $\{p_1, p_2\}$  become colinear,  $f$  depends only on their sum. Expressing the momenta as  $p_1 = \lambda p$  and  $p_2 = (1 - \lambda)p$ , we can write this as

$$\partial_\lambda f(\lambda p, (1 - \lambda)p, \dots, p_N) = 0 . \quad (\text{E.4})$$

- $f$  is a C-safe observable,
- $\lambda \in (0, 1)$  tunes the momentum sharing between the first two momenta.

This feature of a particular jet algorithm is interesting as in perturbative QCD, the cross-section for emission of an infinitesimally low-momentum gluon or a colinear gluon is divergent [307], and thus an algorithm sensitive to these effects may produce non-physical results, or those not tractable in perturbative QCD. However, this effect is regularized in practice by the fact that particle detectors have limited angular resolution and minimum energy measurement thresholds.

### *E.2.3 Inputs to clustering: Identifying showers and displacement*

When describing jet algorithms, their inputs are often abstractly referred to as pseudojets as in Section E.2. In practice, these often consist of information from a particle detector calorimeter, that may have undergone some pre-processing, such as clustering of calorimeter cells into larger energy deposits (like *topo-clusters* in the ATLAS calorimeters [137]), or calibration of the energy deposits to handle different detector energy responses to hadronic and electromagnetic (EM) showering. These inputs can also include tracking information from a detector, which – when paired with calorimetry – can provide a powerful additional handle for distinguishing between hadronic and EM showers, potential overlap of leptons, and displaced decays in the jet origin. This last point is particularly relevant to *jet flavor tagging*, the process of identifying the flavor of quark that initiated a particular jet. Specifically, displaced vertex information is a powerful discriminant in identifying *b*-quark jets [185, 308, 309], owing to the meta-stable *B*-mesons that are produced in intermediate states<sup>[8]</sup> (Section 2.1.2.4). In practice, tracking information is often combined with calorimeter measurements via algorithms such as Particle Flow [310] or Unified Flow Objects [311], where calorimeter energy deposits are identified as stemming from charged or neutral particles and calibrated accordingly.

### *E.2.4 Jet energy scale calibrations*

In general, measuring the momentum of jets requires significant effort in detector calibrations. Part of this is due to the differing natures of electromagnetic and hadronic showers – both of which a calorimeter must handle, as hadronic showers will typically produce an appreciable number of neutrally-charged  $\pi^0$  mesons that most frequently decay via  $\pi^0 \rightarrow \gamma\gamma$  and thus

---

8. One might naïvely expect the *b*-quark mass to play a significant role in tagging, but while it is notably more massive than the light quarks *u, d, s*, this mass difference is still not sufficient to make this a particularly useful observable.

siphon off some energy back into the electromagnetic sector<sup>[9]</sup>. Detector calibrations also have to handle intrinsic non-linearity in energy response due to the detector design, non-uniformity in detector readout – and the effects of pile-up products overlapping with jets from the hard-scatter process. In the ATLAS experiment, this is accomplished through a multi-tier calibration process as shown in Figure E.3. This process involves corrections for pile-up contamination, as well as energy and  $\eta$  corrections – which are dependent on the uncalibrated energy and  $\eta$ , and derived through a method known as *numerical inversion* that corrects the mean jet energy and  $\eta$  response [313]:

1. For each variable we are calibrating, compute the central tendency of its true value as a function of the reconstructed quantity,

$$f(x) = F(Y|X = x) , \tag{E.5}$$

along with the associated spread (standard deviation)  $\sigma(x)$ .

- $F$  is some function of central tendency (e.g. mean, mode)
- $X, Y$  are the distributions of reconstructed and true variable

2. From the central tendency, compute the *response* function as

$$R(x) = f(x)/x , \tag{E.6}$$

which is a function of the reconstructed  $x$ .

3. Define

$$\tilde{R}(y) = R\left(f^{-1}(y)\right) , \tag{E.7}$$

---

9. Typically about one quarter of the jet energy goes into the electromagnetic sector by this process [312], so the effects are far from negligible.

the *numerically-inverted* response function. This function gives the response as a function of the true variable value.

4. Correct the jet as  $Y \rightarrow Y/\tilde{R}(Y)$ , where we assume the distribution of true values is given by

$$Y|(X = x) \sim \text{Gauss}(f(x), \sigma(x)) . \quad (\text{E.8})$$

Requiring truth-level information, this calibration is heavily dependent on MC simulation, which carries some uncertainties due to limits in parton shower modeling. This is accounted for with a final *in-situ* calibration applied to the data, which matches the data and MC jet response as measured with respect to well-calibrated reference objects<sup>[10]</sup>.

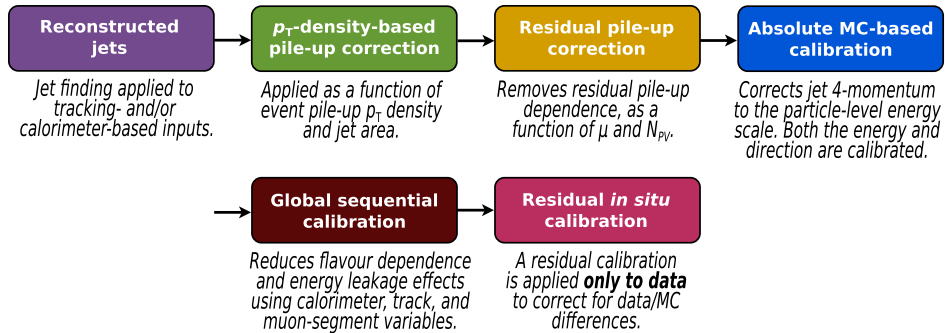


Figure E.3: An overview of the different stages of the jet energy scale calibration method in ATLAS. Taken from Ref. [211].

10. The “well-calibrated reference objects” include jets in the central detector region, as well as photons and Z-bosons. For details, see Ref. [211].

# APPENDIX F

## PARTICLE DETECTORS

The purpose of this appendix is to provide some general background information on particle detector designs and methods. This is only a partial overview of particle detection methods; for comprehensive review of general detector designs and operation, see Ref. [314–316]<sup>[1]</sup>.

### F.1 Sampling Calorimeters

A sampling calorimeter is one designed with interleaved sections of active material (wherein energy measurements are performed) and dead material (wherein they are not). This dead material – also known as the *absorber* – is typically one with a relatively low *radiation length*, which is the mean distance an electron traverses the material during which it loses  $1 - 1/e$  of its energy. The radiation length is given (approximately) by the formula [9, 318]

$$X_0 = 716 \text{ g cm}^{-2} \frac{A}{Z(Z+1) \ln \frac{287}{\sqrt{Z}}}, \quad (\text{F.1})$$

- $A$  is the atomic mass number,
- $Z$  is the atomic number.

The function of the absorber is to cause electromagnetic and hadronic showers to develop over shorter distances, allowing them to be contained within a smaller volume (and thus a smaller detector). The calorimeter “samples” the shower between these absorbers, so that it effectively sees slices of the shower as opposed to the entire thing.

Building a sampling calorimeter as opposed to a fully active one is a practical choice, as it reduces the detector size – and perhaps more importantly, the cost. Unfortunately, using a sampling calorimeter comes with a price in measurement precision, as one cannot

---

1. For a historical review focused on radiation counters – such as Geiger-Müller tubes and crystal counters – see Ref. [317]. Despite advancements in detector technologies since the 1940s, in both sensor design and signal processing, many of the basic mechanisms and methods are unchanged.

directly measure the energy deposited *within* the absorber. A calorimeter’s energy resolution is typically modeled as [319]

$$\frac{\sigma}{E} = \frac{a}{\sqrt{E}} \oplus \frac{b}{E} \oplus c, \quad (\text{F.2})$$

- $\sigma$  is the absolute energy resolution,
- $E$  is the impinging particle energy,
- $a, b, c$  are parameters determined by detector design.

where these three terms are referred to respectively as the *stochastic*, *noise* and *constant* terms. The use of absorber layers adds a contribution to the stochastic term, with proportionality given by

$$\left(\frac{a}{\sqrt{E}}\right)_{\text{sampling}} \propto \sqrt{\frac{t}{E_0}}, \quad (\text{F.3})$$

- $t$  is the absorber thickness in radiation lengths,
- $E_0$  is the original particle’s energy.

as low-energy particles produced in the shower may be stopped entirely by the absorber. This term typically dominates in sampling calorimeters [320].

## F.2 Electromagnetic and Hadronic Calorimeters

As discussed in Section 4.2.4, the ATLAS detector has separate calorimeter systems optimized for measuring electromagnetic and hadronic showers. The optimization – which is a combination of how the calorimeters are designed, and how their output signals are calibrated – is a consequence of differences in how these two types of showers develop<sup>[2]</sup>.

Electromagnetic showers are produced by impinging high-energy electrons and photons, which produce more electrons and photons via bremsstrahlung and pair production [9]. The

---

2. In fact, as we will note further below, the exact distinction between electromagnetic and hadronic showers is a little arbitrary.

electrons produced in the showering process eventually deposit their energy via ionization and excitation. By contrast, hadronic showers involve numerous mechanisms for energy transfer, and typically evolve over longer distances. Approximately one quarter of all energy in a hadronic shower is in fact transferred to the electromagnetic sector, via production of neutral pions  $\pi^0$  and the  $\pi^0 \rightarrow \gamma\gamma$  decay [312]. Some energy is also deposited by the shower via ionization of matter by high-energy hadrons, or transferred to gamma rays via matter excitation and nuclear processes. Some energy, however, is lost to effects such as nuclear binding processes, pion absorption [321], out-of-time energy depositions, heavy spallation fragments [322], as well as the production of muons and neutrinos via  $\pi^+$  decays. Owing to these different mechanisms and inefficiencies, the *response* of a calorimeter – how its recorded signal relates to the shower energy – will be different for hadronic energy deposits than for electromagnetic ones. This issue is typically addressed by constructing separate calorimeters dedicated to electromagnetic and hadronic showers. The latter is typically located outside the former – farther from the interaction point – as the hadronic showers develop over longer distances, so while they may start in the electromagnetic calorimeter they will continue into the hadronic one<sup>[3]</sup>.

### F.3 Gaseous Detectors: Proportional Counters and Geiger-Müller Tubes

Gaseous radiation detectors consist of an anode-cathode pair, with some voltage difference maintained between them. The space between the anode and cathode contains a gas that is ionized by impinging particles, producing electron-ion pairs. Under influence of the induced electric field (from the anode-cathode potential difference), the electrons drift to the cathode,

---

3. Herein lies a perhaps trivial but important point: hadronic showers can (and do) initiate and develop in electromagnetic calorimeters, although in detectors like ATLAS they will typically punch through and continue to develop within the dedicated hadronic calorimeter.

producing a voltage pulse – which can be read out to measure the ionization.

Whether the output of the detector can be used only to determine that a particle passed through, or can measure that particle’s energy, depends on the strength of the induced electric field. As shown in Figure F.1, there is typically a range of applied voltages in which the amplitude of the detector’s output voltage pulse amplitudes are linearly proportional to the impinging particle’s energy. A detector operating in this applied voltage regime is referred to as a *proportional counter*, and can be used to conduct energy measurements.

If the applied voltage is increased further, the pulse amplitude is no longer proportional to the particle energy, and the detector effectively provides a binary output: It detects whether or not a particle passed through it in some time window, without information on how energetic that particle was. Such a type of detector is referred to as a “Geiger-Müller counter”. Compared with proportional counters, Geiger-Müller counters have the obvious disadvantage of not performing an energy measurement. However, as the drift time for the ionization electrons will decrease as the applied voltage is increased, they will have improved timing resolution – measuring *when* a particle passes through the detector. In practice both types of detectors can be used together, such as in the ATLAS muon spectrometer (Section 4.2.5), to attempt to leverage the advantages of each and provide precise measurements of impinging particles’ position, time and energy.

## F.4 Photomultiplier Tubes

PMTs are measuring devices sensitive to single photons [323–325], consisting of photocathode and electron multiplier components: an incident photon produces an electron in the photocathode via the photoelectric effect. This electron is then accelerated in to the multiplier by an electric field. The multiplier consists of a series of *dynodes*, metal surfaces on which more secondary electrons are produced via secondary emission. This process is repeated multiple times, to greatly amplify the signal, as shown in Figure F.2.

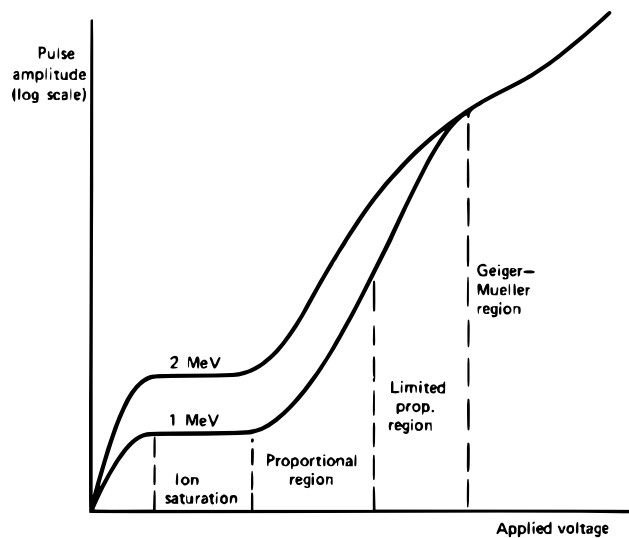


Figure F.1: The different supply voltage regions in which proportional and Geiger-Müller counters operate. The latter operates in a voltage regime where all pulses, independent of incoming particle energy, are of the same magnitude. Taken from Ref. [315].

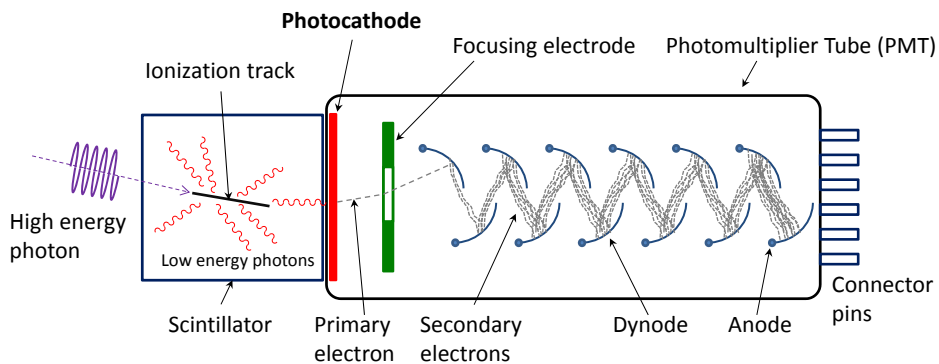


Figure F.2: A diagram of a photomultiplier tube coupled with a scintillator. Taken from Ref. [326].

One consequence of this design is that PMTs are susceptible to producing fake signals – known as *dark current* – due to a number of effects: leakage currents between the photocathode window and the external PMT structure, thermionic emission of electrons from the electrode or dynodes, and stripping of electrons from metal surfaces by strong internal electric fields [327, 328]. The magnitude and rate of dark current signals affects the PMT sensitivity, and thus is useful to characterize for determining the sensitivity of a detector that uses these devices for signal readout. In practice, the effects of the dark current can be minimized not only via optimizing the PMT operating environment (in terms of supply voltage and temperature), but by using multiple PMTs for scintillator readout and requiring coincident signals.

## APPENDIX G

### MEASURING PHOTOMULTIPLIER TUBE DARK CURRENTS FOR THE MILLIQAN EXPERIMENT

Here, I will give a brief overview of the milliQan experiment, and my work on characterizing the dark current of photomultiplier tubes (PMTs) to be used in the detector. This project primarily served as an early foray into detector hardware work, and also produced preliminary measurements of PMT dark current for the collaboration – together with an experimental setup for performing these.

#### G.1 The milliQan experiment

The milliQan experiment [329, 330] is a beyond-Standard Model (BSM) physics search, targeting milli-charged particles – those with effective electric charges of  $10^{-1}$  -  $10^{-3}e$  – that may be produced in proton-proton collisions at the CMS experiment. The detector, located approximately 33 m away from the CMS interaction point at a position of  $\eta = 0.1$  (in the CMS coordinate system), consists of two systems [115], the *bar* and *slab* detectors. Although different in shape, each consists of an array of plastic scintillators, interspersed with PMTs for readout. A demonstrator detector – effectively consisting of a stripped-down version of the full bar detector – was previously deployed, with the full detector currently taking data during Run 3 of the LHC. Figure G.1 shows the different detector system designs, and Figure G.2 shows the sensitivity of the initial search performed using the demonstrator detector.

#### G.2 Characterizing PMT dark current

As discussed in Appendix F.4, PMTs are highly sensitive photodetectors – but due to their design, are susceptible to producing a *dark current* even in the absence of any light signals.

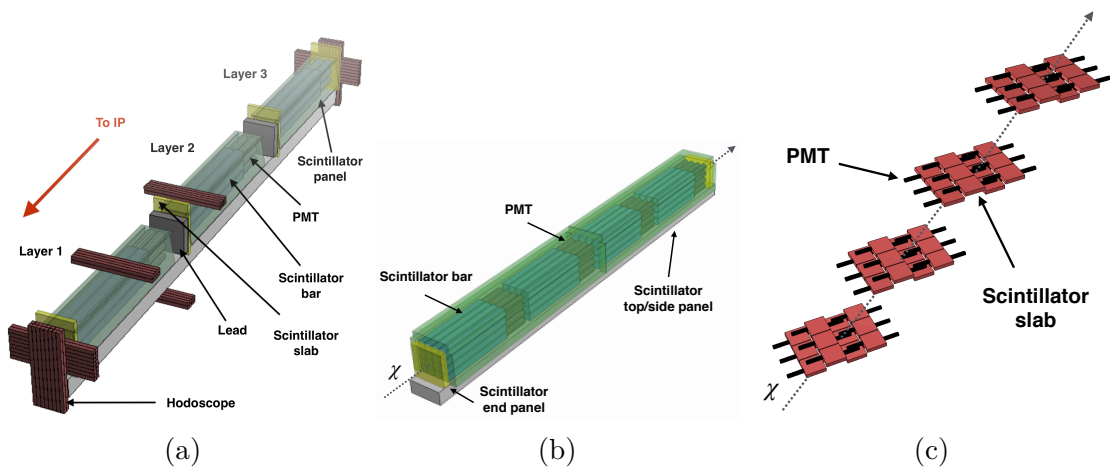


Figure G.1: A rendering of the milliQan (a) demonstrator, (b) bar, and (c) slab detectors. Taken from Ref. [115, 330].

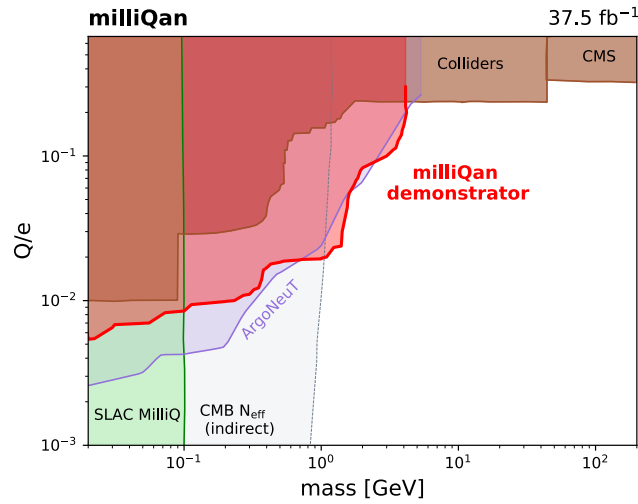


Figure G.2: The search sensitivity of the milliQan demonstrator, in terms of the charge and mass of the target milli-charged particles. Taken from Ref. [330].

Being able to characterize this dark current, in terms of both its magnitude and the rate at which such spurious signals is produced, is crucial for evaluating the sensitivity of a detector using PMTs and what level of background measurements will be produced by this process. This is particularly important to measure for the milliQan detector, as not only is it searching for feebly-interacting particles, but it uses a custom high-voltage powering scheme for the PMT supply voltage. Any potential instabilities in this supply voltage could influence the characteristics of the dark current. To perform this measurement, a setup was constructed as shown in Figure G.3<sup>[1]</sup>. The resulting dark current rate – measured as the rate of voltage pulses passing a  $-10$  mV falling trigger, is shown in Figure G.4. Note that this measurement only provided an initial characterization of the PMT dark current rate during detector design and commissioning – as described in Ref. [115], final dark current rate estimates were performed in-situ. Likely owing to differences in setup and how the dark rate is defined<sup>[2]</sup>, the in-situ measurements found a dark rate of approximately 2 kHz, with which these initial measurements are clearly not consistent. Nonetheless, the setup constructed in Figure G.3 may be useful for future PMT characterization measurements – potentially for future detectors such as the FORMOSA experiment [331].

---

1. The setup was in fact designed to also measure *PMT linearity*, how the PMT output voltage peak height changes as a function of input light intensity. To this end, a filter wheel was installed – a light filter whose opacity varies as a function of angle, and which can be rotated via a stepper motor – together with a LED pulser. However, owing to a lack of available tools for calibrating the light source and filter, the actual intensity of the light reaching the PMT was not known, severely limiting the usefulness of measurements in any linearity tests. However, with proper calibration (or better understanding of the filter wheel opacity profile), this setup may be used in the future for PMT linearity tests.

2. Specifically, the measurement here reported the rate at which, using the “standard” PMT base-plate, voltage pulses were produced that exceeded a size of 10 mV. There were updates to these base-plates for the final detector design, and together with a different metric for what size of signal qualifies as a dark current pulse (versus the background electrical noise), this may lead to a significantly different dark rate definition and resulting measurement.

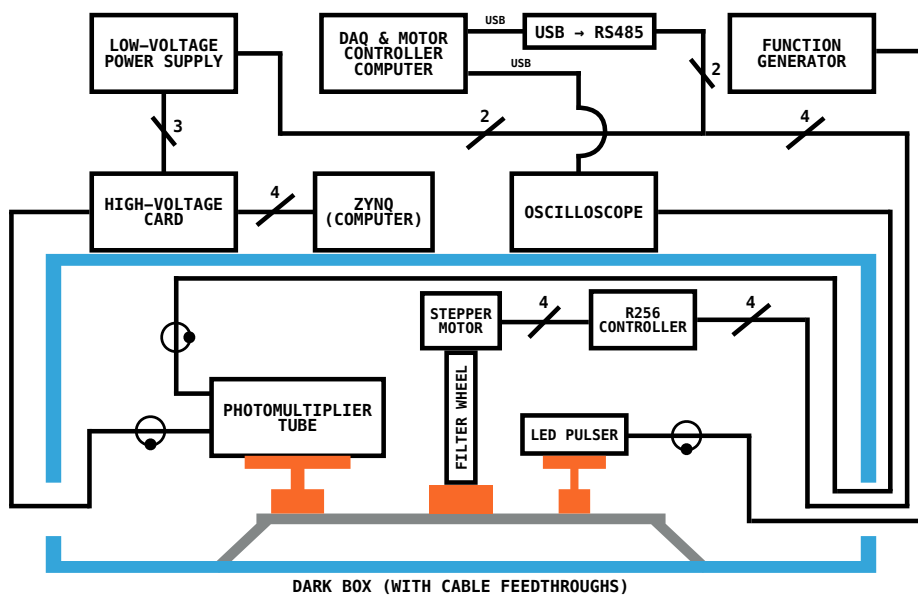


Figure G.3: A diagram of the experimental setup used to measure PMT dark current, as well as perform linearity measurements. For dark current measurements, the LED pulser was turned off.

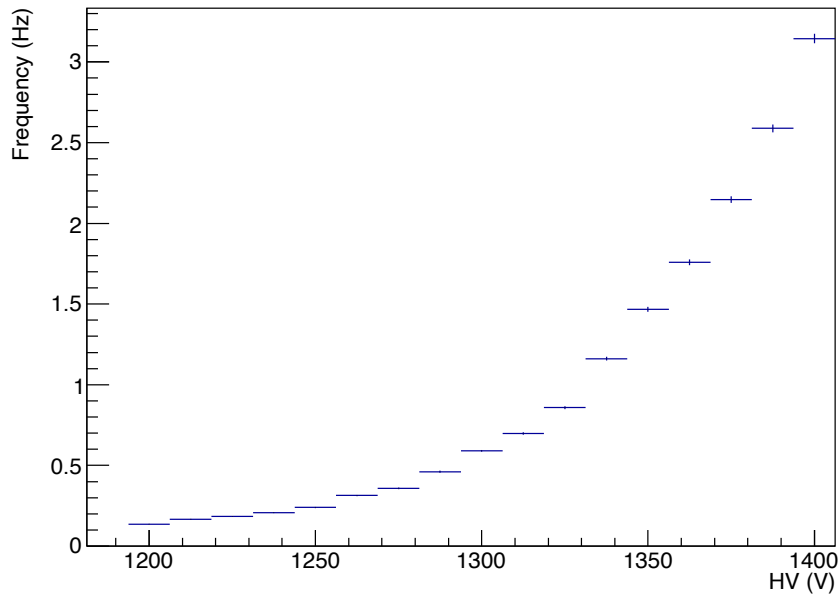


Figure G.4: The dark count rate for the R878 PMT, as measured using the setup in Figure G.3, with a falling  $-10$  mV trigger used to count negative voltage pulses produced by the PMT. Note that while the measured quantity shows clear dependence on the supply voltage – a good sign that this measurement was not distorted or bottle-necked by a potential low sampling rate of the data acquisition system – it is not consistent with the final, in-situ dark rate measurement described in Ref. [115].

## REFERENCES

- [1] L. EVANS and P. BRYANT. “LHC Machine”. *JINST* 3:08, S08001, 2008. DOI: 10.1088/1748-0221/3/08/S08001.
- [2] THE ATLAS COLLABORATION. “The ATLAS Experiment at the CERN Large Hadron Collider”. *JINST* 3:08, S08003, 2008. DOI: 10.1088/1748-0221/3/08/S08003.
- [3] THE CMS COLLABORATION. “The CMS experiment at the CERN LHC”. *JINST* 3:08, S08004, 2008. DOI: 10.1088/1748-0221/3/08/S08004.
- [4] C. ITZYKSON and J. B. ZUBER. Quantum Field Theory. International Series In Pure and Applied Physics. New York: McGraw-Hill, 1980.
- [5] L. de BROGLIE. “Recherches sur la théorie des Quanta”. Theses. Migration - université en cours d’affectation, Nov. 1924.
- [6] M. D. SCHWARTZ. Quantum Field Theory and the Standard Model. Cambridge University Press, Mar. 2014. DOI: 10.1017/9781139540940.
- [7] W. N. COTTINGHAM and D. A. GREENWOOD. An Introduction to the Standard Model of Particle Physics. 2nd ed. Cambridge University Press, 2023.
- [8] WIKIMEDIA COMMONS USERS MISSMJ, CUSH. Standard Model of Particle Physics. Modified by J. T. Offermann, 2023. URL: [https://commons.wikimedia.org/wiki/File:Standard\\_Model\\_of\\_Elementary\\_Particles\\_and\\_Gravity.svg?uselang=en#Licensing](https://commons.wikimedia.org/wiki/File:Standard_Model_of_Elementary_Particles_and_Gravity.svg?uselang=en#Licensing).
- [9] R. L. WORKMAN et al. on behalf of the Particle Data Group. “Review of Particle Physics”. *PTEP* 2022, p. 083C01, 2022. DOI: 10.1093/ptep/ptac097.
- [10] A. EINSTEIN. “Zur Elektrodynamik bewegter Körper”. *Ann. Phys* 322:10, pp. 891–921, 1905. eprint: <https://onlinelibrary.wiley.com/doi/pdf/10.1002/andp.19053221004>.

- [11] G. BREIT and E. WIGNER. “Capture of Slow Neutrons”. *Phys. Rev.* 49, pp. 519–531, 1936. DOI: 10.1103/PhysRev.49.519.
- [12] W. GERLACH and O. STERN. “Der experimentelle Nachweis der Richtungsquantelung im Magnetfeld”. *Z. Phys.* 9:1, pp. 349–352, 1922. DOI: 10.1007/BF01326983.
- [13] D. CASTELVECCHI. “The Stern–Gerlach experiment at 100”. *Nat. Rev. Phys.* 4:3, pp. 140–142, 2022. DOI: 10.1038/s42254-022-00436-4.
- [14] M. E. PESKIN and D. V. SCHROEDER. An Introduction to quantum field theory. Reading, USA: Addison-Wesley, 1995.
- [15] I. SHIMIZU. “Search for Majorana neutrinos”. *Prog. Theor. Exp. Phys*, ptad038, 2023. eprint: <https://academic.oup.com/ptep/advance-article-pdf/doi/10.1093/ptep/ptad038/49676377/ptad038.pdf>.
- [16] E. NOETHER. “Invariante Variationsprobleme”. *Nachr. Ges. Wiss. Göttingen, Math.-Phys. Kl.* 1918, pp. 235–257, 1918. URL: <http://eudml.org/doc/59024>.
- [17] M. BAÑADOS and I. A. REYES. “A short review on Noether’s theorems, gauge symmetries and boundary terms”. *Int. J. Mod. Phys. D* 25:10, p. 1630021, 2016. arXiv: 1601.03616 [hep-th].
- [18] P. B. PAL. “Dirac, Majorana and Weyl fermions”. *Am. J. Phys.* 79, pp. 485–498, 2011. arXiv: 1006.1718 [hep-ph].
- [19] C. S. WU, E. AMBLER, R. W. HAYWARD, D. D. HOPPES, and R. P. HUDSON. “Experimental Test of Parity Conservation in Beta Decay”. *Phys. Rev.* 105, pp. 1413–1415, 1957. DOI: 10.1103/PhysRev.105.1413.
- [20] R. DAVIS, D. S. HARMER, and K. C. HOFFMAN. “Search for Neutrinos from the Sun”. *Phys. Rev. Lett.* 20, pp. 1205–1209, 1968. DOI: 10.1103/PhysRevLett.20.1205.

- [21] Q. R. AHMAD et al. on behalf of the SNO Collaboration. “Measurement of the rate of  $\nu_e + d \rightarrow p + p + e^-$  interactions produced by  $^8\text{B}$  solar neutrinos at the Sudbury Neutrino Observatory”. *Phys. Rev. Lett.* 87, p. 071301, 2001. arXiv: [nuc1-ex/0106015](https://arxiv.org/abs/nuc1-ex/0106015).
- [22] K. ABE et al. on behalf of the T2K Collaboration. “Evidence of Electron Neutrino Appearance in a Muon Neutrino Beam”. *Phys. Rev. D* 88:3, p. 032002, 2013. arXiv: [1304.0841](https://arxiv.org/abs/1304.0841) [hep-ex].
- [23] G. BELLINI, L. LUDHOVA, G. RANUCCI, and F. L. VILLANTE. “Neutrino oscillations”. *Adv. High Energy Phys.* 2014, p. 191960, 2014. arXiv: [1310.7858](https://arxiv.org/abs/1310.7858) [hep-ph].
- [24] Z. MAKI, M. NAKAGAWA, and S. SAKATA. “Remarks on the Unified Model of Elementary Particles”. *Prog. Theor. Phys.* 28:5, pp. 870–880, 1962. eprint: <https://academic.oup.com/ptp/article-pdf/28/5/870/5258750/28-5-870.pdf>.
- [25] A. ALLEGA et al. on behalf of the SNO+ Collaboration. “Improved search for invisible modes of nucleon decay in water with the SNO+ detector”. *Phys. Rev. D* 105:11, p. 112012, 2022. arXiv: [2205.06400](https://arxiv.org/abs/2205.06400) [hep-ex].
- [26] I. NEUTELINGS. “SM Particle Masses” Software Module, part of the CodeSnippets package. GitHub repository, code located at `LaTeX/TikZ/physics/SM_particles_masses.tex`. URL: [https://github.com/IzaakWN/CodeSnippets/blob/master/LaTeX/TikZ/physics/SM\\_particles\\_masses.tex](https://github.com/IzaakWN/CodeSnippets/blob/master/LaTeX/TikZ/physics/SM_particles_masses.tex), 2022.
- [27] Y. NAMBU. “Quasi-Particles and Gauge Invariance in the Theory of Superconductivity”. *Phys. Rev.* 117, pp. 648–663, 1960. DOI: [10.1103/PhysRev.117.648](https://doi.org/10.1103/PhysRev.117.648).
- [28] J. GOLDSTONE. “Field theories with «Superconductor »solutions”. *Nuovo Cimento* 19:1, pp. 154–164, 1961. DOI: [10.1007/BF02812722](https://doi.org/10.1007/BF02812722).
- [29] S. ELITZUR. “Impossibility of spontaneously breaking local symmetries”. *Phys. Rev. D* 12, pp. 3978–3982, 1975. DOI: [10.1103/PhysRevD.12.3978](https://doi.org/10.1103/PhysRevD.12.3978).

- [30] J. FRÖHLICH, G. MORCHIO, and F. STROCCHI. “Higgs phenomenon without symmetry breaking order parameter”. *Nucl. Phys. B* 190:3, pp. 553–582, 1981. DOI: [https://doi.org/10.1016/0550-3213\(81\)90448-X](https://doi.org/10.1016/0550-3213(81)90448-X).
- [31] A. MAAS. “Brout–Englert–Higgs physics: From foundations to phenomenology”. *Prog. Part. Nucl. Phys.* 106, pp. 132–209, 2019. DOI: <https://doi.org/10.1016/j.pnpnp.2019.02.003>.
- [32] K. G. WILSON and M. E. FISHER. “Critical Exponents in 3.99 Dimensions”. *Phys. Rev. Lett.* 28, pp. 240–243, 1972. DOI: [10.1103/PhysRevLett.28.240](https://doi.org/10.1103/PhysRevLett.28.240).
- [33] R. BRUN. “Particles Composition and Interactions Using the Nuon Model”. *J. Mod. Phys.* 14, pp. 623–665, 2023. DOI: [10.4236/jmp.2023.145036](https://doi.org/10.4236/jmp.2023.145036).
- [34] V. C. RUBIN, J. FORD W. K., and N. THONNARD. “Rotational properties of 21 SC galaxies with a large range of luminosities and radii, from NGC 4605 (R=4kpc) to UGC 2885 (R=122kpc).” *ApJ* 238, pp. 471–487, 1980. DOI: [10.1086/158003](https://doi.org/10.1086/158003).
- [35] A. A. PENZIAS and R. W. WILSON. “A Measurement of Excess Antenna Temperature at 4080 Mc/s.” *ApJ* 142, pp. 419–421, 1965. DOI: [10.1086/148307](https://doi.org/10.1086/148307).
- [36] R. H. DICKE, P. J. E. PEEBLES, P. G. ROLL, and D. T. WILKINSON. “Cosmic Black-Body Radiation”. *Astrophys. J.* 142, pp. 414–419, 1965. DOI: [10.1086/148306](https://doi.org/10.1086/148306).
- [37] R. DURRER. “The cosmic microwave background: the history of its experimental investigation and its significance for cosmology”. *Class. Quant. Grav.* 32:12, p. 124007, 2015. arXiv: [1506.01907](https://arxiv.org/abs/1506.01907) [astro-ph.CO].
- [38] F. ZWICKY. “On the Masses of Nebulae and of Clusters of Nebulae”. *ApJ* 86, p. 217, 1937. DOI: [10.1086/143864](https://doi.org/10.1086/143864).
- [39] A. ARBEY and F. MAHMOUDI. “Dark matter and the early Universe: a review”. *Prog. Part. Nucl. Phys.* 119, p. 103865, 2021. arXiv: [2104.11488](https://arxiv.org/abs/2104.11488) [hep-ph].

- [40] D. CLOWE et al. “A direct empirical proof of the existence of dark matter”. *Astrophys. J. Lett.* 648, pp. L109–L113, 2006. arXiv: astro-ph/0608407.
- [41] G. 'T HOOFT. “Naturalness, chiral symmetry, and spontaneous chiral symmetry breaking”. *NATO Sci. Ser. B* 59, pp. 135–157, 1980. DOI: 10.1007/978-1-4684-7571-5\\_9.
- [42] S. P. MARTIN. “A Supersymmetry primer”. *Adv. Ser. Direct. High Energy Phys.* 18, pp. 1–98, 1998. arXiv: hep-ph/9709356.
- [43] J. WESS and B. ZUMINO. “Supergauge transformations in four dimensions”. *Nuclear Physics B* 70:1, pp. 39–50, 1974. DOI: 10.1016/0550-3213(74)90355-1.
- [44] S. FERRARA, B. ZUMINO, and J. WESS. “Supergauge multiplets and superfields”. *Phys. Lett. B* 51:3, pp. 239–241, 1974. DOI: 10.1016/0370-2693(74)90283-4.
- [45] R. D. PECCEI and H. QUINN. “CP Conservation in the Presence of Pseudoparticles”. *Phys. Rev. Lett.* 38, pp. 1440–1443, 1977. DOI: 10.1103/PhysRevLett.38.1440.
- [46] R. FOOT and R. R. VOLKAS. “Neutrino physics and the mirror world: How exact parity symmetry explains the solar neutrino deficit, the atmospheric neutrino anomaly and the LSND experiment”. *Phys. Rev. D* 52, pp. 6595–6606, 1995. arXiv: hep-ph/9505359.
- [47] B. DASGUPTA and J. KOPP. “Sterile Neutrinos”. *Phys. Rept.* 928, pp. 1–63, 2021. arXiv: 2106.05913 [hep-ph].
- [48] N. ARKANI-HAMED, A. G. COHEN, and H. GEORGI. “Electroweak symmetry breaking from dimensional deconstruction”. *Phys. Lett. B* 513, pp. 232–240, 2001. arXiv: hep-ph/0105239.
- [49] M. SCHMALTZ and D. TUCKER-SMITH. “Little Higgs review”. *Ann. Rev. Nucl. Part. Sci.* 55, pp. 229–270, 2005. arXiv: hep-ph/0502182.

- [50] A. DJOUADI et al. on behalf of the MSSM Working Group. “The Minimal Supersymmetric Standard Model: Group Summary Report.” Rep. hep-ph/9901246, PM-98-45. 1999. URL: <https://cds.cern.ch/record/376049>.
- [51] S. DIMOPOULOS and H. GEORGI. “Softly broken supersymmetry and SU(5)”. *Nucl. Phys. B.* 193:1, pp. 150–162, 1981. DOI: 10.1016/0550-3213(81)90522-8.
- [52] L. GIRARDELLO and M. GRISARU. “Soft breaking of supersymmetry”. *Nucl. Phys. B.* 194:1, pp. 65–76, 1982. DOI: [https://doi.org/10.1016/0550-3213\(82\)90512-0](https://doi.org/10.1016/0550-3213(82)90512-0).
- [53] T. BANKS. *Modern Quantum Field Theory: A Concise Introduction*. Cambridge University Press, 2008. DOI: 10.1017/CB09780511811500.
- [54] G. 'T HOOFT. “How instantons solve the U(1) problem”. *Phys. Rep.* 142:6, pp. 357–387, 1986. DOI: [https://doi.org/10.1016/0370-1573\(86\)90117-1](https://doi.org/10.1016/0370-1573(86)90117-1).
- [55] S. L. ADLER. “Axial-Vector Vertex in Spinor Electrodynamics”. *Phys. Rev.* 177, pp. 2426–2438, 1969. DOI: 10.1103/PhysRev.177.2426.
- [56] J. S. BELL and R. JACKIW. “A PCAC puzzle:  $\pi^0 \rightarrow \gamma\gamma$  in the  $\sigma$  model”. *Nuovo Cim. A* 60, pp. 47–61, 1969. DOI: 10.1007/BF02823296.
- [57] A. HOOK. “TASI Lectures on the Strong CP Problem and Axions”. In: *Proceedings of Theoretical Advanced Study Institute Summer School 2018 “Theory in an Era of Data” — PoS(TASI2018)*. Vol. 333, p. 004. 2019. arXiv: 1812.02669 [hep-ph].
- [58] C. ABEL et al. “Measurement of the Permanent Electric Dipole Moment of the Neutron”. *Phys. Rev. Lett.* 124:8, p. 081803, 2020. arXiv: 2001.11966 [hep-ex].
- [59] F. WILCZEK. “Problem of Strong P and T Invariance in the Presence of Instantons”. *Phys. Rev. Lett.* 40:5, pp. 279–282, 1978. DOI: 10.1103/PhysRevLett.40.279.
- [60] S. WEINBERG. “A New Light Boson?” *Phys. Rev. Lett.* 40:4, pp. 223–226, 1978. DOI: 10.1103/PhysRevLett.40.223.

- [61] R. D. PECCEI. “The Strong CP problem and axions”. *Lect. Notes Phys.* 741, pp. 3–17, 2008. arXiv: hep-ph/0607268.
- [62] C. A. J. O’HARE. “Cosmology of axion dark matter”. *PoS COSMICWISPerS*, p. 040, 2024. arXiv: 2403.17697 [hep-ph].
- [63] K. J. BAE, H. BAER, and H. SERCE. “Prospects for axion detection in natural SUSY with mixed axion-higgsino dark matter: back to invisible?” *JCAP* 06, p. 024, 2017. arXiv: 1705.01134 [hep-ph].
- [64] W. A. BARDEEN and S.-H. H. TYE. “Current Algebra Applied to Properties of the Light Higgs Boson”. *Phys. Lett. B* 74, pp. 229–232, 1978. DOI: 10.1016/0370-2693(78)90560-9.
- [65] W. A. BARDEEN, R. D. PECCEI, and T. YANAGIDA. “Constraints on Variant Axion Models”. *Nucl. Phys. B* 279, pp. 401–428, 1987. DOI: 10.1016/0550-3213(87)90003-4.
- [66] D. B. KAPLAN. “Opening the Axion Window”. *Nucl. Phys. B* 260, pp. 215–226, 1985. DOI: 10.1016/0550-3213(85)90319-0.
- [67] M. SREDNICKI. “Axion Couplings to Matter. 1. CP Conserving Parts”. *Nucl. Phys. B* 260, pp. 689–700, 1985. DOI: 10.1016/0550-3213(85)90054-9.
- [68] J. E. KIM. “Light Pseudoscalars, Particle Physics and Cosmology”. *Phys. Rept.* 150, pp. 1–177, 1987. DOI: 10.1016/0370-1573(87)90017-2.
- [69] J. E. KIM and G. CAROSI. “Axions and the strong CP problem”. *Rev. Mod. Phys.* 82, pp. 557–601, 2010. arXiv: 0807.3125 [hep-ph].
- [70] P. SIKIVIE. “Experimental Tests of the ‘Invisible’ Axion”. *Phys. Rev. Lett.* 51, pp. 1415–1417, 1983. DOI: 10.1103/PhysRevLett.51.1415.
- [71] H. JACKSON, A. DROSTER, and K. V. BIBBER. “Axions as Dark Matter and HAYSTAC”. In: *3rd World Summit on Exploring the Dark Side of the Universe*. Pp. 195–202. 2020.

- [72] R. KHATIWADA et al. on behalf of the ADMX Collaboration. “Axion Dark Matter Experiment: Detailed design and operations”. *Rev. Sci. Instrum.* 92:12, p. 124502, 2021. arXiv: 2010.00169 [astro-ph.IM].
- [73] J. LIU et al. on behalf of the BREAD Collaboration. “Broadband Solenoidal Haloscope for Terahertz Axion Detection”. *Phys. Rev. Lett.* 128:13, p. 131801, 2022. arXiv: 2111.12103 [physics.ins-det].
- [74] J. E. KIM. “Weak-Interaction Singlet and Strong CP Invariance”. *Phys. Rev. Lett.* 43:2, pp. 103–107, 1979. DOI: 10.1103/PhysRevLett.43.103.
- [75] M. A. SHIFMAN, A. I. VAINSHTEIN, and V. I. ZAKHAROV. “Can confinement ensure natural CP invariance of strong interactions?” *Nucl. Phys. B.* 166:3, pp. 493–506, 1980. DOI: 10.1016/0550-3213(80)90209-6.
- [76] M. DINE, W. FISCHLER, and M. SREDNICKI. “A simple solution to the strong CP problem with a harmless axion”. *Phys. Lett. B* 104:3, pp. 199–202, 1981. DOI: 10.1016/0370-2693(81)90590-6.
- [77] A. R. ZHITNITSKY. “On Possible Suppression of the Axion Hadron Interactions.” *Sov. J. Nucl. Phys.* 31, p. 260, 1980.
- [78] J. DIEHL and E. KOUTSANGELAS. “DFSZ-type axions and where to find them”. *Phys. Rev. D* 107:9, p. 095020, 2023. arXiv: 2302.04667 [hep-ph].
- [79] D. ESPRIU, F. MESCIA, and A. RENAU. “Axion-Higgs interplay in the two Higgs-doublet model”. *Phys. Rev. D* 92:9, p. 095013, 2015. arXiv: 1503.02953 [hep-ph].
- [80] J. SUN and X.-G. HE. “DFSZ axion couplings revisited”. *Phys. Lett. B* 811, p. 135881, 2020. DOI: 10.1016/j.physletb.2020.135881.
- [81] L. DI LUZIO, M. GIANNOTTI, E. NARDI, and L. VISINELLI. “The landscape of QCD axion models”. *Phys. Rept.* 870, pp. 1–117, 2020. arXiv: 2003.01100 [hep-ph].

- [82] C. ANTEL et al. “Feebly Interacting Particles: FIPs 2022 workshop report”. *Eur. Phys. J. C* 83, p. 1122, 2023. arXiv: 2305.01715 [hep-ph].
- [83] G. BARENBOIM, E. J. CHUN, S. JUNG, and W. I. PARK. “Implications of an axino LSP for naturalness”. *Phys. Rev. D* 90, p. 035020, 2014. DOI: 10.1103/PhysRevD.90.035020.
- [84] G. HOSHINO. Searching for the DFSZ Axino in Collider Experiments. Phenomenology Symposium (PHENO). Collaborated with K. M. DONA, K. HARIGAYA, D. W. MILLER, J. T. OFFERMANN, B. POL, and B. J. ROSSER, 2023. URL: <https://indico.cern.ch/event/1218225/contributions/5384880/>.
- [85] . “LHC Design Report Vol.1: The LHC Main Ring”. Rep. CERN-2004-003-V1, CERN-2004-003, CERN-2004-003-V-1. 2004. DOI: 10.5170/CERN-2004-003-V-1.
- [86] E. LOPIENSKA. The CERN accelerator complex, layout in 2022. Complexe des accélérateurs du CERN en janvier 2022. General Photo, 2022. URL: <https://cds.cern.ch/record/2800984>.
- [87] J. COUPARD et al. “LHC Injectors Upgrade, Technical Design Report: v.2: Ions”. Rep. CERN-ACC-2016-0041. 2016. DOI: 10.17181/CERN.L6VM.UOMS.
- [88] E. BOLTEZAR et al. “The New CERN 50-MeV Linac.” In: *10th International Linear Accelerator Conference*. S2-2. 1980. URL: <https://accelconf.web.cern.ch/179/papers/s2-2.pdf>.
- [89] J. VOLLAIRE et al. Linac4 design report. Ed. by M. VRETENAR. Vol. 6/2020. CERN Yellow Reports: Monographs. Geneva: CERN, Sept. 2020. DOI: 10.23731/CYRM-2020-006.
- [90] S. MATTEI. “H<sup>-</sup> ion source for CERN’s Linac4 accelerator: simulation, experimental validation and optimization of the hydrogen plasma”. Presented July 24, 2017. École Polytechnique, Lausanne, 2017.

- [91] Y. BELCHENKO, G. DIMOV, and V. DUDNIKOV. “A powerful injector of neutrals with a surface-plasma source of negative ions”. *Nucl. Fusion* 14:1, p. 113, 1974. DOI: 10.1088/0029-5515/14/1/017.
- [92] M. BACAL and G. W. HAMILTON. “H<sup>-</sup> and D<sup>-</sup> Production in Plasmas”. *Phys. Rev. Lett.* 42, pp. 1538–1540, 1979. DOI: 10.1103/PhysRevLett.42.1538.
- [93] H. VERBEEK, W. ECKSTEIN, and R. BHATTACHARYA. “Negative hydrogen ion formation by backscattering from solid surfaces”. *Surf. Sci.* 95:2, pp. 380–390, 1980. DOI: 10.1016/0039-6028(80)90184-3.
- [94] T. S. PETTERSSON and P. LEFÈVRE on behalf of the LHC Study Group. “The Large Hadron Collider: conceptual design”. Rep. CERN-AC-95-05-LHC. 1995. URL: <https://cds.cern.ch/record/291782>.
- [95] W. HERR and B. MURATORI. Concept of luminosity. Ed. by D. BRANDT. Proceedings from the CERN Accelerator School at DESY, Zeuthen, Germany, in September 2003. Geneva: CERN, 2006. DOI: 10.5170/CERN-2006-002.361.
- [96] M. G. HOLLOWAY and C. P. BAKER. “Note on the Origin of the Term ‘barn’”. Rep. LAMS-523. Submitted in September 1944, 1947.
- [97] R. CALAGA. “Crab Cavities for the High-luminosity LHC”. In: *18th International Conference on RF Superconductivity*. THXA03. 2018. DOI: 10.18429/JACoW-SRF2017-THXA03.
- [98] THE ATLAS COLLABORATION. “Standard Model Summary Plots June 2024”. Rep. ATL-PHYS-PUB-2024-011. 2024. URL: <https://cds.cern.ch/record/2903866>.
- [99] THE ATLAS COLLABORATION. Delivered Luminosity versus time for 2011-2024 (p-p data only). 2024. URL: <https://twiki.cern.ch/twiki/bin/view/AtlasPublic/LuminosityPublicResultsRun3>.

- [100] D. E. SOPER. “Parton distribution functions”. *Nucl. Phys. B Proc. Suppl.* 53:1 Lattice 96, pp. 69–80, 1997. DOI: 10.1016/S0920-5632(96)00600-7.
- [101] J. WENNINGER. “Operation and Configuration of the LHC in Run 2”. Rep. CERN-ACC-NOTE-2019-0007. 2019. URL: <https://cds.cern.ch/record/2668326>.
- [102] S. FARTOUKH et al. “LHC Configuration and Operational Scenario for Run 3”. Rep. CERN-ACC-2021-0007. 2021. URL: <https://cds.cern.ch/record/2790409>.
- [103] THE ATLAS COLLABORATION. “ATLAS inner detector: Technical Design Report, 2”. Rep. CERN-LHCC-97-017, ATLAS-TDR-5. 1997. URL: <https://cds.cern.ch/record/331064>.
- [104] D. DOMINGUEZ, K. P. MOLES, and S. MEHLHASE. ATLAS detector schematics. 2021. URL: <https://cds.cern.ch/record/2777214>.
- [105] J. PEQUENÃO. Computer generated image of the ATLAS inner detector. 2008. URL: <https://cds.cern.ch/record/1095926>.
- [106] M. CAPEANS et al. on behalf of the ATLAS Collaboration. “ATLAS Insertable B-Layer Technical Design Report”. Rep. CERN-LHCC-2010-013, ATLAS-TDR-19. 2010. URL: <https://cds.cern.ch/record/1291633>.
- [107] G. AAD et al. “ATLAS pixel detector electronics and sensors”. *JINST* 3, P07007, 2008. DOI: 10.1088/1748-0221/3/07/P07007.
- [108] T. KITTELMANN, V. TSULAIA, J. BOUDREAU, and E. MOYSE. “The Virtual Point 1 event display for the ATLAS experiment”. *J. Phys. Conf. Ser.* 219:3, p. 032012, 2010. DOI: 10.1088/1742-6596/219/3/032012.
- [109] A. VOGEL. ATLAS Transition Radiation Tracker (TRT): Straw Tube Gaseous Detectors at High Rates. Tech. rep. Geneva: CERN, 2013. URL: <https://cds.cern.ch/record/1537991>.

- [110] M. AABOUD et al. on behalf of the ATLAS Collaboration. “Performance of the ATLAS Transition Radiation Tracker in Run 1 of the LHC: tracker properties”. *JINST* 12:05, P05002, 2017. arXiv: 1702.06473 [hep-ex].
- [111] J. M. STAHLMAN. “Commissioning and Performance of the ATLAS Transition Radiation Tracker with First High Energy pp and Pb-Pb collisions at LHC”. *Phys. Procedia* 37, pp. 506–514, 2012. DOI: <https://doi.org/10.1016/j.phpro.2012.02.396>.
- [112] V. L. GINZBURG and I. M. FRANK. “Radiation of a uniformly moving electron due to its transition from one medium into another”. *J. Phys. (USSR)* 9, pp. 353–362, 1945.
- [113] A. P. KOBZEV. “On the radiation mechanism of a uniformly moving charge”. *Phys. Part. Nuclei* 45:3, pp. 628–653, 2014. DOI: 10.1134/S1063779614030046.
- [114] THE ATLAS COLLABORATION. “ATLAS magnet system: Technical design report”. Rep. CERN-LHCC-97-18. 1997. DOI: 10.17181/CERN.905C.VDTM.
- [115] A. BALL et al. on behalf of the milliQan Collaboration. “Sensitivity to millicharged particles in future proton-proton collisions at the LHC with the milliQan detector”. *Phys. Rev. D* 104:3, p. 032002, 2021. arXiv: 2104.07151 [hep-ex].
- [116] G. AAD et al. on behalf of the ATLAS Collaboration. “The ATLAS Experiment at the CERN Large Hadron Collider”. *JINST* 3:08, S08003, 2008. DOI: 10.1088/1748-0221/3/08/S08003.
- [117] A. YAMAMOTO et al. “Progress in ATLAS central solenoid magnet”. *Trans. Appl. Supercond.* 10:1, pp. 353–356, 2000. DOI: 10.1109/77.828246.
- [118] THE ATLAS COLLABORATION. “ATLAS liquid argon calorimeter: Technical design report”. Rep. CERN-LHCC-96-041 ; ATLAS-TDR-2. 1996. URL: <https://cds.cern.ch/record/331061>.

- [119] H. ZHANG on behalf of the ATLAS Liquid Argon Calorimeter Group. “The ATLAS Liquid Argon Calorimeter: Overview and Performance”. *J. Phys. Conf. Ser.* 293:1, p. 012044, 2011. DOI: 10.1088/1742-6596/293/1/012044.
- [120] THE ATLAS COLLABORATION. “ATLAS tile calorimeter: Technical Design Report”. Rep. CERN-LHCC-96-042 ; ATLAS-TDR-3. 1996. DOI: 10.17181/CERN.JRBJ.7028.
- [121] THE ATLAS COLLABORATION. “Technical Design Report for the Phase-II Upgrade of the ATLAS Tile Calorimeter”. Rep. CERN-LHCC-2017-019, ATLAS-TDR-028. 2017. URL: <https://cds.cern.ch/record/2285583>.
- [122] THE ATLAS COLLABORATION. “ATLAS muon spectrometer: Technical Design Report”. Rep. CERN-LHCC-97-22, ATLAS-TDR-10. 1997. URL: <https://cds.cern.ch/record/331068>.
- [123] W. PANDURO VAZQUEZ on behalf of the ATLAS Collaboration. “The ATLAS Data Acquisition system in LHC Run 2”. *J. Phys. Conf. Ser.* 898:3, p. 032017, 2017. DOI: 10.1088/1742-6596/898/3/032017.
- [124] G. AAD et al. on behalf of the ATLAS Collaboration. “Operation of the ATLAS trigger system in Run 2”. *JINST* 15:10, P10004, 2020. arXiv: 2007.12539 [physics.ins-det].
- [125] B. STELZER on behalf of the ATLAS Collaboration. “The New Small Wheel Upgrade Project of the ATLAS Experiment”. Rep. ATL-MUON-PROC-2014-008. 2016. DOI: 10.1016/j.nuclphysbps.2015.09.182.
- [126] T. KAWAMOTO et al. on behalf of the ATLAS Collaboration. “New Small Wheel Technical Design Report”. Rep. CERN-LHCC-2013-006, ATLAS-TDR-020. 2013. URL: <https://cds.cern.ch/record/1552862>.

- [127] Y. GIOMATARIS, P. REBOURGEARD, J. ROBERT, and G. CHARPAK. “MICROMEAS: a high-granularity position-sensitive gaseous detector for high particle-flux environments”. *Nucl. Instrum. Methods Phys. Res. A* 376:1, pp. 29–35, 1996. DOI: 10.1016/0168-9002(96)00175-1.
- [128] I. R. HRISTOVA on behalf of the ATLAS Collaboration. “The Phase-I Upgrade of the ATLAS First Level Calorimeter Trigger”. Rep. ATL-DAQ-PROC-2014-015. 2014. URL: <https://cds.cern.ch/record/1711197>.
- [129] M. BEGEL et al. “Global Feature Extractor of the Level-1 Calorimeter Trigger: ATLAS TDAQ Phase-I Upgrade gFEX Final Design Report”. Rep. ATL-COM-DAQ-2016-184. 2016. URL: <https://cds.cern.ch/record/2233958>.
- [130] G. AAD et al. on behalf of the ATLAS Collaboration. “The ATLAS trigger system for LHC Run 3 and trigger performance in 2022”. *JINST* 19:06, P06029, 2024. arXiv: 2401.06630 [hep-ex].
- [131] O. ABERLE et al. High-Luminosity Large Hadron Collider (HL-LHC): Technical design report. CERN Yellow Reports: Monographs. Geneva: CERN, 2020. DOI: 10.23731/CYRM-2020-0010.
- [132] L. GONELLA on behalf of the ATLAS ITk Collaboration. “The ATLAS ITk detector system for the Phase-II LHC upgrade”. *Nucl. Instrum. Meth. A* 1045, p. 167597, 2023. DOI: 10.1016/j.nima.2022.167597.
- [133] P. FERNANDEZ MARTINEZ on behalf of the ATLAS Collaboration. “Overview of the ATLAS High-Granularity Timing Detector: project status and results”. *PoS EPS-HEP2023*, p. 525, 2024. DOI: 10.22323/1.449.0525.
- [134] THE ATLAS COLLABORATION. ATLAS Inner Tracker Layout 03-00-00. 2023. URL: <https://atlas.web.cern.ch/Atlas/GROUPS/PHYSICS/PLOTS/ITK-2023-001/>.

- [135] THE ATLAS COLLABORATION. “Technical Design Report for the Phase-II Upgrade of the ATLAS TDAQ System”. Rep. CERN-LHCC-2017-020, ATLAS-TDR-029. 2017. DOI: 10.17181/CERN.2LBB.4IAL.
- [136] THE ATLAS COLLABORATION. “Technical Design Report for the Phase-II Upgrade of the ATLAS Trigger and Data Acquisition System - Event Filter Tracking Amendment”. Rep. CERN-LHCC-2022-004, ATLAS-TDR-029-ADD-1. 2022. DOI: 10.17181/CERN.ZK85.5TDL.
- [137] G. AAD et al. on behalf of the ATLAS Collaboration. “Topological cell clustering in the ATLAS calorimeters and its performance in LHC Run 1”. *Eur. Phys. J. C* 77, p. 490, 2017. arXiv: 1603.02934 [hep-ex].
- [138] P.-A. DELSART et al. `DeriveJetScales/devel_advfit` Software package. URL: [https://gitlab.cern.ch/jaoffer/DeriveJetScales/-/tree/devel\\_advfit\\_rebase](https://gitlab.cern.ch/jaoffer/DeriveJetScales/-/tree/devel_advfit_rebase), 2022.
- [139] J. T. OFFERMANN. `ApplyJetCalib` Software package. URL: <https://gitlab.cern.ch/jaoffer/applyjetcalib>, 2022.
- [140] G. POSPELOV on behalf of the ATLAS Hadronic Calibration Group. “The overview of the ATLAS local hadronic calibration”. *J. Phys. Conf. Ser.* 160:1, p. 012079, 2009. DOI: 10.1088/1742-6596/160/1/012079.
- [141] THE ATLAS COLLABORATION. “Point Cloud Deep Learning Methods for Pion Reconstruction in the ATLAS Experiment”. Rep. ATL-PHYS-PUB-2022-040. 2022. URL: <https://cds.cern.ch/record/2825379>.
- [142] S. AGOSTINELLI et al. “GEANT4—a simulation toolkit”. *Nucl. Instrum. Methods Phys. Res. A* 506:3, pp. 250–303, 2003. DOI: 10.1016/S0168-9002(03)01368-8.

- [143] Z. BHATTI et al. on behalf of The ATLAS Collaboration. “Search for displaced decays of long-lived, massive particles in events with missing transverse energy and displaced vertices in  $\sqrt{s} = 13$  TeV  $pp$  collisions with the ATLAS detector”. Rep. ATL-COM-PHYS-2024-022. 2024. URL: <https://cds.cern.ch/record/2886709>.
- [144] V. BELIS, P. ODAGIU, and T. K. ÅRRESTAD. “Machine learning for anomaly detection in particle physics”. *Rev. Phys.* 12, p. 100091, 2024. arXiv: 2312.14190 [physics.data-an].
- [145] T. SJÖSTRAND. “Monte Carlo Generators”. In: *2006 European School of High-Energy Physics*. Pp. 51–74. Nov. 2006. arXiv: hep-ph/0611247.
- [146] M. A. DOBBS et al. “Les Houches guidebook to Monte Carlo generators for hadron collider physics”. In: *3rd Les Houches Workshop on Physics at TeV Colliders*. Pp. 411–459. Mar. 2004. arXiv: hep-ph/0403045.
- [147] A. BUCKLEY et al. “General-purpose event generators for LHC physics”. *Phys. Rept.* 504, pp. 145–233, 2011. arXiv: 1101.2599 [hep-ph].
- [148] V. D. ELVIRA. “Impact of Detector Simulation in Particle Physics Collider Experiments”. *Phys. Rept.* 695, pp. 1–54, 2017. arXiv: 1706.04293 [hep-ex].
- [149] T. YAMANAKA on behalf of the ATLAS Collaboration. “The ATLAS calorimeter simulation FastCaloSim”. *J. Phys. Conf. Ser.* 331, p. 032053, 2011. DOI: 10.1088/1742-6596/331/3/032053.
- [150] THE ATLAS COLLABORATION. “The new Fast Calorimeter Simulation in ATLAS”. Rep. ATL-SOFT-PUB-2018-002. 2018. URL: <https://cds.cern.ch/record/2630434>.
- [151] J. DUARTE and J.-R. VLIMANT. “Graph Neural Networks for Particle Tracking and Reconstruction”. 2020. arXiv: 2012.01249 [hep-ph].

- [152] D. DARULIS, R. TYSON, D. G. IRELAND, D. I. GLAZIER, B. MCKINNON, and P. PAULI. “Machine Learned Particle Detector Simulations”. 2022. arXiv: 2207.11254 [physics.data-an].
- [153] F. Y. AHMAD, V. VENKATASWAMY, and G. FOX. “A Comprehensive Evaluation of Generative Models in Calorimeter Shower Simulation”. 2024. arXiv: 2406.12898 [physics.ins-det].
- [154] A. ARVANITAKI, N. CRAIG, S. DIMOPOULOS, and G. VILLADORO. “Mini-Split”. *JHEP* 02, p. 126, 2013. arXiv: 1210.0555 [hep-ph].
- [155] G. F. GIUDICE and A. ROMANINO. “Split supersymmetry”. *Nucl. Phys. B* 699 [Erratum: Nucl.Phys.B 706, 487–487 (2005)], pp. 65–89, 2004. arXiv: hep-ph/0406088.
- [156] H. BAER, T. KRUPOVNICKAS, A. MUSTAFAYEV, E.-K. PARK, S. PROFUMO, and X. TATA. “Exploring the BWCA (bino-wino co-annihilation) scenario for neutralino dark matter”. *JHEP* 12, p. 011, 2005. arXiv: hep-ph/0511034.
- [157] G. H. DUAN, K.-I. HIKASA, J. REN, L. WU, and J. M. YANG. “Probing bino-wino coannihilation dark matter below the neutrino floor at the LHC”. *Phys. Rev. D* 98:1, p. 015010, 2018. arXiv: 1804.05238 [hep-ph].
- [158] G. AAD et al. on behalf of the ATLAS Collaboration. “Search for invisible Higgs-boson decays in events with vector-boson fusion signatures using  $139 \text{ fb}^{-1}$  of proton-proton data recorded by the ATLAS experiment”. *JHEP* 08, p. 104, 2022. arXiv: 2202.07953 [hep-ex].
- [159] R. E. SHROCK and M. SUZUKI. “Invisible decays of Higgs bosons”. *Phys. Lett. B* 110:3, pp. 250–254, 1982. DOI: 10.1016/0370-2693(82)91247-3.
- [160] G. GELMINI and M. RONCADELLI. “Left-handed neutrino mass scale and spontaneously broken lepton number”. *Phys. Lett. B* 99:5, pp. 411–415, 1981. DOI: 10.1016/0370-2693(81)90559-1.

- [161] B. FUKS, M. KLASSEN, D. R. LAMPREA, and M. ROTHERING. “Gaugino production in proton-proton collisions at a center-of-mass energy of 8 TeV”. *JHEP* 10, p. 081, 2012. arXiv: 1207.2159 [hep-ph].
- [162] B. FUKS, M. KLASSEN, D. R. LAMPREA, and M. ROTHERING. “Precision predictions for electroweak superpartner production at hadron colliders with RESUMMINO”. *Eur. Phys. J. C* 73, p. 2480, 2013. arXiv: 1304.0790 [hep-ph].
- [163] G. AAD et al. on behalf of the ATLAS Collaboration. “Search for charginos and neutralinos in final states with two boosted hadronically decaying bosons and missing transverse momentum in  $pp$  collisions at  $\sqrt{s} = 13$  TeV with the ATLAS detector”. *Phys. Rev. D* 104:11, p. 112010, 2021. arXiv: 2108.07586 [hep-ex].
- [164] F. STAUB, T. OHL, W. POROD, and C. SPECKNER. “A Tool Box for Implementing Supersymmetric Models”. *Comput. Phys. Commun.* 183, pp. 2165–2206, 2012. arXiv: 1109.5147 [hep-ph].
- [165] F. STAUB. “SARAH 4: A tool for (not only SUSY) model builders”. *Comput. Phys. Commun.* 185, pp. 1773–1790, 2014. arXiv: 1309.7223 [hep-ph].
- [166] J. ALWALL et al. “The automated computation of tree-level and next-to-leading order differential cross sections, and their matching to parton shower simulations”. *JHEP* 07, p. 079, 2014. arXiv: 1405.0301 [hep-ph].
- [167] C. S. REDINO and D. WACKEROTH. “Exploring the hadronic axion window via delayed neutralino decay to axinos at the LHC”. *Phys. Rev. D* 93:7, 2016. arXiv: 1512.06822 [hep-ph].
- [168] C. S. REDINO. “Modified Supersymmetric Dark Sectors”. PhD thesis. SUNY, Buffalo, 2015.

- [169] THE ATLAS COLLABORATION. “Performance of the reconstruction of large impact parameter tracks in the ATLAS inner detector”. Rep. ATL-PHYS-PUB-2017-014. 2017.
- [170] H. OIDE. “VrtSecInclusive: an inclusive displaced vertex reconstruction package in release 21”. Rep. ATL-COM-INDET-2018-006. 2018. URL: <https://cds.cern.ch/record/2303549>.
- [171] THE ATLAS COLLABORATION. “Performance of vertex reconstruction algorithms for detection of new long-lived particle decays within the ATLAS inner detector”. Rep. ATL-PHYS-PUB-2019-013. 2019. URL: <https://cds.cern.ch/record/2669425>.
- [172] THE ATLAS COLLABORATION. “VrtSecInclusive” Software Module, part of the Athena package, version 21.2. CERN GitLab repository. URL: [https://gitlab.cern.ch/atlas/athena/-/blob/21.2/Reconstruction/VKalVrt/VrtSecInclusive/python/VrtSecInclusive\\_Configuration.py](https://gitlab.cern.ch/atlas/athena/-/blob/21.2/Reconstruction/VKalVrt/VrtSecInclusive/python/VrtSecInclusive_Configuration.py), 2020.
- [173] T. HASTIE, R. TIBSHIRANI, and J. FRIEDMAN. The Elements of Statistical Learning. 2nd ed. Springer Series in Statistics. Springer, 2009. DOI: 10.1007/978-0-387-84858-7.
- [174] Y. COADOU. “Boosted Decision Trees”. In: *Artificial Intelligence for High Energy Physics*, chap. 2, pp. 9–58. World Scientific, 2022. DOI: 10.1142/9789811234033\_0002.
- [175] G. AAD et al. on behalf of the ATLAS Collaboration. “Electron and photon efficiencies in LHC Run 2 with the ATLAS experiment”. *JHEP* 05, p. 162, 2024. arXiv: 2308.13362 [hep-ex].
- [176] M. AABOUD et al. on behalf of the ATLAS Collaboration. “Electron reconstruction and identification in the ATLAS experiment using the 2015 and 2016 LHC proton-proton collision data at  $\sqrt{s} = 13$  TeV”. *Eur. Phys. J. C* 79:8, p. 639, 2019. arXiv: 1902.04655 [physics.ins-det].

- [177] THE ATLAS COLLABORATION. Electron Likelihood Loose Offline Config 2017 CutBL Smooth. Configuration file, 2021. URL: [https://atlas-groupdata.web.cern.ch/atlas-groupdata/ElectronPhotonSelectorTools/offline/mc20\\_20210514/ElectronLikelihoodLooseOfflineConfig2017\\_CutBL\\_Smooth.conf](https://atlas-groupdata.web.cern.ch/atlas-groupdata/ElectronPhotonSelectorTools/offline/mc20_20210514/ElectronLikelihoodLooseOfflineConfig2017_CutBL_Smooth.conf).
- [178] G. AAD et al. on behalf of the ATLAS Collaboration. “Muon reconstruction and identification efficiency in ATLAS using the full Run 2  $pp$  collision data set at  $\sqrt{s} = 13$  TeV”. *Eur. Phys. J. C* 81:7, p. 578, 2021. arXiv: 2012.00578 [hep-ex].
- [179] M. AABOUD et al. on behalf of the ATLAS Collaboration. “Measurement of the photon identification efficiencies with the ATLAS detector using LHC Run 2 data collected in 2015 and 2016”. *Eur. Phys. J. C* 79:3, p. 205, 2019. arXiv: 1810.05087 [hep-ex].
- [180] M. CACCIARI, G. P. SALAM, and G. SOYEZ. “The anti- $k_t$  jet clustering algorithm”. *JHEP* 04, p. 063, 2008. arXiv: 0802.1189 [hep-ph].
- [181] THE ATLAS COLLABORATION. “Tagging and suppression of pileup jets”. Rep. ATLAS-CONF-2014-018. 2014. URL: <https://cds.cern.ch/record/1700870>.
- [182] THE ATLAS COLLABORATION. “Forward Jet Vertex Tagging: A new technique for the identification and rejection of forward pileup jets”. Rep. ATL-PHYS-PUB-2015-034. 2015. URL: <https://cds.cern.ch/record/2042098>.
- [183] M. AABOUD et al. on behalf of the ATLAS Collaboration. “Identification and rejection of pile-up jets at high pseudorapidity with the ATLAS detector”. *Eur. Phys. J. C* 77:9 [Erratum: *Eur.Phys.J.C* 77, 712 (2017)], p. 580, 2017. arXiv: 1705.02211 [hep-ex].
- [184] THE ATLAS COLLABORATION. Pileup jet recommendations. Jet Pile-up Tagging Recommendations for R21. ATLAS internal TWiki. URL: [https://twiki.cern.ch/twiki/bin/view/AtlasProtected/PileupJetRecommendations#Jet\\_Pile\\_up\\_Tagging\\_Recommen\\_AN1](https://twiki.cern.ch/twiki/bin/view/AtlasProtected/PileupJetRecommendations#Jet_Pile_up_Tagging_Recommen_AN1).

- [185] THE ATLAS COLLABORATION. “Optimisation and performance studies of the ATLAS  $b$ -tagging algorithms for the 2017-18 LHC run”. Rep. ATL-PHYS-PUB-2017-013. 2017. URL: <https://cds.cern.ch/record/2273281>.
- [186] J. R. KLEIN and A. ROODMAN. “Blind Analysis In Nuclear And Particle Physics”. *Annu. Rev. Nucl. Part. Sci.* 55, pp. 141–163, 2005. DOI: <https://doi.org/10.1146/annurev.nucl.55.090704.151521>.
- [187] R. L. WASSERSTEIN and N. A. LAZAR. “The ASA Statement on  $p$ -Values: Context, Process, and Purpose”. *Am. Stat.* 70:2, pp. 129–133, 2016. DOI: 10.1080/00031305.2016.1154108.
- [188] A. DAFINCA, J. HENDERSON, and A. R. WEIDBERG. “Single event upset studies using the ATLAS SCT”. *JINST* 9:01, p. C01050, 2014. DOI: 10.1088/1748-0221/9/01/C01050.
- [189] G. AAD et al. on behalf of the ATLAS Collaboration. “ATLAS data quality operations and performance for 2015–2018 data-taking”. *JINST* 15:04, P04003, 2020. arXiv: 1911.04632 [physics.ins-det].
- [190] M. BOONEKAMP, F. GIANOTTI, R. A. MCPHERSON, M. NESSI, and P. NEVKSI. “Cosmic Ray, Beam-Halo and Beam-Gas Rate Studies for ATLAS Commissioning”. Rep. ATL-GEN-2004-001, ATL-COM-GEN-2004-001. 2004. URL: <https://cds.cern.ch/record/719263>.
- [191] S. GIBSON. Collimator-halo & beam-gas background signatures in the ATLAS Inner Detector. Joint ATLAS-CMS beam-induced backgrounds and radiation losses working group meeting, 2011. URL: <https://indico.cern.ch/event/138668/#3-collimator-halo-beam-gas-bac>.
- [192] M. AABOUD et al. on behalf of the ATLAS Collaboration. “Search for long-lived, massive particles in events with displaced vertices and missing transverse momentum

- in  $\sqrt{s} = 13$  TeV  $pp$  collisions with the ATLAS detector”. *Phys. Rev. D* 97:5, p. 052012, 2018. arXiv: 1710.04901 [hep-ex].
- [193] P. M. S. BLACKETT and G. P. S. OCCHIALINI. “Some photographs of the tracks of penetrating radiation”. *Proc. R. Soc. Lond. A* 139, pp. 699–726, 1933. DOI: 10.1098/rspa.1933.0048.
- [194] G. AAD et al. on behalf of the ATLAS Collaboration. “Performance of algorithms that reconstruct missing transverse momentum in  $\sqrt{s} = 8$  TeV proton-proton collisions in the ATLAS detector”. *Eur. Phys. J. C* 77:4, p. 241, 2017. arXiv: 1609.09324 [hep-ex].
- [195] M. CACCIARI, G. P. SALAM, and G. SOYEZ. “The Catchment Area of Jets”. *JHEP* 04, p. 005, 2008. arXiv: 0802.1188 [hep-ph].
- [196] G. AAD et al. on behalf of the ATLAS Collaboration. “Search for long-lived, massive particles in events with displaced vertices and multiple jets in  $pp$  collisions at  $\sqrt{s} = 13$  TeV with the ATLAS detector”. *JHEP* 2306, p. 200, 2023. arXiv: 2301.13866 [hep-ex].
- [197] R. D. COUSINS. “Lectures on Statistics in Theory: Prelude to Statistics in Practice”. 2018. arXiv: 1807.05996 [physics.data-an].
- [198] E. T. JAYNES. *Probability Theory: The Logic of Science*. Cambridge University Press, 2003.
- [199] R. J. BARLOW. “Practical statistics for particle physics”. *CERN Yellow Rep. School Proc.* 5, pp. 149–197, 2020. arXiv: 1905.12362 [physics.data-an].
- [200] M. BONAMENTE. “Three Fundamental Distributions: Binomial, Gaussian, and Poisson”. In: *Statistics and Analysis of Scientific Data*, pp. 35–54. New York, NY: Springer New York, 2017. DOI: 10.1007/978-1-4939-6572-4\_3.

- [201] D. LUENGO, L. MARTINO, M. BUGALLO, V. ELVIRA, and S. SÄRKKÄ. “A survey of Monte Carlo methods for parameter estimation”. *EURASIP J. Adv. Signal Process.* 2020:1, p. 25, 2020. DOI: 10.1186/s13634-020-00675-6.
- [202] S. CATANI, F. KRAUSS, R. KUHN, and B. R. WEBBER. “QCD matrix elements + parton showers”. *JHEP* 11, p. 063, 2001. arXiv: hep-ph/0109231.
- [203] THE LHC SUSY CROSS SECTION WORKING GROUP. SUSY Cross Sections. 2023. URL: <https://twiki.cern.ch/twiki/bin/view/LHCPhysics/SUSYCrossSections> (visited on 12/18/2023).
- [204] G. LUISONI and S. MARZANI. “QCD resummation for hadronic final states”. *J. Phys. G* 42:10, p. 103101, 2015. arXiv: 1505.04084 [hep-ph].
- [205] J. C. COLLINS, D. E. SOPER, and G. F. STERMAN. “Factorization of Hard Processes in QCD”. *Adv. Ser. Direct. High Energy Phys.* 5, pp. 1–91, 1989. arXiv: hep-ph/0409313.
- [206] J. J. ETHIER and E. R. NOCERA. “Parton Distributions in Nucleons and Nuclei”. *Annu. Rev. Nucl. Part. Sci.* 70:Volume 70, 2020, pp. 43–76, 2020. DOI: 10.1146/annurev-nucl-011720-042725.
- [207] J. BUTTERWORTH et al. “PDF4LHC recommendations for LHC Run II”. *J. Phys. G* 43, p. 023001, 2016. arXiv: 1510.03865 [hep-ph].
- [208] D. J. GROSS and F. WILCZEK. “Ultraviolet Behavior of Non-Abelian Gauge Theories”. *Phys. Rev. Lett.* 30, pp. 1343–1346, 1973. DOI: 10.1103/PhysRevLett.30.1343.
- [209] H. D. POLITZER. “Reliable Perturbative Results for Strong Interactions?” *Phys. Rev. Lett.* 30, pp. 1346–1349, 1973. DOI: 10.1103/PhysRevLett.30.1346.
- [210] A. DEUR, S. J. BRODSKY, and G. F. de TERAMOND. “The QCD Running Coupling”. *Nucl. Phys.* 90, p. 1, 2016. arXiv: 1604.08082 [hep-ph].

- [211] G. AAD et al. on behalf of the ATLAS Collaboration. “Jet energy scale and resolution measured in proton–proton collisions at  $\sqrt{s} = 13$  TeV with the ATLAS detector”. *Eur. Phys. J. C* 81:8, p. 689, 2021. arXiv: 2007.02645 [hep-ex].
- [212] K. CRANMER, G. LEWIS, L. MONETA, A. SHIBATA, and W. VERKERKE on behalf of the ROOT Development Team. “HistFactory: A tool for creating statistical models for use with RooFit and RooStats”. Rep. CERN-OPEN-2012-016. 2012. URL: <https://cds.cern.ch/record/1456844?ln=en>.
- [213] G. COWAN, K. CRANMER, E. GROSS, and O. VITELLS. “Asymptotic formulae for likelihood-based tests of new physics”. *Eur. Phys. J. C* 71 [Erratum: *Eur.Phys.J.C* 73, 2501 (2013)], p. 1554, 2011. arXiv: 1007.1727 [physics.data-an].
- [214] A. L. READ. “Presentation of search results: the CLs technique”. *J. Phys. G* 28:10, p. 2693, 2002. DOI: 10.1088/0954-3899/28/10/313.
- [215] Y. LECUN, L. BOTTOU, Y. BENGIO, and P. HAFFNER. “Gradient-based learning applied to document recognition”. *Proceedings of the IEEE* 86:11, pp. 2278–2324, 1998. DOI: 10.1109/5.726791.
- [216] X. ZHAO, L. WANG, Y. ZHANG, X. HAN, M. DEVECI, and M. PARMAR. “A review of convolutional neural networks in computer vision”. *Artif. Intell. Rev.* 57:4, p. 99, 2024. DOI: 10.1007/s10462-024-10721-6.
- [217] F. MURTAGH. “Multilayer perceptrons for classification and regression”. *Neurocomputing* 2:5, pp. 183–197, 1991. DOI: 10.1016/0925-2312(91)90023-5.
- [218] J. COGAN, M. KAGAN, E. STRAUSS, and A. SCHWARZTMAN. “Jet-Images: Computer Vision Inspired Techniques for Jet Tagging”. *JHEP* 02, p. 118, 2015. arXiv: 1407.5675 [hep-ph].

- [219] L. de OLIVEIRA, M. KAGAN, L. MACKEY, B. NACHMAN, and A. SCHWARTZMAN. “Jet-images — deep learning edition”. *JHEP* 07, p. 069, 2016. arXiv: 1511.05190 [hep-ph].
- [220] P. T. KOMISKE, E. M. METODIEV, and M. D. SCHWARTZ. “Deep learning in color: towards automated quark/gluon jet discrimination”. *JHEP* 01, p. 110, 2017. arXiv: 1612.01551 [hep-ph].
- [221] A. BOGATSKIY, T. HOFFMAN, D. W. MILLER, and J. T. OFFERMANN. “PELICAN: Permutation Equivariant and Lorentz Invariant or Covariant Aggregator Network for Particle Physics”. 2022. arXiv: 2211.00454 [hep-ph].
- [222] A. BOGATSKIY, T. HOFFMAN, D. W. MILLER, J. T. OFFERMANN, and X. LIU. “Explainable equivariant neural networks for particle physics: PELICAN”. *JHEP* 03, p. 113, 2024. arXiv: 2307.16506 [hep-ph].
- [223] A. BOGATSKIY, B. ANDERSON, J. T. OFFERMANN, M. ROUSSI, D. W. MILLER, and R. KONDOR. “Lorentz Group Equivariant Neural Network for Particle Physics”. 2020. arXiv: 2006.04780 [hep-ph].
- [224] A. BUTTER, G. KASIECZKA, T. PLEHN, and M. RUSSELL. “Deep-learned Top Tagging with a Lorentz Layer”. *SciPost Phys.* 5:3, p. 028, 2018. arXiv: 1707.08966 [hep-ph].
- [225] M. ERDMANN, E. GEISER, Y. RATH, and M. RIEGER. “Lorentz Boost Networks: Autonomous Physics-Inspired Feature Engineering”. *JINST* 14:06, P06006, 2019. arXiv: 1812.09722 [hep-ex].
- [226] H. PAN and R. KONDOR. “Permutation Equivariant Layers for Higher Order Interactions”. In: *Proceedings of The 25th International Conference on Artificial Intelligence and Statistics*. Vol. 151. Proceedings of Machine Learning Research, pp. 5987–6001. PMLR, Mar. 2022. URL: <https://proceedings.mlr.press/v151/pan22a.html>.

- [227] E. T. BELL. “The Iterated Exponential Integers”. *Ann. Math.* 39:3, pp. 539–557, 1938. DOI: 10.2307/1968633.
- [228] X. DOU, H.-K. HWANG, and C.-Y. LI. “Bell Numbers in Matsunaga’s and Arima’s Genjikō Combinatorics: Modern Perspectives and Local Limit Theorems”. *Electron. J. Comb.* 29:P2.2, 2022. DOI: 10.37236/10762.
- [229] G. AAD et al. on behalf of the ATLAS Collaboration. “Measurement of differential cross-sections in  $t\bar{t}$  and  $t\bar{t}$ +jets production in the lepton+jets final state in pp collisions at  $\sqrt{s} = 13$  TeV using 140 fb<sup>-1</sup> of ATLAS data”. *JHEP* 08, p. 182, 2024. arXiv: 2406.19701 [hep-ex].
- [230] G. AAD et al. on behalf of the ATLAS Collaboration. “Observation of quantum entanglement with top quarks at the ATLAS detector”. *Nature* 633:8030, pp. 542–547, 2024. arXiv: 2311.07288 [hep-ex].
- [231] A. M. SIRUNYAN et al. on behalf of the CMS Collaboration. “Measurement of differential  $t\bar{t}$  production cross sections using top quarks at large transverse momenta in pp collisions at  $\sqrt{s} = 13$  TeV”. *Phys. Rev. D* 103, p. 052008, 2021. DOI: 10.1103/PhysRevD.103.052008.
- [232] G. AAD et al. on behalf of the ATLAS Collaboration. “Search for heavy right-handed Majorana neutrinos in the decay of top quarks produced in proton–proton collisions at  $\sqrt{s} = 13$  TeV with the ATLAS detector”. 2024. arXiv: 2408.05000 [hep-ex].
- [233] G. AAD et al. on behalf of the ATLAS Collaboration. “Search for flavour-changing neutral-current couplings between the top quark and the Higgs boson in multi-lepton final states in 13 TeV pp collisions with the ATLAS detector”. *Eur. Phys. J. C* 84:7, p. 757, 2024. arXiv: 2404.02123 [hep-ex].

- [234] A. TUMASYAN et al. on behalf of the CMS Collaboration. “Search for CP violating top quark couplings in pp collisions at  $\sqrt{s} = 13$  TeV”. *JHEP* 07, p. 023, 2023. arXiv: 2205.07434 [hep-ex].
- [235] R. KOGLER et al. “Jet Substructure at the Large Hadron Collider: Experimental Review”. *Rev. Mod. Phys.* 91:4, p. 045003, 2019. arXiv: 1803.06991 [hep-ex].
- [236] A. J. LARKOSKI, I. MOULT, and B. NACHMAN. “Jet Substructure at the Large Hadron Collider: A Review of Recent Advances in Theory and Machine Learning”. *Phys. Rept.* 841, pp. 1–63, 2020. arXiv: 1709.04464 [hep-ph].
- [237] G. KASIECZKA, T. PLEHN, J. THOMPSON, and M. RUSSEL. Top Quark Tagging Reference Dataset. Version v0. 2019. DOI: 10.5281/zenodo.2603256.
- [238] A. BUTTER et al. “The Machine Learning landscape of top taggers”. *SciPost Phys.* 7, p. 014, 2019. arXiv: 1902.09914 [hep-ph].
- [239] C. BIERLICH et al. “A comprehensive guide to the physics and usage of PYTHIA 8.3”. *SciPost Phys. Codeb.* 2022, p. 8, 2022. arXiv: 2203.11601 [hep-ph].
- [240] J. de FAVEREAU et al. on behalf of DELPHES 3. “DELPHES 3, A modular framework for fast simulation of a generic collider experiment”. *JHEP* 02, p. 057, 2014. arXiv: 1307.6346 [hep-ex].
- [241] J. PEARKES, W. FEDORKO, A. LISTER, and C. GAY. “Jet Constituents for Deep Neural Network Based Top Quark Tagging”. 2017. arXiv: 1704.02124 [hep-ex].
- [242] P. T. KOMISKE, E. M. METODIEV, and J. THALER. “Energy flow networks: deep sets for particle jets”. *JHEP* 2019:1, p. 121, 2019. eprint: 1810.05165.
- [243] H. QU and L. GOUSKOS. “Jet tagging via particle clouds”. *Phys. Rev. D* 101:5, 2020. DOI: 10.1103/PhysRevD.101.056019.
- [244] H. QU, C. LI, and S. QIAN. “Particle Transformer for Jet Tagging”. In: *ICML 2022*. Vol. 162. PMLR, pp. 18281–18292. PMLR, 2022. arXiv: 2202.03772 [hep-ph].

- [245] S. GONG et al. “An efficient Lorentz equivariant graph neural network for jet tagging”. *JHEP* 2022:7, p. 30, 2022. arXiv: 2201.08187.
- [246] J. T. OFFERMANN, T. HOFFMAN, and A. BOGATSKIY. Top Jet W-Momentum Reconstruction Dataset. Version 1.0.0. July 2023. DOI: 10.5281/zenodo.8197723.
- [247] J. T. OFFERMANN, X. LIU, and T. HOFFMAN. HEPData4ML Software package. URL: <https://github.com/janToffermand/HEPData4ML>, 2023.
- [248] D. E. KAPLAN, K. REHERMANN, M. D. SCHWARTZ, and B. TWEEDIE. “Top Tagging: A Method for Identifying Boosted Hadronically Decaying Top Quarks”. *Phys. Rev. Lett.* 101, p. 142001, 2008. arXiv: 0806.0848 [hep-ph].
- [249] Z. JIANG et al. “Machine learning evaluation in the Global Event Processor FPGA for the ATLAS trigger upgrade”. *JINST* 19:05, P05031, 2024. arXiv: 2406.12875 [physics.ins-det].
- [250] A. BOGATSKIY, T. HOFFMAN, and J. T. OFFERMANN. “19 Parameters Is All You Need: Tiny Neural Networks for Particle Physics”. In: *37th Conference on Neural Information Processing Systems*. Oct. 2023. arXiv: 2310.16121 [hep-ph].
- [251] K. GUMPULA et al. “Graph Neural Network for Object Reconstruction in Liquid Argon Time Projection Chambers”. *J. Phys. Conf. Ser.* 2438:1, p. 012091, 2023. DOI: 10.1088/1742-6596/2438/1/012091.
- [252] A. AURISANO et al. “Graph neural network for neutrino physics event reconstruction”. *Phys. Rev. D* 110, p. 032008, 2024. DOI: 10.1103/PhysRevD.110.032008.
- [253] J. M. MUNOZ, I. BATATIA, and C. ORTNER. “Boost invariant polynomials for efficient jet tagging”. *Mach. Learn.: Sci. Technol.* 3:4, 04LT05, 2022. DOI: 10.1088/2632-2153/aca9ca.
- [254] R. DAS, G. KASIECZKA, and D. SHIH. “Feature selection with distance correlation”. *Phys. Rev. D* 109:5, p. 054009, 2024. arXiv: 2212.00046 [hep-ph].

- [255] T. CORNELISSEN, M. ELSING, I. GAVRILENKO, W. LIEBIG, E. MOYSE, and A. SALZBURGER on behalf of the ATLAS Inner Detector software group. “The new ATLAS track reconstruction (NEWT)”. *J. Phys. Conf. Ser.* 119:3, p. 032014, 2008. DOI: 10.1088/1742-6596/119/3/032014.
- [256] M. AABOUD et al. on behalf of the ATLAS Collaboration. “Performance of the ATLAS Track Reconstruction Algorithms in Dense Environments in LHC Run 2”. *Eur. Phys. J. C* 77:10, p. 673, 2017. arXiv: 1704.07983 [hep-ex].
- [257] THE ATLAS TRACKING COMBINED PERFORMANCE GROUP. ATLAS Tracking Software Tutorial. ATLAS Track Reconstruction – General Overview. 2023. URL: <https://atlassoftwaredocs.web.cern.ch/internal-links/tracking-tutorial/idoverview/>.
- [258] THE ATLAS COLLABORATION. `atlassoftwaredocs` Software package. Internal GitLab repository from which ATLAS software documentation is generated. URL: <https://gitlab.cern.ch/atlas-sw-git/atlassoftwaredocs>, 2024.
- [259] T. G. CORNELISSEN et al. “The global  $\chi^2$  track fitter in ATLAS”. *J. Phys.: Conf. Ser.* 119, p. 032013, 2008. DOI: 10.1088/1742-6596/119/3/032013.
- [260] H. GRAY. Track reconstruction with the ATLAS experiment. Joint Experimental Particle and Astroparticle seminar of UZH and ETH, Zürich, 2016. URL: <https://indico.cern.ch/event/504284/#1-track-reconstruction-in-the>.
- [261] THE ATLAS TRACKING COMBINED PERFORMANCE GROUP. ATLAS Tracking Software Tutorial. July 2021. URL: <https://atlassoftwaredocs.web.cern.ch/trackingTutorial/idoverview/>.
- [262] D. ADAMS et al. “Recommendations of the Physics Objects and Analysis Harmonisation Study Groups 2014”. Rep. ATL-COM-PHYS-2014-451. 2014. URL: <https://cds.cern.ch/record/1700874>.

- [263] THE ATLAS COLLABORATION. “AssociationUtils” Software Module, part of the Athena package, version 21.2. CERN GitLab repository. URL: <https://gitlab.cern.ch/atlas/athena/blob/21.2/PhysicsAnalysis/AnalysisCommon/AssociationUtils>, 2022.
- [264] M. CACCIARI and G. P. SALAM. “Pileup subtraction using jet areas”. *Phys. Lett. B* 659:1, pp. 119–126, 2008. arXiv: 0707.1378 [hep-ph].
- [265] A. WHARTON, W. YAO, and R. JANSKY. “ATLAS Inner Detector Track Quality Cuts for Run 2”. Rep. ATL-COM-PHYS-2014-1084. 2014. URL: <https://cds.cern.ch/record/1752536>.
- [266] THE ATLAS COLLABORATION. “Selection of jets produced in 13TeV proton-proton collisions with the ATLAS detector”. Rep. ATLAS-CONF-2015-029. 2015. URL: <https://cds.cern.ch/record/2037702>.
- [267] G. AAD et al. on behalf of the ATLAS Collaboration. “Readiness of the ATLAS Liquid Argon Calorimeter for LHC Collisions”. *Eur. Phys. J. C* 70, pp. 723–753, 2010. arXiv: 0912.2642 [physics.ins-det].
- [268] E. S. KUWERTZ et al. “ATLAS Data Quality Operations and Performance during Run 2”. Rep. ATL-COM-DAPR-2019-001. 2019. URL: <https://cds.cern.ch/record/2663169>.
- [269] G. AAD et al. on behalf of the ATLAS Collaboration. “Search for long-lived, massive particles in events with a displaced vertex and a muon with large impact parameter in  $pp$  collisions at  $\sqrt{s} = 13$  TeV with the ATLAS detector”. *Phys. Rev. D* 102:3, p. 032006, 2020. arXiv: 2003.11956 [hep-ex].
- [270] J. T. OFFERMANN, E. A. THOMPSON, E. K. FILMER, and C. OHM. `ax_crossing_estimate` Software package. `user/jaofferme/devel` code branch. URL: <https://gitlab>

b.cern.ch/atlas-phys-susy-wg/RPVLL/DisplacedVertices/dv-post-processing/ax\_crossing\_estimate/.

- [271] S. NADARAJAH. “A generalized normal distribution”. *J. Appl. Stat.* 32:7, pp. 685–694, 2005. DOI: 10.1080/02664760500079464.
- [272] M. OREGLIA. “A Study of the Reactions  $\psi' \rightarrow \gamma\gamma\psi$ ”. PhD thesis. Stanford University, Dec. 1980.
- [273] J. T. OFFERMANN and R. USHIODA. `dvm_tracking_uncertainties` Software package. Built on the `ax_crossing_estimate` project, which has contributions from E. FILMER, E. A. THOMPSON and C. OHM. URL: [https://gitlab.cern.ch/jaoffer/dvm\\_tracking\\_uncertainties](https://gitlab.cern.ch/jaoffer/dvm_tracking_uncertainties).
- [274] G. B. ARFKEN, H. J. WEBER, and F. E. HARRIS. “Chapter 17 - Group Theory”. In: *Mathematical Methods for Physicists*, 7th ed., pp. 815–870. Boston: Academic Press, 2013. DOI: 10.1016/B978-0-12-384654-9.00017-7.
- [275] S. CARROLL. “Chapter 1 - Special Relativity and Flat Spacetime”. In: *Spacetime and Geometry: An Introduction to General Relativity*, 1st ed., pp. 1–47. San Francisco: Addison Wesley, 2004. DOI: 10.1017/9781108770385.
- [276] EUROPEAN MATHEMATICAL SOCIETY. “Bilinear form”. In: *Encyclopedia of Mathematics*, EMS Press, Dec. 2016. URL: [http://encyclopediaofmath.org/index.php?title=Bilinear%5C\\_form&oldid=39935](http://encyclopediaofmath.org/index.php?title=Bilinear%5C_form&oldid=39935).
- [277] G. B. ARFKEN, H. J. WEBER, and F. E. HARRIS. “Chapter 4 - Tensors and Differential Forms”. In: *Mathematical Methods for Physicists*, 7th ed., pp. 205–249. Boston: Academic Press, 2013. DOI: 10.1016/B978-0-12-384654-9.00004-9.
- [278] G. B. ARFKEN, H. J. WEBER, and F. E. HARRIS. “Chapter 3 - Vector Analysis”. In: *Mathematical Methods for Physicists*, 7th ed., pp. 123–203. Boston: Academic Press, 2013. DOI: 10.1016/B978-0-12-384654-9.00003-7.

- [279] J. MATHEWS. “Coordinate-free rotation formalism”. *Am. J. Phys.* 44:12, pp. 1210–1210, 1976. eprint: [https://pubs.aip.org/aapt/ajp/article-pdf/44/12/1210/11888900/1210\\\_1\\\_online.pdf](https://pubs.aip.org/aapt/ajp/article-pdf/44/12/1210/11888900/1210\_1\_online.pdf).
- [280] S. VILLAR, D. W. HOGG, K. STOREY-FISHER, W. YAO, and B. BLUM-SMITH. “Scalars are universal: Gauge-equivariant machine learning, structured like classical physics”. *Adv. Neural Inf. Process. Syst.* 34, pp. 28848–28863, 2021. arXiv: 2106.06610 [cs.LG].
- [281] F. OULD-SAADA. NIKHEF Topical Lectures: Lectures on Supersymmetry. 2005.
- [282] G. LÜDERS. “On the Equivalence of Invariance under Time Reversal and under Particle-Antiparticle Conjugation for Relativistic Field Theories”. *Kong. Dan. Vid. Sel. Mat. Fys. Med.* 28N5:5, pp. 1–17, 1954.
- [283] W. PAULI. “Pauli Manuscript Collection: Exclusion principle, Lorentz group and reflection of space-time and charge”. Typed (copy) with handwritten annotations by Wolfgang Pauli. Only the first page has a reference number. Mar. 1955. URL: <https://cds.cern.ch/record/96173>.
- [284] J. S. BELL and R. E. PEIERLS. “Time reversal in field theory”. *Proc. R. Soc. Lond. A* 231:1187, pp. 479–495, 1955. DOI: 10.1098/rspa.1955.0189.
- [285] S. DAR. “The Neutron EDM in the SM: A Review”. 2000. arXiv: hep-ph/0008248.
- [286] J. H. CHRISTENSON, J. W. CRONIN, V. L. FITCH, and R. TURLAY. “Evidence for the  $2\pi$  Decay of the  $K_2^0$  Meson”. *Phys. Rev. Lett.* 13, pp. 138–140, 1964. DOI: 10.1103/PhysRevLett.13.138.
- [287] R. GOLUB and S. K. LAMOREAUX. “Neutron electric-dipole moment, ultracold neutrons and polarized  $^3\text{He}$ ”. *Phys. Rep.* 237:1, pp. 1–62, 1994. DOI: 10.1016/0370-1573(94)90084-1.
- [288] A. ANGHEL et al. “The PSI ultra-cold neutron source”. *Nucl. Instrum. Methods Phys. Res. A* 611:2, pp. 272–275, 2009. DOI: 10.1016/j.nima.2009.07.077.

- [289] B. LAUSS. “Ultracold Neutron Production at the Second Spallation Target of the Paul Scherrer Institute”. *Phys. Procedia* 51, pp. 98–101, 2014. DOI: 10.1016/j.phpro.2013.12.022.
- [290] N. F. RAMSEY. “A Molecular Beam Resonance Method with Separated Oscillating Fields”. *Phys. Rev.* 78, pp. 695–699, 1950. DOI: 10.1103/PhysRev.78.695.
- [291] G. P. SALAM. “Towards Jetography”. *Eur. Phys. J. C* 67, pp. 637–686, 2010. arXiv: 0906.1833 [hep-ph].
- [292] R. BROCK et al. on behalf of the CTEQ Collaboration. “Handbook of perturbative QCD: Version 1.0”. *Rev. Mod. Phys.* 67, pp. 157–248, 1995. DOI: 10.1103/RevModPhys.67.157.
- [293] E. SHURYAK. “Chapter 17: The QCD flux tubes”. In: *Lectures on nonperturbative QCD ( Nonperturbative Topological Phenomena in QCD and Related Theories)*, Dec. 2018. arXiv: 1812.01509 [hep-ph].
- [294] A. ALI and G. KRAMER. “Jets and QCD: A Historical Review of the Discovery of the Quark and Gluon Jets and its Impact on QCD”. *Eur. Phys. J. H* 36, pp. 245–326, 2011. arXiv: 1012.2288 [hep-ph].
- [295] S. MORETTI, L. LÖNNBLAD, and T. SJÖSTRAND. “New and old jet clustering algorithms for electron - positron events”. *JHEP* 08, p. 001, 1998. arXiv: hep-ph/9804296.
- [296] D. KROHN, J. THALER, and L.-T. WANG. “Jet Trimming”. *JHEP* 02, p. 084, 2010. arXiv: 0912.1342 [hep-ph].
- [297] S. D. ELLIS, C. K. VERMILION, and J. R. WALSH. “Recombination Algorithms and Jet Substructure: Pruning as a Tool for Heavy Particle Searches”. *Phys. Rev. D* 81, p. 094023, 2010. arXiv: 0912.0033 [hep-ph].
- [298] A. J. LARKOSKI, S. MARZANI, G. SOYEZ, and J. THALER. “Soft Drop”. *JHEP* 05, p. 146, 2014. arXiv: 1402.2657 [hep-ph].

- [299] M. DASGUPTA, A. FREGOSO, S. MARZANI, and G. P. SALAM. “Towards an understanding of jet substructure”. *JHEP* 09, p. 029, 2013. arXiv: 1307.0007 [hep-ph].
- [300] M. DASGUPTA, A. FREGOSO, S. MARZANI, and A. POWLING. “Jet substructure with analytical methods”. *Eur. Phys. J. C* 73:11, p. 2623, 2013. arXiv: 1307.0013 [hep-ph].
- [301] P. T. KOMISKE, E. M. METODIEV, B. NACHMAN, and M. D. SCHWARTZ. “Pileup Mitigation with Machine Learning (PUMML)”. *JHEP* 12, p. 051, 2017. arXiv: 1707.08600 [hep-ph].
- [302] D. BERTOLINI, P. HARRIS, M. LOW, and N. TRAN. “Pileup Per Particle Identification”. *JHEP* 10, p. 059, 2014. arXiv: 1407.6013 [hep-ph].
- [303] G. SOYEZ, G. P. SALAM, J. KIM, S. DUTTA, and M. CACCIARI. “Pileup subtraction for jet shapes”. *Phys. Rev. Lett.* 110:16, p. 162001, 2013. arXiv: 1211.2811 [hep-ph].
- [304] S. D. ELLIS and D. E. SOPER. “Successive combination jet algorithm for hadron collisions”. *Phys. Rev. D* 48, pp. 3160–3166, 1993. arXiv: hep-ph/9305266.
- [305] Y. L. DOKSHITZER, G. D. LEDER, S. MORETTI, and B. R. WEBBER. “Better jet clustering algorithms”. *JHEP* 08, p. 001, 1997. arXiv: hep-ph/9707323.
- [306] M. WOBISCH and T. WENGLER. “Hadronization corrections to jet cross-sections in deep inelastic scattering”. In: *Workshop on Monte Carlo Generators for HERA Physics (Plenary Starting Meeting)*. Pp. 270–279. Apr. 1998. arXiv: hep-ph/9907280.
- [307] S. SAPETA. “QCD and Jets at Hadron Colliders”. *Prog. Part. Nucl. Phys.* 89, pp. 1–55, 2016. arXiv: 1511.09336.
- [308] K. MOCHIZUKI. “b-jet identification algorithms and performance in the ATLAS experiment”. *Nucl. Part. Phys. Proc.* 273-275, pp. 2536–2538, 2016. DOI: <https://doi.org/10.1016/j.nuclphysbps.2015.09.450>.

- [309] C. FERRO. “B-tagging in CMS”. *EPJ Web Conf.* 28, p. 12055, 2012. arXiv: 1201.5292 [hep-ex].
- [310] M. AABOUD et al. on behalf of the ATLAS Collaboration. “Jet reconstruction and performance using particle flow with the ATLAS Detector”. *Eur. Phys. J. C* 77:7, p. 466, 2017. arXiv: 1703.10485 [hep-ex].
- [311] G. AAD et al. on behalf of the ATLAS Collaboration. “Optimisation of large-radius jet reconstruction for the ATLAS detector in 13 TeV proton–proton collisions”. *Eur. Phys. J. C* 81:4, p. 334, 2021. arXiv: 2009.04986 [hep-ex].
- [312] T. GABRIEL, D. GROOM, P. JOB, N. MOKHOV, and G. STEVENSON. “Energy dependence of hadronic activity”. *Nucl. Instrum. Methods Phys. Res. A* 338:2, pp. 336–347, 1994. DOI: 10.1016/0168-9002(94)91317-X.
- [313] A. CUKIERMAN and B. NACHMAN. “Mathematical Properties of Numerical Inversion for Jet Calibrations”. *Nucl. Instrum. Meth. A* 858, pp. 1–11, 2017. arXiv: 1609.05195 [physics.data-an].
- [314] W. R. LEO. *Techniques for Nuclear and Particle Physics Experiments: A How to Approach*. 2nd ed. Berlin: Springer, 1994. DOI: 10.1007/978-3-642-57920-2.
- [315] G. F. KNOLL. *Radiation Detection and Measurement*. 4th ed. Hoboken, NJ: John Wiley & Sons, 2010.
- [316] D. GREEN. *The physics of particle detectors*. Vol. 12. Cambridge Monographs on Particle Physics, Nuclear Physics and Cosmology. Cambridge University Press, 2000.
- [317] S. C. CURRAN and J. D. CRAGGS. *Counting tubes: theory and applications*. 1st ed. Laboratory technique monograph. New York: Academic Press, 1949. URL: <https://catalog.hathitrust.org/Record/001485199>.
- [318] Y.-S. TSAI. “Pair production and bremsstrahlung of charged leptons”. *Rev. Mod. Phys.* 46, pp. 815–851, 1974. DOI: 10.1103/RevModPhys.46.815.

- [319] C. W. FABJAN and F. GIANOTTI. “Calorimetry for particle physics”. *Rev. Mod. Phys.* 75, pp. 1243–1286, 2003. DOI: 10.1103/RevModPhys.75.1243.
- [320] R. WIGMANS. “Sampling calorimetry”. *Nucl. Instrum. Methods Phys. Res. A* 494:1 Proceedings of the 8th International Conference on Instrumentation for Colliding Beam Physics, pp. 277–287, 2002. DOI: 10.1016/S0168-9002(02)01481-X.
- [321] A. FERRARI and P. R. SALA. “Physics processes in hadronic showers”. *Frascati Phys. Ser.* 21, pp. 31–55, 2001. URL: <https://lappweb.in2p3.fr/archives/Calor2000/Contributions/Tutorials/ferrari.pdf>.
- [322] D. E. GROOM. “Energy flow in a hadronic cascade: Application to hadron calorimetry”. *Nucl. Instrum. Methods Phys. Res. A* 572:2, pp. 633–653, 2007. arXiv: physics/0605164 [physics.ins-det].
- [323] S. C. CURRAN and W. R. BAKER. “Photoelectric Alpha-Particle Detector”. *Rev. Sci. Instrum.* 19:2, pp. 116–116, 1948. DOI: 10.1063/1.1741210.
- [324] B. LUBSANDORZHIEV. “On the history of photomultiplier tube invention”. *Nucl. Instrum. Methods Phys. Res. A* 567:1 Proceedings of the 4th International Conference on New Developments in Photodetection, pp. 236–238, 2006. DOI: 10.1016/j.nima.2006.05.221.
- [325] S. V. POLYAKOV. “Chapter 3 - Photomultiplier Tubes”. In: *Single-Photon Generation and Detection*, vol. 45. Experimental Methods in the Physical Sciences, pp. 69–82. Academic Press, 2013. DOI: 10.1016/B978-0-12-387695-9.00003-2.
- [326] WIKIMEDIA COMMONS USER QWERTY123UIOP. Photo Multiplier Tube And Scintillator. 2013. URL: <https://commons.wikimedia.org/wiki/File:PhotoMultiplierTubeAndScintillator3.pdf>.

- [327] S. DONATI. “Photomultipliers”. In: *Photodetectors: Devices, Circuits and Applications*, chap. 4, pp. 31–102. John Wiley & Sons, Ltd, 2020. eprint: <https://onlinelibrary.wiley.com/doi/pdf/10.1002/9781119769958.ch4>.
- [328] PHOTONIS. Photomultiplier tubes: Principle & Applications. 2002. URL: [https://ps.ec.uchicago.edu/library/photomultipliers/Photonis\\_PMT\\_basics.pdf](https://ps.ec.uchicago.edu/library/photomultipliers/Photonis_PMT_basics.pdf).
- [329] J. H. YOO on behalf of the milliQan Collaboration. “The milliQan Experiment: Search for milli-charged Particles at the LHC”. *PoS ICHEP2018*, p. 520, 2019. arXiv: 1810.06733 [physics.ins-det].
- [330] A. BALL et al. “Search for millicharged particles in proton-proton collisions at  $\sqrt{s} = 13$  TeV”. *Phys. Rev. D* 102:3, p. 032002, 2020. arXiv: 2005.06518 [hep-ex].
- [331] S. FOROUGHI-ABARI, F. KLING, and Y.-D. TSAI. “Looking forward to millicharged dark sectors at the LHC”. *Phys. Rev. D* 104:3, p. 035014, 2021. arXiv: 2010.07941 [hep-ph].